LUND UNIVERSITY

The GLAST Satellite Calorimeter

Johansson, Georg

2008

Link to publication

Citation for published version (APA):
Johansson, G. (2008). *The GLAST Satellite Calorimeter*. [Doctoral Thesis (monograph), Department of Biomedical Engineering].

Total number of authors:
1

General rights
Unless other specific re-use rights are stated the following general rights apply:
Copyright and moral rights for the publications made accessible in the public portal are retained by the authors and/or other copyright owners and it is a condition of accessing publications that users recognise and abide by the legal requirements associated with these rights.
• Users may download and print one copy of any publication from the public portal for the purpose of private study or research.
• You may not further distribute the material or use it for any profit-making activity or commercial gain
• You may freely distribute the URL identifying the publication in the public portal

Read more about Creative commons licenses: https://creativecommons.org/licenses/

Take down policy
If you believe that this document breaches copyright please contact us providing details, and we will remove access to the work immediately and investigate your claim.

LUND UNIVERSITY

PO Box 117
221 00 Lund
+46 46-222 00 00

The GLAST Satellite Calorimeter

A CsI detector assembly for studies of cosmic high-energy gamma rays

Georg Johansson

Akademisk avhandling som för avläggande av teknologie doktorsexamen vid tekniska fakulteten vid Lunds Universitet kommer att offentligen försvaras onsdagen den 21 maj 2008, kl 10.15 i hörsal E:1406, E-huset, Ole Römers väg 3, LTH, Lunds Universitet, Lund.
Fakultetsopponent: Prof. Thomas Lindblad, Partikel- och Astropartikelfysik, Institutionen för Fysik, Kungliga Tekniska Högskolan, Stockholm

Academic thesis which, by due permission of the Faculty of Engineering at Lund University, will be publicly defended on Wednesday the 21st of May, at 10.15 a.m. in lecture hall E:1406, building E, Ole Römers väg 3, Lund University, Lund, for the degree of Doctor of Philosophy in Engineering.
Faculty opponent: Prof. Thomas Lindblad, Particle and Astroparticle Physics Group, Department of Physics, Royal Institute of Technology, Stockholm

Cover: Illustration of the GLAST satellite in orbit and a CsI crystal
Image montage by Karin Lagerström
Original image:
http://glast.gsfc.nasa.gov/public/resources/images/spacecraft_07_bkgd.html
CsI crystal photo by Georg Johansson

©Georg Johansson 2008

ISBN 978-91-628-7505-3
Report 1/08
ISSN 0346-6221
ISRN LUTEDX/TEEM--1087--SE
Printed in Sweden by Tryckeriet i E-huset, Lund 2008

Abstract

The Gamma Ray Large Area Space Telescope (GLAST) is a multi-national satellite mission with aim to study the high-energy gamma ray sky. The main instrument is the Large Area Telescope (LAT) that consists of 16 towers, each housing a silicon strip precision tracker and a CsI(Tl) calorimeter. The calorimeter is made in a hodoscopic fashion from position sensitive crystal rods measuring $333.0 \times 26.7 \times 19.9$ mm^3. Each calorimeter tower contains 8 layers of crystals (approximately 8.6 radiation lengths deep) with 12 crystals in each layer. The energy range is 30 MeV – 300 GeV.

The crystal production comprised over 2000 crystals, of which 1536 build up the GLAST calorimeter and the rest are spare and test modules. All crystals had to pass an acceptance test. The quality control procedure included tests of optical and mechanical properties and radiation hardness. The test program was successfully developed and carried through within the given time frame. Light output was found to be within 10 % for more than 1800 crystals. Light output tapering could be made within the desired range for all crystals. Mechanical dimensions were held within ± 0.3 mm. All data well met the design goals for GLAST.

During production of flight crystals small sample crystals were irradiated using a hot ^{60}Co gamma source to verify the material's radiation hardness. Correlation tests of full-sized crystals using both gamma rays and 180 MeV proton irradiation showed an accurate correspondence to the degradation of a sample crystal. The average light yield loss of a sample crystal after the specified total dose of 100 Gy was 12 %. All crystal boules were found to be well within the specified requirement of no more than 50 % light loss.

An assembly of 48 crystals arranged in 8 layers of six crystals each was tested in an accelerated particle beam at CERN in order to verify the shower reconstruction capability of the GLAST LAT calorimeter. The crystals, wrapping material and read-out photo diodes were identical with flight specifications. The test calorimeter was calibrated with muons and shower reconstruction was performed with electron beams with energies of 20, 50, 80 and 120 GeV. The required performance of the GLAST calorimeter was specified to have an energy resolution σ of maximum 20 % (for photons) in the tested energy range, position resolution σ (for muons) better than 1.5 cm and angular resolution σ (for muons) better than $15^\circ \cdot \cos^2\theta$ (with θ being the off-axis angle).The analysis of the prototype calorimeter showed that the energy resolution σ could be made better than 13 %, the position resolution σ (for showers) was of the order of a few mm, both along the longitudinal axis of the crystal and transverse, and the angular resolution σ (for showers) was better than 1°.

Populärvetenskaplig sammanfattning på svenska

GLAST är ett multinationellt forskningsprojekt med uppgift att konstruera ett satellitburet instrument som ska mäta högenergetisk kosmisk gammastrålning i rymden. GLAST står för Gamma-ray Large Area Space Telescope och är ett forskningsprojekt som drivs av den amerikanska rymdflygstyrelsen NASA i samarbete med ett flertal universitet runt om i världen. Förutom flera amerikanska universitet, bl a Stanford University, deltar forskare från Sverige, Frankrike, Tyskland, Italien och Japan. Från Sverige deltar forskare från Högskolan i Kalmar, Kungliga Tekniska Högskolan och Stockholm Universitet.

Gammastrålning kan inte passera jordens atmosfär. Därför måste man genomföra satellit- eller ballongexperiment. Strålningen skapas i kosmiska processer som är så energikrävande att de aldrig skulle kunna återskapas på jorden. Genom att studera gammastrålningen kan man få information om de processer och astronomiska objekt som skapar den. En första målsättning med projektet är därför att göra en kartläggning av himlavalvet över de gammakällor som finns. Speciellt vill man studera enskilda astronomiska objekt som emitterar särskilt intensiv gammastrålning, s k Gamma Ray Bursts, GRB:s. En synnerligen spännande möjlighet är att man eventuellt kan upptäcka gammastrålning från universums s k mörka materia. Detta är en mystisk form av materia som finns i universum och som t o m utgör största delen (cirka 85 %) av materian i universum. Vad denna materia består av är det ännu ingen som vet, men det finns teorier inom partikelfysiken som stämmer väl överens med existensen av universums mörka materia.

Ombord på GLAST-satelliten finns flera instrument, varav den s k LAT-detektorn är ett huvudinstrument. Den är uppbyggd av 4×4 identiska moduler, som vardera innehåller dels en kiselstripp-detektor för precisionsmätning av gammastrålningens riktning, dels en kalorimeter av cesiumjodid-kristaller för mätning av energin hos gammastrålningen. Kalorimetern består av sammanlagt 1536 stycken kristaller, som är cirka 30 cm långa och 2×3 cm^2 i tvärsnitt. När kristallmaterialet genomkorsas av gammastrålning börjar det lysa för ett kort ögonblick, man säger att materialet scintillerar. Mängden ljus som bildas motsvarar gammastrålningens energi. Genom att montera fotodioder på kristallernas ändytor kan mängden ljus som produceras i kristallen mätas, och

därmed kan man alltså mäta gammaenergin indirekt. Gammaenergier mellan 30 MeV och 300 GeV kommer att kunna mätas på detta sätt.

Många gammastrålar som träffar kalorimetern orsakar aldrig några spår i kiselstripp-detektorn. Man har då bara informationen från kalorimetern för att bestämma riktningen på strålningen. Var strålningen passerar en kristall, kan uppskattas genom att jämföra signalerna från de bägge fotodioderna, som sitter i var sin ände av kristallen; den närmaste ser mest ljus. Genom att lägga ihop informationen från alla kristallager kan man så rekonstruera gammastrålningens riktning.

Ett betydande svenskt bidrag till GLAST har varit produktionen av mer än 2000 kristallelement till kalorimetern. Materialet inhandlades från det ukrainska företaget Amcrys-H. De individuella kristallernas optiska kvalitet kontrollerades noggrant i det testlaboratorium som gruppen byggde upp vid Högskolan i Kalmar. Dessutom kontrollerades regelbundet materialets strålhärdighet för att garantera detektorns livstid i rymden, där strålbelastningen från ordinär kosmisk strålning är avsevärd.

En väsentlig funktionskontroll av kalorimeterkonstruktionen var ett testexperiment som den svenska forskargruppen genomförde vid CERN-laboratoriet utanför Genve tillsammans med den franska GLAST-gruppen i Bordeaux. En detektoruppställning liknande en modul i den färdiga LAT-detektorn testades i en partikelstråle från en av CERN:s acceleratorer. På så sätt kunde energiupplösning och riktningsupplösning hos en integrerad detektor verifieras. Resultatet visade att LAT-kalorimetern kan göras bättre än vad som ursprungligen antogs.

Preface

When I started as a graduate student in the GLAST project the contract with the crystal vendor Amcrys-H Ltd in Ukraine had just been signed. They were contracted to manufacture more than 2000 CsI crystals for the GLAST instrument. Crystal properties, such as optical, mechanical and radiation hardness, were accurately specified. Upon delivery from the manufacturer the actual properties of all individual crystals had to be verified. A thorough test program was worked out in close collaboration with the GLAST group at the Naval Research Laboratory in Washington D.C. It was our task in Kalmar to carry through this test program.

My responsibility was to implement the test program in the lab we built up in Kalmar. This included planning of the equipment, setting up working conditions, starting up the instrumentation, calibrating the equipment and optimizing all necessary routines. I commenced this work by spending a two week period in the GLAST group at NRL to learn about the preliminary studies already made there. One step in understanding the optical performance of the crystals as detector elements was to simulate the light transport inside a crystal, and thus theoretically model the influence of surface roughening. For this purpose I developed a Monte Carlo program.

The initial plan was that after quality assurance tests in Kalmar the crystals were to be shipped to the Saclay laboratory in France, where the French GLAST team would equip them with diodes and wrapping material, turning them into complete crystal detector elements (CDEs). The CDEs would then be assembled into towers of 8×12 crystals before being shipped to NRL. The French team had many ideas concerning wrapping techniques, optical diode bonding and mechanical support structures. This led to a close collaboration between the Kalmar group and the French team, which gave me the opportunity to visit the Saclay laboratory outside Paris.

After I had been with the GLAST collaboration for a year we decided to change the design of the calorimeter mechanical support structure, which led to changes in both the crystal dimensions and wrapping material. The latter in turn having the consequence that the crystal surface treatment had to be re-optimized. These changes were done after the first batch of crystals had been delivered and evaluated, which meant that test procedures had to be altered and re-tuned according to the new crystal specifications. It fell on my responsibility to investigate the implication of the changes and implement them into the test

procedure. This process, which eventually resulted in a better crystal specification, together with circumstances connected to the funding situation in France (which unfortunately forced the French instrumentation group at Saclay to leave GLAST), delayed the start of production of flight crystals with at least a year. During the following production phase of flight crystals I was responsible for the analysis of test results with focus on the optical performances of individual crystals. It was also my responsibility to control the overall test procedure.

Another important part of the test program comprised various measurements to verify the radiation hardness of the crystal material and its optical performance after having been exposed to large doses of ionizing radiation. This part of the program included three different types of measurements: gamma irradiation of small sample crystals, gamma irradiation of a full-size crystal and proton irradiation of a full-size crystal. Results have been published, see [46] (this article is also included in appendix A). For all measurements I made the calculation and simulation of the radiation dosage obtained from a certain exposure time with that particular equipment. This analysis is of course unique for each individual setup and the particular irradiation equipment used. I also partially planned and participated in the experimental runs, in particular the irradiation of full-size crystals from a hot ^{60}Co gamma source and in a 180 MeV proton beam from the cyclotron in Uppsala.

During two weeks in August 2003 the French GLAST group at Bordeaux in France and the Kalmar group performed a beam test experiment at CERN. An assembled prototype calorimeter of CDEs (identical to the final GLAST flight CDEs) and a design similar to the GLAST calorimeter was tested in an accelerator beam from the SPS machine at CERN. The purpose of this test experiment was to get a first rough verification of the design goals for the GLAST calorimeter as an electromagnetic shower detector.

This experiment included a large number of runs at various beam energies and with different particle beams as well as at a number of different beam inclination angles. I participated both in the setup of the experiment and the actual run conductance. My main contribution, though, has been with the subsequent analysis of data from the experiment. This process began with thoroughly calibrating the test setup for all the different run conditions. The electromagnetic shower reconstruction which followed focused on determining the energy resolution, position resolution and angular resolution of the shower axis. This result is intended to be published.

Contents

Abstract **i**

Populärvetenskaplig sammanfattning på svenska **iii**

Preface **v**

1 Introduction **1**

2 History of Cosmic Gamma Rays **3**
2.1 Gamma Rays 3
2.2 The EGRET Mission 4

3 GLAST **7**
3.1 Scientific Objectives 7
3.1.1 Particle Acceleration in Active Galactic Nuclei, Pulsars and Supernova Remnants 7
3.1.2 Resolve the Gamma Ray Sky: Unidentified Sources and Diffuse Emission 8
3.1.3 High-energy Behavior of Gamma Ray Bursts and Transients 8
3.1.4 Dark Matter and the Early Universe 9
3.2 The GLAST Instruments 10
3.2.1 The Large Area Telescope 10
3.2.2 GLAST Burst Monitor 16

4 Calorimetry and the GLAST Calorimeter **19**
4.1 The Interaction of Radiation with Matter 19
4.1.1 Electrons 20
4.1.2 Photons 23
4.2 CsI(Tl) as Detector Material 30
4.2.1 Scintillation Mechanisms 31
4.2.2 Light Read-out Techniques (PMT, Photo Diode) 33
4.2.3 Crystal Shapes, Light Collection and Surface Treatment . 36
4.2.4 Crystal Growth and Manufacturing 39
4.2.5 Radiation Damage 41
4.3 The GLAST Calorimeter 43

4.3.1 Description of the Design 43
4.3.2 Design Requirements and Goals (Full Calorimeter) 44

5 The Acceptance Tests of CsI Crystals 47
5.1 Optical Acceptance Tests 48
5.1.1 Introduction: Production Flow 49
5.1.2 Optical Test Station 49
5.1.3 Optical Test Procedure 55
5.2 Results of the Optical Acceptance Tests 69
5.2.1 Simulations 69
5.2.2 Test Station Measurements and CDEs 73
5.2.3 Retreatment of Crystal Surfaces 77
5.2.4 Test Results 77
5.3 The Mechanical Acceptance Tests 86
5.3.1 The Mechanical Requirements 86
5.3.2 The Mechanical Test Station and Procedure 86
5.3.3 Mechanical Test Results 88
5.4 The Radiation Hardness Acceptance Tests 91
5.4.1 The Boule Tests 91
5.4.2 The Full Length Crystal Tests 94
5.4.3 Test Results 95

6 Beam Test Experiment 99
6.1 Introduction 99
6.1.1 Purpose of the Test 99
6.1.2 Acquisition Runs 100
6.2 The Test Setup 101
6.2.1 The Silicon Strip Telescope 101
6.2.2 The Calorimeter 102
6.2.3 Read-out Electronics and Data Acquisition 104
6.3 Calibration Procedure 105
6.3.1 Electronic Calibration 106
6.3.2 Energy Calibration 107
6.3.3 Relative Calibration 110
6.3.4 Position Calibration 111
6.4 Electromagnetic Shower Reconstruction 113
6.4.1 Methods of Energy Reconstruction 113
6.4.2 Results of the Energy Reconstruction Test 117
6.4.3 Position Reconstruction 133
6.4.4 Fitting the Shower Direction 140

7 Summary and Conclusions 145
7.1 Summary of Results 145
7.2 Collaboration with Amcrys–H 146
7.3 Simulation of Optical Behaviour 147
7.4 Optical Acceptance Tests 147

7.5 Radiation Hardness 147
7.6 Beam Tests of a Detector Assembly 148
7.7 Concluding Remarks 149

Acknowledgements **151**

Bibliography **153**

Appendix A: Radiation tests of CsI(Tl) crystals for the GLAST satellite mission **157**

Chapter 1

Introduction

The Gamma Ray Large Area Space Telescope (GLAST) is a space mission presently scheduled for launch in May 2008. This satellite-born instrument is intended to explore the cosmic high-energy gamma-ray sky over a wide energy range, and with an unprecedented accuracy. It was designed to refine measurements done by previous gamma-ray missions and to further explore objects in the sky seen by the previous telescopes but which remained unidentified. A brief historical view of the field of cosmic gamma rays and preceding telescopes is given in chapter 2. With the GLAST instrument it will be possible to study a wide range of scientific objectives, including the nature of cold dark matter and its possible connection to super-symmetric particles (section 3.1.4). This is of particular interest for the Swedish part of the GLAST collaboration. Chapter 3 includes a brief description of some of the scientific objectives that drove the design of GLAST. It also contains a more detailed description of the GLAST instrument. The GLAST project is multinational with participants from USA, Sweden, Italy, France, Japan and Germany. The project as a whole is supervised and conducted by the US space agency NASA.

The GLAST design makes use of recent technologies and developments in order to achieve an instrument with significantly better resolutions, sensitivity and energy range than previous ones. The GLAST satellite houses two instruments: the Large Area Telescope (LAT) and the GLAST Burst Monitor (GBM). The LAT measures gamma rays above 30 MeV and includes several different technologies. The energy of the gamma rays is measured with the electromagnetic calorimeter. This is a m^3-sized detector made from CsI. It is segmented in a hodoscopic fashion and consists of 1536 crystal logs being 33 cm long. The method of electromagnetic calorimetry in general is described in chapter 4 as well as the requirements and design goals for the GLAST calorimeter. A major Swedish contribution has been procurement and quality assurance tests of more than 2000 CsI crystals for the mission, spare units, beam tests and development work. The first part of this thesis work concerns the development of an accurate test program for the CsI crystals and the investigation of their optical properties. This is described in chapter 5.

This part of the work took about one year longer than originally planned due to design changes and correction of production procedures at the manufacturer. Some of the results have been published in [46] (see also appendix A).

A prototype calorimeter being an assembly of 48 crystals was tested in an accelerator beam at CERN in order to measure electron-induced electromagnetic showers. The purpose of this test experiment was to verify the performance of an integrated assembly of CsI crystal logs mounted in a similar hodoscopic fashion as in the LAT calorimeter. The second part of this thesis work has been the analysis of data from the CERN test experiment. The goal of this analysis has been to verify the performance of the test calorimeter as a shower detector. In particular, the results should be in agreement with the design parameters for the GLAST detector, such as energy resolution and angular resolution. The CERN test experiment and data analysis together with results are described in chapter 6. These results are intended to be published.

Chapter 2

History of Cosmic Gamma Rays

This chapter provides a brief historical overview of the observations and instruments preceding the Gamma ray Large Area Space Telescope. Focus will be on the so called EGRET instrument, which was the high energy gamma ray telescope that drove the design of GLAST.

2.1 Gamma Rays

The discovery and study of gamma rays began in the end of the 18th and the beginning of the 19th century. After having discovered the X-rays, scientists found, during studies of uranium, radiation similar to the X-rays. What scientists had found was natural radioactivity.

The study and detection of gamma rays from space is more recent in science. Astronomical processes emitting gamma rays were predicted mainly in works by Feenberg and Primakoff [1], Hayakawa [2] and Morrison [3]. Most of the energy in the gamma rays from space is absorbed by the Earth's atmosphere, and therefore detectors have to be on-board a satellite or flown in a balloon. The first gamma ray telescope was carried in orbit on the Explorer-XI satellite in 1961, detecting less than 100 photons which appeared to come from all directions in space. These were thought to come from a uniform gamma ray background in the form of cosmic rays (charged particles) interacting with clouds of gas.

In the late 1960's and early 1970's gamma rays from outer space were detected by chance by a constellation of defense satellites, the Vela satellites, which were put in orbit to monitor the Earth's atmosphere to discover flashes of gamma rays from nuclear bomb blasts. Instead, the detected bursts of gamma rays came from outer space. These events are today referred to as "gamma ray bursts" (GRB), and are associated with objects that are among the most powerful seen in the universe, lasting from fractions of seconds to minutes and releasing an enormous amount of energy. GRB studies is one of the primary objectives of

GLAST, see subsection 3.1.3.

More significant detection of cosmic gamma rays took place in 1967 by the instrument on-board the OSO-3 satellite (621 events). Even greater leaps forward were taken with the SAS-2 (1972) and the COS-B (1975-1982) satellites [4]. These confirmed earlier observations and produced the first detailed map of the sky at gamma wavelengths, and also detected some point sources. However, the poor resolution of the instruments made it impossible to identify these objects with individual stars or other astronomical objects.

1977 NASA announced the construction of a satellite dedicated to study gamma ray astronomy. The Compton Gamma Ray Observatory (CGRO) was launched in 1991 and de-orbited in June 2000. It carried four major experiments with much improved spatial and timing resolution as compared to previous telescopes, thus taking advantage of the advances in detector technology during the 1980's.

The four instruments of CGRO were the Burst And Transient Source Experiment (BATSE), the Oriented Scintillation Spectrometer Experiment (OSSE), the Imaging Compton Telescope (COMPTEL) and the Energetic Gamma Ray Experiment Telescope (EGRET). The last being the predecessor of GLAST. CGRO covered an energy range of 20 keV to 30 GeV. Three methods were used to image the sources: partial or total absorption of the photon energy within a high-density medium (scintillating crystals), collimation using heavy absorbing material to block out most of the sky and realize a small field of view and, at higher energies, use the conversion process of a gamma photon to an electron-positron pair in a spark chamber, which leave a clear directional signature of the incoming ray. On the scientific agenda were a number of different phenomenon [5]: solar flares, gamma ray bursts, pulsars, nova and supernova explosions, accreting black holes of stellar mass, quasar emission and interaction of cosmic rays with interstellar medium.

One of the major discoveries made by EGRET is objects called blazars, i.e. quasars emitting most of its electromagnetic energy in the energy range 30 MeV to 30 GeV. EGRET also produced an all-sky map which is dominated by emission from interactions between cosmic rays and interstellar gas in the plane of our galaxy. COMPTEL discovered a new class of solar flares with long-duration high-energy gamma ray emission.

2.2 The EGRET Mission

Because EGRET was an instrument similar to GLAST, it is interesting to compare some details of these two experiments.

The purpose of EGRET was to obtain an advancement in high-energy astrophysics (20 MeV to 30 GeV) using a telescope with better sensitivity and greater angular and energy resolutions than previous missions. Gamma rays in this energy range are produced in the most energetic and violent phenomena known in the universe, generally associated with dynamic and non-thermal processes. Also, gamma rays have a very low interaction cross-section and can therefore

travel over great distances. So in the search for knowledge about these powerful forces a study of high-energetic gamma rays is necessary. A few examples of the scientific objectives of EGRET were [5]:

- To search for localized gamma ray sources and measure intensity, energy spectrum, position and time variation.
- Examine supernova remnants searching for evidence of cosmic-ray particle acceleration.
- Search for gamma ray bursts and study their spectra.
- Get a detailed picture of the diffuse emission for our galaxy, study the dynamics.
- Study the emission from other galaxies.

The anti-coincidence shield, a dome of plastic scintillator, surrounded the instrument and rejected charged particles (see figure 2.1). Below this there were two multilevel thin-plate spark chamber systems. The upper system was narrow spaced and was detecting gamma rays by the electron-positron pair-production process (about 35% probability above 200 MeV). It consisted of 28 spark chamber modules interleaved by 27 plates, which were 0.02 radiation lengths thick (see page 23 for a definition of the radiation length). The lower system was a wide spaced spark chamber system, and it was surrounded (above and below) by scintillator plates, also called the time of flight coincidence system, which prevented logging events going in the wrong direction or going too slow trough the detector. The initial direction could be determined from the upper spark chamber system and then the trajectory was followed down trough the lower system which then showed the entry points in the calorimeter [6].

The calorimeter consisted of a NaI crystal, eight radiation lengths deep and 76×76 cm^2 in cross section, read out by PM-tubes. The scattering characteristics from the spark chambers also aided in the determination of energy. Over the central part of the energy range the resolution was about 20% (FWHM) and fell off to about 25% above several GeV, mainly due to shower leakage, and below 100 MeV, due to energy loss in the spark chamber plates [6].

GLAST is constructed in a similar manner as EGRET. However, the techniques have been refined and other (better) materials are used. For example, the calorimeter, which in EGRET was a single large piece of scintillator crystal, is in GLAST segmented. This allows imaging of the electromagnetic shower in the calorimeter, making it possible to compensate for shower leakage and thus extending the energy range. Table 2.1 shows some of the main parameters of EGRET as compared to the minimum specified values for GLAST.

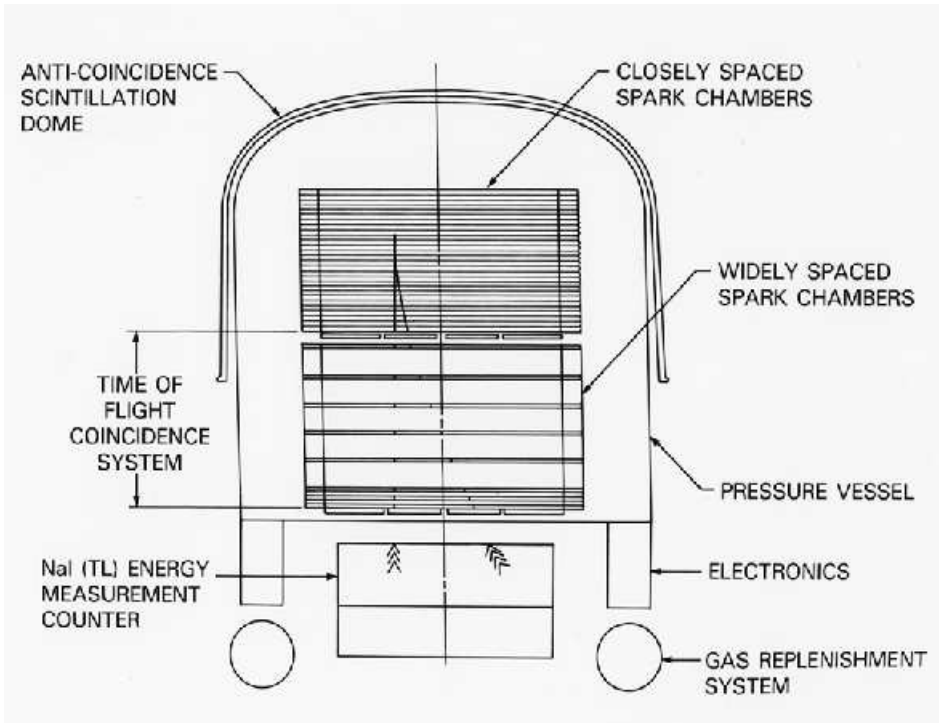

Figure 2.1: *A schematic picture of EGRET showing the different subsystems of the instrument (from [7]).*

Quantity	**EGRET**	**GLAST (min spec)**
Energy Range	30 MeV - 30 GeV	30 MeV - 300 GeV
Peak Effective Area	1500 cm^2	> 8000 cm^2
Field of View	0.5 sr	> 2 sr
Angular Resolution	$5.8°$ at 100 MeV	$< 3.5°$ at 100 MeV $< 0.15°$ at 10 GeV
Energy Resolution σ	10%	$< 10\%$
Dead-time per Event	100 ms	< 100 μs
Source Location Determination	$15'$	$< 0.5'$

Table 2.1: *The performance of EGRET versus the minimum specifications for GLAST [8].*

Chapter 3

GLAST

The first section of this chapter presents the primary objectives of the GLAST satellite mission. The second section gives a description of the two instruments on-board and their detector design.

3.1 Scientific Objectives

EGRET answered several questions about the high-energy gamma ray sky, but some of the objectives were not satisfactory answered. In addition, new astronomical objects were discovered but not identified. So EGRET also raised new questions but had not the resolution to answer them. Supposedly GLAST will be able to answer several of these due to its better resolutions.

3.1.1 Particle Acceleration in Active Galactic Nuclei, Pulsars and Supernova Remnants

Observing gamma rays is a direct probe of the mechanisms of particle acceleration at work in astrophysical systems. GLAST's sensitivity for these observations will be about 50 times better than previous missions [9]. EGRET detected more than 60 AGNs (almost all blazars) and the data has strengthened the model of AGNs as super-massive black holes with accretion disks and jets. Simulations and extrapolation of data from EGRET has shown that GLAST will be able to detect about 10000 AGNs in two years survey, giving a large population to study the properties of AGN [10] [11]. GLAST will also be able to contribute to a multi-wavelength study, combining its measurements with results from X-ray, optical and radio telescopes.

EGRET observed at least six isolated neutron stars [9] producing pulsed gamma rays (pulsar magnetospheres are thought to accelerate particles to approximately 10 GeV). Because of GLAST's large sensitivity and good spatial and spectral resolutions at large angles it will increase the database with at least an order of magnitude. The increased sensitivity at higher energies will

also allow detection of older pulsars, which EGRET could not detect because they are thought to have fainter emission but harder spectra.

Cosmic rays with energies above 10^{15} eV are thought to be shock-accelerated in SNRs [9]. X-ray and TeV observations have shown electron acceleration up to TeV energies by detection of such processes as non-thermal bremsstrahlung and inverse Compton emission from a few SNR shells. EGRET detected gamma ray sources toward a few remnants (about 10), but its angular resolution made a firm identification impossible.

3.1.2 Resolve the Gamma Ray Sky: Unidentified Sources and Diffuse Emission

The interstellar emission from the Milky Way is an intense interstellar background, which has to be modeled in detail in order to determine the galactic gamma ray background. Once a reliable background has been recorded GLAST is thought to be able to find several hundred or more galactic sources in addition to the approximately 10000 expected extragalactic sources [9]. Knowledge about the background is also important to be able to distinguish the signals from the dark matter (see subsection 3.1.4).

The number of unidentified sources increased from around 20 with COS-B to 170 with EGRET. These have remained unidentified mainly due to large error boxes in the EGRET data. Many sources are in areas related to star formation and in such areas SNRs and massive stars are often seen. Among the candidate objects are pulsars, binary systems (including a neutron star) and isolated accreting black holes [9].

Interstellar emission from the Milky Way is a prominent feature of the gamma ray sky and is produced by the interaction of cosmic rays with nuclei and with low energy photons. The densities of cosmic rays and interstellar matter are probed by the measurement of gamma ray spectra. GLAST will help answering the question whether unresolved point sources buried in the structured emission contribute to the diffuse emission.

3.1.3 High-energy Behavior of Gamma Ray Bursts and Transients

There have been recent breakthroughs in the understanding of gamma ray bursts (GRBs) with discoveries of X-ray, optical and radio afterglow. Also delayed gamma emission has been seen. GRBs involve extremely powerful, relativistic explosions, but what triggers them is still unknown. Theories suggest black hole creation and tracers of star formation at early epochs. It is thought that an explosion creates a super-relativistic blast wave resulting in afterglow that cascades down from gamma ray to radio frequencies. A GRB is a chaotic process. Yet has not two similar bursts been detected. Variation of the bursts between a fraction of a second to several hundred seconds has been seen.

GLAST will improve the measurements on the most critical part of a burst, the first explosion, thanks to a much shorter dead-time between events compared

to EGRET (GLAST having a dead-time of 20 μs as compared to EGRET's 100 ms). Furthermore, GLAST will according to detailed simulations detect about 40 times as many bursts (little more than 200 per year) as EGRET [9].

3.1.4 Dark Matter and the Early Universe

The rotation curves of galaxies, structure-formation arguments and the dynamics and weak lensing of clusters of galaxies all provide strong evidence for the existence of a vast amount of dark matter in the universe, particularly in galactic halos. GLAST will perform relevant measurements in the search for dark matter.

Supernova studies have suggested an acceleration of the cosmic expansion [12]. Together with the spectacular WMAP microwave background measurements [13] a model has been worked out for the structure of the universe which is in nice agreement with the inflationary prediction of the matter and cosmological constant contributions adding up to unity, being of the order of 0.3 and 0.7, respectively. The baryonic contribution to the matter constant is much less than the measured value, leading to the requirement of non-baryonic dark matter. The neutrinos, with its very small but non-zero mass, is an example of non-baryonic matter. The discovery and detection of it proves the existence of such matter. However, the neutrino masses are most likely not enough to compensate for all of the "missing" matter which is required [14]. One group of candidates for the non-baryonic component is Weakly Interactive Massive Particles (WIMPs). One of the more prominent candidates in this group is provided by the lightest super-symmetric particle, the neutralino χ. Its generic couplings and mass range (estimated to be 100 GeV - 10 TeV, [14]) naturally gives a relic density in the range required to explain halo dark matter. As suggested by Bergström et. al. [15] neutralinos can be detected either directly (due to its weak interactions it can be possible to detect the recoil energy caused by scattering of WIMPs) or indirectly, via annihilation into antimatter, neutrinos or gamma rays. If the neutralinos are the dark matter needed on galactic scales (and up) there should be a substantial flux of these particles in the Milky Way halo.

From GLAST's point of view the annihilations resulting in one or two gamma rays are of interest. The annihilation of two neutralinos, interacting with one another, will result in either two gamma rays, each carrying the energy equal to the mass m_χ of a neutralino, or one Z^0 boson and one gamma ray with energy equal to $m_\chi \left(1 - m_Z^2/4m_\chi^2\right)$. The detection probability of these mono-energetic photons depends on the density profile of the dark matter halo, which today is poorly known. However, N-body simulations [16] have suggested what the profile finally will look like, and, if it is correct, it would lead to a much enhanced annihilation rate towards the centre of the Milky Way. It would also show a characteristic angular dependence of the signal, something which will be of much help when trying to distinguish it from the galactic and extragalactic gamma ray background.

3.2 The GLAST Instruments

GLAST hosts two instruments, the Large Area Telescope (LAT) and the Gamma Ray Burst Monitor (GBM). The LAT consists of four subsystems: an anti-coincidence shield, a precision tracker, a calorimeter and the data acquisition system. The design is modular and the tracker and calorimeter is arranged in 4×4 "towers" with the anti-coincidence shield surrounding the tracker modules. The tracker is a pair conversion instrument, with an energy dependent conversion probability of the incoming gamma into an electron-positron pair which is detected in the layers of the tracker and the energy of the pair is measured when reaching the calorimeter. The GBM has a large field-of-view in order to fast and accurately locate gamma ray bursts and provide the LAT with triggers.

3.2.1 The Large Area Telescope

GLAST's main instrument is the Large Area Telescope (LAT) (see figure 3.1). The LAT is constructed in a way similar to EGRET, i.e. an anti-coincidence shield, a tracker and a calorimeter, though there are differences in choices of materials and used techniques (see figure 3.2). Great care has been taken into a design which will be able to measure direction and energy of gamma rays with good resolution over a wide field-of-view, while rejecting background from cosmic rays. The technologies chosen are such with a history of successful application and high reliability in space science and high-energy physics. The different detectors have been simulated, and tested in beams to verify simulations. The tracker and the calorimeter are composed of 16 identical modular towers, arranged four by four, supported by a low-mass grid structure. Each tower contains read-out electronics for the detector elements.

The performance of LAT is essential for the search for traces of the dark matter annihilations. The measurements made by EGRET in the region of the galactic center [17] show high statistical evidence for a gamma ray source. However, due to its limited angular resolution, EGRET was not able to determine whether the source is diffuse or point-like, though it seemed more diffuse than point-like. The detected flux around the galactic centre exceeds the gamma ray flux expected from the diffuse component using the standard model of the interaction of cosmic rays with the interstellar medium. The flux detected around the galactic center may come from a superposition of the cosmic gamma ray background and gamma photons from the annihilation of dark matter. Simulations and calculations in [18] points out that GLAST will, thanks to its larger effective area, better energy and angular resolution and wider energy range as compared to EGRET, be able to give a much more detailed picture of the nature of the excess gamma flux. Apart from the mono-energetic spectral lines mentioned on page 9, the annihilation of a WIMP pair may contain a generation of π^0 which decay into two gamma photons. That is, the same photon energy as coming from the cosmic ray background. The spectral shape of the background is modeled using theory and by extrapolating data from higher latitudes and longitudes. The hope is to identify a WIMP induced distortion of

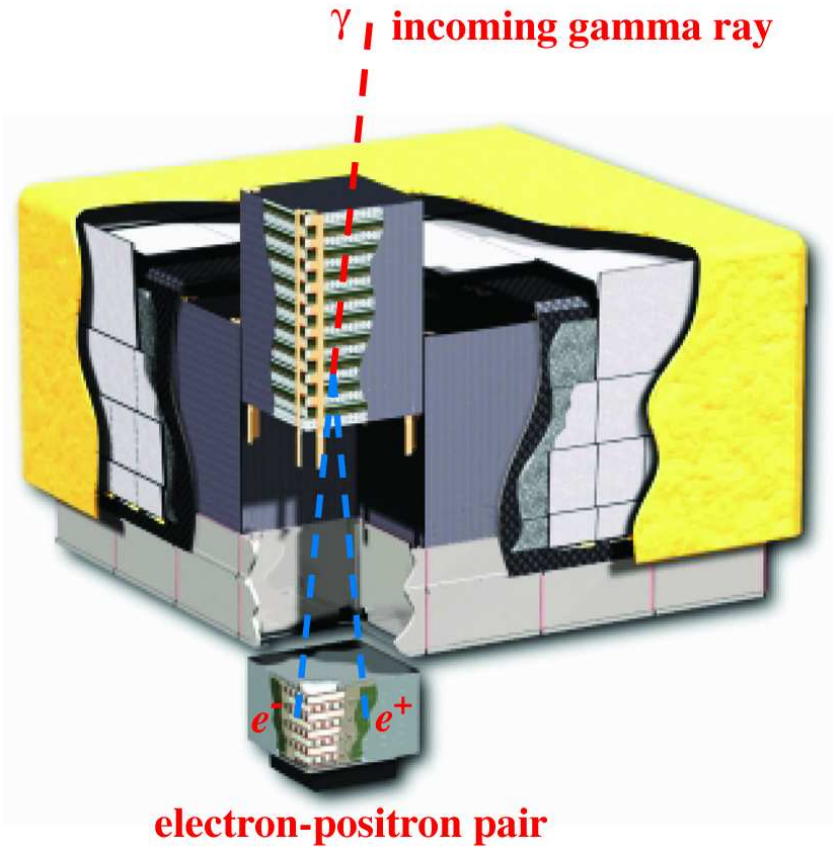

Figure 3.1: *Schematic view of the Large Area Telescope*

the background spectrum at relatively high energies (above 1 GeV), [18].

The Anti-Coincidence Detector

The anti-coincidence detector (ACD) is the first line of defense against the high flux of charged particle background (cosmic electrons, protons and nuclei), estimated to be up to 10^5 times higher than the desired signal rate. The ACD covers the entire tracker towers down to the calorimeter. It will be the main instrument identifying other than gamma ray particles.

The shield is composed of 89 plastic scintillator tiles, about 1 cm thick and of various dimensions, from which light is collected via wave-shifting fibers (see figure 3.3). The tiles overlap in one dimension and scintillating fiber ribbons covers the gaps in the other dimension. Two sets of clear fiber light guides runs from the tiles to the photo multiplier tubes (PM-tubes) used for readout. Two separate PM-tubes per tile are used, in total 194; each can individually

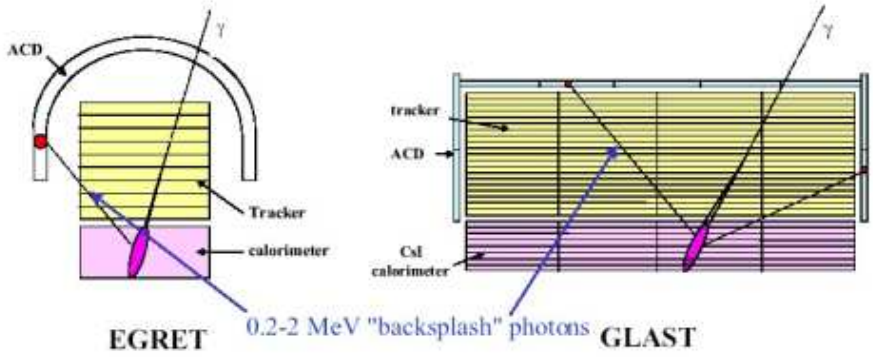

Figure 3.2: *A schematic view showing the ACD function of both EGRET and GLAST for comparison.*

Figure 3.3: *A photo of one of the plastic scintillator tiles used in GLAST together with the wave-shifting fibers to be connected to the PMT used for readout. Photo taken from [19].*

.

be powered on/off and adjusted in high voltage gain. The average detection efficiency is designed to be at least 0.9997 over the entire area of the ACD, providing the system with a fast veto signal. The tiles are surrounded by a thermal blanket, designed to maintain the working temperature at specified level, and a micrometeoroid shield to protect the instrument from small meteoroids and space debris. These 3 layers together have a thickness less than 0.04 radiation lengths.

The Tracker

The tracker utilizes the phenomenon of pair conversion; the incoming photon interacts with heavy nuclei in a layer of high-density material, the conversion foil made of tungsten. This interaction creates an electron-positron pair which in turn is detected with repeated layers of silicon strip detectors. The trajectories of the pair is then reconstructed and provides the direction of the incoming photon (see figure 3.4). The process of pair production provides a unique signature for photons in the whole telescope, another defense against the high background flux.

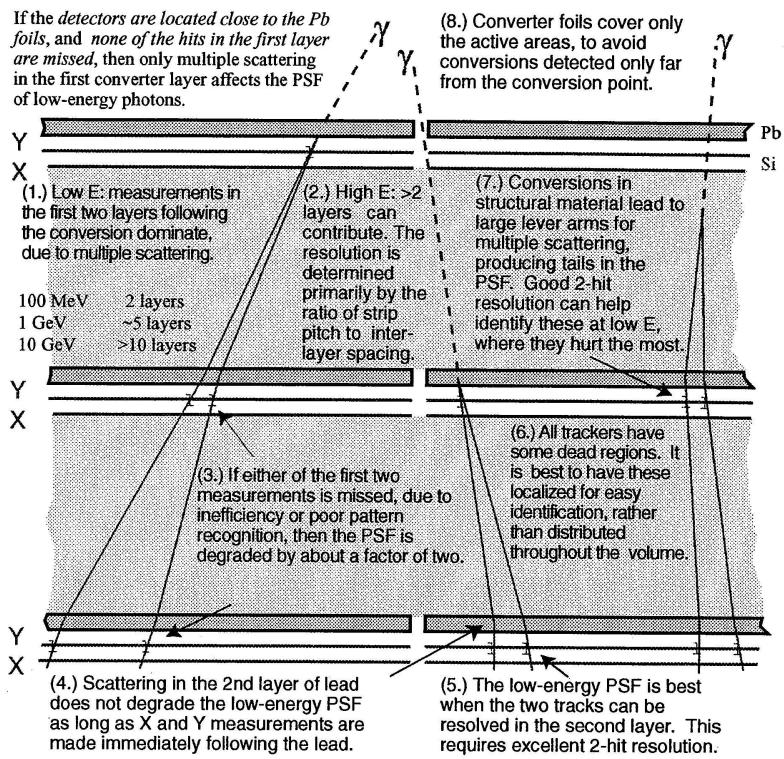

Figure 3.4: *Schematic picture of how the tracker gets its signals. Picture adapted from [9].*

Each tracker tower module is made up of 19 trays, and the trays in turn are composed of a panel upon which are mounted the converter foils, the detectors and readout electronics. Apart from the top and bottom tray they each support silicon strip detectors on both the upper and lower face. The top tray has silicon detectors only on the lower face and the bottom tray has silicon only on its upper face. The top 16 trays have converter foils on their lower faces mounted, as seen from the top, before the silicon detector. The detector is divided into two parts with respect to the thickness of the conversion foils ("front" and "back" detectors). The top 12 trays includes converter foils with a thickness of 3.0 % of a radiation length; the following four trays have foils that are 18 % of a radiation length thick. The last two trays have no converter foil at all. On each tray the strips run in parallel, one layer measures one coordinate and alternating trays are rotated 90° with respect to each other. In that way each converter foil is followed by a pair of detector planes measuring both X and Y coordinates along the particle track with the third dimension of the trajectory is given by the measurements of all trays. The gap between the planes in such an $X - Y$ pair is 2 mm.

The use of silicon-strip detectors was chosen instead of the other two alternatives considered, gas micro-strip detectors and scintillating fibers, mainly because it, in a thin detector plane, has high detection efficiency (≥ 99 %), very good position resolution (in this application ≤ 60 μm) and large signal to noise ratio ($\geq 20 : 1$). Strips used here are 400 μm thick and the pitch is 228 μm.

Pair conversion trackers contain more material than normally put into a tracker device. Multiple scattering and bremsstrahlung production limits the obtainable resolution. To get optimal results the electron-positron pair must be detected immediately after the conversion. At low energies (about 100 MeV) missing the first layer means a factor of 2 in resolution. Therefore the detector layers are mounted as close to the converter foil as possible.

A crude energy measurement for photons missing the calorimeter can be made by analyzing the multiple scattering angles from the electron-positron pair.

The tracker is designed so that at least 65% of the photons with energy greater than 10 GeV shall convert into an e^-e^+ pair (25% of the conversions shall be in the front detector). The reliability shall be at least 96% over five years (concerning component failure).

The Calorimeter

The primary task of the calorimeter is to perform accurate energy measurements of the electromagnetic shower resulting from the pair conversion in the tracker. It is designed to make measurements in the energy range of 30 MeV to 300 GeV, as required, possibly higher. Furthermore, it will assist in the rejection of cosmic ray background by correlating the position and the direction of the shower in the calorimeter with the trajectory measured in the tracker. To be able to better monitor and image the shower the calorimeter is segmented, which is a significant improvement compared to EGRET which had only one

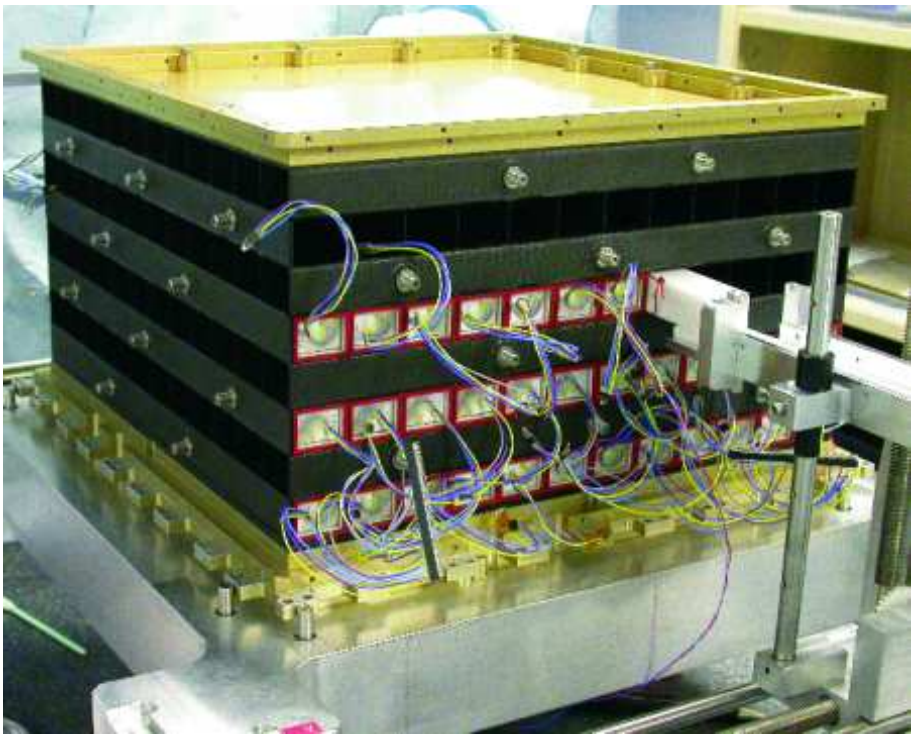

Figure 3.5: *Shown is one of the towers of the calorimeter. The picture was taken during the insertion of crystals into the carbon fiber composite structure. (Photo from [20]).*

large scintillating crystal.

A calorimeter tower module (see figure 3.5) is composed of 96 crystal detector elements (CDEs), mechanical support structures and readout electronics. A CDE has five components: one crystal log of scintillating thallium-doped cesium iodide (CsI(Tl)), two dual PIN photo diodes (DPD), an optical bond, highly reflecting wrapping material and two end caps. The crystal logs measure 326.0 $\times$ 19.9 $\times$ 26.7 mm^3 and are read out at their end faces using the DPDs. In order to meet the specified requirement on the wide energy range without saturation, and to be able to measure with high resolution, the photo diodes have two separated sensitivity areas, one large being 147 mm^2, handling the lower energy regions, and one small being 25.2 mm^2, handling the higher energy range. There are two individual amplifiers for each diode area, called LEX1 and LEX8 for the big area and HEX1 and HEX8 for the small area. For the small area, the gain of HEX8 is approximately eight times that of HEX1. The amplifiers for the big area are similar, i.e. the gain of LEX8 is eight times the gain of LEX1. In the overlap between the small and the big area the gain of LEX1 is eight times that of HEX8. So the highest gain (LEX8) is approximately 512 times the lowest

gain (HEX1). Each gain is adjustable.

The mechanical support structure is made of carbon fiber composite and the crystals are arranged in a hodoscopic fashion, i.e. alternating orthogonal layers. Each calorimeter tower is 8 layers deep with 12 CDEs in each layer. The total depth of the calorimeter will correspond to 8.6 radiation lengths.

Triggering

The LAT is self-triggering and the tracker provides the principal trigger, the so called level 1 trigger, when detection of a conversion pair in three adjacent $X - Y$ layers has occurred. The level 1 trigger also checks if there is a signal in the ACD which would indicate a charged particle background event. Due to that some high energy photons will not convert until they reach the calorimeter (i.e. leave no trace in the tracker) there is a possibility for the calorimeter to trigger the LAT and start the data collection at level 1.

The level 2 trigger uses a fast and efficient track finding algorithm performed on each tower in parallel. The purpose is to check for track alignment between the calorimeter and the tracker. It also traces the signal back to the ACD-tiles to search for vetoes. Vetoes at level 2 are not applied to calorimeter triggered events since a charged background particle would have triggered the tracker.

The third and last trigger level performs an event reconstruction for the full instrument. The complete ACD hit patter is then compared with the tracks in the tracker and calorimeter, thus avoiding the case in which back-scattered particles from the calorimeter hits the ACD and creating a veto (see figure 3.2).

3.2.2 GLAST Burst Monitor

The GBM provides a fast trigger when a gamma ray burst occurs, in approximately 2 s the space craft has calculated a course location of the burst and can alert the LAT to redirect and start taking data for detection of high-energy gamma afterglow. It can also provide a fast signal to ground-based systems to re-point their telescopes, in the search for afterglow in other wavelengths, for example in the optical or radio band.

The GBM is a complementary instrument on GLAST and will be sensitive to photon energies in the range 5 keV to 30 MeV, providing an overlap with the LAT and the two instruments will be an excellent tool for analysis of energy spectra in a very large band. The detectors (figure 3.6) are mounted on the two sides of the satellite not occupied by the solar panels. The GBM energy range is divided into two sub ranges.

The lower region from 5 keV to about 1 MeV is covered by 12 thallium-doped sodium iodide crystals (NaI(Tl)) arranged in four groups with three detectors in each group and pointing in different directions of the sky. The detectors are 1.27 cm thick and 12.7 cm in diameter, the thickness is optimized for this energy range and NaI was chosen for its relatively low cost matched with a high efficiency. The crystals are read out using a PM-tube of the same diameter as the crystal. The NaI detectors provides the trigger for GBM, when at least two

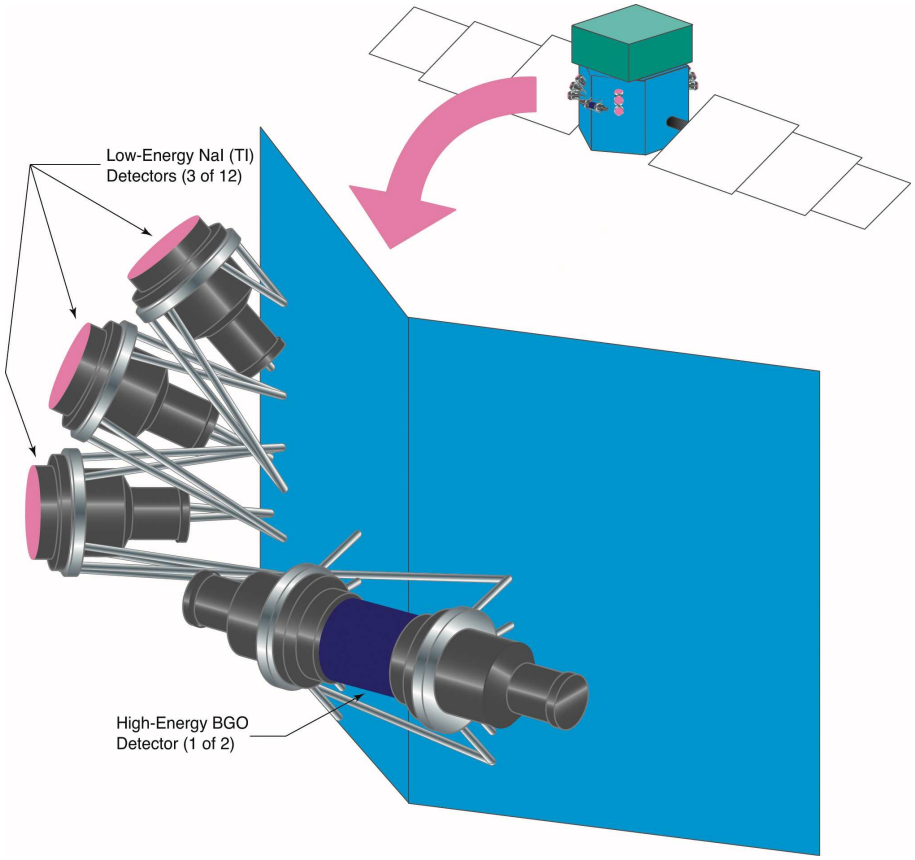

Figure 3.6: *Shown are the NaI and BGO detectors belonging to the GBM.*

of the detectors shows an increase in counting rate above some threshold value decided by the background. The location of the burst is also calculated from the data from the NaI detectors by comparing the counting rates in the different detector elements.

The upper energy region from 150 keV to 30 MeV is covered by two cylindrical bismuth germanate (BGO) crystals being 12.7 cm long and 12.7 cm in diameter. Readout is done in both ends using the same type of PM-tubes as for the NaI detectors. It provides a good overlap in the lower end with the NaI detectors and in the upper end with LAT.

Chapter 4

CsI(Tl) Calorimetry and the GLAST Calorimeter

The GLAST calorimeter measures the energy of the incoming particle by absorption. The amount of light produced in the electromagnetic shower within the calorimeter gives the energy estimation. This chapter presents an overview of the interaction mechanisms for energy loss of photons and electrons in matter followed by a description of the technique of using scintillating materials for calorimetry with emphasis on CsI(Tl). The design of the GLAST calorimeter is then presented followed by its design requirements and goals.

4.1 The Interaction of Radiation with Matter

The principle of detecting radiation involves transfer of some or all of its energy to the detector material, so the operation of the detector depends on how the radiation to be detected interacts with the material of the detector. To predict the response and analyzing results must be based on familiarity with the fundamental mechanisms by which radiation interact and lose energy in matter. The types of radiation can be divided into four groups; heavy charged particles (protons, α-particles and heavy ions), neutrons, fast electrons and gamma- and X-rays. The charged particles continuously interact through the coulomb force with the electrons and, less likely though, nuclei in any medium through which the radiation passes. The neutral particles must first undergo a catastrophic interaction resulting in full or partial energy transfer to electrons, nuclei or charged particle products of nuclear reactions. If such a catastrophic interaction does not take place then there is no way of telling the particle ever passed through the detector. Heavy charged particles will only be mentioned briefly and neutrons will be left out of the discussion here, since the main interest is gamma rays and the gamma induced electromagnetic showers. The description here follows [21] and [22].

The cross-section is a quantity often used when describing particle interac-

tion and is the quantity which gives a measure of the probability for a reaction to occur and may be calculated if the form of the basic interaction between the particles is known. If there exist a flux of F particles per unit time incident on a target particle then some of them will be scattered into a solid angle $d\Omega$ per unit time, when averaged over a period of time this number will tend toward a fixed number $dN_s/d\Omega$, where N_s is the average number of particles scattered per unit time. The differential cross-section is defined as

$$\frac{d\sigma}{d\Omega}(E,\Omega) = \frac{1}{F} \cdot \frac{dN_s}{d\Omega}, \tag{4.1}$$

that is, $d\sigma/d\Omega$ is the number of particles scattered into $d\Omega$ per unit time and flux. This value generally varies with both energy and the angle at which the particle is scattered. Integration over all angles will yield the total cross-section $\sigma(E)$ for a specific energy. In real cases though, the target contains many interaction centers and assuming that the target centers are uniformly distributed, then the number of centers per unit perpendicular area seen by the incident particles is $N \cdot \delta x$, with N being the density of centers and δx the thickness of the material along the direction of the beam. Then the average number of scattered particles, at all angles, will be

$$N_{tot} = n_{inc} \cdot N \cdot \delta x \cdot \sigma(E), \tag{4.2}$$

where n_{inc} is the total number of incident particles. Dividing both sides with n_{inc} gives the probability for a single particle to undergo scattering.

4.1.1 Electrons

Like all charged particles electrons and positrons passing through matter lose energy by collisions acting through the Coulomb force. The major difference in the characteristics of scattering is that the electrons and positrons often have paths with large deviations from the original trajectory due to its low mass, i.e. the same rest mass as the orbital electrons with which it is interacting. Under certain conditions backscattering is not unusual. Another effect of their small mass is that there is a probability for the electrons to lose energy by emitting radiation when scattered in the electrical field of a nucleus, so called bremsstrahlung. Heavy charged particles often have quite straight paths through matter because their mass is much greater than the electron mass with which they interact.

Collision Loss

The result of the collision of the incident charged particle and the orbital electrons in the material is that energy is transferred to the orbital electron and either raising it to a higher lying shell, excitation, or remove it completely from the absorbing atom, ionization. The energy transferred is at the expense of the incident particle and its velocity is decreased. When entering the absorbing medium the charged particle immediately interacts with many electrons simultaneously and the net effect is a decrease in velocity, a continuous process until

the particle is stopped. The average energy loss per unit path length is often called the stopping power and is expressed as dE/dx. It was first calculated for heavy charged particles by Bohr, using classical arguments (energy transfer parametrized in terms of impact parameter) but later calculations based on quantum mechanics (parametrized in terms of momentum transfer) was performed by Bethe, Bloch and others, refining the results. The equation is called the Bethe-Bloch formula and it differs somewhat for heavy charged particles and electrons/positrons, mainly due to the difference in mass. If the incident particle is a heavy charged particle it can be considered undeflected from its original path because its mass is many order of magnitudes larger than the mass of the electrons with which it interacts, but in the case of an incident electron it can no longer be assumed to be undeflected because now the collision takes place between two identical particles. The formula describes the average energy loss due to ionization only, it does not take into account the energy loss due to bremsstrahlung (see page 22). Below are the formulas for the two cases [22].

Heavy charged particles:

$$-\frac{dE}{dx} = 2\pi N_a r_e^2 m_e c^2 \rho \frac{Z}{A}\frac{z^2}{\beta^2}\left[ln\left(\frac{2m_e\gamma^2 v^2 W_{max}}{I^2}\right) - 2\beta^2 - \delta - 2\frac{C}{Z}\right] \tag{4.3}$$

where
$2\pi N_a r_e^2 m_e c^2 = 0.1535$ MeV·cm^2/g
$r_e = 2.817 \cdot 10^{-13}$ cm, classical electron radius
$m_e = 9.109 \cdot 10^{-34}$ g, electron mass
$N_a = 6.022 \cdot 10^{23}$ mol^{-1}, Avogadro's number
I, the mean excitation potential
Z, atomic number of absorbing material
A, atomic weight of absorbing material
ρ, density of absorbing material
z, charge of incident particle in units of e^-
$\beta = v/c$, of the incident particle
$\gamma = 1/\sqrt{1-\beta^2}$
δ, density correction - applicable at extremely relativistic energies
C, shell correction - applicable at low energies
$W_{max} = (2m_e c^2\beta^2\gamma^2)/(1 + 2\frac{m_e}{M}\sqrt{1+\beta^2\gamma^2} + (\frac{m_e}{M})^2)$, maximum energy transfer in a single collision (head-on) with M being the mass of the incident particle

Electrons/Positrons:

$$-\frac{dE}{dx} = 2\pi N_a r_e^2 m_e c^2 \rho \frac{Z}{A}\frac{1}{\beta^2}\left[ln\frac{\tau^2(\tau+2)}{2(I/m_e c^2)^2} + F(\tau) - \delta - 2\frac{C}{Z}\right] \tag{4.4}$$

where τ is the kinetic energy of the incident particle expressed in units of $m_e c^2$ and $F(\tau)$ is a function depending on the incoming particle being an electron:

$$F(\tau) = 1 - \beta^2 + \frac{\frac{\tau^2}{8} - (2r+1)ln2}{(\tau^2+1)}, \tag{4.5}$$

or a positron:

$$F(\tau) = 2ln2 - \frac{\beta^2}{12}\left(23 + \frac{14}{\tau+2} + \frac{10}{(\tau+2)^2} + \frac{4}{(\tau+2)^3}\right). \tag{4.6}$$

The mean excitation potential is essentially the average orbital frequency ν from Bohr's classical formula (see [22]) times Planck's constant. Theoretically it is the logarithmic average of orbital frequencies weighted by so-called oscillator strengths of the atomic levels, in practice a very difficult quantity to calculate. Instead empirical values have been deduced from actual measurements [22].

The density and shell effects become important at high and low energies, respectively. The density effect arises from the fact that the electric field of the incident particle tends to polarize the atoms and as a result electrons far from the path of the particle will be shielded from the full electric field intensity. Collisions with these outer lying electrons will therefore contribute less than predicted by the Bethe-Bloch formula without the correction [22]. The term "density effect" stems from the fact that this correction depends on the density of orbital electrons and therefore also on the density of the absorber. The shell correction account for effects when the velocity of the incident particle is of the order of the orbital velocity of the bound electrons. Then the assumption that the target electrons are stationary is no longer valid. For heavy charged particles the Bethe-Bloch formula finally breaks down at low energies because the ion starts picking up electrons. Further corrections have been worked out and can also be taken into account but is generally not necessary because of a very small contribution in the order of 1% or less.

Bremsstrahlung

Electrons have a finite probability to be considerably scattered in the electric field of a nucleus and in that way lose energy by emitting electromagnetic radiation, or "bremsstrahlung". Classically this can be understood as radiation arising from the acceleration of the electron in the electric field of the nucleus. The emission probability increases with energy and is inversely proportional to the square of the particle mass, i.e. the lighter the particle is the greater is the cross-section. Since the emission depends on the strength of the electrical field felt by the electron, the amount of screening from the atomic electrons plays an important role. The theory behind screening and how to use it in the calculation of the cross-section is too extensive to bring up here. For example the calculation of the total cross-section will in the end yield an integration which can be solved analytically in the limiting cases of no screening or complete screening, all other cases must be solved numerically [22].

A general expression for radiation losses $-dE/dx$ deduced from classical theory can be written as (see [21])

$$-\left(\frac{dE}{dx}\right)_{rad} = \frac{NEZ(Z+1)e^4}{137m_e^2c^4}\left(4\ln\frac{2E}{m_ec^2} - \frac{4}{3}\right) \tag{4.7}$$

As can be seen from the formula (4.7) the radiative losses are most important for high energy electrons and absorber materials with large atomic number. Apart from the collision losses, in which the electron loses its energy continuously in small steps, almost all the radiation energy can be emitted in one or two photons. So there are large fluctuations in the energy lost and radiation emitted.

The energy loss by radiation depends strongly on the material. A critical energy can be defined at which the collision loss equals the radiation loss. Above this energy radiation losses dominates over collision losses. A frequently used parametrization of the energy loss is in terms of the radiation length, defined as the distance over which the electron energy is reduced by a factor $1/e$ due to radiation loss only. Considering the high-energy range where collision losses can be ignored relative to the radiation losses then the energy after a certain distance x is:

$$E = E_0 e^{-x/L_{rad}} \tag{4.8}$$

where L_{rad} is the radiation length. If the distance traveled is expressed in L_{rad} instead of x then the energy loss due to emission of radiation is roughly material independent. The radiation length in CsI(Tl) is 1.86 cm [23], and as a comparison it is 0.56 cm in lead (Pb) and 36.1 cm in water [22].

4.1.2 Photons

Since photons (gamma rays are at focus in this thesis) carry no charge the continuous energy loss process through collisions with bound electrons is not possible, instead the photon must either transfer all or part of its energy to atomic electrons in abrupt steps, dramatically changing the history of the photon either by partial energy loss and scattering through a significant angle or that the photon disappears, i.e. transferring all its energy to an electron. Whereas the charged particles are continuously degraded in energy when passing through material the photon either interact or not, i.e. measuring a beam of mono-energetic particles after passing a thin slab of material the charged particles will show a lower energy but (basically) unchanged in intensity and the photons will all have the same energy but will be attenuated in intensity. If the probability of interaction is low the photon can pass through the detector without the slightest hint it were ever there. There are three frequent interactions which will be dealt with here; photoelectric effect, Compton scattering and pair production. Another possible interaction, which is much less probable, is nuclear reactions, which will be omitted here.

Photoelectric Effect

This interaction involves the absorption of the photon by an atomic electron followed by the ejection of the electron from the atom. All the energy from

the photon is transferred to the work of overcoming the binding energy of the bounded electron and the rest of the energy is turned into kinetic energy, E_K:

$$E_K = h\nu - E_b \tag{4.9}$$

where $h\nu$ is the energy of the photon and E_b is the binding energy of the electron. This interaction cannot occur with a free electron since it would be impossible for the electron to both absorb the photon and conserve momentum; this requires the presence of a recoiling nucleus. For energies from about 100 keV and above the photon is most likely going to be absorbed by an electron in the K-shell which has the highest binding energy. The cross-section drops drastically for photons just below the lower K-shell energy limit (because the electrons in the K-shell no longer are available for absorption), and continuing towards even lower energies the cross-section starts to increase again as the energies of the L-shell are approached, and after passing this, it drops again, and so on. The interaction cross-section depends both on the photon energy E and atomic number Z but no simple analytic expression exists for all Z over a substantial energy range. At energies above the MeV level the dependence on Z goes as the power of 4 to 5. This implies that high-Z materials are favorable in the absorption of photons. The equation describing the cross-section (for energies above the K-shell) is:

$$\sigma_{ph} = 4\alpha^4\sqrt{2}Z^5\phi_0\left(\frac{m_e c^2}{h\nu}\right) \tag{4.10}$$

with $\alpha = 1/137$ and $\phi_0 = (8\pi r_e^2)/3 = 6.651 \cdot 10^{-25}$ cm^2.

Compton Scattering

Compton scattering takes place between the photon and a free electron assumed to be at rest. Theoretically the electron can be free but in matter most electrons are bounded. If the photon energy is high with respect to the electron binding energy, this can be neglected and the electron can be considered to be free. The energy and momentum must be conserved so the scattered photon, which now has transferred part of its energy into kinetic energy of the electron, and the electron are scattered through an angle on either side of the original path of the photon. The formulas for the energies of the scattered photon and electron, respectively, are (standard relativistic kinematics):

$$h\nu' = \frac{h\nu}{1 + \gamma(1 - \cos\theta)} \tag{4.11}$$

$$T_e = h\nu - h\nu' = \frac{h\nu\gamma(1 - \cos\theta)}{(1 + \gamma(1 - \cos\theta)} \tag{4.12}$$

where $h\nu$ is the initial photon energy, γ is $h\nu/m_e c^2$, and θ is the angle between the original path of the photon and the scattered photon. If now ϕ is the angle

between the original path of the photon and the scattered electron then the relations are:

$$\cos\theta = 1 - \frac{2}{(1+\gamma)^2 \tan^2\phi + 1} \tag{4.13}$$

$$\cot\phi = (1+\gamma)\tan\frac{\theta}{2} \tag{4.14}$$

For small scattering angles θ very little energy is transferred, and the larger the angle the greater energy is transferred to the electron. The cross-section for the angular distribution is calculated using the Klein-Nishina formula, obtained from quantum electrodynamics [22]:

$$\frac{d\sigma}{d\Omega} = \frac{r_e^2}{2\left[1+\gamma\left(1-\cos\theta\right)\right]^2} \cdot \left(1+\cos^2\theta + \frac{\gamma^2\left(1-\cos\theta\right)^2}{1+\gamma\left(1-\cos\theta\right)}\right) \tag{4.15}$$

Integrating this over all solid angles, $d\Omega$, gives the total probability per electron for Compton scattering to occur.

$$\sigma_C = 2\pi r_e^2 \left\{ \frac{1+\gamma}{\gamma^2}\left[\frac{2\left(1+\gamma\right)}{1+2\gamma} - \frac{1}{\gamma}\ln\left(1+2\gamma\right)\right] + \frac{1}{2\gamma}\ln\left(1+2\gamma\right) - \frac{1+3\gamma}{\left(1+2\gamma\right)^2} \right\} \tag{4.16}$$

Using the Klein-Nishina formula the maximum recoil energy for an electron can be calculated as:

$$T_{max} = h\nu\left(\frac{2\gamma}{1+2\gamma}\right) \tag{4.17}$$

and this is known as the "Compton edge". Since it is the energy transferred to the recoil electron which is of importance, it is of interest to understand its energy spectrum because this is what can be measured. In the energy spectrum of the recoil electron there will be a continuum reaching from zero energy up to the energy of the Compton edge where the spectrum abruptly will fall off (see figure 4.1).

Pair Production

The process of pair production $\gamma \rightarrow e^+e^-$ requires the photon energy to be at least 1.022 MeV, i.e. twice the rest mass energy of an electron. The process of pair creation requires, just as in the case of photoelectric effect, the presence of a recoiling nucleus (or electron) for conservation of the momentum. If a photon has energy higher than the double rest mass, the excess goes to kinetic energy of the pair. The pair production is theoretically related to bremsstrahlung and is therefore also depending on the amount of screening of the nucleus, which in turn has effects on the cross-section. As mentioned in the section about

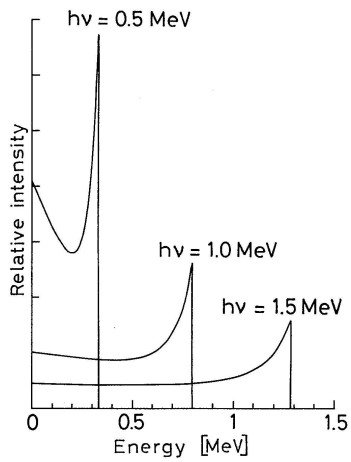

Figure 4.1: *Shown is the typical continuum followed by the characteristic cut-off in the electron recoil energy spectrum from Compton scattering. The initial photon energy is $h\nu$. In a real spectrum the photo-peak (from the photoelectric effect) at energy $h\nu$ would be superimposed to the Compton spectrum. Figure from [22].*

bremsstrahlung this leads to expressions which has to be numerically integrated for all other cases than no screening or complete screening.

After slowing down in the medium the positron will eventually annihilate with an electron in the absorber creating a secondary product of the initial interaction in the form of two photons with energy of 511 keV each.

When measuring the direction of a gamma ray the opening angle between the electron and positron from pair production contains vital information. Because of momentum conservation the deflection of the electron and the positron from the initial photon direction have to be of equal amount. The opening angle thus gives the direction of the incident gamma ray. It is therefore important for the GLAST tracker to be constructed in such a way that the detection of the electron-positron pair takes place as soon as possible after the conversion of the photon. The segmentation and detailed geometry of the tracker, where the first 12 layers of converter foils are thinner than the last four, minimizes the probability/interference of multiple scattering between adjacent detection layers in order to get an early measurement of the opening angle. As mentioned in the previous section for electron energy loss, the electrons and positrons suffer significant deviations from their initial direction when losing energy by collision.

The dominating interaction depends on the energy of the photon and the absorbing material as indicated in figure 4.2.

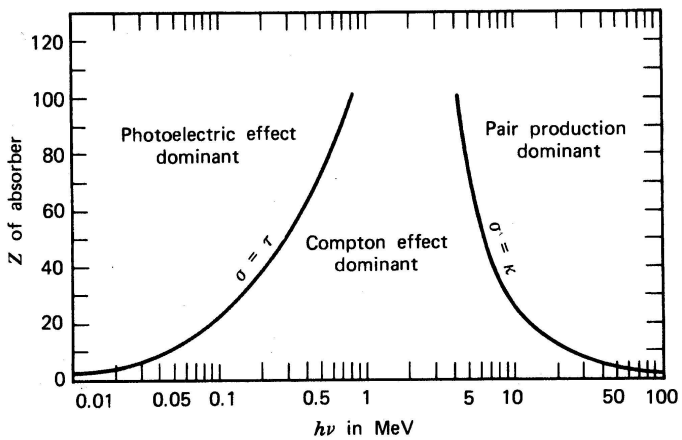

Figure 4.2: *Graphs of Z versus energy showing the dominant interaction regions for the three different processes of photon absorption. Figure from [21].*

Electron-Photon Showers

Photons of very high energy cause a cascade, or electromagnetic "shower", of photons, electrons and positrons when entering a medium. This is due to alternating pair production and bremsstrahlung. When entering the absorbing matter the photon will convert into an electron-positron pair which in turn will emit bremsstrahlung photons. These will in turn convert into new electron-positron pairs and so on. This will continue until the kinetic energy of the electron-positron pairs drop to a critical value after which the energy loss preferably takes place via collision losses, thus halting the shower. The process is of statistical nature. A simple model can be constructed using the notion of radiation length, describing the mean number of particles and their mean energy as a function of penetration depth. Suppose the shower originates from a particle with energy E_0. On average this will have converted into an electron-positron pair after one radiation length with each particle now carrying $E_0/2$. After two radiation lengths each particle will, on average, have emitted a bremsstrahlung photon with approximately half the energy of the charged particle. At this stage there are four particles, two photons and an electron-positron pair, which each has an energy of $E_0/4$. After yet another radiation length the bremsstrahlung photons will have converted into an e^-e^+ pair and the original pair will have emitted new bremsstrahlung. So that after t radiation lengths the number of particles will be

$$N \simeq 2^t \tag{4.18}$$

each with an energy of $E(t) \simeq E_0/2^t$. Same result would be obtained had the original particle been an electron or positron. Assuming that the shower

stops abruptly, the maximum depth can be found as the critical energy (i.e., the energy of each particle when the production of new particles stops):

$$E_c = E(t_{max}) = E_0/2^{t_{max}} \tag{4.19}$$

so that:

$$t_{max} = \ln(E_0/E_c)/(\ln 2). \tag{4.20}$$

However, the shower seldom stops abruptly; instead there are fluctuations of the degradation over many radiation lengths resulting in a long tail in the plotted function of energy loss versus penetration depth (in radiation lengths). More precise calculations have to be performed with Monte Carlo simulations, often showing an exponential rise which reaches a broad maximum before falling off.

As the shower develops in the absorber it also spreads out in the lateral dimension, often referred to as the transverse profile of the cascade. The effects causing this are for example the opening angle of the e^-e^+ pair, multiple scattering of the electrons and the emission of bremsstrahlung which can move far away from the longitudinal axis. As with the radiation length there is a convenient unit which is basically independent of the absorbing medium, the Moliere radius, defined as

$$R_M = L_{rad} \cdot \frac{E_s}{E_c} \tag{4.21}$$

where $E_s = m_e c^2 \sqrt{4\pi/\alpha} = 21.2$ MeV and E_c is the critical energy. The shower is during the first radiation lengths concentrated around a dense core which then is surrounded by a tenuous halo extending to quite large distances. Approximately 90% of the shower is contained within a distance of $2R_M$ from the longitudinal axis. Worth to notice here is that the Moliere radius does not depend on the energy of the incoming photon.

Knowledge of the longitudinal and transverse shower profiles are of much importance when designing electromagnetic calorimeters for particle physics since the concept often is to completely absorb the showers induced in the bulk of the detector and measure the energy of the original incoming particle, which initiated the shower. For high energy particles this means that these detectors often are large. The longitudinal shower profile is for GLAST well-described by a gamma distribution [25]:

$$\frac{dE}{dt} = E_0 b \frac{(bt)^{a-1} e^{-bt}}{\Gamma(a)} \tag{4.22}$$

where t is the calorimeter depth, a and b are fitting parameters. This allows for a good correction of energy leakage out the back of the calorimeter. Figure 4.3 shows the longitudinal shower profile through eight layers of crystals tested in an 50 GeV electron beam at CERN in 2003.

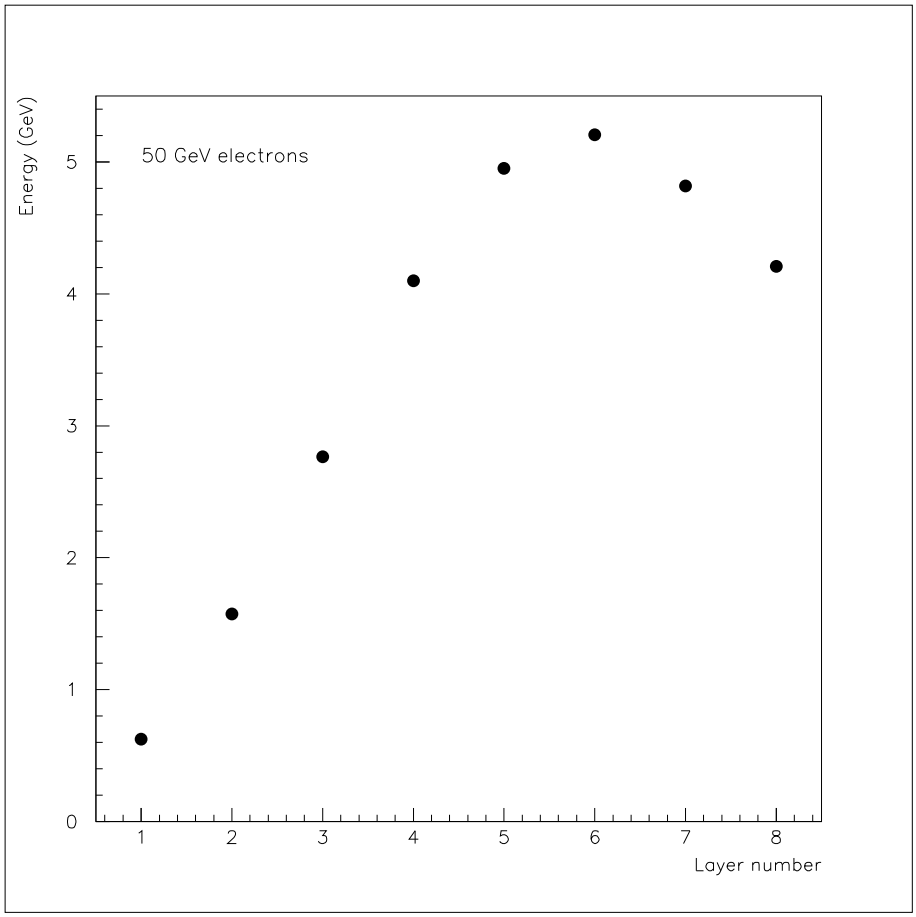

Figure 4.3: *Longitudinal shower profile through eight layers of CsI crystals for GLAST in a 50 GeV electron beam.*

Absorption and Attenuation

Summing the probabilities per atom for the different interactions gives the total cross-section σ_{tot} and if this in turn is multiplied by the density of atoms $N = N_a\rho/A$ (N_a is Avogadro's number, ρ the density of the material and A the molecular/atomic weight) it will yield a quantity known as the total absorption coefficient:

$$\mu = N\sigma_{tot} \tag{4.23}$$

and is the inverse of the mean free path. If I_0 is the intensity incident on an absorber of thickness x then the outgoing intensity I is given by

$$I = I_0 e^{-\mu x} \tag{4.24}$$

4.2 CsI(Tl) as Detector Material

The detection of ionizing radiation by measuring light scintillation pulses produced in certain materials is a technique which has been used for decades and has been thoroughly studied. Four groups of materials are generally considered; inorganic and organic crystals (includes plastic scintillators since organic crystals are solved in the plastic material), liquids and gases. The most widely used are the inorganic, to which CsI belongs, and the organic crystals. The scintillation mechanism differs somewhat between the different types of scintillators. The following properties are wanted in the ideal scintillator material:

- It should convert the kinetic energy of the incident particle into detectable light with high efficiency. Moreover, the conversion should be linear, i.e. the light yield should be proportional to the deposited energy over a wide range.
- To obtain good light collection it should be transparent to the wavelengths of its own emitted light.
- The decay time of the luminescence should be short in order to achieve fast signal pulses.
- The refractive index should be near that of glass (~ 1.5) to ensure good optical contact with the widely used glass windows of photomultiplier tubes and photo diodes used for detection of the light.
- Also preferable is if different kinds of particles give different shapes of the output pulse so that it is possible to distinguish between them.
- It should be possible to manufacture the material into the desired dimensions at a reasonable cost.
- The material should be resistant to environmental factors and should not deteriorate with time.
- It should have a high Young's modulus, shear modulus, ultimate strength and fatigue resistance.

Of course no material meets all these criteria simultaneously and the choice will have to be a compromise. Generally speaking the inorganic crystals have a high light output but are quite slow in their response. Whereas the organic crystals are faster they also produce less light. The application also has to be taken into account. For example, the inorganic crystals has a higher atomic number and therefore absorb energy better (a detector meant to absorb a certain energy will be thicker if an organic crystal is used). They also have better linearity whereas the organic provides a fast signal so they are well suited for quick trigger signals.

Scintillators are luminescent materials. When exposed to certain forms of energy, e.g. light, heat and radiation, and in some cases also mechanical stress,

they absorb the energy and re-emit it as visible light. The luminescence is often divided into fluorescence and phosphorescence, depending on the timescale of the reemission. Fluorescence is when the reemission takes place immediately after absorption (within approximately 10^{-8} s). Phosphorescence, or afterglow, is when the remission is delayed because the excited states are metastable (the delay time varies from microseconds to hours depending on material).

The time evolution of the reemission process may be described by an exponential decay. For some cases it is enough using one decay constant but many scintillators are more complex where the use of two decay constants is necessary to achieve an accurate description. For most scintillation materials one of the decay constants are much faster than the other so they are usually referred to as the fast and slow components. The fast component generally dominates though the relative amplitude of the two components differs between materials. The decay can be described by

$$N = Ae^{-t/\tau_f} + Be^{-t/\tau_s} \tag{4.25}$$

where N is the number of photons emitted at time t, τ_f and τ_s are the fast and slow decay constants respectively. In the above expression the rise time from zero photons to the maximum has been neglected because generally it is much less than the time for a significant decay.

4.2.1 Scintillation Mechanisms

The mechanism of scintillation in organic materials is due to the excitation of free valence electrons, shared by many molecules of aromatic hydrocarbon containing linked or condensed benzene-ring structure. The ground states of the molecules are at different levels due the possibility of different vibrational states of the molecule.

The majority of the inorganic crystals used are of alkali halides, either in pure crystal form or with a small amount of activator impurity added to the crystal structure. The most commercially wide spread amongst the inorganic crystals are sodium iodide, doped with thallium, NaI(Tl), followed by cesium iodide, also with thallium as the impurity activator, CsI(Tl). Other material are CsF_2, CsI(Na), and among the non-alkali materials, $Bi_4Ge_3O_{12}$ (bismuth germanate or BGO for short) and BaF_2. In the crystal lattice structure the electrons have available only discrete bands of energy which determines the possible energy states , as compared to the molecular nature of the inorganic crystals. In the valence band, the lower band, the electrons are bound to the lattice sites, whereas in the conduction band, the higher band, the electrons are free to migrate through the crystal. In between lies the band gap (also called the forbidden band) where electrons never can be found in pure crystals. An electron absorbing energy can be lifted from the valence band to the conduction band leaving a hole in the normally filled valence band. The deexcitation of the electron in which a photon is emitted is an inefficient scintillation mechanism because the emitted photon is likely to be absorbed again (self-absorption in

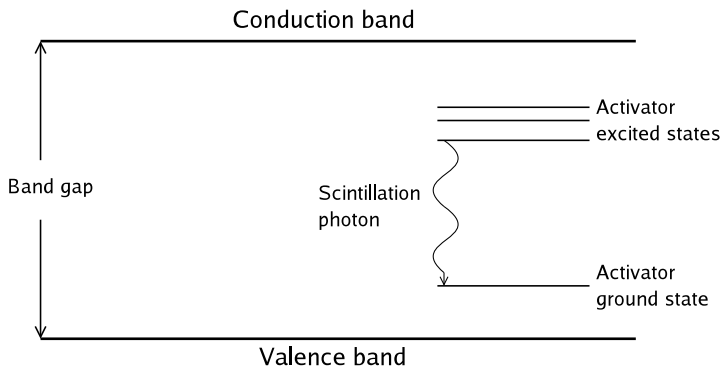

Figure 4.4: *Principle of energy levels in an inorganic scintillator. Shown is the band gap and the energy states of the activator substance.*

the bulk of the crystal) and the energy of the band gap often results in photons with energies higher than that of visible light. Both problems are overcome by doping the crystal with an impurity activator. A properly chosen activator has its ground state somewhat above the valence band of the crystal and its excited states somewhat below the conduction band, so as to create possible energy states within the forbidden band trough which the electron can deexcite back to the valence band (cf. figure 4.4).

Another process, not very unlike the one mentioned above, is also possible. Just below the conduction band there is a band called the exciton band [21]. If the amount of energy absorbed by the electron is slightly less than the energy required to lift it to the conduction band it combines with the hole in a loosely bound pair, the exciton, which is free to migrate throughout the crystal until it encounters an activator center.

A charged particle passing through the detection material will create a large number of electron-hole pairs by elevating the electrons to the conduction band. The positive holes are now free to drift through the crystal, as is the electron, and when encountering an activator atom it will ionize it, since the ionization energy is smaller than that of a lattice site. A free electron arriving at the ionized impurity site will drop into it creating a neutral impurity which has its own set of possible energy transitions inside the forbidden gap. Therefore it is not possible for the photons emitted at the deexcitation of the impurity to be absorbed by the crystal lattice (because the energy is too low) and thereby fulfilling the requirement for a scintillator that it should be transparent to its own emission. This is the minimum essential condition in finding a good scintillator material, i.e. finding the proper doping atom and the suitable concentration of it. Typical half-lives of the excited states are on the order of 10^{-7} s, and because the migration time for an electron to reach the site of an impurity is much shorter the excited configurations are basically formed at once so that the decay time and behaviour depends on the half-life characteristics of these states.

Inefficient processes can also occur. The impurity excitation can be such that a transition to the ground state is not possible if not additional energy is added. It could, for example, be in the form of thermal energy, raising the electron to a higher state from which a transition is possible. This delays the emission of the photon and causes a background light, so called afterglow. There is also a possibility for the excited activator sites to return to the ground state via a radiationless transition without emitting a photon. These impurity centers are called traps.

The total light yield in CsI(Tl), i.e. the number of photons created per unit energy, is of the order of 65000 photons/MeV [21]. The absolute scintillation efficiency, i.e. the fraction of the incoming energy that is transformed into light energy is of the order of 10% [21]. This is what limits the resolution at low energies, less photons means less statistics and thus increasing the statistical error. The efficiency of the detector element as a whole depends on a number of factors, e.g. how well the light is collected to the photo sensitive device, the spectral match of the light from the scintillating material and the pickup device and the linearity of the system.

A disadvantage for some of the inorganic crystal (of course for the most commonly used) is that they are hygroscopic, i.e. they deteriorate because of the humidity in the air. CsI(Tl) is just slightly hygroscopic and can be handled for some time in normal room conditions, though it was a specified requirement for the GLAST crystals that the relative humidity was to be kept below 40 % and that protective gloves were used when handling the crystal to prevent absorption of humidity from the skin.

4.2.2 Light Read-out Techniques (PMT, Photo Diode)

The idea of detecting radiation using scintillating material is to transform the visible light produced in the scintillator material into an electric signal which can easily be processed. The two devices in use are the photomultiplier tube and the photo diode. The size, construction and function differ a lot between the two. To achieve the most efficient light collection the wavelength emission spectrum of the scintillator should be carefully matched with the response of the device chosen. The wavelength at which the maximum occurs for the scintillator should be well within the wavelength boundaries of the photomultiplier tube, or photo diode, for best results.

Photomultiplier Tube

The invention of the photomultiplier tube (PMT) meant a drastic increase in the use of scintillators as detectors for radiation. The basic principle of the PMT is the photoelectric effect. The basic components are the cathode made by a photosensitive material, a metal or a semiconductor, followed by a number of dynode stages and last the anode, all contained in a vacuum sealed glass housing. The PMT requires high voltage (kilovolts) between the cathode and anode. The light from the scintillator enters the glass window at the photo cathode

where an electron absorbs the energy of a light photon and gains kinetic energy. The kinetic energy allows the electron to leave the surface of the photosensitive material and enter the electric field applied. It is then accelerated against the first dynode where it hits the surface and some of its kinetic energy is transferred to the electrons on the surface of the dynode which in turn are emitted as secondary electrons and again accelerated against the next dynode stage where the procedure is repeated, causing a cascade of electrons down the dynode stages. Arriving at the anode this cascade gives a current pulse, typically of the order of $10^7 - 10^{10}$ electrons, which is to be amplified and analyzed.

The process of releasing an electron can be described by three events. The electron absorption of an incident photon and transfer of some of its energy to kinetic energy, this is described by Einsteins formula for photoelectric effect (equation (4.9)). The electron then has to migrate to the surface, on its way it will suffer from energy loss due to collisions with other electrons. The last step is to escape the surface of the cathode by overcoming the inherent potential barrier that exists between a material and vacuum; this requires that the electron has enough energy left when reaching the surface. In metals the energy loss by collisions with other electrons are quite severe and the range before the kinetic energy is less than that of the potential barrier (also called the escape depth) is only a few nanometers. In well prepared semiconductors the escape depth can be up to about 25 nm. A layer this thin will be semi-transparent and the probability for a photon to interact is less than 50 %.

The quantum efficiency is a measure of how many useful electrons escape the surface and become part of a signal; it is defined as the number of electrons released divided by the number of photons impinging on the cathode. The quantum efficiency is a function of the wavelength of the light and most of the photosensitive materials have their maximum in the range 350 to 450 nm. It has been more and more common to use photo cathodes of semiconductor type which are made of antimony (Sb) and one or more alkali metals. The semiconductors reach a higher quantum efficiency than metals as photosensitive material; for many metals it is not greater than 0.1% while the quantum efficiency maximum of semiconductors are of the order of 10 to 30%.

An effect which has to be taken into account is the thermal noise which is manifested by spontaneous electron emission. At room temperature some thermal kinetic energy is always present even though it is often very low. However, the thermal kinetic energy is a statistical distribution with its maximum at low thermal kinetic energy but with long tails going to lower and higher energy. This implies that some electrons at some point will have energy close to that of a photon and if this electron is near the surface it can escape and cause an unwanted signal. The high escape potential barrier of metals makes the thermal noise low but for the semiconducting photo cathodes it is considerably larger, so the gain in quantum efficiency is at the expense of increased thermal noise.

The multiplier section of the PMT is based on the same principle as described for the cathode but now the electron emitted by the photo cathode plays the role of the incident particle (instead of a photon). The original electron is accelerated in an applied electric field against a set of electrodes, the dynodes.

Upon striking the surface of the dynode the incident electron transfers some of its energy in collision losses in the dynode allowing a number of secondary electrons to gain enough energy to escape. As mentioned earlier, electrons in a pure metal have low probability to reach the surface and escape, therefore semiconducting materials are used here as well. However, since the dynode has to maintain an electric field to guide and accelerate the electrons, the second emission material has to be on top of a conducting material. The gain of the dynode stage is defined as the number of secondary electrons emitted divided by the number of primary incident electrons, and its called the secondary emission factor, δ. A good dynode material shall have high δ, have a stability of secondary emission effect under high currents and low thermal emission (low noise). The majority of the conventional PM-tubes have between 10 to 14 dynode stages with a total overall gain of the order of 10^7. The configuration of the dynodes varies and the response time and the range of linearity depend on the configuration.

In certain applications it might not be possible to optically connect the PMT directly to the crystal, it could for example be due to the shape of the crystal or that the crystal is placed in a significantly magnetic or electric field. This problem is solved by using a light guide, i.e. an optical fiber of the same area as the readout area of the crystal using internal reflection to transfer the light to the PMT. If the spectral emission of the crystal for some reason is not completely matched to the absorption peak of the PMT photo cathode, the fiber used can be of wave-shifting type. The light entering the fiber will be absorbed and re-emitted in another wavelength which better matches the spectral absorption peak of the PMT used.

The anti-coincident veto shield of GLAST uses such wave-shifting fibers, one of the reasons being the shape of the scintillator tiles, the fibers in forms of strips are attached to the tiles covering the instrument and the strips are then attached to the PMT by mapping them onto the cathode surface.

Photo Diodes

Advances in the development of semiconductor photo diodes has led to the possibility of a substitution for PM-tubes. The advantages of the photo diode, as compared to the PM-tube, are higher quantum efficiency (possibility for better energy resolution), smaller dimensions, less power consuming and virtually insensitive to external magnetic fields. On the other hand the photo diodes give quite small signals which requires the preamplifier to be situated rather close to the photo diode as to avoid external noise to affect the signal. Furthermore, the diodes are substantially noisier than the PMTs. PMTs can under the right circumstances detect single photons, something which diodes of today hardly can do.

The process of turning photons into a current pulse is similar to the process described for radiation loss in inorganic scintillators. The incident photon will be absorbed by an electron, lifting it into the conduction band of the semiconductor and thus creating an electron-hole pair which is now free to migrate throughout the bulk. The applied voltage need only to be of the order of tens to hundreds

of volts for a good charge collection, instead of the more than 1000 volts needed for PM-tubes. The spectral response of the photo diode extends more into the region of longer wavelengths than typical PM-tubes, something which is important for scintillators with emission spectra with a substantial part of its light in the longer wavelengths as for example CsI(Tl) and BGO. Since there is no internal amplification (no cascade like in the PM-tube) the current signal is weak and a preamplifier situated close to the diode is necessary to avoid external noise pickup becoming an issue. The thermal noise in photo diodes are in the order of a magnitude larger than for PM-tubes and the diodes show a strong temperature dependence. An increase in temperature is followed by an increase in the leakage current.

If higher voltage is applied to the photo diode then the output current signal can be increased, these diodes are called avalanche photo diodes. The initial free electron is accelerated sufficiently by the applied electric field to create secondary electron-hole pairs by collision thus internally amplifying the signal.

As the photo diodes are getting more reliable and cheaper they are becoming more and more common instead of the PMT, mainly due to the many advantages mentioned above. Concerning the GLAST calorimeter, photo diodes were chosen instead of PMTs because of the advantage of size. The segmentation of the calorimeter would not have been possible to achieve efficiently with PMTs, since it would require much more volume and introduced more dead material. Also, the diodes has a better spectral match with the CsI(Tl) than most PMTs, thus providing better overall quantum efficiency.

4.2.3 Crystal Shapes, Light Collection and Surface Treatment

Crystal size and geometry plays an important role to achieve the desired behaviour of the application. It can range from thin tiles used for triggering or charged particle rejection to scintillators large enough to completely absorb particles of very high energy. Scintillators used for scintillation counting, detection and collection of energy spectra of nuclear substances (β- and γ-decay) are commercially available in a variety of sizes, most of them are cylindrical to easily fit with commercially common PM-tubes. A general aspect for all scintillators in use is that they have to be completely isolated from ambient light, both the scintillator and the PMT or photo diode has to be wrapped or concealed in light tight material.

To collect as much light as possible is important to achieve a good energy resolution. Two processes are dominating in the loss of light, the attenuation in the crystal material (which includes both absorption and scattering) and losses at the surfaces of the crystal. The intensity of light propagating through a medium decreases, due to attenuation, as:

$$L(x) = L_0 e^{-x/l} \tag{4.26}$$

where x is the distance traveled by the light, L_0 the initial light intensity and

l the attenuation length. The loss of light due to the attenuation becomes substantial when the distance traveled is of the order of the attenuation length, and since this generally is of the order of 1 m it becomes an issue only for large detectors. Since the crystals of GLAST have the shape of narrow rods, the geometrical boundaries and the properties of the surrounding medium will have a larger influence on the performance than the degradation due to attenuation.

The light produced in the crystal is emitted in all directions and depending on the shape of the crystal more or less light will reach the light sensor but far from all. The amount reaching the interface between the bulk and the surrounding medium can either be internally reflected or escape depending on the incident angle. Light will be internally reflected if it has an angle of incidence greater than the critical angle,

$$\sin\theta_C = \frac{n_{surr}}{n_{scint}} \tag{4.27}$$

where n_{surr} and n_{scint} are the refractive indices of the surrounding medium and the scintillator, respectively. For angles less than θ_C partial reflection occurs and the rest is transmitted. The light which escapes might be lost depending on the conditions of the surroundings. Apart from the reduction of efficiency and energy resolution this loss might cause a non-uniformity of the pulse height response of the crystal, i.e. the same amount of energy deposited at different locations can give different output signals. The easiest way to recollect the escaped light is to surround the scintillator with a reflective material, as to redirect the light back into the crystal. The reflection may be specular or diffuse. A diffuse reflector is basically independent of the angle of incidence, while in the case of specular reflection the angle of reflection equals the angle of incidence.

For a long time aluminum foil was used for specular reflection, but gradually other materials have been used. For diffuse reflection magnesium oxide in the form of powder or white paint is frequently used. The choice of surrounding medium depends on the application, the expected result and the properties of the crystal. The GLAST crystals uses a specular multi-layer Mylar (polymer) film, VM2000 [24]. The reasons for choosing this material were that it gives a high light output, 20-30% higher than standard diffusive wrappings (for example Tyvek or Tetratex). It is also a stable and rigid material. It is stiff and rather difficult to fold or wrap, something which is overcome by hot molding around an aluminum mandrel with the form of a crystal. The hot molding does not result in any loss of light yield or mechanical stability [25].

The need for an efficient reflector is minimized if the amount of internally reflected light is maximized. The amount of internally reflected light can be manipulated with the following two parameters. The index of refraction of the surrounding medium should be as low as possible to get an as small critical angle as possible. Highly polish the surface to increase the probability of internal reflection. However, the internal reflection can be a problem. If the refractive indices of the scintillator and the optical window of the PMT or photo diode is not carefully matched then there will be some internal reflection at the surface

used for readout and the reflected light will then be trapped inside the crystal (if more than one surface is used there is a possibility that the light can escape at that surface). For large scintillators multiple PM-tubes can be used to increase readout efficiency, as was the case for EGRET. The crystals of GLAST also utilizes multiple readout by a simultaneous readout of the two end faces of the crystal logs, giving the opportunity to image the shower (determining the entrance point in each crystal) and secure energy readout if one end fails (see subsection 4.3.1).

Since gamma rays do not leave any trace, i.e. a light pulse, in a scintillator until an interaction has taken place, whereas charged particles will interact immediately when entering the bulk, thin scintillators are excellent for charged particle rejection if only the electromagnetic radiation is to be detected. This property is used in the anti-coincidence detector of GLAST (cf. page 11). Scintillator tiles can also be used in pairs for coincidence detection of charged particles to provide a trigger for data collection, for example cosmic muons or in a beam of charged particles (most commonly used as trigger/rejection tiles are plastic scintillators). Another consequence of the fact that gamma rays may travel a distance before the first interaction is that, even though this first interaction will most probably for high energy gammas yield an e^-e^+ pair which will be the starting point of the electromagnetic shower, there will be a difference in the results depending on whether the incoming particle is an electron or a photon. If the calorimeter is designed to completely absorb a particle of certain energy the thickness needed varies depending on whether the particle is an electron, which immediately will interact when entering the bulk, or a photon, whose starting point will fluctuate and on average the deposition of energy will be deeper inside the detector. Also the fluctuations in the amount of energy deposited in a given slab of the material will be larger. Often large calorimeters (or parts of it) are tested in a beam of mono-energetic electrons and then the above effect has to be accounted for [26].

Crystals of CsI(Tl) having the shape of long narrow rods were used in, for example, the BELLE and BABAR (e^-e^+ colliders) calorimeters [27, 28, 29]. These calorimeters are "barrel" shaped, i.e. surrounding the site of the particle collisions. This means that the longitudinal axis of the crystal logs are pointing towards the particle impinging on the calorimeter. The crystals of BELLE and BABAR are read out at the opposite end using diodes (mainly because the crystals are situated in a strong magnetic field). In this application a uniform light yield is wanted, that is, the light output shall not vary (too much) depending on where along the longitudinal axis the energy deposition takes place. For example, the BABAR crystals having a non-uniformity greater than 2% had their wrapping material partially treated with black strips as to locally affect the light yield and bring it inside the wanted uniformity [29].

The scintillator elements in GLAST are position sensitive in one dimension. The crystals have the shape of long narrow rods, being $326.0 \times 19.9 \times 26.7$ mm^3, which are read out with photo diodes at each end of the longitudinal axis. Comparing the pulses (typical signal size was 50 mV from the PMT and around 3-4 V after amplification) from the two ends gives a measure on the position

along the crystal where the particle entered. How well the position can be determined depends strongly on the properties of the reflective material chosen and the surface treatment of the crystal. As mentioned above, long crystals (i.e. one dimension is substantially larger than the other two) have been used before, but in most cases non-uniformity along the crystal was unwanted. In the case of position sensitive scintillators, however, this non-uniformity is wanted. It is essential to be able to distinguish between the two output signals. The signal as seen from one end drops off close to exponentially depending on the attenuation length. It is however possible to treat one or more of the crystal surfaces to change the shape of the plot of the decrease in signal when the distance between the read-out end and the point of interaction is increased. A near linear dependence can be achieved by gently roughening the surfaces. The crystals of GLAST have this roughening applied to its long skinny surfaces (measuring 19.9 $\times$ 326 mm^2) and they are wrapped in a highly, specularly reflective polymeric film. The chosen film used for wrapping ensures a strong signal (high light yield).

4.2.4 Crystal Growth and Manufacturing

Amcrys-H Ltd situated in Kharkov, Ukraine, was chosen to be the supplier of crystals for the GLAST-project, a company having a long experience of making single crystals of various materials.

The manufacturing utilizes the Bridgman-Stockbarger method which has been modified and automated. The traditional method was patented in the 1920's [30] and was at that time the state-of-the-art in producing large single crystals. In the original method the raw material is kept in a cylindrical crucible which is placed in an oven divided into two sections, one hot section where the temperature is approximately 100 °C above the melting point, and one cold section where the temperature is 100 °C below the melting point. After the raw material has melted in the hot section the crucible is slowly moved into the cold section, allowing the crystal to form and the interface between the liquid and the solid is roughly along the line dividing the oven into the two sections.

The main disadvantages of this method is the difficulty to maintain a uniform distribution of the activator substance which affects the light yield and because the growing crystal is in contact with the crucible. A modification of the method is having a seed of crystal which is fed by a melt and then to pull the crystal out of the melt, this is the method Amcrys uses. When pulling large diameter crystals there are some problems associated with the pulling, for example the temperature gradient of the initial radial growth is difficult to keep stable and if the activator used is volatile it will evaporate more at the initial stage due to a larger ratio of melt/crystal surface area, resulting in large variations of activator concentrations between the top and the bottom of the ingot.

The method of pulling has been refined using a conical crucible which is constantly fed with fresh melt. The idea is to keep the free surface of the melt as small (and constant) as possible during the whole process. The process starts with the seed at the bottom of the crucible where the diameters are almost

equal. When the radial growth of the crystal begins, the level of the melt is then increased and simultaneously the seed is pulled upwards allowing the ingot to continue to grow radially. The crystal is pulled up at the same, or a slightly higher, speed than the level of the melt and thus keeping the free surface of the melt at a minimum. When the desired diameter is achieved the heightening of the melt stops but the pulling of the crystal continues, keeping the constant melt level by feeding new melt as the crystal is pulled (see figure 4.5). The growth process is controlled automatically using computers and the system is able to keep the crystal diameter at an accuracy of 1% at diameter 400-450 mm (pulling speed 6-6.5 mm/h) and the activator distribution is held within 10 % of the average concentration, both radially and axially [31]. Amcrys was not willing to reveal the absolute activator concentration but provided a relative number for each boule.

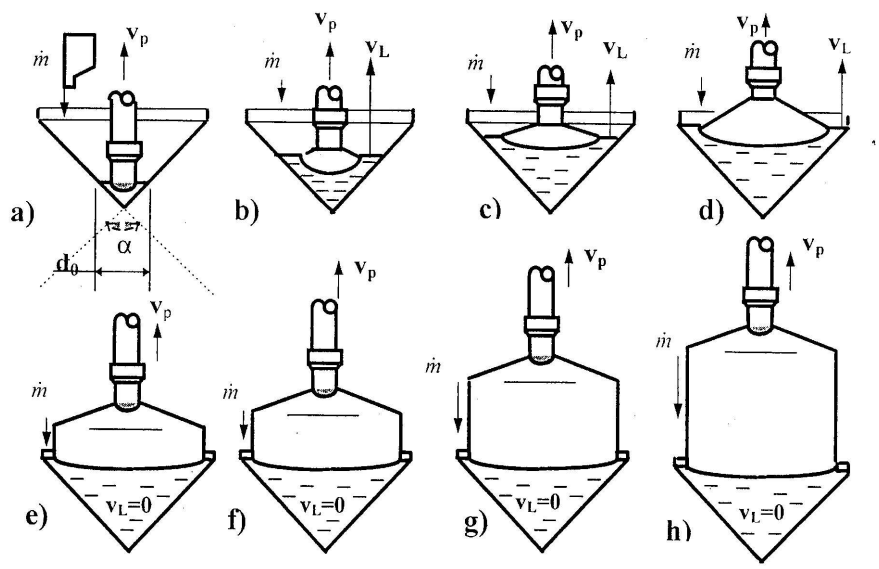

Figure 4.5: *Shown is a schematic drawing of the crystal pulling method. (a) is the starting stage. (b–d) radial growth and (e-h) vertical growth. Picture from [31].*

Since the radiation hardness is lower if the crystal contains contaminations (see next section) the raw material used for the melt has to be as pure as possible. Purification takes place both before and during the growth process. Before the raw material is melted it is high-temperature (400 °C) dried in vacuum. A chemically active metal is then added to the melt, forming insoluble oxides in the melt which settles at the bottom of the feeder. By doing so, any residual oxygen is prevented from contaminating the crystal. In addition, the melt is fed from its container using pressurized inert gas (Ar or N) and the atmosphere around the melt from which the crystal is pulled is also held under a slight

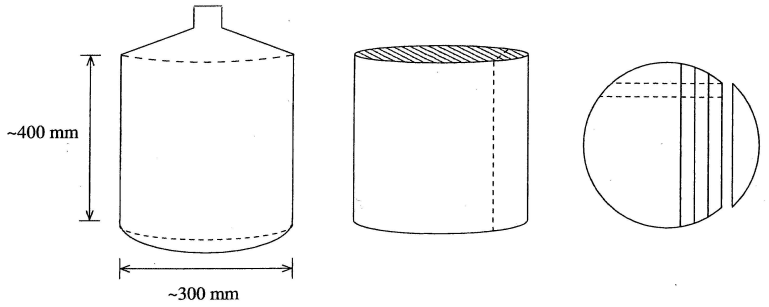

Figure 4.6: *Shown is the initial crystal boule cut into crystal logs. Left: Sketch of what the boule looks like when it is finished, dashed lines indicate where it is cut to the cylindrical shape. Middle: Boule is cut into two pieces, the smaller is used for analysis of the quality. Right: Indicates how the boule is first cut into slices (solid lines) then how the slices are cut into bars.*

excess pressure. The inert gas is purified before use in the growth process, the purpose is to remove water (moist),O_2 and CO_2 [31].

The cylindrical boule was initially cut axially into two pieces, where the smaller was used for analysis of the quality (see figure 4.6). Samples used for radiation hardness tests were taken from this piece. The larger part was taken to production of detector crystals. The first step was to saw this larger part into slices with a height a little more than the crystal height. These slices were then cut into the logs which were to become the final detector crystals. The chamfers were machined and the length corrected. All surfaces were then polished after which the crystals had their dimensions verified. The crystals produced from that boule were then put to rest, i.e. let any handling induced stress or shock in the crystal lattice settle (see page 48). Finally, each crystal was individually tuned optically by having its long skinny surfaces roughened, to achieve the specified optical performance. On average the crystals were treated and optically tested 2–3 times before fitting into the optical requirements. Each crystal boule was provided with a unique production number for identification of the boule samples. Each crystal cut from the boule was in turn provided with a serial number based on its origin in the boule according to figure 4.7.

4.2.5 Radiation Damage

Since the environments where scintillators are used by default are very radiation-intense, and since the scintillators are used to absorb the energy of the radiation, they are exposed to high doses. It is therefore important that the scintillating material has a high radiation hardness so that the deterioration of the material (and thus the size of the output signal) is held within an acceptable level during the designed lifetime. The absorbed dose is material dependent and is usually

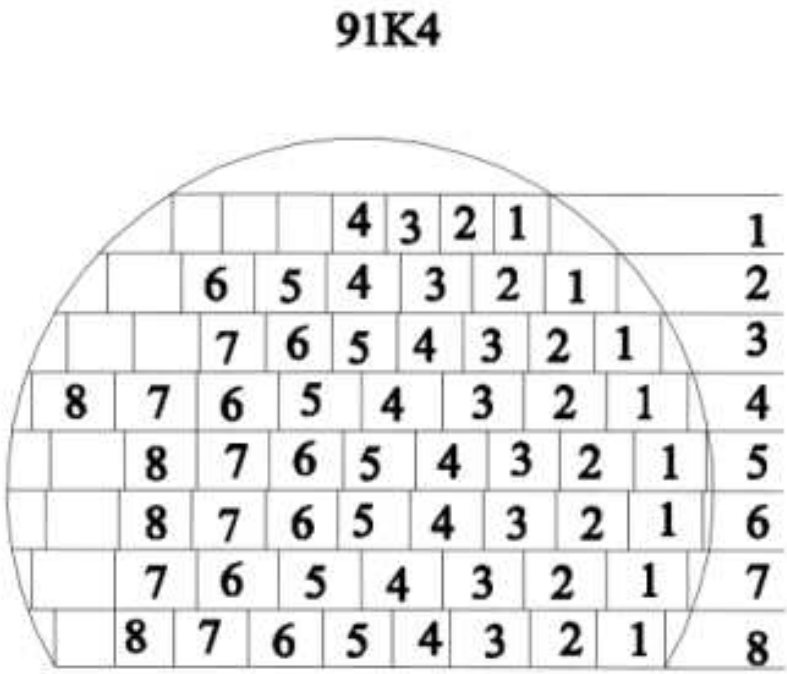

Figure 4.7: *Map showing how the crystals obtain their serial numbers from the position in the boule. 91K4 is the number of the boule. After that comes the number of row as indicated to the right in the map and last comes the number of the position in the row. For example, the lower right crystal in this map gets the number 91K4-8-1.*

measured in Grey (Gy) or rad, where 1 rad = 0.01 Gy = 0.01 J/kg. The effects of radiation damage on CsI(Tl) is well-known due to extensive studies, but the mechanisms causing this loss of light is not yet fully understood. The radiation damage is suggested to consist of two different phenomena, the decrease of the attenuation length through formation of color centers, and a decrease of the emission centers (the scintillation mechanism is affected). As suggested in [32] the decrease in attenuation length is the first effect to occur and is the dominant effect. It is not until radiation doses in the order of 10^5 Gy are reached that the scintillation mechanism is affected. The decrease of the attenuation length is strongly connected with the concentration and distribution of the activator substance, the color centers are created locally at the impurity sites causing a trap for the excitons and the free electrons/holes where deexcitation occurs without the emission of a detectable photon. The degree of deterioration depends on the concentration of the impurity [33, 34] which will be a compromise between the desired light yield and the allowed amount of radiation damage,

and it is therefore important that the concentration is held at an as constant level as possible during the crystal growth. Another impurity which is thought to cause an increase of the radiation damage is oxygen contamination [35] [36]. The radiation damage is further discussed in section 5.4, where the radiation hardness tests for the GLAST project are discussed.

4.3 The GLAST Calorimeter

This section will describe the design drivers of the GLAST calorimeter and give a detailed description of it. Also presented are the specified design requirements and the goals.

4.3.1 Description of the Design

The science requirements demanded a large effective (and active) area to be able to reach the desired resolution and range of the instrument. The active area was increased by a factor 3.5 as compared to EGRET and the depth of the calorimeter practically unchanged, while the source sensitivity was desired to be a factor 50 larger and the high energy threshold at least a factor of 10 larger. This meant taking full advantage of newly improved detector technology together with experiences from EGRET. The principles during the design and planning was to refine each element (tracker, calorimeter, ACD), to use proven technology, such which had excellent heritage from various other high energy physics experiments, to build the instrument in modules in order to achieve an efficient assembly with exchangeable parts and minimizing the effects of component failure, to enable an extended energy range and support background rejection by using a high segmentation and to use redundant readout paths to avoid single point failure of the electronics. The calorimeter was designed to achieve a good energy resolution over the full energy range together with the ability to have good pattern recognition. A large field of view is important for almost all sources to be studied, which requires that the height of the instrument to be significantly less than its width.

The CsI(Tl) as calorimeter material readout with photo diodes was chosen for the excellent heritage of CsI, fine energy resolution, good spectral match with PIN diodes, large signal from the diode (5000–7000 electrons/MeV for the large diode), low voltage operation and a rugged compact system. A challenge was however the dynamic range needed in the electronics, and the integration of the single crystal bars in the mechanical structure.

The segmentation of the calorimeter is of great importance for its enhanced performance. The energy resolution and the energy range depend strongly on the longitudinal segmentation, as well as on the depth of the calorimeter. The longitudinal segmentation enables energy measurements up to a TeV. The measurement of the longitudinal shower profile is fitted to an analytical description of the energy dependent mean longitudinal profile. The energy resolution is restricted by fluctuations in how much energy leaks out from the back of the

calorimeter, with a depth of 8.6 radiation lengths the maximum of the mean longitudinal shower profile is contained within the calorimeter up to approximately 100 GeV. The longitudinal segmentation is also helpful in background rejection.

The lateral segmentation is necessary to achieve enough imaging capability to correlate events in the tracker with energy depositions in the calorimeter, which is crucial for the desired background rejection. The imaging capability can also help measuring the direction, with a resolution of a few degrees (see section 6.4.4), of high-energy photons that do not convert in the tracker.

Each CsI(Tl)-bar is optically isolated from its neighbors and provides three spatial coordinates for each energy deposition; two discrete coordinates from the physical location of the crystal bar, and the third, more precise, coordinate measured in the long dimension of the crystal. Simple analytical forms are used to convert the light asymmetry (see section 5.1.3) into position. This imaging method gives a position resolution in the order of a few millimeters [25], see also section 6.4.3.

The size of the CsI(Tl)-bars is a compromise between electrical channel count and desired segmentation. The dimensions of the cross-section (19.9×26.7 mm^2) is comparable to the radiation length of CsI(Tl), being 18.6 mm, and the Moliere radius, being 38 mm. The segmentation is sufficient to allow spatial imaging of the shower and accurately reconstruct the direction of the incident photon, with most of the position information provided by the light asymmetry measurement. The total number of readout channels is 3072 which has to be read over a large dynamic range (approximately $5 \cdot 10^5$) with small non-linearity and minimal dead-time. The difficulty with the dynamic range was solved by introducing two independent signal chains through the use of a dual pin diode, i.e. a diode with two separate areas with a ratio of 4:1. The large area is assigned the low energy range, 2–800 MeV, and the small area handles the high energy range, from 40 MeV and up. The significant overlap permits cross-calibration of the electronics. The redundancy of the readout comes from reading both crystal ends, meaning that if one end is lost, then the position of the energy deposition can not be retrieved from the light asymmetry measurement in that crystal, but the energy measurement will not be significantly degraded. The position can be satisfactory retrieved from the surrounding crystals.

4.3.2 Design Requirements and Goals (Full Calorimeter)

The design requirements and goals presented in this section are taken from [37, 38].

The GLAST calorimeter shall according to design support measurements in the energy range of 20 MeV to 300 GeV, with a goal to extend the energy range up to 1 TeV. The understanding of the energy deposition in the tracker is of critical importance only in the lower energy range. Since the thickness of the tracker is approximately 1.3 radiation lengths the calorimeter has to be able to handle energy measurements well below 20 MeV.

The energy resolution ($1\ \sigma$) for photons with on-axis incidence was required

to be better than 20% in the high energy range, 10 – 300 GeV. In the low energy region the resolution was to be less than 10% (1 σ) for energies between 100 MeV – 10 GeV. Below 100 MeV the energy resolution was to be better than 20% for photons interacting in the calorimeter only. The energy resolution for off-axis photons, i.e. angles of incidence greater than 60°, was to be better than 6%, with a goal of 3%, for energies greater than 10 GeV.

The angular resolution was specified to be better than $15° \cdot \cos^2\theta$ (1 σ), with θ being the off axis angle, for cosmic muons traversing all eight layers. Each CDE was required to be capable of positioning a minimum ionizing energy deposition with a resolution (1 σ) of 1.5 cm.

The dead time, that is, the time it takes to capture an event and measure the energy deposition (called so because the triggering system is shut off during this time, the instrument is "dead" for any new events), was required to be less than 100 μs with a goal of reaching below 20 μs. The calorimeter active depth was to be greater than 8.4 radiation lengths for normally incident photons. It should be possible to do energy calibration in orbit using energy depositions from different cosmic ray particles. Relative light yield in each crystal shall be determined to better than 3% and the absolute light yield to less than 10%.

The calorimeter modules were each to have a projected area greater than 1050 cm^2 of CsI(Tl) for normally incident rays. The passive material, i.e. everything other than CsI, was required not to exceed 16% of the total module mass, which was restricted to 93.25 kg (the total for the full calorimeter is 1492 kg). The size of each module was to be kept within 364 mm in width and 224.3 mm in height. The power was limited to 5.6875 W per module, in total 91 W.

The performance has been simulated and in some cases tested and the result shows that all requirements will be satisfied. For example, the dead time is expected to be just below 20 μs and the power consumption will be kept around 67 W (all modules).

Table 2.1 on page 5 shows some of the requirements of GLAST as compared to the performance of EGRET.

Chapter 5

The Acceptance Tests of CsI Crystals

The total amount of crystals used in the 16 towers on-board the satellite is 1536. Added to that is another two modules of which one is to be a spare module and the other is the so called verification module used for thermal cycling tests, vibrational tests, balloon flight test. In total a minimum of 1728 crystals had to be tested and accepted.

The acceptance tests were necessary to validate the crystal quality in three aspects:

- The mechanical tests were performed to verify the mechanical shape and dimensions of the crystals. The tolerances set to the mechanical dimensions were to ensure that the crystal properly would integrate with the carbon fiber support structure.
- The optical tests were performed to ensure that light taper and asymmetry were within specified limits, and that the variations in light yield between crystals were kept at an acceptable level. Furthermore the light taper curves had to be monotonic and the energy resolution had to be within specifications.
- The purpose of the radiation hardness tests were to ensure that the crystals do not deteriorate more than specified due to the high background radiation, i.e. to ensure the designed life-time of the detector.

Due to the slight hygroscopic nature of CsI(Tl) the test environment had to be controlled. Temperature had to be kept between 18 and 25°C and the air humidity was not allowed to be more than 40%. The CsI(Tl) can be considered brittle if subject to forces or loads of great impulse, dropping the crystal would break it (like glass) and hitting it with a hard object cause cracks or release of chips. However, if the crystal is subjected to minor loads over a substantial period of time, the crystal shows slightly viscous behaviour, which manifests

itself as a change of the crystal shape. A straight crystal placed on a pencil on a table will after a day be bent out of the tolerances from its own weight. L-shaped aluminum profiles were used to maintain straightness during storage as well as during shipment. Table 5.1 displays a selection of the most important limits of the different parameters which were to be verified.

Parameter	**Specified Max**	**Specified Min**
Light Yield	Aver. of all crystals + 10%	Aver. of all crystals -10%
Light Taper	70%	50%
Asymmetry Value	0.480	0.240
Length	326.00 mm	325.40 mm
Width	26.70 mm	26.30 mm
Height	19.90 mm	19.50 mm
Chamfer Distance	31.78 mm	31.58 mm
Radiation Hardness	Not Specified	50% of init. L.Y.

Table 5.1: *Crystal parameters and their limits*

The work order was as follows. Upon arrival in Kalmar the shipping crates were opened and all enclosed documents inspected. The crystals were counted and their serial numbers checked against the enclosed packing list. The crystals were then left without handling for at least a week to allow for relaxation of any shipping induced phenomena, such as a change of light yield due to mechanical stress or shock [39].

The first of the requirements to be tested were the optical properties. Each crystal was tested in one of the two optical test stations (hereafter labeled TS1 and TS2). Next the crystals proceeded to the mechanical measurements to verify the dimensions, including the chamfers distances and widths. The last step in the acceptance procedure was the visual inspection, meant to show any crystal anomalies, such as inclusions (for example air bubbles or impurities) or visible crystal lattice boundaries. If all test results were within specified range the last step before packing the crystals was to slightly roughen its end surfaces (the readout surfaces) as to increase the adhesive properties when gluing the photo diode to the surface. If any crystal failed in any of the tests this specimen was put aside for possibly further treatment in Kalmar. For example, if a crystal failed to reach the optical requirement further treatment of the surfaces could bring the optical properties back into the specified range. If a crystal had the correct dimensions but were outside the shape tolerances, it was in some cases possible to adjust the shape. Crystals which could not be treated in Kalmar were replaced by the vendor.

5.1 Optical Acceptance Tests

This section will give a detailed description of the optical acceptance tests performed in Kalmar. The test setup will be presented along with the programs

used for data acquisition and analysis. The required optical parameters will be defined and explained. The test procedure is described and developments during the period of the tests will be discussed. The results of the optical tests are presented in section 5.2.

5.1.1 Introduction: Production Flow

Amcrys manufactured the crystals, grew the boules as described in subsection 4.2.4, cut crystals from the boule, machined them into the correct shape and dimensions and tuned the optical properties before delivery to Sweden. Prior to the optical and mechanical tests the boule samples of the boules from which the crystals delivered to Kalmar were cut had to pass the radiation hardness test. In Kalmar the crystals were subjected to optical and mechanical quality assurance tests, visual inspection and end face treatment to enhance the diode glue joint. The crystals which passed the tests were shipped to the Naval Research Laboratory (NRL) in Washington D.C., USA. There the diodes were glued to the readout faces and the wrapping was applied, thus completing a Crystal Detector Element, CDE. Finally, before the assembly in a tower, the CDEs were tested with cosmic muons.

5.1.2 Optical Test Station

A version of the optical test equipment described in this section existed at all three locations, i.e. Amcrys, Kalmar and NRL, where crystal handling took place. The mechanical and electronic construction of the test stations, the programs used and the calibration procedure are presented.

Requirements

The crystal optical test station is required to verify all parameters (subsection 5.1.3) of the single crystal behaviour as defined from the specifications of the full calorimeter (subsection 4.3.2). The following features of the test station are necessary:

- Ability to simultaneously measure at both crystal end faces.
- Noise reduction by triggering only when both ends show signal.
- A reliable reference source of EM-shower inducing particles of well-defined energy.
- Accurately determine the position of the energy deposition.
- Easy and fast handling allowing more than 2000 crystals to be measured.
- Accurate and simple analysis of test results.
- An environment without any interfering background light or radiation.

Design and Construction

An optical test station was built up of a "black box" providing the required light-shielded environment for measurement. Furthermore there were the front-end electronic modules and the computerized data acquisition system. The analysis of the test data was carried out with a separate program.

Mechanical Construction. The black box was made from black anodized aluminum plates as to obtain a completely dark environment for the crystal tests. It housed an automated test bench, including two PMTs (Hamamatsu R669) and an aluminum crystal support. To control the position of the energy deposition a movable lead casing holding a ^{22}Na source (standard gamma source) was used together with an electric motor (Velmex VP9001). The precision in the source positioning was ± 2 mm, the majority of the uncertainty coming from crystal positioning and the size of the slit in the lead casing (the uncertainty in the positioning from the electric motor was negligible). A picture of the box is shown in figure 5.1. The principal layout is shown in figure 5.6. The right PMT was mounted on a sledge and could be moved longitudinally along the crystal direction, as to apply pressure on the optical connection or control the width of the air gaps. When the crystal was placed on its support and the right PMT adjusted, the source could automatically be moved to the various measuring

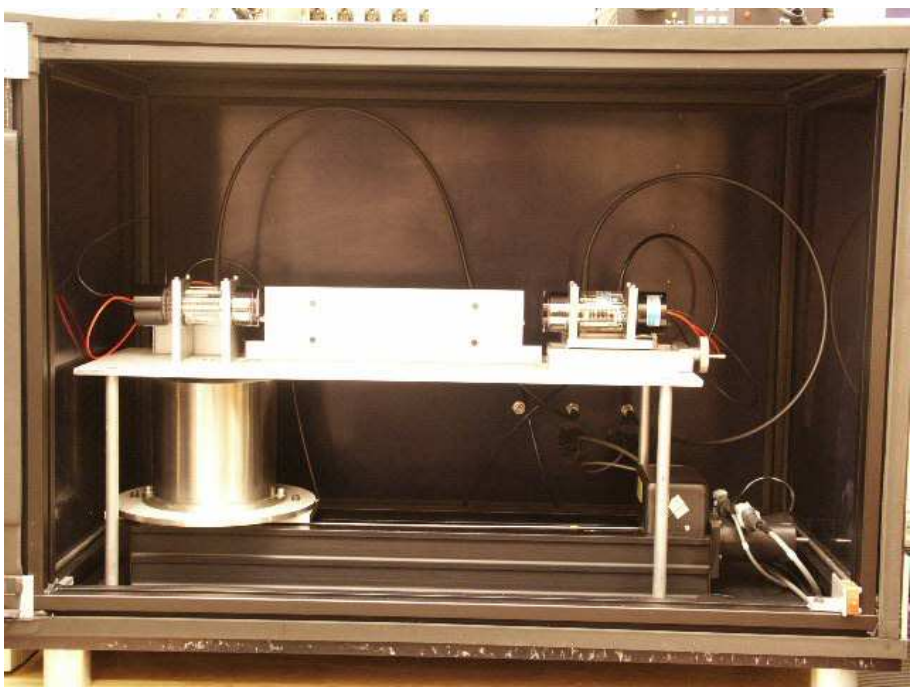

Figure 5.1: *The interior of the black box of the optical test station.*

positions along the crystal.

Front-end Electronics. The interface between the data acquisition computer and the front-end electronics was a custom made NIM module, denoted DAQ-Control[1]. It controlled the high-voltage to the PMTs, drove the electric motor to position the source, transferred PMT signals to the computer and featured a coincidence trigger, i.e. both PMTs had to show a signal for the event to be recorded. The high voltage unit was a Canberra Model 3125 Dual HV Power Supply which can keep the voltage stable to within 0.02% and give a maximum voltage of 5 kV. The PMT signals were fed to an ORTEC amplifier, Model 855 Dual Spectral Amplifier, using the unipolar input with a gain of about 30. The signal from the amplifier was then lead to a Canberra ADC Model 8701, which has a voltage range of 0 to 10 V. The resolution of the histogram was set to 1024 channels. The read-out of the ADC was handled by the DAQControl unit, which transferred data to the online computer. A schematic view of the signal flow is shown in figure 5.2 and a picture of the electronic modules in the NIM-crate can be seen in figure 5.3.

DAQ Software. The DAQ program used the Lab-View platform [40, 41]. The operator could control the longitudinal positioning of the source along the crystal, the high voltage to the PMTs and the data collection time for each position. During the measurement the program histogrammed signals from each PMT and the sum signal of the two PMTs (cf. figure 5.10). The histograms were updated every 2 seconds. A normal trigger rate was between 500 to 1000 Hz. The first crystals to be tested were the 96 crystals for the Engineering Module 1[2].

[1] Constructed by the GLAST group at NRL.

[2] One complete module used for verification of the mechanical design, including for example vibrational tests simulating the launch.

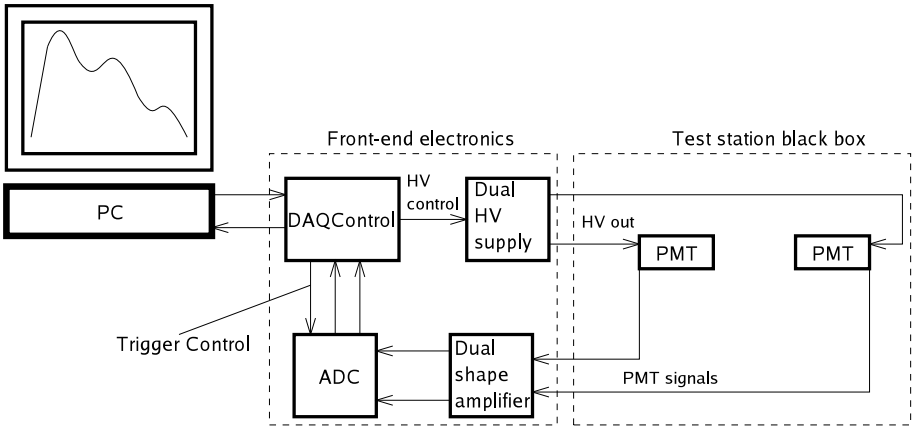

Figure 5.2: *Shown is a schematic drawing of the acceptance test setup.*

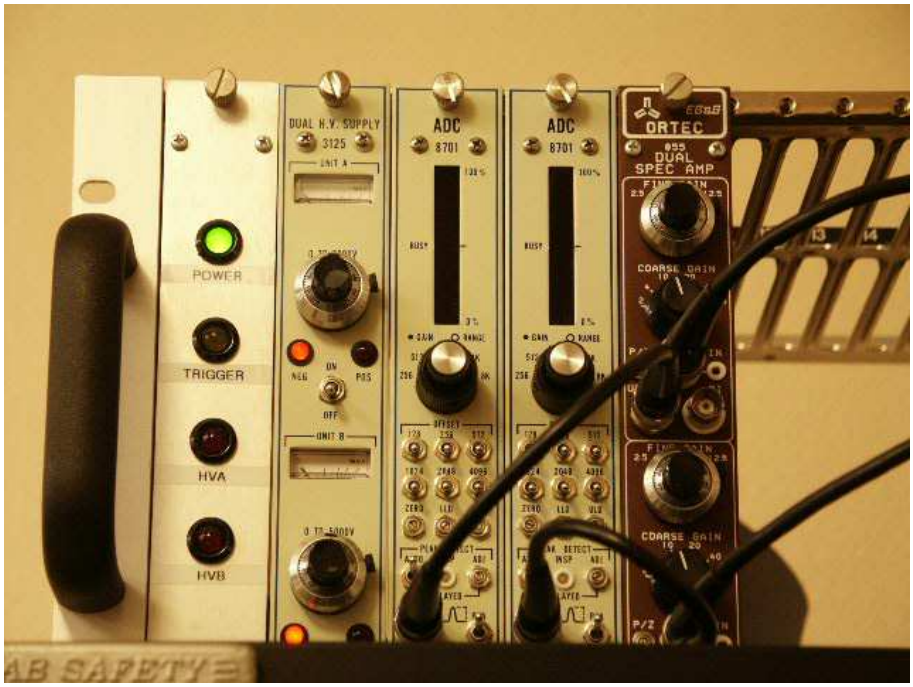

Figure 5.3: *A photo of the front-end NIM electronics. From left-to-right: DAQControl, HV-supply, two ADC units and the amplifier.*

Calibration measurements were done at 11 positions with 300 seconds collection time at each position. During production of flight crystals it was necessary to have a delivery rate of 200 crystals per month, and during that period it was considered enough to measure only 5 positions along the crystal. The measuring time at each position was kept at 300 seconds. The data was stored in LabView histogram-files, one file per position.

Analysis Software. The analysis of test data was also done with a LabView-based program.

A mathematical expression fitted to each histogram consisted of a Gaussian distribution (the gamma peak), an exponential decrease (noise slope) and a constant (an approximation of the Compton background continuum):

$$f(x) = \frac{A}{\sqrt{2\pi\sigma^2}} e^{-(x-x_0)^2/2\sigma^2} + Be^{-(x-x_B)/\tau} + C \tag{5.1}$$

The parameters given by the analysis are for the Gaussian: the integral A, the standard deviation σ and the centroid x_0. The taper plot in figure 5.4 (see also figure 5.7 on page 57), was created by plotting the fitted Gaussian centroids as a function of the source position.

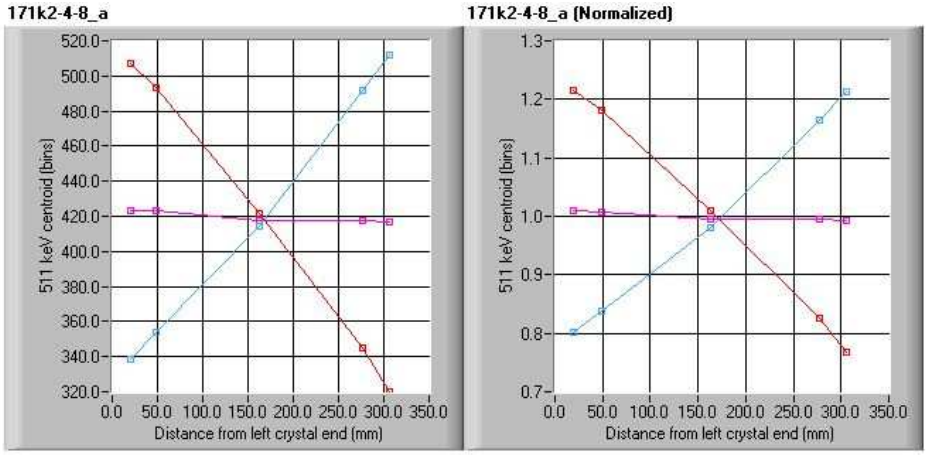

Figure 5.4: *The light output taper curve from a GLAST crystal.*

The parameters for the background are for the exponential: the height B at x_B (x_B was given as the start of the fit range) and the e-folding length τ and for the constant background C. All parameters were considered to be free, except x_B (start of the fit range).

The ^{22}Na decay products are a 1275 keV gamma ray and a positron. The positron will after annihilation give two 511 keV gamma rays. The Compton background has its edge (maximum) at approximately 1100 keV, which is, with the resolution of the GLAST crystals, too close to the 1275 keV gamma line to get an accurate fit. Therefore, the 511 keV peak from positron annihilation was used instead as a measure of the standard energy deposition from ^{22}Na. The analysis program performed this fit in an automated procedure for each position and for the three histograms (left PMT, right PMT and the average of the two). An example of the fit results (for one position and PMT) is shown in figure 5.5.

Calibration of the Test Station

During production of flight crystals two separate production lines were used consisting of two identical optical and mechanical test stations. The stability of the optical test stations was monitored with a reference crystal. The reference crystal was a standard flight crystal extracted from the production. It was kept vacuum sealed, at constant temperature and in a dark compartment at all times except when making the reference measurements. The reference crystal was measured twice a week during the time of production. It was measured with the source in the center position. The light yield from those measurements was monitored to keep track of any drifts in the signals.

It was desired for easy online interpretation for each test station to have its PMTs calibrated with respect to each other. This meant that an identical input

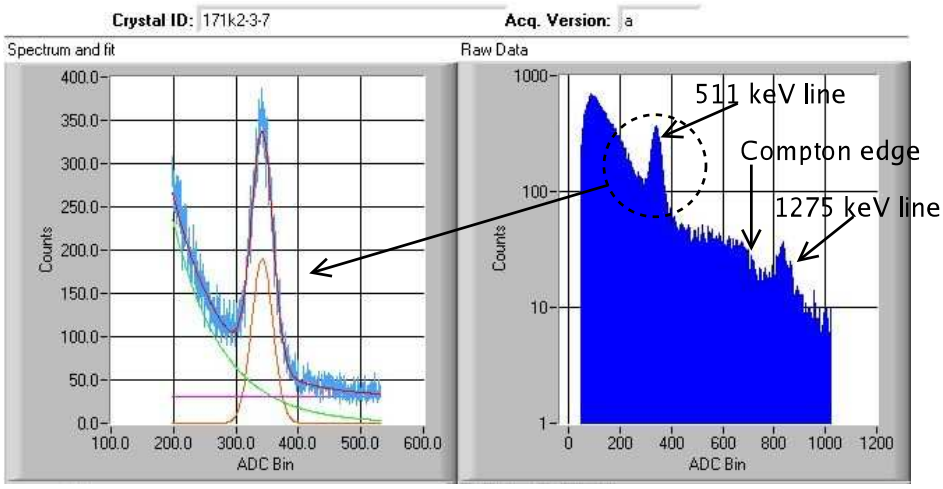

Figure 5.5: *An example of the fit of the 511 keV annihilation peak from ^{22}Na as measured with one PMT.*

light signal should result in identical output signals from the two PMTs. The signal from the PMTs also had to fit into the voltage range of the ADC. Finally, the two test stations had to be cross-calibrated with respect to each other.

The startup of each test station began with checking the box for light leakage. This was done without a crystal and monitoring the signal from the PMTs on an oscilloscope while ramping up the high voltage, so not to damage the PMTs. When no signal was detected from light in the room, a flashlight was used to carefully shine light on the corners and cable feed-throughs of the box. Generally the boxes had to be further treated to prevent light leakage.

When the box was light tight a crystal was inserted. The ^{22}Na source was positioned at the first measuring point 20 mm from the end, (start position in figure 5.6) and then the high voltage for one of the PMTs was carefully ramped up and the signal was monitored by the oscilloscope (the other PMT was switched off). The ADC range was 0-10 V so it was decided that a suitable signal size for the 511 keV peak would be somewhere between 2 and 4 V, which would make it possible also to fit the 1275 keV peak from the ^{22}Na into the spectrum. The high voltage was increased enough to clearly see traces from the two gamma lines on the oscilloscope, which meant a typical value of about 1200-1300 V. The pulse height from the PMT was then in the order of 100 mV. The approximate amplifier gain needed would be around 30. The signal after the amplifier was also connected to the oscilloscope and monitored. The gain was adjusted so that the approximate signal size was reached. The same procedure was then repeated for the other PMT by positioning the source at the other end (end position in figure 5.6).

Now that the both PMTs had their setting coarsely adjusted the data acquisition was started but still controlling the high voltage manually. The high

voltage setting was adjusted so that the left PMT with the source in the leftmost position, showed the same signal as the right PMT with the source in the rightmost position. The crystal was turned around and the procedure was repeated until the crystal ends showed the same peak value independently of which PMT it was close to.

The test stations were cross-calibrated with respect to each other using the reference crystal mentioned earlier.

5.1.3 Optical Test Procedure

This section will introduce and define the parameters describing the optical properties of the GLAST crystals. The test procedure will be discussed together with optical connection and test station variations. As will be seen, this lead to that the acceptance specification had to be modified. The effect of different wrapping material will also be considered.

Purpose and Parameter Definitions

The purpose of the optical tests were to verify the optical characteristics specified by the requested performance of the GLAST calorimeter. These requirements were presented in subsection 4.3.2 for the full calorimeter. When looking at individual crystal bars it is a matter of verifying the energy resolution and the longitudinal position resolution.

The measuring points along the longitudinal axis of the crystal, with respect to its left end face, were 20 (start position), 49 (asymmetry -12), 163 (center), 277 (asymmetry +12) and 306 (end position), all distances in mm (see figure 5.6). The light taper was to be achieved by treating (roughening) the two long

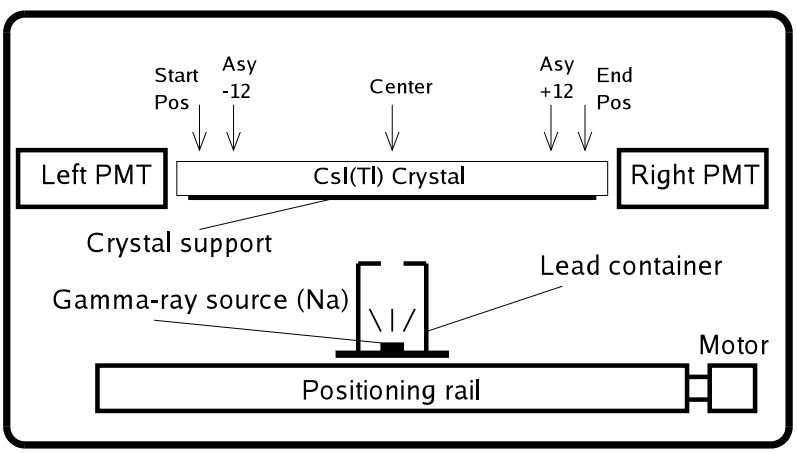

Figure 5.6: *A schematic picture of the interior of the black box. The five measuring positions used during production rate are indicated.*

sides measuring 326 × 19.9 mm^2. The other two larger surfaces should be polished, but could be treated to help achieve the correct taper if necessary.

The crystal optical performance is characterized by defining a set of parameters. These parameters are:

- the light taper values $\mathcal{T}_\mathcal{L}$ and $\mathcal{T}_\mathcal{R}$
- the light asymmetry value $\mathcal{A}$
- the average light yield Y_{av} for each crystal and the deviation of Y_{av} from the average light yield of all crystals $\Delta Y_{av} = Y_{allav} - Y_{av}$
- light yield variation ΔY within each crystal
- the FWHM (Γ) of the 511 keV peak

The PMT signals referred to in this section ($\mathcal{L}_\mathcal{S}$ and $\mathcal{L}_\mathcal{E}$ e.g.) are defined as the mean value of a Gaussian fit (as described on page 53) to the 511 keV peak.

Light Taper Values $\mathcal{T}_\mathcal{L}$ and $\mathcal{T}_\mathcal{R}$. These values are defined as the following ratios:

$$\mathcal{T}_\mathcal{L} = \frac{\mathcal{L}_\mathcal{E}}{\mathcal{L}_\mathcal{S}} \qquad \mathcal{T}_\mathcal{R} = \frac{\mathcal{R}_\mathcal{S}}{\mathcal{R}_\mathcal{E}} \tag{5.2}$$

$\mathcal{L}_\mathcal{E}$ and $\mathcal{L}_\mathcal{S}$ are the signals from the left PMT when the ^{22}Na source is positioned at the end and start positions, respectively. Similarly, for the right PMT $\mathcal{R}_\mathcal{S}$ and $\mathcal{R}_\mathcal{E}$. I.e., the taper value is constructed from the ratio between the far and close positions of the source as seen from a PMT. See figure 5.7.

Light Asymmetry Value $\mathcal{A}$. The light asymmetry value as defined by equation (5.3) will be used in the final instrument when determining the position along the longitudinal axis of the crystal of a measured event.

$$\mathcal{A} = \frac{\mathcal{R} - \mathcal{L}}{\mathcal{R} + \mathcal{L}} \tag{5.3}$$

The light asymmetry values along the crystal forms the light asymmetry curve (see figure 5.8). During calibration when the position of the source is known the asymmetry value can be calculated for each position. The slope of the asymmetry curve is used as the calibration constant. The longitudinal position for a measured event is given by:

$$\mathcal{P} = \mathcal{P}_0 + \mathcal{A} \cdot \mathcal{S}, \tag{5.4}$$

where $\mathcal{S}$ is the calibration constant and $\mathcal{P}_0$ is the intersection between the asymmetry curve and the position axis. However, the analysis program was not constructed to map the asymmetry curve. Instead, the requirement specification refers to the asymmetry value as:

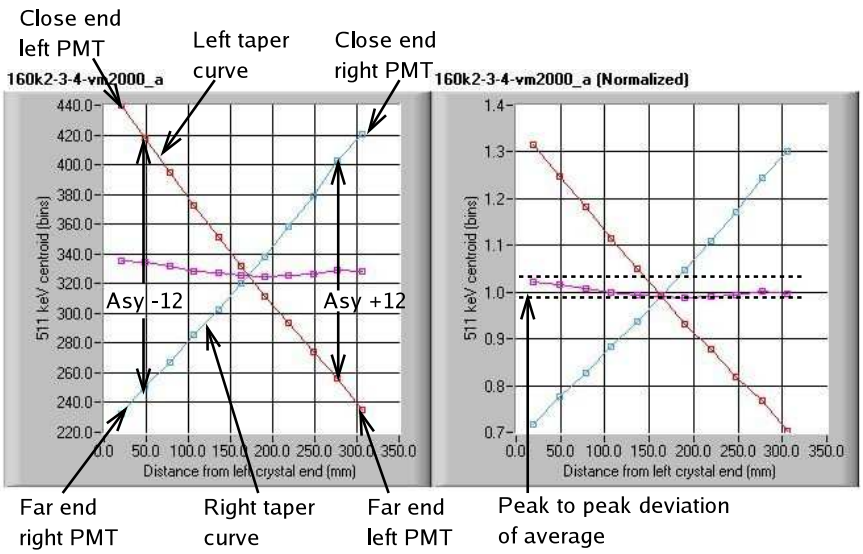

Figure 5.7: *A light taper curve which results from the analysis program. Plotted are the left and right taper curves and the average.*

$$\mathcal{A} = \frac{\mathcal{R}_{+12} - \mathcal{L}_{+12}}{\mathcal{R}_{+12} + \mathcal{L}_{+12}} - \frac{\mathcal{R}_{-12} - \mathcal{L}_{-12}}{\mathcal{R}_{-12} + \mathcal{L}_{-12}} \tag{5.5}$$

This value is constructed from the signals from both PMTs with the ^{22}Na source at the two positions closest to ± 12 cm, from the crystal center (the end points of the asymmetry curve), cf. figure 5.6. All $\mathcal{L}$- and $\mathcal{R}$-values should be normalized with $\mathcal{L}$ and $\mathcal{R}$ at the crystal center. As the name suggests it is a measure of how the intersection of the taper curves is positioned with respect to the crystal center. This quantity will always be a positive quantity since the $\mathcal{L}_{+12} < \mathcal{R}_{+12}$ and $\mathcal{L}_{-12} > \mathcal{R}_{-12}$.

Average Light Yield Y_{av}. The light output from the crystal when the ^{22}Na source is at position p is the average sum signal from the two PMTs:

$$S_p = \frac{L_p + R_p}{2} \tag{5.6}$$

The average light yield is then formed as

$$Y_{av} = \frac{1}{n_p} \sum S_p \tag{5.7}$$

where n_p is the number of positions measured along the crystal. The average light yield was taken as a relative measure of the amount of light produced by a certain energy deposition. It was used as an accumulative value comparing the

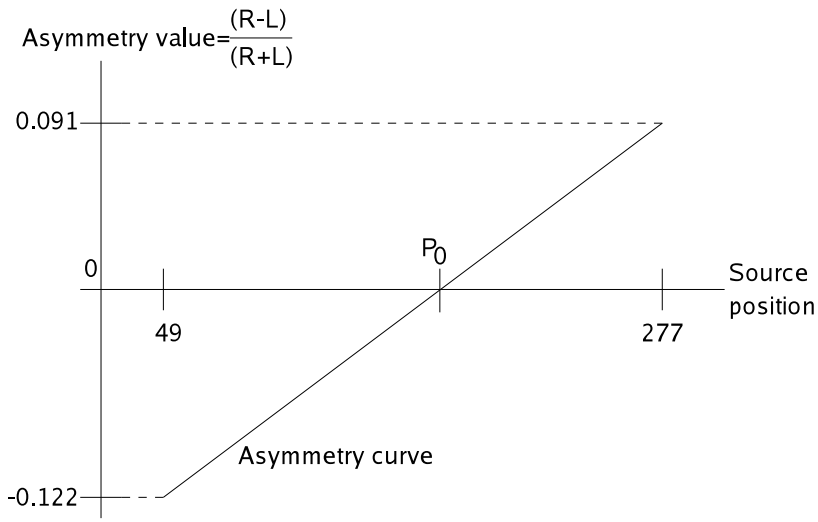

Figure 5.8: *Asymmetry curve created from the two positions 49 mm and 277 mm. The asymmetry value according to the specification is the sum of the magnitudes of the values from the two positions.*

crystals during production as to get a measure of the deviation of light yields from the average of all crystals

$$(\Delta Y_{av})_i = Y_{all\ av} - (Y_{av})_i \qquad i \in [0, N] \tag{5.8}$$

where

$$Y_{all\ av} = \frac{1}{N} \sum_{j=1}^{N} (Y_{av})_j \tag{5.9}$$

Peak to Peak Variation ΔY. The relative variation in total light output along the crystal (see figure 5.7) is defined as

$$\Delta Y = \frac{S_{max} - S_{min}}{Y_{av}} \tag{5.10}$$

Signal Resolution Γ. The full-width at half-maximum (FWHM) of the 511 keV peak was used as a measure of the energy resolution.

$$\Gamma_p = 2 \cdot \sqrt{2 \ln 2} \cdot \sigma \approx 2.35 \cdot \sigma, \tag{5.11}$$

where σ is the standard deviation of the fitted Gaussian.

The crystal resolution was defined as the average FWHM of all positions:

$$\Gamma = \frac{1}{n_p} \sum \Gamma_p \tag{5.12}$$

Goals

All values were specified as measured with the ^{22}Na source and analyzed with respect to its 511 keV conversion peak. The light taper curve was to be monotonous with the goal of having a linear or near linear dependence. The absolute light yield was an accumulated measure where the individual light yield was to be compared with the average of all crystals. The required parameter limits are listed in table 5.2.

Parameter	**Symbol**	**Min. Value**	**Max. Value**
Light taper value	$\mathcal{T}$	50%	70%
Light asymmetry	$\mathcal{A}$	0.24	0.48
Dev. of light yield fr. aver.	ΔY_{av}	0%	10%
Peak to peak variation	ΔY	0%	10%
Crystal resolution FWHM	Γ	0%	13%

Table 5.2: *Optical parameter requirements*

Test Procedure

Before starting the optical test, crystal wrapping was changed from Tyvek and aluminum foil used during shipment and storage into the high reflective VM2000. Figure 5.9 shows the two wrappings which are further discussed on page 66. A number of crystals (usually four at a time) were then put inside the black box and were left there shielded from ambient light for at least half an hour before measurement began. This allowed noise from long lived fluorescence states to decay.

Each crystal had a V-shaped scratch mark on one of its largest surfaces, located near one of the readout faces. This 'V' defined the orientation for crystal placement in the test station. The surface with the mark should be the top surface and the 'V' should point to the right PMT.

Before data acquisition was started, the right PMT was adjusted into its position for measurement. After crystal insertion the following data had to be written into the DAQ-software:

- crystal identification number
- name and location of operator
- environmental circumstances
- search path for the output file

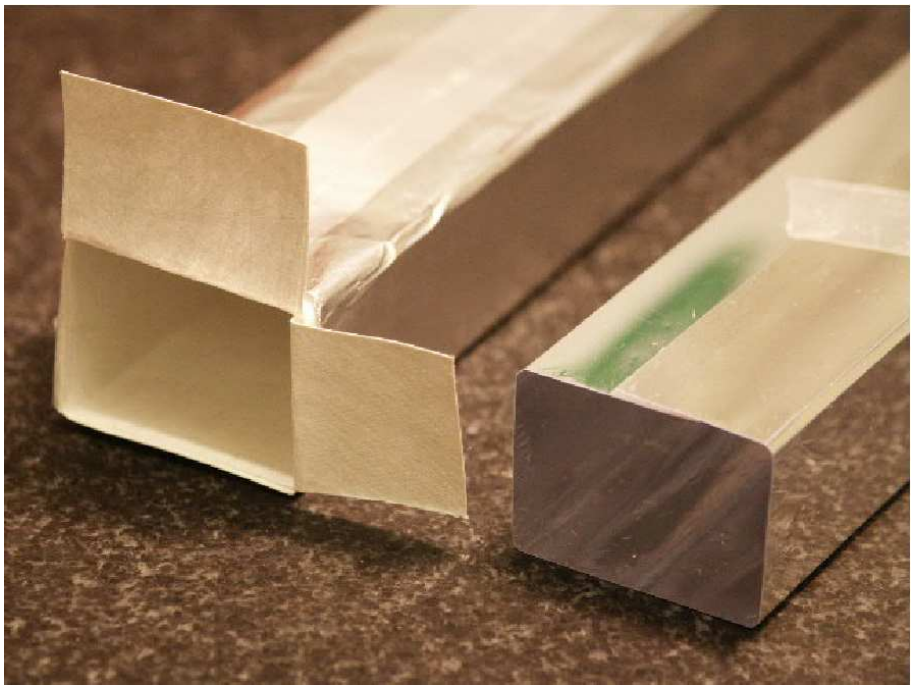

Figure 5.9: *Left: Tyvek + aluminum foil. Right: VM2000. The wrappings are shown without crystals.*

Other quantities also controllable from the program were the positions for the source, the time duration for each measuring position and the individual values of the high voltage to the PMTs. However, once the test stations had been calibrated these parameters were not to be changed.

The initial activity of the ^{22}Na source was 20 μCi which resulted in a trigger rate of between 500 and 1000 Hz. With a measuring time of 300 s this gave a Gaussian integral containing around 3000 events, with some variation depending on the source location. Figure 5.10 shows the screen information of the DAQ program during the measurement. This screen-shot shows the three displayed histograms after a 300 s measurement which is almost complete.

After measurement the crystal was removed from the test station and the wrapping material changed back to the Tyvek and aluminum sleeve. The acquired data was analyzed with the analysis software. Initial values for the fit parameters had to be defined in order to control which part of the histogram to analyze. More than one peak was present in the histogram.

The data from the DAQ-program were stored in LabView histogram files. Data from the two test stations were remotely saved on a stand-alone computer used merely for storage of measurement data. The results from the analysis were stored in picture files (.jpg format), one for each histogram (cf. figure

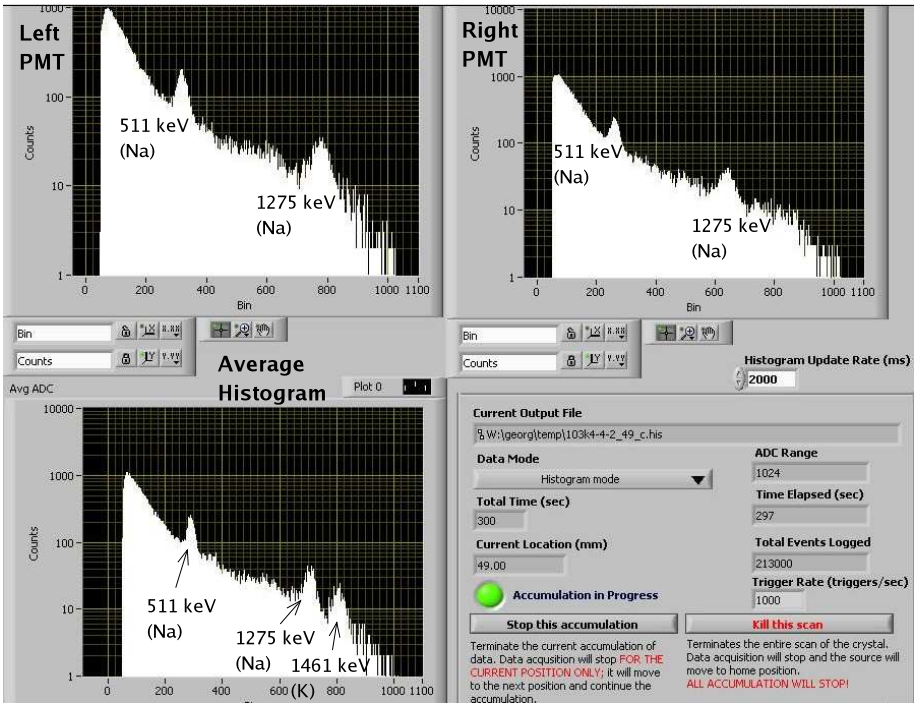

Figure 5.10: *A screen-shot of an ongoing data acquisition run. The source is in the second position (Asy-12); the peak in the left histogram is in a higher bin than in the right histogram. The third peak in the average histogram is the 1.461 MeV line from radioactive* ^{40}K*, which is present in the concrete of the building. This peak only shows up in the sum histogram because these photons enters the crystal uniformly.*

5.5) in each position and one for the taper curves (cf. figure 5.7), a Microsoft Excel Sheet and a text file (.txt). The two latter contained the numerical values and uncertainties of the fitted parameters and the values of the required optical parameters.

The Crystal-PMT Optical Connections

During the testing of pre-production crystals and at the early stages of flight crystal production pads of silicon rubber, Sylgard (from Dow Corning) [42], was used as the optical coupling between the crystal and the PMT. It was initially noticed that the orientation of the crystal in the test station affected the optical coupling. Consequently, it was decided that each crystal should be marked with a small V-shaped scratch mark at one end of its long "upper" surface. The V-marked end should be placed close to the right PMT. An example of how the result was affected from the different orientations is illustrated in figure 5.11. If the optical coupling at the two ends had been the same and independent of

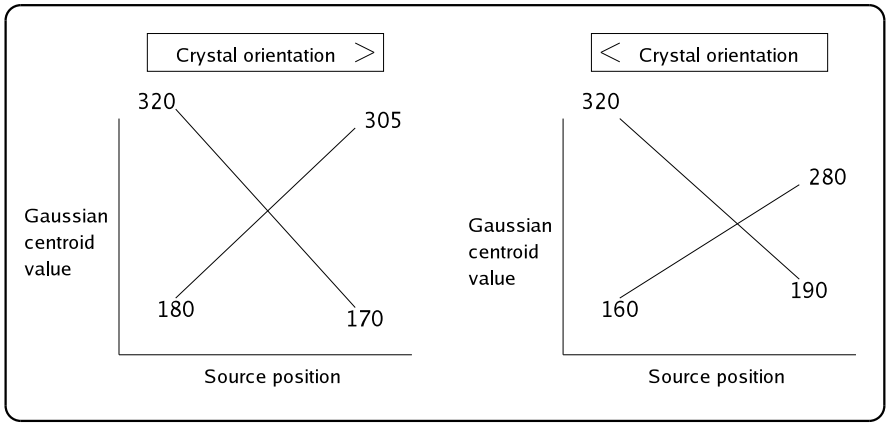

Figure 5.11: *An example showing how the taper curves initially could change with crystal orientation. Gaussian centroid in arbitrary units.*

the crystal orientation, then the two taper curves would only depend on crystal intrinsic properties and the two diagrams in figure 5.11 would be symmetric.

The importance of the optical coupling for the reliability of test result is obvious. Hence, it was necessary to find a stable and reliable optical connection to minimize systematics in the crystal calibration. It was found that the optical coupling when using Sylgard pads depends on the following circumstances:

- The parallelness of the end faces of the crystal
- the perpendicularity of the end faces relative the sides of the crystal
- the flatness of the surface
- the line up (parallelness) of the PMTs
- the adjustment of the crystal support relative the PMTs

Figure 5.12 illustrates the case when a Sylgard pad does not completely wet the end face of the PMT. An air gap considerably affects the amount of light reflected back into the crystal. Figure 5.13 shows how the taper curves typically will change, if the Sylgard pad does not wet the PMT surface completely. Since the fraction of the surface that is wet by the Sylgard pad is arbitrary at a specific occasion, the efficiency of the light connection is going to be random from case to case.

The most stable optical connection is a full air gap without any Sylgard pad. It does not depend on any of the above mentioned parameters. A small disadvantage is a lower light output. The light output was found to be sufficient, however.

The change in tapering due to incomplete Sylgard coupling can be understood as follows. If the end face is completely wet by the Sylgard pad then

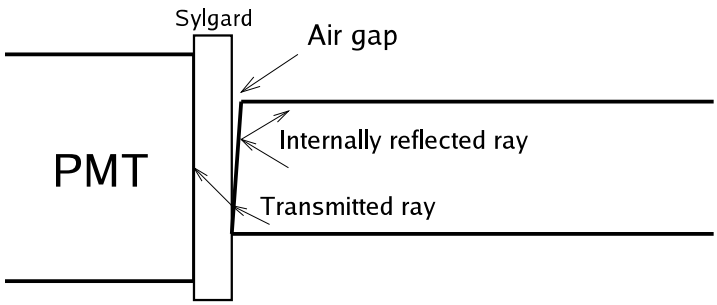

Figure 5.12: *Light reaching the end face at a partial air gap will experience total internal reflection. The angle causing the air gap is exaggerated for clarity.*

there is nothing which could increase the light output. Where the end face is not completely in contact with the Sylgard there is an air gap. This causes the signal from that end to decrease and a possibility for the signal from the opposite end to increase, since the light being internally reflected can reach that end and be transmitted to the PMT.

Consider the two positions closest to the crystal ends. Assume a partial air gap is present at the left end, while the right end is completely wet by the Sylgard (figure 5.13). For the leftmost position of the source, the angles of the light impinging on the left crystal end will have a quite even distribution. With an air gap present a large fraction of these will be internally reflected

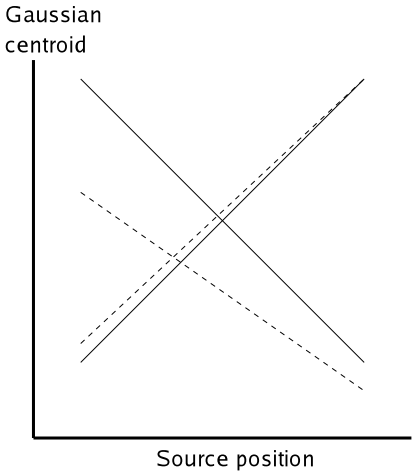

Figure 5.13: *Solid lines represents the taper curves obtained with completely wetted end faces; dashed lines the case if a partial air gap is present in the optical coupling at the left end face.*

and thus decreasing the signal from this end. At the rightmost position of the source, the light reaching the left end has to travel the full length of the crystal. The light having large angles compared to the normal of the end face will reach the side faces before arriving at the end face, which means it has to be reflected, internally or externally (specular), many times. During these reflections there is a probability for the photons to be absorbed or scattered. The angular distribution will now have a larger fraction of angles close to the normal. Thus this signal will not be affected as much as the position close to the end. The right taper curve will also be affected to a certain degree. Some of the internally reflected light from the leftmost position (far position as seen from the right end) will reach the right end and be registered there. Thus a portion of the light which should have been registered at the left end will instead be transferred to the right end, lifting the lower part of the taper curve and thus increasing the right taper value.

Conclusively, the least variable optical connection is an air gap. Apart from variations in the coupling of Sylgard within a test station, there was also a risk of having a systematic difference between the two test stations. This issue, and a presentation of how much the optical parameters are affected when removing the Sylgard pads, are described below.

Differences Between the Test Stations and Updating to the Crystal Acceptance Specification

It was early demonstrated that there existed a systematic difference between the test stations. It was observed that TS2 systematically produced larger light taper values.

The reference crystal was used to measure with Sylgard pads and with 1 mm air gaps in TS2. In both measurements data was taken for the standard orientation and with the crystal turned left-right. Light taper and light yield values leading to the decision not to use Sylgard are presented in table 5.3. The measurements with air gaps were reproducible with good precision when the crystal was turned left-right. The Sylgard measurements, however, showed a substantial random variation.

To achieve good symmetry of the taper curves around the average the gain had to be slightly adjusted. The measurements were then repeated. The air gap values were not changed in a significant way as they should, since a change in gain introduces the same factor in both nominator and denominator of the taper value ratio. TS1 was then calibrated with air gaps against TS2.

As seen from the table there is a non-negligible difference between the test stations when using Sylgard. The test with the reference crystal showed that the light taper values were 20% higher when measured with air gaps. More crystals were then tested with both air gaps and Sylgard pads to get a more accurate estimate of the ratio and to calculate new limits. A more thoroughly mapping of the differences between the test stations were performed later and it is described in subsection 5.2.2.

For each longitudinal position of the source the ratio of the signals measured

Test Station 2				
Before Gain Adjust.	**Sylgard**		**Air Gap**	
Parameter	**Std. Orient.**	**L–R**	**Std. Orient.**	**L–R**
Left Taper Value	63.1%	71.5%	77.6%	82.8%
Right Taper Value	74.0%	68.9%	82.7%	77.6%
Average Light Yield	340.5	329.1	311.0	310.9
After Gain Adjust.	**Sylgard**		**Air Gap**	
Parameter	**Std. Orient.**	**L–R**	**Std. Orient.**	**L–R**
Left Taper Value	59.1%	63.7%	77.6%	82.5%
Right Taper Value	67.1%	61.1%	82.6%	77.7%
Average Light Yield	342.5	342.3	297.7	298.8
Test Station 1				
Before Gain Adjust.	**Sylgard**		**Air Gap**	
Parameter	**Std. Orient.**	**L–R**	**Std. Orient.**	**L–R**
Left Taper Value	63.5%	64.2%	77.1%	80.1%
Right Taper Value	70.0%	65.6%	81.6%	77.7%
Average Light Yield	348.5	356.3	317.7	320.7
After Gain Adjust.	**Sylgard**		**Air Gap**	
Parameter	**Std. Orient.**	**L–R**	**Std. Orient.**	**L–R**
Left Taper Value	Not meas.	Not meas.	77.7%	80.7%
Right Taper Value	Not meas.	Not meas.	81.7%	77.8%
Average Light Yield	Not meas.	Not meas.	293.6	295.8

Table 5.3: *Average light yield in arbitrary units. TS1 not measured with Sylgard after gain adjustment, but calibrated with respect to TS2. The left taper value from standard orientation should be similar to the right taper value from left-right orientation and vice versa.*

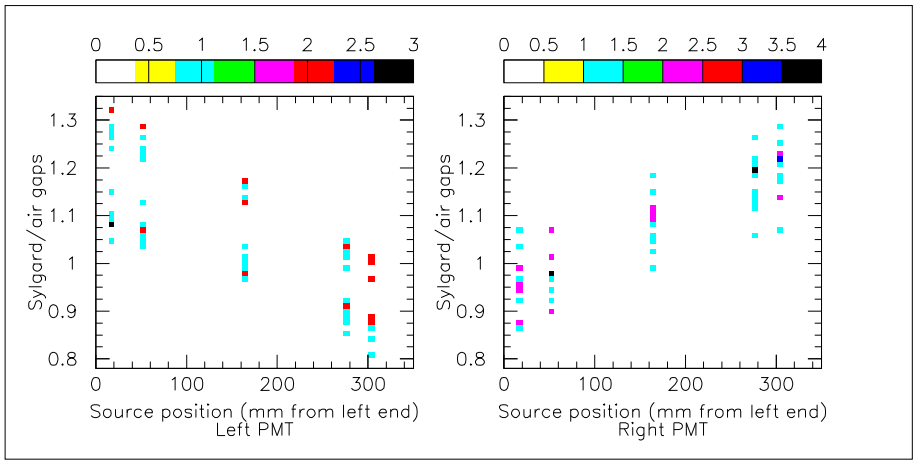

Figure 5.14: *The ratio of the PMT signal as measured with Sylgard divided by the signal obtained with air gaps plotted versus the longitudinal position of the source.*

with Sylgard compared with air gaps show similar behaviour to that seen in the comparison between the wrapping materials VM2000 and Tyvek (cf. page 66), i.e., an approximately linear increase of the difference if going from the close position to the far. For the right crystal ends the difference, for both test stations, are quite evenly distributed. For the left end though, there is a clear distinction between the test stations, the upper group in the left graph in figure 5.14 is the crystals measured in TS1 and the lower group comes from TS2. The conclusion being that the left end of TS2 had most problems achieving a good optical connection. The phenomenon that the ratio of the Sylgard values over the air gap values for the far position is close to, or even less than, one was discussed on page 64.

The ratio of the taper values between Sylgard and air gaps was found to be 0.78. As measured with air gaps the taper values should be within the interval of 64% (corresponding to the lower 50% value) and 89% (corresponding to the upper 70% limit).

The asymmetry value when measured with Sylgard was twice that from air gap measurements. Thus the lower asymmetry value of 0.24 as measured with Sylgard should correspond to 0.12 when measuring with air gaps. Note that when the taper values increase, the asymmetry value decreases, see equations (5.2) and (5.5).

The ratio of Sylgard over air gap for the averages (the light yield measure) was almost constant along the positions. The light yield (mean of averages) is about 9% larger if measured with Sylgard as compared to air gaps (based on the data from TS1). The reflectance for normal incident light, $R = [(n_1 - n_2)/(n_1 + n_2)]^2$ is about 1% when going from CsI to Sylgard and about 8% when going from CsI to air. This is a rough estimation of the light loss, but it corresponds quite well to the difference in the light yield for the compared optical couplings.

After the completion and muon test of a few hundred CDEs, it turned out that the crystals with the poorest optical properties as measured with air gaps did not perform satisfactory as a CDE. The above mentioned comparative test between Sylgard and air gaps was repeated, with more crystals and all crystals tested in both test stations. The results were equivalent to the first test and additionally a constant shift between the test stations when measuring with Sylgard was confirmed. However, based on the CDE performance it was decided that the low asymmetry and high light taper limits were to be tightened. The new requirement specification is given in table 5.4. More details on the discussion of muon tested CDEs is given in subsection 5.2.2 on page 73.

Crystal Wrapping

During the early prototype stages of the calorimeter the crystals were wrapped in diffuse reflective Tyvek closest to the crystal. The final calorimeter construction used a carbon fiber structure to hold the CDEs. One of the first ideas was to mold the reflective material to the cavity walls. The material chosen was the specular reflective VM2000, a polymeric Mylar film. The VM2000 is easily heat shaped and could be applied tight fit around the crystal, chamfer shape included.

Parameter	New Min	New Max
$\mathcal{T}$	67%	89%
$\mathcal{A}$	0.20	0.60
ΔY_{av}	0%	10%
ΔY	0%	10%
Γ	0%	13%

Table 5.4: *Optical parameter requirements as measured with full air gaps. (See page 55 for definition of the parameters)*

The difference between Tyvek and VM2000 is the difference between diffuse and specular reflection, respectively. It is obvious that the different properties of reflection will affect the CDE results when used as wrapping around a crystal. The light output will be higher with VM2000, but other properties will also be affected.

During the pre-production process the crystal optical requirements were specified with respect to the Tyvek wrapping. However, when wrapped in VM2000 and measured with diodes in a muon telescope the crystals turned out to have too little tapering. A first test in the optical test stations in Kalmar using VM2000 showed that the light yield would increase with approximately 30% and the light taper values would increase with about 25% (i.e. less tapering). It was also noted that the change in signal was not constant for the different positions of the source, but seemed to be roughly linearly dependent.

After the decision to change to VM2000 as wrapping material the specification was updated accordingly and acceptance testing had to be carried out with the new wrapping. The change also affected Amcrys' manufacturing process, they had to apply more roughening to the treated surfaces in order to fit the crystals within the new specification.

The increase in light yield when going from Tyvek to VM2000 averaged at 36% with a minimum of 32% and a maximum of 42%. The increase in signal strength for each measured position did indeed vary depending on the position of the source from the PMT. The increase is less at the position close to the PMT. As can be seen from figure 5.15, the dependence of the increase is approximately linear, with an accuracy of $\pm 10\%$.

The fact that the increase in light output when going to VM2000 show variation depending on source position can be understood by considering the differences between the diffuse and specular reflection. For light created with the source at the close position, the majority of the registered light will be direct light (no or very few reflections before escaping the end face). If the wrapping is specular the light which initially have a direction away from the surface of the PMT and which encounters a side face of the crystal and is externally reflected, will continue to move away from the end surface as shown in figure 5.16. However, if the wrapper is a diffuse reflector this light might be redirected towards the end face and escape. Thus, if the two wrappings would have the same reflectiveness, then the specular wrapping would give a smaller signal with

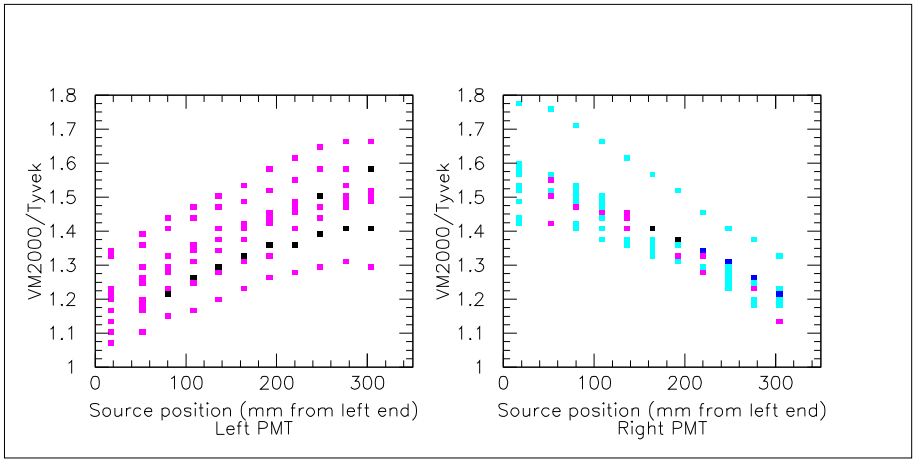

Figure 5.15: *Change of output signal as a function of source position for left and right PMT.*

the source close to the readout surface. When the source is at the far position, the light having an initial direction towards the far PMT has generally to be reflected several times before reaching the PMT. With a specular wrapping the probability is much higher that this light actually will reach the end than with a diffuse wrapping, where the probability is smaller due to the fact that, for each external reflection, the light might be directed back towards the opposite face or another side face (figure 5.16).

The change of light taper does vary somewhat between crystals, and crystal ends. The results for nine test crystals are presented in table 5.5, with average and RMS values for the taper values, the asymmetry values and the light yield.

If using an air gap of approximately 2 mm, the increase of the taper values

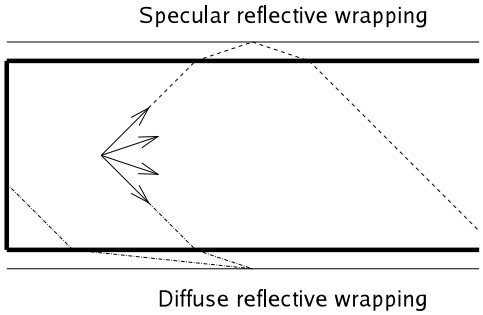

Figure 5.16: *An illustration showing the difference between a specular wrap and a diffuse wrap. The bottom ray is subject to a diffuse reflection and can after the reflection take on any direction.*

Ratio	Average	RMS
Left Taper	1.248	0.0442
Right Taper	1.284	0.0634
Asymmetry	0.719	0.0395
Light Yield	1.355	0.0327

Table 5.5: *Ratios of VM2000 over Tyvek measurements for light taper, asymmetry and light yield values.*

is somewhat smaller, around 10-15%. The change of light yield is higher with air gaps than Sylgard pads, around 50%.

5.2 Results of the Optical Acceptance Tests

In this section the results from the optical acceptance tests are presented. First to be discussed is a ray-tracing program constructed to simulate the shape of the taper curves, the effect of different wrapping materials and the effect of different optical connections. The performance of a CDE (measured with diodes) will be compared to the measurements with PMTs. Also discussed are the results of surface retreatments due to inadequate optical performances as delivered from Amcrys. Last in this section the results of the optical parameters from the acceptance test are presented for the entire crystal set.

5.2.1 Simulations

After the delivery and test of the first crystals it was observed that several taper curves were not monotonic. Toward the high end of the taper curves the derivative changed sign. In the preproduction crystal specification it was stated that the last 3 cm (close to the PMTs) of the surfaces treated to achieve the taper were to be polished. It was suspected that this caused the observed effect. A ray tracing program was then developed to achieve a better understanding of what caused the shape of the taper curve. The code was later extended to also include comparisons of the two different wrappings and optical connections.

Model Description

The crystal was defined as a three-dimensional box cavity in which a ray of light was allowed to travel. The light ray was created at random height and width uniformly (the cross section) in the crystal and at a chosen position along the longitudinal axis. The direction of the ray was also isotropically thrown. Traveling through the crystal the light ray would eventually reach a surface, where the readout faces and the large side faces were considered to be polished and the two smaller side faces roughened. At one of the four polished sides the ray could either be internally reflected or escape. If it escaped at an end face the ray was registered as “detected”. If it escaped a polished side surface it reached the wrapping material where it was either reflected or absorbed.

It was readily demonstrated that the main features of the taper curve can be altered by the roughened side faces. These surfaces were studied under a microscope in order to get an estimate of what fraction of the surface that was affected by the roughening. The surface was studied with a magnification of 800 times. The inspection showed that tiny chips had been torn off the smooth surface, creating rough spots. In the simulation when a light ray reached one of these faces it was first determined if the ray arrived at a rough or polished spot. If hitting a rough spot there was a certain probability for the ray to be internally reflected with a random new direction. It could also escape, again with a random new direction. If hitting a polished spot it was treated as the polished faces.

When escaping and reaching the wrapping material there was a certain probability for absorption. This probability was considered to be higher for Tyvek as compared to VM2000. Furthermore, in the case of Tyvek the ray was always given a random new direction if it was not absorbed. The VM2000 reflects the ray specularly (like a mirror).

Simulation Results

The coarse goals of the simulation studies were to verify the observed results and to gain a better understanding of what influences the taper curves. The linearity and monotonicity of the taper curves are discussed in the following paragraph. Also covered by the simulations are the change of wrapping material and the removal of the Sylgard pads in favour of air gaps. In all simulations 10^6 light rays were created in order to obtain adequate statistics.

Shape of the Taper Curve. The shape of the taper curve and the taper value $\mathcal{T}$ was tested by changing the conditions on the smaller side faces where the roughening was applied. The conclusion of the microscope study was that, on average, about 20% of the surface consisted of rough spots. The conditions in the simulation were as in the specifications during that stage of optical tests, i.e. Tyvek wrapping and Sylgard pads as optical connection.

Studying three different cases provided enough ground for conclusions. The size of the end zone, being the part of a roughened surface close to the PMT, was taken to be 35 mm. The roughness of the major part of the surface was estimated to 15%. The roughening of the end zones was varied. All taper curves shown have the values from the different positions normalized to the first measuring point. Thus any differences in light yield cannot be deduced from the taper curves presented here.

The top left graph in figure 5.17 was generated with a constant taper, i.e. the same roughening applied to the whole surface. These taper curves are near linear with only a slight exponential shape to it. The top right graph had a roughness of the end zones of 9% (i.e. less than the rest of the roughened surfaces). The linearity is somewhat better but the most obvious difference is in the three positions closest to the PMTs. The lower left graph had polished end zones with the roughness set to only 1%. These taper curves are clearly not

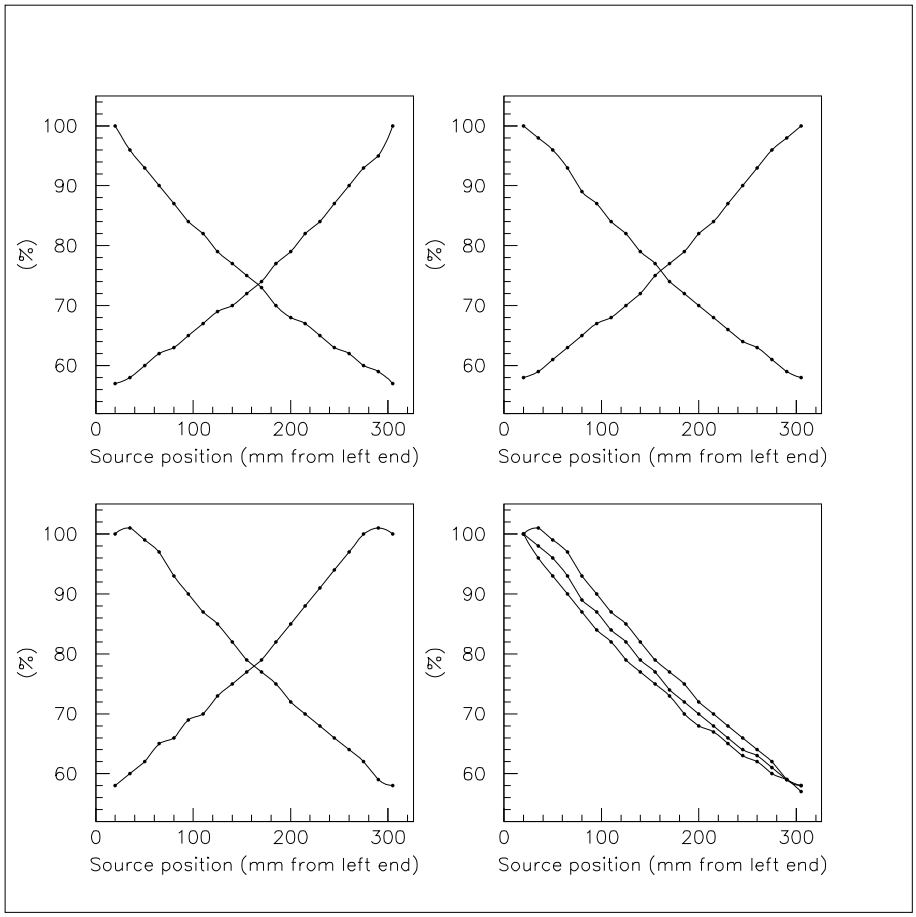

Figure 5.17: *Taper curves emerging from three different treatments of the end zones of the roughened surfaces. See text for details.*

monotonic and there is no doubt that the effect arises from how the end zone is treated. The lower right graph shows the left taper curves for all three cases plotted in the same graph, the curves appears from left to right as presented in this paragraph.

Conclusion: it is possible to control the shape of the taper curve and in particular a linear taper curve would be possible to obtain by applying different degrees of roughness to the smaller side surfaces.

Wrapping Materials. Comparing different wrapping materials meant a change of the conditions for the light rays escaping from one of the side faces. The Tyvek wrapping reflected the impinging light diffusively which in the simulation program meant that the rays were given random new directions when reaching the

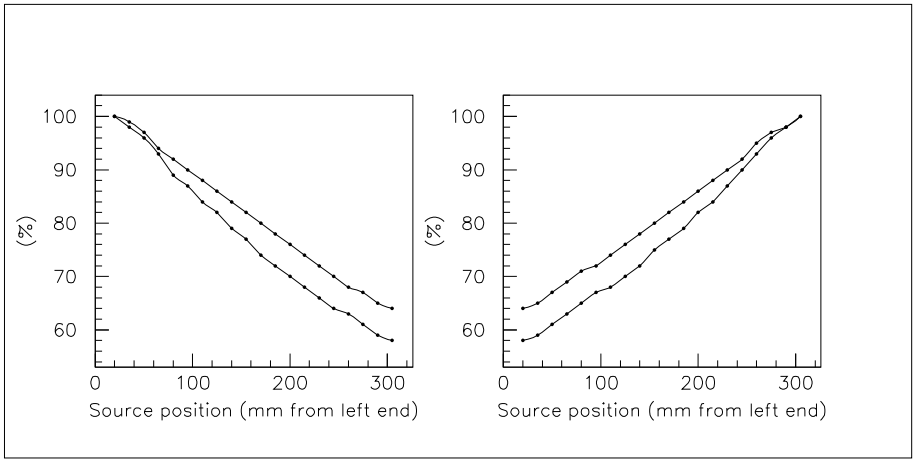

Figure 5.18: *Taper curves comparing VM2000 (upper curves) with Tyvek. Sylgard used as optical connection. Left and right taper curves, respectively.*

wrapper. The specular reflection of VM2000 required the program to change sign of the direction component normal to the surface hit by the light ray.

The second case mentioned above (end zones 9% roughened) was used for comparison between wrapper. The Sylgard pads were used as optical connection. With the parameter setting used for the roughening, this resulted in taper values of 56% with the Tyvek wrapper. The average light yield, here defined as the average number of rays managing to escape the end faces, was 16%.

Keeping the settings of the roughened surfaces but changing the wrapper to the VM2000 resulted in taper values of 64%, and an average light yield of 23%. The increase of the taper values from the simulation is 14% (figure 5.18) and the increase in light yield is 46% when going from Tyvek to VM2000.

Comparing the results from the simulation to what was measured with Sylgard pads shows a reasonable correspondence (page 66). The measured increase of taper values are larger than the simulated whereas the measured change in light yield is smaller. As described earlier the measurements with the Sylgard had a great deal of uncertainty. The values obtained measuring with air gaps (see page 69) comes closer to the simulation than the Sylgard. However, comparing the wrappings with air gaps in the simulation yields the same results. I.e. the simulated differences in taper values are lower and the light yield is higher than the measured values. To conclude, the simulated change is in the direction of and comparable to what was measured.

Optical Connection. The comparison of the two optical connections simply meant changing the refractive index of the interface at the crystal readout face. These simulations were carried out using the VM2000 wrapper.

The light taper values obtained with Sylgard were 64% and if simulated with air gaps this value is 83% (figure 5.19). This gives a ratio between the Sylgard

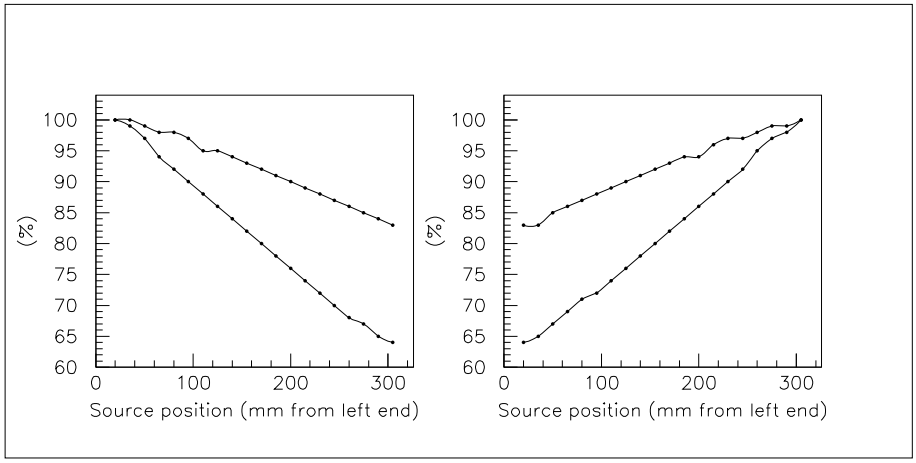

Figure 5.19: *Taper curves showing the differences between the optical connections, air gaps (top curves) and Sylgard. Left and right taper curves, respectively.*

and airgaps of 0.77, which agrees well with the measured values, subsections 5.1.3 and 5.2.2.

The light asymmetry value calculated for the Sylgard simulation is 0.366 and for the air gaps it is 0.152. The Sylgard asymmetry value is around 2.5 times that of air gaps, to be compared with the factor of 2 obtained from measurements.

Concerning the light yield the simulations suggest that the Sylgard value is nearly twice that obtained with air gaps. This is in qualitative agreement with measurements. But quantitatively it is considerably larger, most likely due to the fact that the Sylgard connection generally was far from perfect in reality (cf. subsection 5.1.3).

5.2.2 Test Station Measurements and CDEs

After the completion and measurement with cosmic muons carried out at NRL of a few hundred CDEs it turned out that some of them did not show fully satisfactory optical performance. Identification showed that these crystals were among the crystals which showed the poorest optical performance as measured in the test stations with PMTs and air gaps.

The optical coupling comparative test (subsection 5.1.3) was repeated with a larger number of crystals to obtain a higher systematic accuracy and to verify previous results. In the first test, six crystals were measured in TS1 and seven in TS2. This time 12 crystals were tested in both test stations. For each test station the taper and asymmetry values as measured with Sylgard were compared to the values obtained using air gaps. The measurements with Sylgard were compared between the two test stations, as well as the air gaps measurements.

For the individual comparisons between Sylgard and air gaps we saw basically the same results as in the first test. In TS1, the ratios of the Sylgard

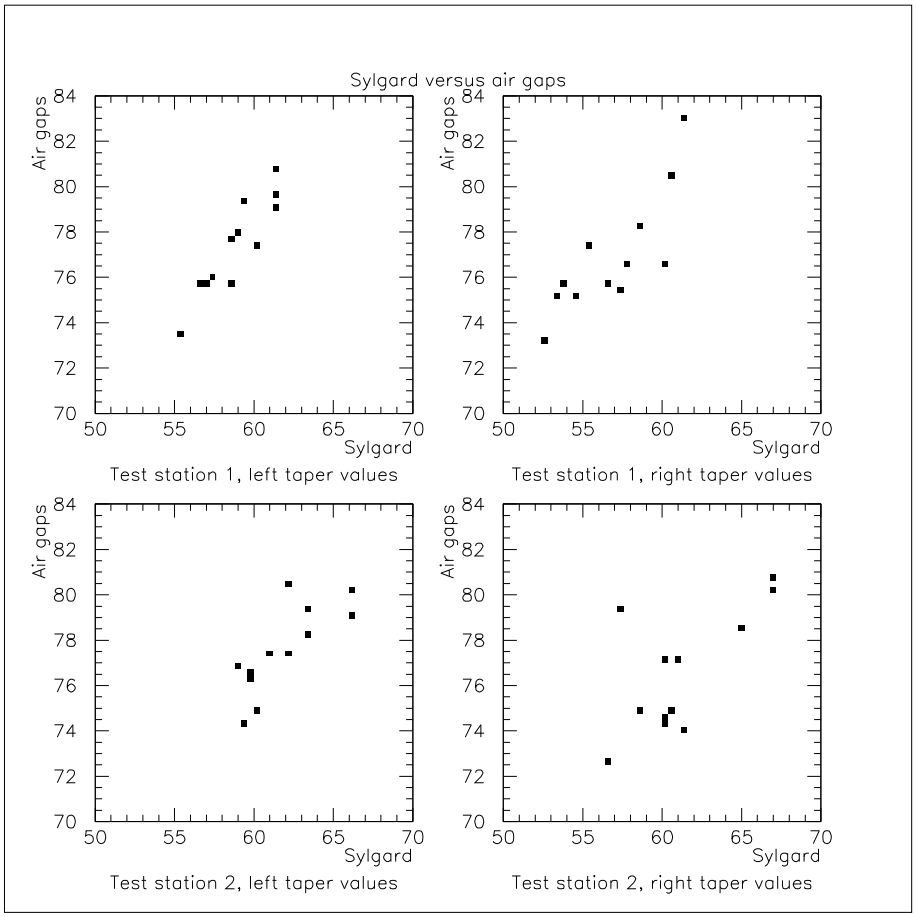

Figure 5.20: *Top: Air gaps versus Sylgard measurements, left and right taper values from TS1. Bottom: Ditto from TS2.*

taper values over the air gap taper values were 0.76 and 0.74 for the left and right PMT respectively. The previous result used in the modification of the acceptance specification was 0.78 . The asymmetry ratio was 2.0, as in the first test. In TS2 the two taper ratios were higher and the asymmetry ratio lower, as was to be expected in the case of a less good optical connection. The ratios were 0.80, 0.80 and 1.78 for the left and right taper values and the asymmetry value, respectively. Also, the spread in data from TS2 was somewhat larger (see figure 5.20).

What had not actually been tested before, but indeed suspected, was that there was a constant offset between the two test stations when measuring with Sylgard pads. This was now confirmed. On average, the left taper values were 5% larger and the right taper values were 8% larger in TS2. The asymmetry values as measured in TS2 were only 90% of that in TS1 (see left graph in

figure 5.21). When the Sylgard pads were replaced with air gaps, there were no significant differences between the two test stations (see right graph in figure 5.21). Conclusively, the measurements were much more reliable and comparable if using air gaps. More important: there were no systematic shift between the test stations.

Comparing the light asymmetry as measured with PMTs and air gaps with the ready CDEs measured with diodes and cosmic muons showed that the correlation was an offset rather than a factor (see figure 5.22). Because of the behaviour as a CDE, it was decided that the light asymmetry limit should be tightened. The asymmetry and taper values are further discussed in subsection 5.2.4.

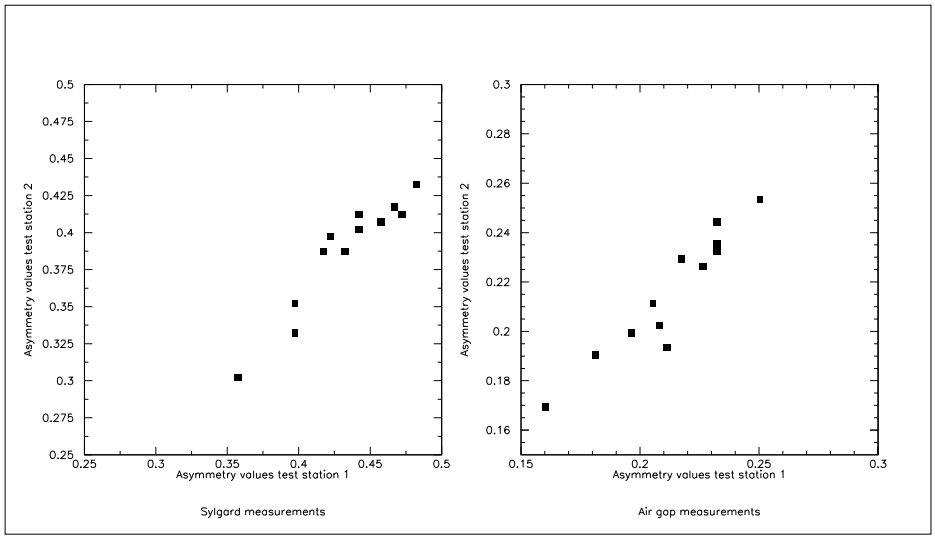

Figure 5.21: *Asymmetry values plotted from TS2 versus TS1 as measured with Sylgard (left) and air gaps (right).*

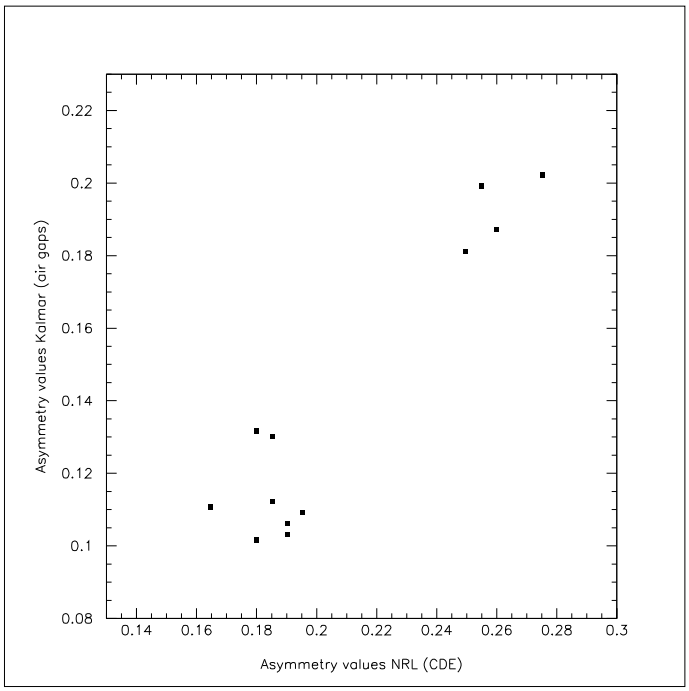

Figure 5.22: *Asymmetry values are plotted as measured with air gaps in the test stations versus the measurements with cosmic muons on ready CDEs.*

5.2.3 Retreatment of Crystal Surfaces

Due to the new limits of the asymmetry value several crystals had to be retreated for tapering. Some of the crystals were also taken out of the process due to too much taper (i.e. too low taper values) and/or asymmetry. In the case of poor optical performance the tapered surfaces needed further roughening, whereas the crystals with too much taper had to be polished.

The roughening was carefully applied with a fine grit paper. After roughening the dust was removed, using a brush for coarse cleaning and then carefully wiping the surface with a cloth wetted with alcohol. The polishing was performed with a cloth slightly wetted with alcohol which was gently rubbed against the tapered surfaces. All crystals treated could be adjusted to the specified limits and used as flight crystals.

The roughened crystals were measured twice after the retreatment. The first measurement was done immediately after re-tapering. It was noticed that the light yield always increased slightly as compared to the measurements made before the surface treatment. The second measurement was performed a week later. It was then found that the optical properties became somewhat better. That is, the light taper values had decreased somewhat compared to the first measurement and the asymmetry value was slightly larger. However, the light yield from this second measurement could be both larger and smaller than the first measurement. Grinding the surface induces mechanical stress in the crystal. The second measurement allowed for this stress to relax. In total we re-tapered 92 crystals due to poor optical characteristics.

77 crystals had been put aside from the production due to too steep taper curves and too high asymmetry values. 50 of these were later decided to keep as they were, while 27 were successfully polished.

5.2.4 Test Results

This section will present the results from the measurements of the optical parameters (cf. section 5.1.3) of all flight crystals. The statistics are from the 1807 crystals tested and accepted for production of CDEs. 431 crystals were measured with Sylgard pads and the remaining 1376 crystals were measured with an air gap instead as light connection to the PMTs.

Full Width at Half Maximum

Figure 5.23 shows the distribution of FWHM values of the 511 keV peak for all crystals measured with air gaps (left) and Sylgard (right). All crystals are well below the specified maximum value of 13%. The requirements defined the FWHM value to be the average of the normalized sum signal histogram for all measured positions (cf. subsection 5.1.3 on page 58). The result was divided between the two optical couplings, to show that the two 'clusters' appearing do not depend on the optical coupling. Inspection of crystals measured in both test stations shows that there is a difference between the test stations. This is likely due to different noise levels in the PMTs.

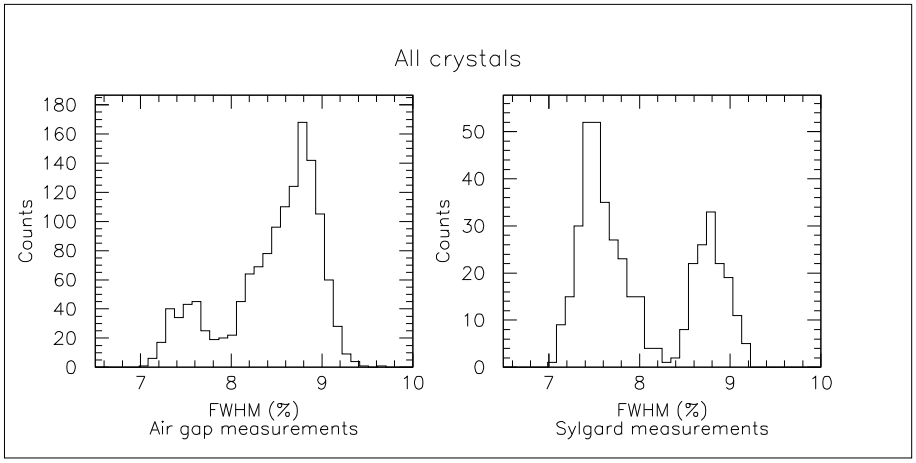

Figure 5.23: *Distribution of FWHM of the 511 keV annihilation peak for all crystals. Left: air gaps. Right: Sylgard.*

Energy Resolution

The energy resolution FWHM of the 511 keV peak is, for position at 49 mm (figure 5.24), 11.0% and 11.4% for the left and right PMT, respectively. Typically the energy resolution for the individual PMT signals is around 10%. The resolution of the normalized sum signal peak (lower left histogram) is 8.0%, which is a factor of $1/\sqrt{2}$ relative to the resolution in the individual spectra. This result is expected if summing two independent stochastic variables with normal distribution. The light which is created in the crystal is emitted isotropically. The light is subsequently randomized before reching the PMTs. Thus every registered light pulse is the result of an independent stochastic process.

The FWHM values typically increases with 1 %-unit in the individual PMT histogram when moving the source from the close position to the far position.

Position Resolution

The longitudinal position of an event is found by equation (5.4):

$$\mathcal{P} = \mathcal{P}_0 + \mathcal{A} \cdot \mathcal{S}$$

where $\mathcal{A}$ is the asymmetry value, equation (5.3):

$$\mathcal{A} = \frac{\mathcal{R} - \mathcal{L}}{\mathcal{R} + \mathcal{L}}$$

and $\mathcal{S}$ is the calibration constant (cf. page 56). An estimate of the longitudinal position resolution can be derived from the crystal's asymmetry using the spectral resolution. The calibration of the crystal's asymmetry curve is based on the two positions, 49 mm and 277 mm, used for the specific asymmetry value as described in subsection 5.1.3 (cf. page 56). The error in the longitudinal

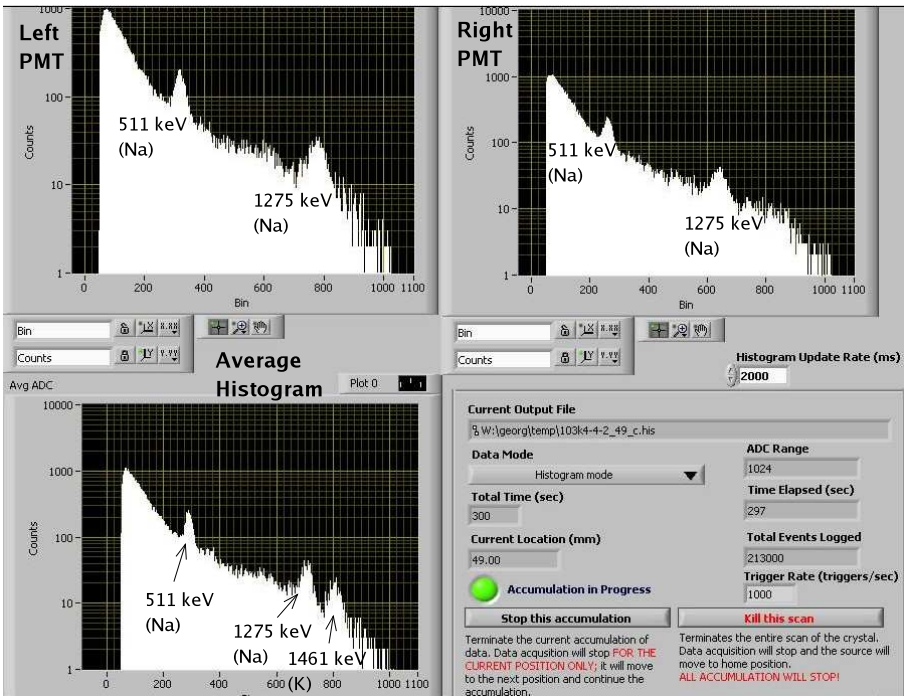

Figure 5.24: *Online histograms taken with the source in the second position 49 mm (Asy-12). Notice that the 511 keV line is narrower in the sum spectrum as compared to the individual PMT spectra.*

position depends on the error of the measured $\mathcal{A}$ and the calibration constant $\mathcal{S}$. The error in $\mathcal{S}$ can be estimated from the measurements in the optical test station. It depends on the error in the two asymmetry values and the error in positioning the source. The two asymmetry values in turn depends on the error in the four PMT signals. Carrying out this error propagation for a typical crystal with respect to the 511 keV line, yields that the relative error (σ) in $\mathcal{S}$ is 3.0%.

An estimation of the position error for a minimum-ionizing event can be calculated using the energy deposition of a traversing muon, which is around 12 MeV in each crystal. The standard deviation of the position is then of the order of 7 mm.

The optimal case had been if the analysis program had calculated the asymmetry value for each position and created the asymmetry curve, but this was not possible with the available program code. Previous experiments using prototype crystals [43] in an electron beam with an energy of 2 GeV, of which approximately 130 MeV was deposited in each crystal, have shown that the standard deviation of the position error is of the order of 0.28 cm, which we could confirm in the beam test experiment described in subsection 6.4.3.

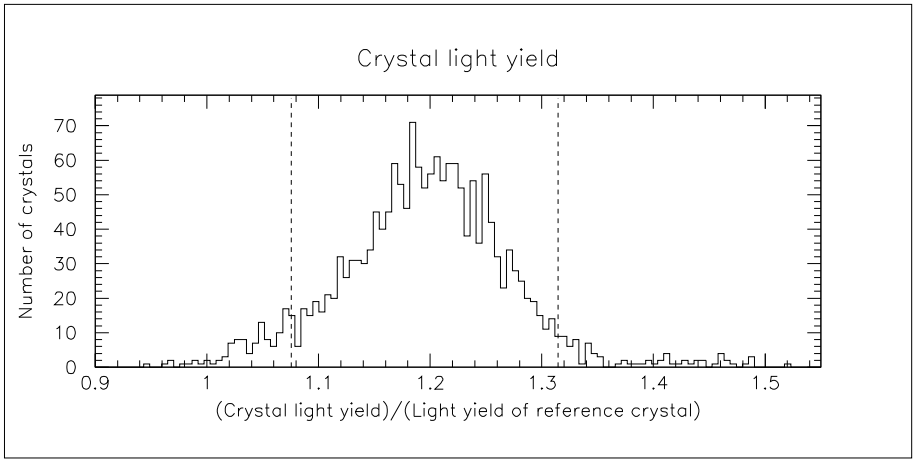

Figure 5.25: *Crystal light yields normalized to the reference crystal. Dashed lines show the limits of the specification requirements.*

Light Yield

The crystal light yields of all crystals are histogrammed in figure 5.25. All values are normalized with respect to the reference crystal. 48 crystals are missing in the distribution due to that they were measured before the reference crystal was adopted.

In total 164 crystals (9.1 % of the total amount) were outside the specified interval. 95 crystals (5.3%) were below the specification and 69 crystals (3.8%) were above. These crystals were later considered to have satisfactory light output and were used without further action.

Peak-to-Peak Variation

Figure 5.26 shows the distribution of peak-to-peak variations for all crystals. This value was according to the specifications to be kept below 10%. One single crystal, at 9.3%, is near that limit, whilst the bulk of the crystals lie below 5%.

Taper Values

The taper values from the measurements with Sylgard are shown in figure 5.27, left taper and right taper values, respectively. The specifications initially stated the upper light taper limit to be 70% (dashed lines in figure 5.27). It was later decided to accept light taper values up to 75% (dotted lines). Crystals with light taper values below the 50% limit were outside the acceptance interval according to specifications. A few just below limit were decided to be used for CDEs anyway, since crystals having a little too much tapering was not considered a critical issue.

Figure 5.28 shows light taper values, left and right, for air gap measurements.

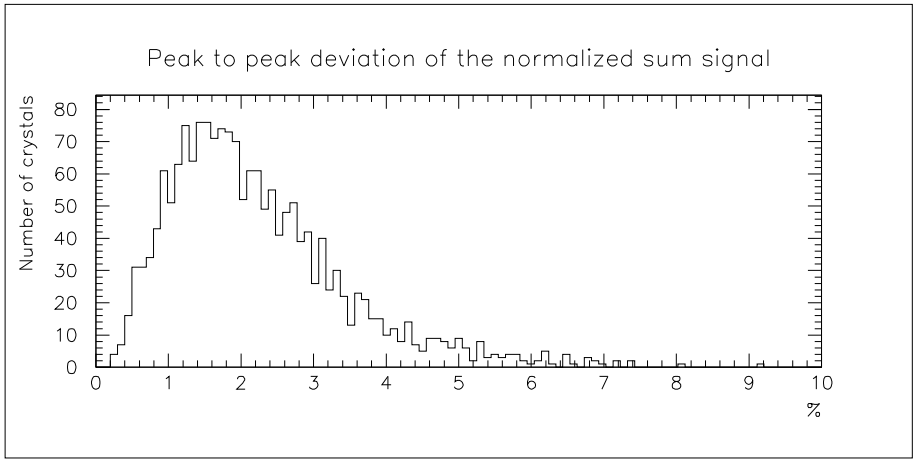

Figure 5.26: *The peak-to-peak deviation of the average light yield for all crystals.*

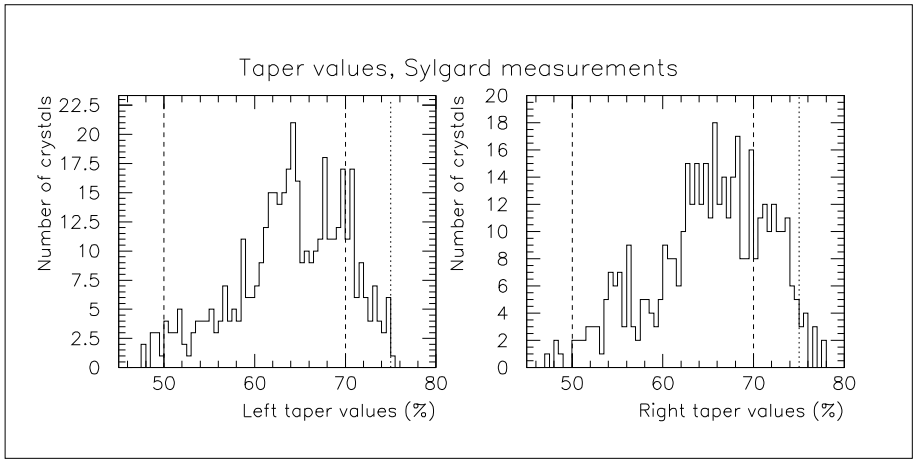

Figure 5.27: *Left and right taper values, respectively. Measured with Sylgard. Dashed lines show the specified limits. The dotted line shows the extended acceptance limit.*

The acceptance interval was 67%-89%. As in the case of Sylgard, the crystals falling just below the lower limit were not considered an issue, these were accepted as they were. Figure 5.29 shows air gap taper values, multiplied by the Sylgard conversion factor to facilitate comparison with the originally specified acceptance interval.

Asymmetry Value

The histograms for the asymmetry values measured with Sylgard and air gaps are shown in figure 5.30. A high taper value corresponds to a low asymmetry

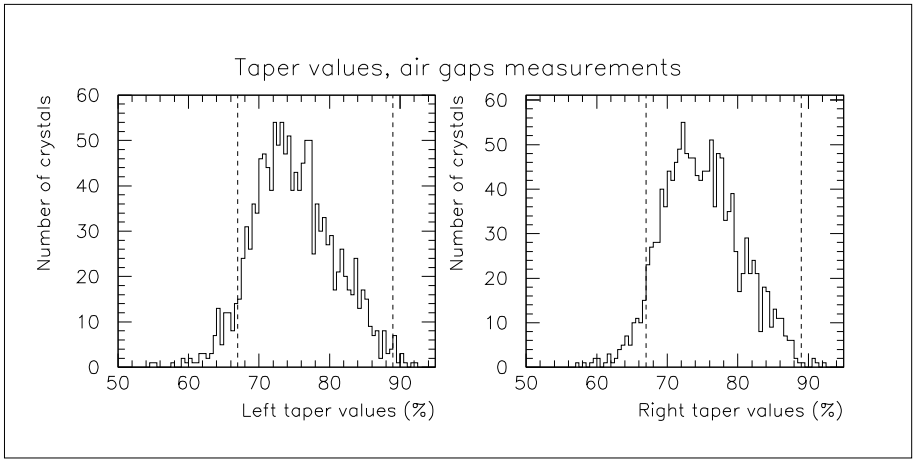

Figure 5.28: *Left and right taper values, respectively. Measured with air gaps. Dashed lines show the acceptance limits.*

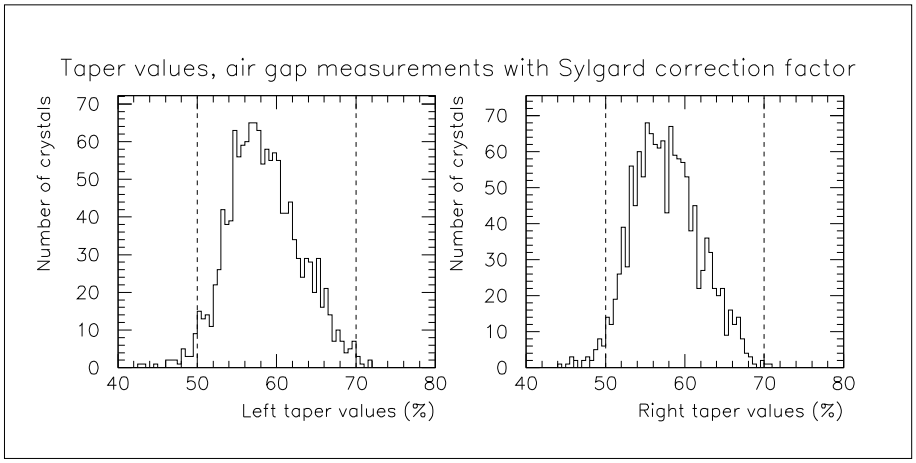

Figure 5.29: *Left and right taper values, respectively, as measured with air gaps and converted to corresponding Sylgard taper values.*

value (bad tapering corresponds to large taper value). From the Sylgard measurements there are a few crystals being below the specified minimum limit of 0.24. These are identical with the crystals having light taper values above 75%.

In subsection 5.1.3 it was estimated that the lower acceptance limit 0.24 for Sylgard measurements should correspond to 0.12 when measuring with air gaps. Correlations with CDE measurements later showed that 0.17 was a more accurate number.

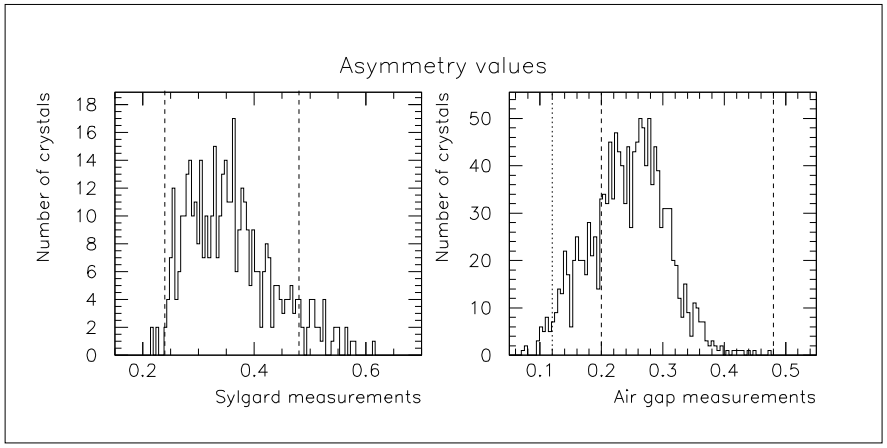

Figure 5.30: *Asymmetry values as measured with Sylgard (left) and air gaps (right).*

Correlation between Taper and Asymmetry

The light taper values, equation (5.2), are constructed from the end positions of the source and measured with the same PMT, whereas the asymmetry value, equation (5.5) is derived from the two positions next to the end positions of the source and using both PMTs, i.e. four read-out values. In spite of these differences between the taper and asymmetry values there is a strong correlation. Plot 5.31 shows the asymmetry values (both from Sylgard and air gaps) versus all taper values. Values are from original measurements, that is, air gap measurements have not been converted to corresponding Sylgard values.

Plotting the rescaled air gap values in the same plot as the Sylgard values, it becomes evident that there is a difference, seen as two different slopes in figure 5.32. The air gaps to Sylgard correction factor works for the taper values. Figure 5.14 on page 65 showed the ratio between Sylgard and air gaps measurements with respect to the position of the source. The dependence was near linear and such that the Sylgard over air gaps ratio values of the far source position (denoted R_F) divided by the close position (denoted R_C) was constant. Looking at the taper equation (5.2) and how to translate measured air gap values to the corresponding Sylgard values, this becomes (left taper value in this example):

$$\mathcal{T}_{\mathcal{L}_{Sylgard}} = \frac{\mathcal{L}_{\mathcal{E}\,Sylgard}}{\mathcal{L}_{\mathcal{S}\,Sylgard}} = \frac{R_F \cdot \mathcal{L}_{\mathcal{E}\,AirGaps}}{R_C \cdot \mathcal{L}_{\mathcal{S}\,AirGaps}} \tag{5.13}$$

Thus the ratio of R_F and R_C can be used as a correction factor. However, using this method in trying to achieve a correction factor for the asymmetry value does not work. The result becomes dependent on the asymmetry value itself. Trying to achieve an offset instead of a factor does also come down to depend on the asymmetry value. Conclusively, a large number of crystals with asymmetry values in the full range would have been needed to empirically derive a correct relation between the Sylgard and air gaps measurements. However,

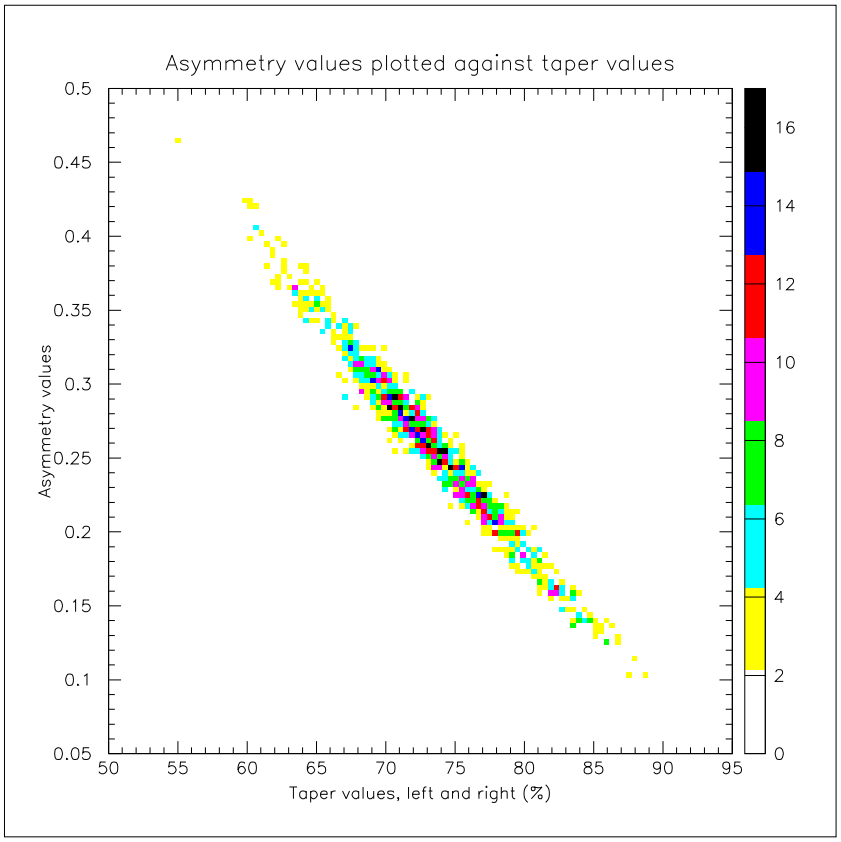

Figure 5.31: *All original measurements of the asymmetry values plotted versus taper values.*

this relation was not necessary since the acceptance interval was determined by the optical behaviour of the completed CDEs.

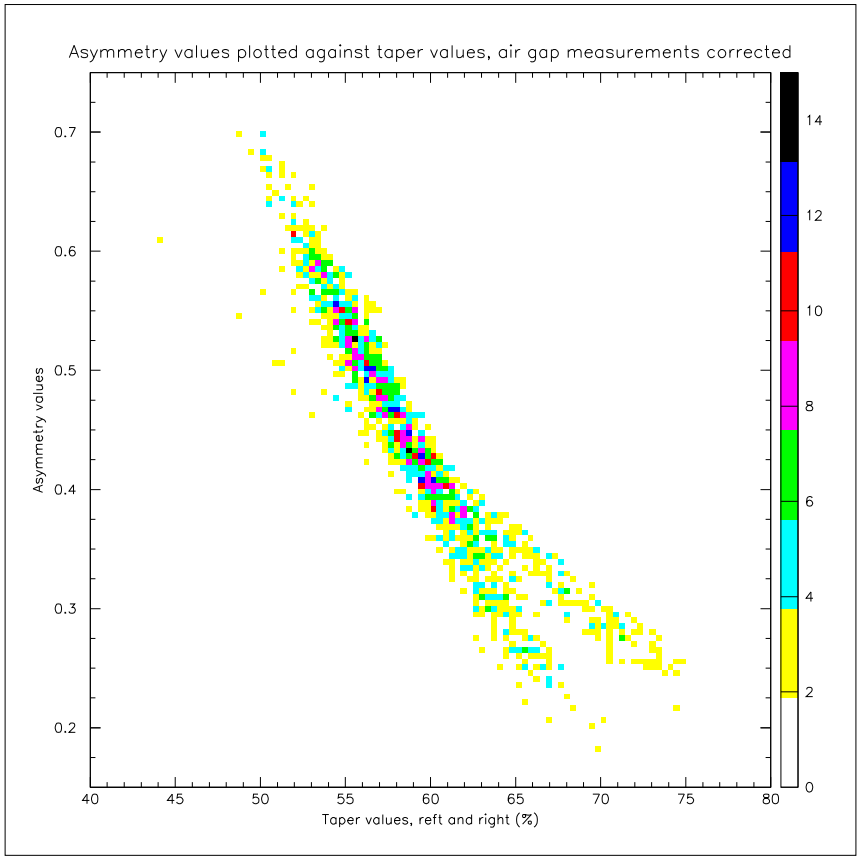

Figure 5.32: *Same as 5.31 but here with the air gaps measurements rescaled.*

5.3 The Mechanical Acceptance Tests

During the launch the GLAST instrument will be subject to a large amount of stress and high vibrational levels. The mechanical crystal support structure is designed to ensure a safe transport of the crystals into orbit.

The mechanical support structure is made from carbon fiber with a wall thickness of 0.4 mm and the rectangular opening being 27.3 mm wide and 20.5 mm high. The crystal is held in place by elastic cords placed along the corners of the cavity. During assembly these cords are extended, to shrink the diameter of the cord, as the crystal is inserted into the cavity. With the crystal in place, the cords are relaxed. They swell and apply pressure to the crystal chamfers.

The mechanical acceptance tests verifies the shape and dimensions of the crystals enabling integration with the support structure.

5.3.1 The Mechanical Requirements

The crystal logs are designed to be rectangular parallelepipeds with a chamfer along the edges of the long dimension. The overall dimensions, as measured at 20°C, should be:

- Length 326.0 mm +0.0, −0.6 mm
- Height 19.9 mm +0.0, −0.4 mm
- Width 26.7 mm +0.0, −0.4 mm
- Chamfer width min: 0.7 mm, max: 1.4 mm
- Chamfer angle $45° \pm 5°$

The chamfer size was specified to ensure the right space for the cords. If the distance is too large then there is a risk that a cord falls off the chamfers and is situated on one of the crystal sides (tilting the crystal). If this distance is too small then there will not be enough pressure on the crystal and there is a risk that it will become loose in the cavity.

Furthermore, the requirements on the surface flatness, parallelism and perpendicularity also had to be specified. If the crystal was placed on a flat surface no point of the surface was allowed to deviate more than 0.20 mm from the flat surface. All points on the crystal surface opposite to that in contact with the flat reference surface had to be within 0.20 mm from the average height (19.7 mm) or width (26.5 mm) depending on crystal orientation. The perpendicularity of the end faces with respect to the sides, and between adjacent side faces was to be kept within 0.3 mm. The crystals should not have any visible cracks or inclusions. Any scratches or dents may not exceed the surface flatness.

5.3.2 The Mechanical Test Station and Procedure

The mechanical acceptance test procedure began with measuring the cross section dimensions and the shape of the crystal log. These measurements were

performed using a setup with 12 measuring gauges, six per opposing surface, measuring at three pairs of points. By measuring the crystal twice and rotating it 90° between measurements along its longitudinal axis, all four surfaces were covered. The data was logged by a computer and afterward the cross-sectional dimensions were calculated and the shape was numerically controlled and visually presented. The test set-up was calibrated using a precision made steel standard log.

The length of the crystal was measured using a fixture with a measuring gauge having its reference point set to the crystal length, 326 mm, calibrated with respect to the steel standard log. The length was measured between two flat surfaces with the crystal lying in a V-block.

It was difficult to efficiently obtain a numerical value of the chamfer to chamfer distance. Instead a go / no-go gauge was used, with the crystal lying in a V-block, checking two opposing chamfers before rotating the crystal to check the other two. A slide with the correct distance between the chamfers was passed along the crystal, covering the full length of the chamfers. If deviations from the specifications were detected using this gauge, the chamfer distances were measured numerically. The four chamfers of the crystal were then examined with a magnifying glass with a 0.1 mm resolution scale. The width of the chamfers were recorded at three points along each chamfer and the entire chamfer was inspected. Figure 5.33 shows a photo of the equipment.

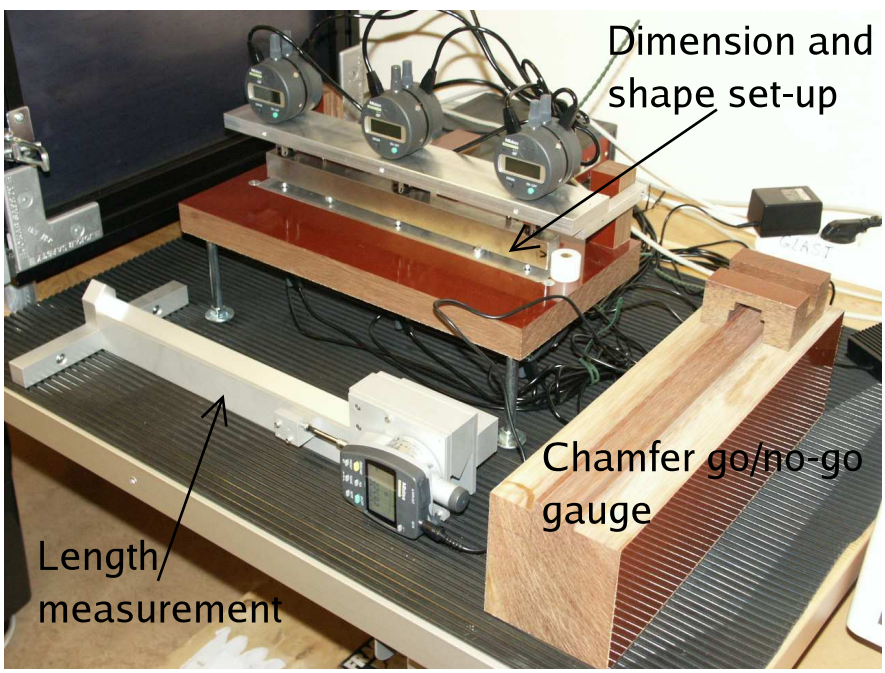

Figure 5.33: *The equipment used for the mechanical tests.*

Data from the measurements were saved on disk by using a computer interface. The data files contained all measured values and all the calculated values. Before each shipment the files were exported to an Excel-sheet, creating a list with all crystal identification numbers and their data. This list was also used for identification upon arrival at NRL.

After measuring the crystals dimensions they were visually inspected. It was checked for inclusions, like bubbles or other contaminations, cracks, dents, chips torn off the surface, visible crystal lattice boundaries, and other surface defects. The visual inspection was also good for noting identification marks in case of confusion of crystal identification numbers, a rough sketch of all crystal surfaces was made. Each crystal was also weighed.

Having passed all tests and inspections the last step was to roughen the end faces slightly. This was done to enhance the adhesive properties of the surface, making the diode glue joint stronger. When roughening the end faces the perpendicularity was to be kept within 0.1 mm.

5.3.3 Mechanical Test Results

In this subsection the statistics of the mechanical values: length, weight, cross-section and chamfer width, will be presented. Some of the crystals which were rejected during the tests could be accepted after having been reworked. Crystals with a bent shape, out of tolerances, could be straightened and brought back into the specifications. The L-shaped aluminum profiles used for storage and during shipping then ensured that the correct shape was preserved. Another example of successful rework were crystals which had too large chamfer to chamfer distances (and too small chamfer width). These chamfers could carefully be ground to fit inside the specifications.

A small number of crystals suffered from a surface deterioration during shipment to Kalmar and in some cases during storage. Fractions of the surface looked as if it had been wetted or 'frosted', these crystals were rejected.

Less than ten crystals had to be rejected because of accidents during handling.

Crystal Dimensions. Dashed lines in the displayed distributions show the specified limits. The crystal heights, 19.9 mm +0.0 −0.4 mm, and the widths, 26.7 mm +0.0 −0.4 mm, are histogrammed in figure 5.34. The histogrammed values are the average for each crystal. No crystal with individual measuring values outside the specified interval was accepted. Figure 5.35 shows the distribution of all crystal lengths.

Chamfer Size. Because of the difficulty to measure the chamfer to chamfer distance, the width of the chamfer was used as an indication of this parameter. Figure 5.36 shows the distribution of the average chamfer widths of all crystals. The chamfer go/no-go gauge verified that the chamfer to chamfer distance was in the correct interval.

Crystal Weight. Figure 5.37 shows the histogram of all crystal weights.

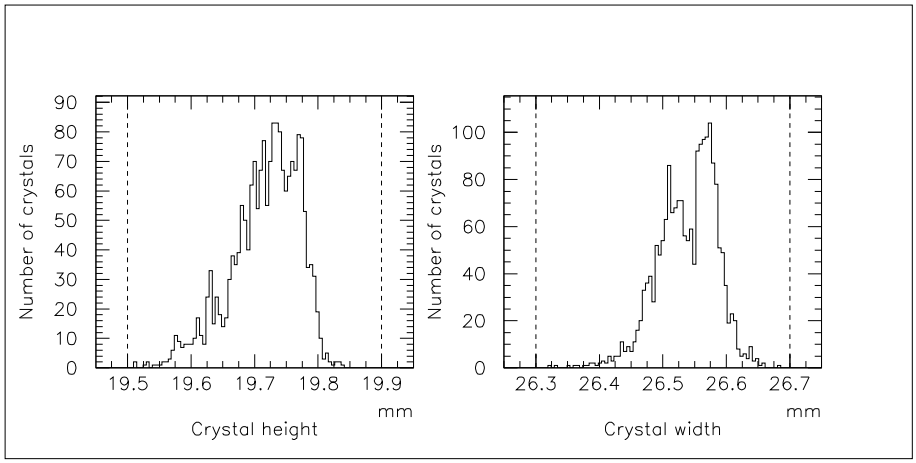

Figure 5.34: *Cross-section height (left) and width (right) of all crystals. Dashed lines show the acceptance limits.*

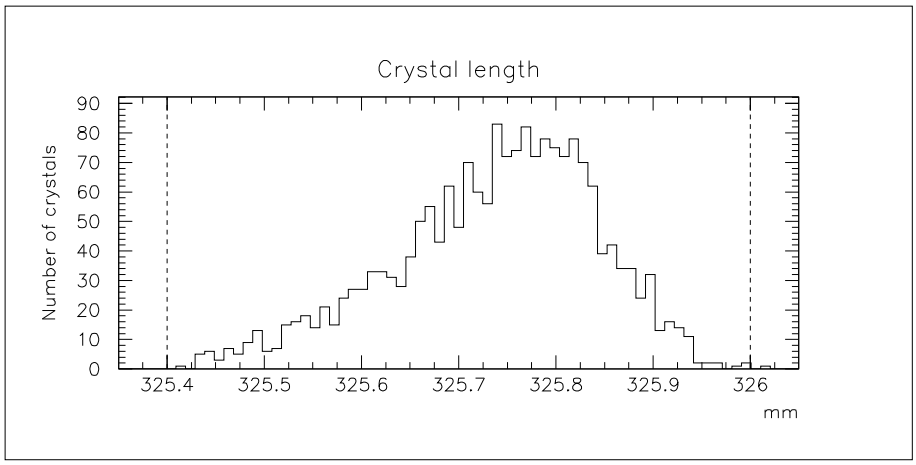

Figure 5.35: *Length of all crystals. Dashed lines show the acceptance limits.*

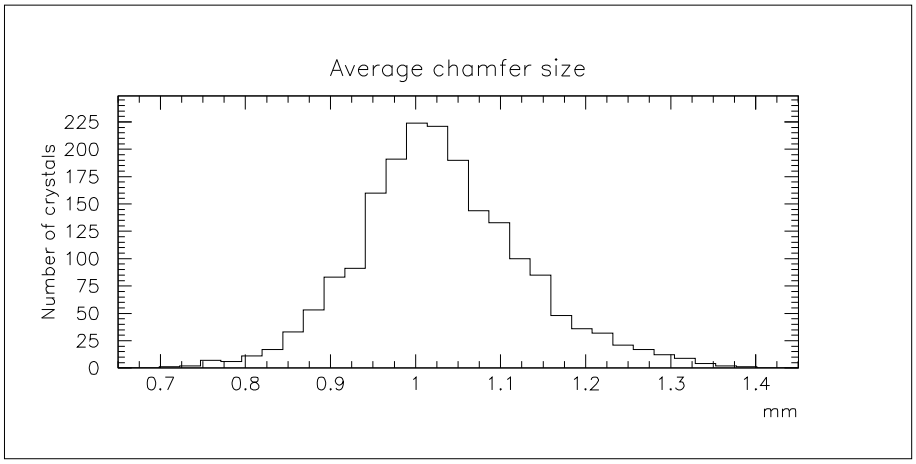

Figure 5.36: *Average chamfer size for all crystals.*

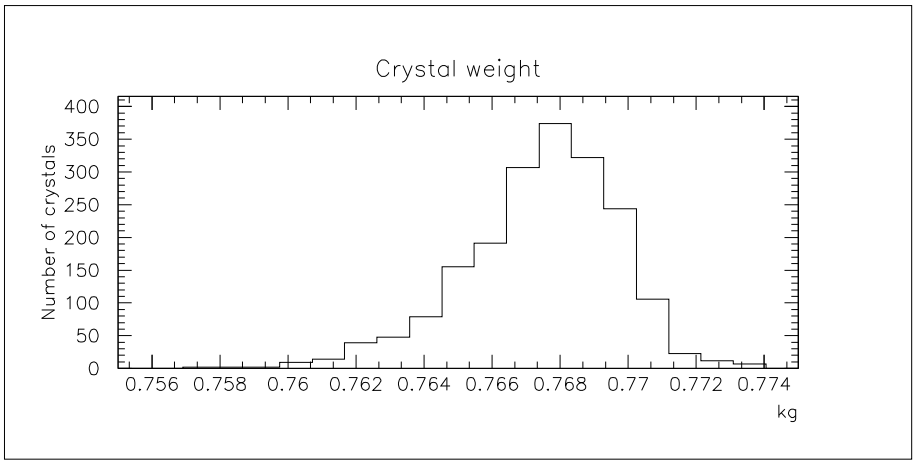

Figure 5.37: *Weight of all crystals.*

5.4 The Radiation Hardness Acceptance Tests

In GLAST's orbit (altitude 600 km) there is no protective atmosphere against the unwanted radiation. Even though the intensity is rather low, the long life time of the mission will cause the radiation environment to deposit a considerable amount of energy in the calorimeter.

The four main components of the radiation environment are galactic cosmic rays, albedo particles (secondary particles created when cosmic rays collide with the upper atmosphere), solar energetic particles and trapped particles. The particles from the solar wind which does not get deflected by the Earth's magnetic field are instead caught in it, becoming the trapped particles (protons with energies between 10 and 100 MeV). In general the belts with these trapped particles (the van Allen radiation belts) are situated at altitudes well above the orbit of GLAST. However, due to an irregularity in the Earth's magnetic fields a part of the belt reach down to 200 km above the south Atlantic Ocean, called the South Atlantic Anomaly (SAA). This will introduce a huge background and the major part of the radiation damage on the instrument will be accumulated when passing that area.

Outside the SAA the galactic cosmic rays is the radiation which will give the largest contribution to the radiation damage. The estimated particle flux is between 200 and 500 $m^{-2}sr^{-1}s^{-1}$. This should be compared to the estimated flux of the trapped particles, which is in the order of 10^6 $m^{-2}sr^{-1}s^{-1}$ [44].

This chapter will describe the radiation hardness acceptance tests, regularly performed on so called boule samples, and the crystal log tests, performed with both gamma rays and protons.

5.4.1 The Boule Tests

The radiation hardness acceptance tests were performed on so called boule samples, a cylindrical sample crystal measuring 25.4 mm in diameter and height. Two samples were taken from each boule, one from the top of the boule and one from the bottom. The thallium concentration may vary along the growth axis of the boule and the highest concentration, which in turn causes a higher degree of radiation damage as mentioned earlier, is found in the bottom sample. The bottom boule sample was tested prior to cutting crystals from that boule to prevent starting manufacturing crystals from a boule which could not be accepted.

Requirements

The dose rate was not to exceed 20 Gy/h. After irradiation with a total dose of 100 Gy of gamma rays from a ^{60}Co-source, the light yield output should not decrease by more than 50%. This should be judged by radiating a small sample crystal from each boule, being cylindrical with a diameter of 2.5 cm and 2.5 cm in height. If a boule sample failed this requirement then all crystals from that boule were to be rejected. The requirement was specified with respect to a crystal log, so there had to be established a correlation between the damage

on the log and the boule sample. This is described in section 5.4.2.

Radiation Hardness Test Sources

Two different gamma sources were used in the boule tests. The first tests were performed at the Nuclear Chemistry Department at KTH, the Royal Institute of Technology, Sweden. Because this source was rather intense, and because radiation damage is dose rate dependent, a less intense source located at the Karolinska Hospital (KS) was used instead. It was used for the majority of the boule sample tests.

The KTH Source. The radioactive source situated at the Nuclear Chemistry Deparment at KTH consists of ^{60}Co in metallic form contained in 203 mm long stainless steel rods. These rods are arranged cylindrically with a diametric distance of 209 mm between the centers of the rods. A motor driven drawer allows the sample which is to be irradiated to be lowered into the center of the cylindrical assembly. The boule samples tested were placed at the bottom of the cylinder where the gamma flux is lowest.

Dose rate calibration was performed using Fricke dosimetry [44]. This is a solution of Fe^{2+} ferrous ions which under influence of ionizing radiation will be further ionized to Fe^{3+} ferric ions. The optical density of the ferric ions is then measured with a spectrophotometer at the wavelength of maximum absorption of the ferric ions, 304 nm. A non-irradiated sample was analyzed and kept as a reference. The solution container had the same dimensions and shape as that of a boule sample, cylindrical 25.4 mm in height and diameter. The sample was irradiated and measured in a number of dose steps and the resulting the dose rate in the Fricke solution was 190 Gy/h. This was used to determine the dose rate in CsI.

After a distance x in a material, a fraction $1 - e^{-\mu x}$ of the impinging gamma rays are absorbed, where μ is the energy dependent absorption coefficient. The decay of ^{60}Co results in gamma rays of two energies, 1.173 and 1.333 MeV. The absorption coefficients in the Fricke solution are, for respective energies, 0.0669 cm^{-1} and 0.0626 cm^{-1}. In CsI they are, respectively, 0.296 cm^{-1} and 0.277 cm^{-1} [45].

To be able to convert the dose rate in the Fricke solution to dose rate in CsI, a Monte Carlo simulation was performed. Gamma rays of the two energies were randomly generated and the rays were divided into four penetration categories, depending on the initial direction:

- both entering and leaving the cylindrical surface,
- entering the top surface and leaving the cylindrical surface,
- entering the top surface and leaving the bottom surface,
- entering the cylindrical surface and leaving at the top surface.

Plotting the number of absorbed rays as a function of penetration depths (figure 5.38) shows a distinct peak just before 25 mm (the diameter of the boule sample)

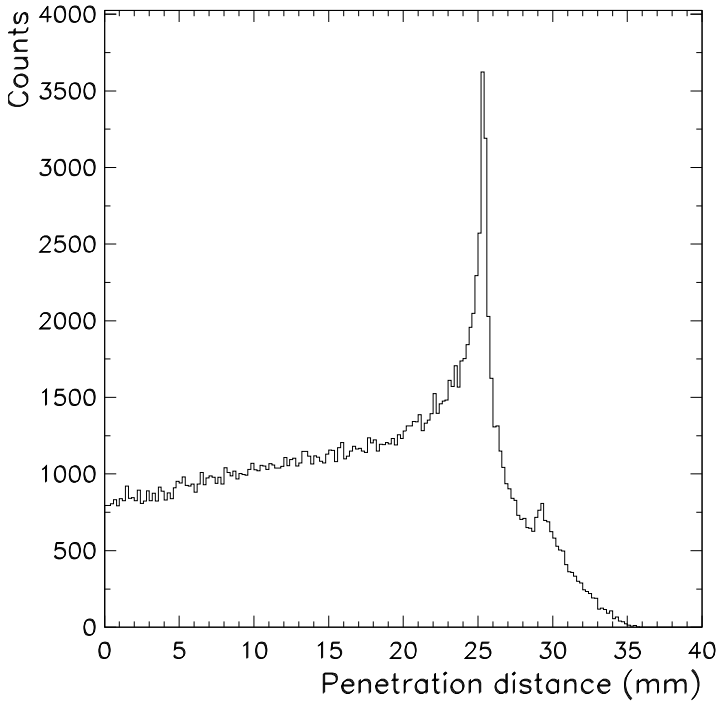

Figure 5.38: *Distribution of the gamma penetration depths in a boule sample for* $2 \cdot 10^6$ *randomly generated gamma rays.*

and a smaller peak around 29 mm, which is due to the rays entering the top surface and leaving the bottom surface. For the largest penetration depth the ratio between the fractions of absorbed rays for CsI and Fricke are 3.08 and 3.14 for the two energies, respectively. For the shortest distance both ratios are approaching 4.42. The result was that the dose rate in CsI was 81% of that in the Fricke solution, i.e. 154 ± 5 Gy/h. The uncertainty mainly comes from determining the volume of the Fricke solution.

The KS Source. The intense gamma source at KTH had a dose rate which was around 10 times higher than what was considered suitable. The configuration of the source also made it difficult to decrease the dose rate in a controlled manner.

At the Karolinska Hospital (KS) in Stockholm a more suitable source was found. It consists of a point source of ^{60}Co used for cancer therapy embedded in a lead casing with adjustable opening size, controlling the size of the radiation field. The sample to be irradiated is placed on a vertically adjustable table; the dose rate is inversely proportional to the square of the distance between the

sample and the source. The calibration of the source is conducted once a year using ion chamber dosimetry in water placed at a distance of 80 cm from the source and measured at 5 cm depth in the water (depth of maximum dose). Considering the absorption coefficient between water and CsI the ratio of dose rates was again found to be 81%. The resulting dose rate in CsI was found to be 31 Gy/h with this source.

Boule Test Setup

The flat surfaces of the boule samples were highly polished for diode mounting, the cylindrical surface was roughened. A PIN diode, a Hamamatsu 3590-05, was attached to the crystal using a wax-like melt mount substance, Cargille, with a refractive index of 1.704. Mounting the diode required heating the substance to 70° C. The crystal and diode was wrapped in diffuse reflecting Tyvek closest to the crystal, which was surrounded by black, light tight Tedlar. The PIN diode was connected to a preamplifier, 5093 eV Products, situated close to the diode. This assembly was housed together with a ^{22}Na-source in a metal box to shield the sensitive diode and preamplifier from interfering external fields. The signal was transferred to a NIM linear amplifier, Tennelec TC205A, and then to a multichannel analyzer, Amptek MCA-8000, using 4096 channels. The 500 seconds long measurement was recorded on a laptop computer. The 511 keV annihilation line from the ^{22}Na source was fitted and the Gaussian centroid was used as a measure of the light yield.

According to Amcrys-H the bottom boule sample has either equal or higher thallium concentration as compared to the top sample. As mentioned before, the higher the thallium concentration the greater the expected radiation damage. Therefore the bottom boule samples were used for the acceptance tests.

5.4.2 The Full Length Crystal Tests

To monitor the correspondence between the radiation hardness tests on boule samples to the degradation in a crystal log due to radiation damage, tests were performed on full length crystals. Two different types of radiation tests were performed, one with gamma rays using the facility at KS, and one with cyclotron accelerated protons of 180 MeV conducted at the The Svedberg Laboratory at Uppsala University. In orbit the majority of the background radiation will come from low energy protons.

Gamma Ray Tests

These measurements were performed with one of the setups used for the optical acceptance tests. In the first gamma ray test a crystal log equipped with a pair of diodes, the same type as used for the boule sample tests, was also irradiated.

During the first gamma ray test it was noticed that the irradiation induced a severe afterglow in the crystals which made measurements practically impossible even after several hours of 'cool down'. The first test did not reach the desired accumulated dose within the time frame for the test. Instead, the decay of the

afterglow was studied. A second test was performed, using only the PMT set-up for measurement and the ^{22}Na-source was replaced by a ^{56}Co-source which emits higher gamma energies for better interpretation. How the afterglow was handled is described in the result section below.

Proton Test

The geometry of the beam of protons produced in the accelerator at the The Svedberg Laboratory was much narrower than the largest crystal cross section. To be able to cover the full crystal length an aluminum foil was used to spread the beam at the beam pipe window. It was not enough though and the crystal had to be tilted 45° with respect to the beam axis to be able to cover the entire crystal length with an acceptable intensity distribution. The crystal was oriented such that the protons penetrated the shortest distance, to achieve a close to uniform deposition of the energy.

The crystal was read out at the two ends with the same type of diodes used with the boule samples. These had to be shielded from the radiation using blocks of lead. The crystal, diode and preamplifier were again housed in a metal box to shield the set-up from external fields. Cosmic muons was used as standard light source inside the crystal. Two plastic scintillators about 2 cm wide were used as a coincidence trigger, placed above and below the crystal.

5.4.3 Test Results

In this section the results from the radiation hardness tests are given. These results have been published in [46] (the article [46] is included in appendix A of this thesis). For a more thorough description of the tests and the results, see [44].

Afterglow

The radiation induced afterglow was present in all of the irradiated crystals and was first monitored for the boule samples. After the first irradiation step was reached, the light yield was measured every 20 minutes for an hour, after which it had stabilized. Shortly after irradiation, when afterglow was still present, the noise increased significantly which was shown by an increase in both light yield and FWHM.

The afterglow in the full sized crystal was, however, far worse. Even after six hours of 'cool down' after the gamma irradiation, the light yield was between 20-30% larger (due to light pile-up) than the preirradiated reference measurement. In order to correct for this light pile up, the crystal was monitored after the last dose step of the first gamma irradiation test. After 70 hours the values became stable and the decay of the afterglow as a function of time was determined. This to allow correlation of the measurements from previous dose steps.

In orbit such large afterglow as was seen in the irradiation tests will not be a significant problem, mainly due to the much lower radiation intensity, but also thanks to a continuous calibration of the calorimeter.

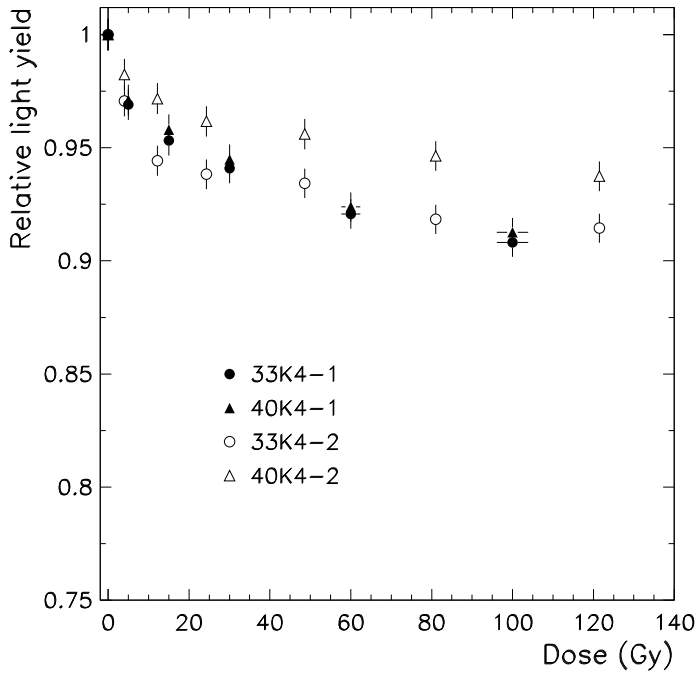

Figure 5.39: *Dose rate dependence of the radiation damage in the boule samples. Filled symbols represent samples irradiated at KTH, open symbols those irradiated at KS.*

Boule Samples

Figure 5.39 shows four boule samples from two different boules, where one sample from each boule was irradiated using the source at KTH (154 Gy/h) and the other two samples were irradiated with the less intense source at KS (31 Gy/h). The suspicion was that the decrease in light yield as a function of accumulated dose is faster for the higher dose rate. Also, for the same accumulated dose, more permanent damage is the result of a higher dose rate. This behaviour is seen in boule 40K4, but is not as obvious for boule 33K4.

The behaviour of the degradation was as had been seen by others [47] in previous studies. That is, up to around 20 Gy there is a fast decrease which then approaches an asymptotic value. The decrease of the light yield was well within the specified limit (not more than 50%) for all tested boules. The largest decrease was found to be 27% after a total dose of 100 Gy, on average the light yield decreased $(12 \pm 3\%)$. The average decrease for a total dose of 200 Gy was $(14 \pm 4\%)$. Figure 5.40 shows the results for all boules tested at KS after a total dose of 100 Gy.

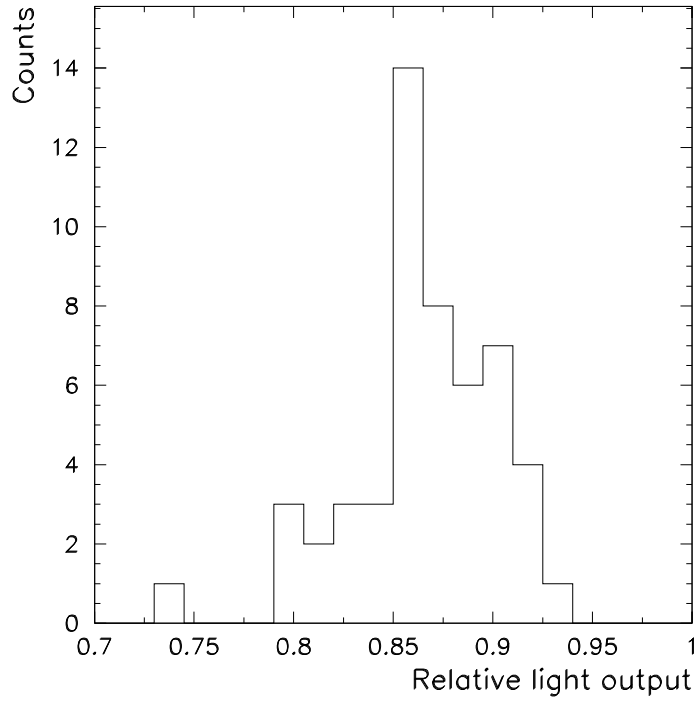

Figure 5.40: *Loss of light output after an accumulated dose of* 100 *Gy for boule samples irradiated using the* ^{60}Co*-source at KS.*

Crystal Logs

The Gamma Ray Test. The full sized crystal irradiated with gamma rays showed after an accumulated dose of 180 Gy an average decrease in light yield of $(24 \pm 4\%)$. The signals from the two PMTs behaved similarly with the source at the same relative position. However, for each PMT there was a significant difference between the close and far position of the source. The close PMT saw an $(18 \pm 4\%)$ decrease in signal, whereas the far PMT suffered a decrease of $(30 \pm 4\%)$ (as compared to the reference measurements performed before irradiation). It was then concluded that the radiation had not only damaged the light producing mechanism, but also affected the transmittance (i.e. an increase of the self-absorption). Considering the decrease for the close PMT (this measurement position is most similar to the boule sample measurement) it corresponds well to the results from the boule sample tests. The results from all dose steps are presented in table 5.6.

Dose(Gy)	Close PMT (%)	Far PMT (%)	Average (%)
0	100	100	100
20	99	82	90
50	86	71	78
150	82	66	74
180	82	70	76

Table 5.6: *The second and third column shows the average of the left and right PMT with the source positioned at the close and far end, respectively. The last column is the average of column two and three.*

The Proton Test. The proton irradiation made the crystal log radioactive. This introduced a vast amount of noise in the crystal and measurements in between the dose steps were not possible. The induced radioactivity and its decay was monitored with a Ge(Li)-detector. A number of radioactive isotopes was identified (for example ^{131}Ba, ^{132}Cs, ^{125}Xe and ^{124}I) when comparing the post-irradiated crystal with the reference measurement of the non-irradiated crystal. Cosmic muons became measurable approximately 24 hours after the irradiation had stopped.

After an accumulated dose of 175 Gy of proton irradiation, the tested crystal showed a decrease of its averaged light yields (i.e. the average from the two ends) of $(22 \pm 5\%)$. This is the same order of magnitude as for the gamma irradiated crystal with a good correspondence.

Chapter 6

Beam Test Experiment

Previous chapters described the manufacturing, the quality testing, the behaviour and the properties of the CsI(Tl) crystals, which equipped with photo diodes and wrapped up are the individual crystal detector elements (CDEs) that make up the calorimeter. The present chapter will describe the behaviour of a test calorimeter assembled from 48 CDEs. The number of crystals in a complete tower of the final instrument is 72. The calorimeter depth of 8 crystals in the test calorimeter was the same, though, as in the final GLAST detector.

During August 2003 the GLAST collaboration was allocated one week of beam time at the SPS accelerator at CERN[1], Geneva. This was the first GLAST prototype calorimeter to be tested, with CDEs identical to the flight case having the same dimensions, wrapping material and the dual photo PIN diodes (DPD) as those CDEs going into space.

6.1 Introduction

The CERN beam experiment was a study of the high energy response of the calorimeter. Particle energies between 10 GeV and 120 GeV was used.

6.1.1 Purpose of the Test

The purposes of the experiment was to make preliminary studies of:

- longitudinal shower profile sampling
- study the transverse profile sampling
- energy reconstruction methods and energy resolution
- impact position resolution and angular resolution of the reconstructed shower direction

[1] Conseil Européen pour la Recherche Nucléaire, i.e. the European Organization for Nuclear Research

- calibration and asymmetry mapping (muons)
- hadron showers (pions)

The longitudinal electromagnetic shower profile and the energy reconstruction are strongly correlated. At the energy levels used in this experiment there are primarily two methods of energy reconstruction: longitudinal shower profile fitting and last layer correction (also referred to as energy leakage compensation). The shower profile fitting is applicable in the whole energy range tested. The last layer correction is depending on the shower maximum being contained within the calorimeter to give satisfactory results.

The main goal of the experiment was to compare the behaviour with the specifications concerning the energy and position resolutions (cf. section 4.3.2). Furthermore, it was desired to study methods of energy reconstruction and get a baseline for the calorimeter's behaviour for shower detection.

6.1.2 Acquisition Runs

Four beam alternatives were available: pure muon beam (minimum ionizing particles), pure electron beam (electromagnetic shower inducing), mixed beam (muons and electrons) and pure pion beam (hadron shower inducing).

The facility used was the beam line H6A at the CERN SPS accelerator. It delivered electrons, muons and pions with energies between 6 and 150 GeV. The beam count rate was around 200 Hz.

Pure Electron Beam

In pure electron beam runs energies 20, 50, 80 and 120 GeV were used. During these runs the number of radiation lengths in front of the detector was altered, thus sampling the shower development at different depths. The beam impact angle on the calorimeter could also be changed in order to study the effect of inclined events. The different angles used, apart from perpendicular, were 15°, 30° and 40°. The position of the beam impact was also variable in both X and Y direction (see figure 6.1).

Pure Muon Beam

Minimum-ionizing muons with an energy of 20 GeV were used for absolute energy calibration. These particles deposit a well-defined energy of 12.5 MeV in each crystal element when they penetrate them perpendicularly (i.e. along the short dimension). The beam was aimed between two crystals at a time (three Y positions) and for each height it was aimed at seven points evenly spaced (5 cm spacing) along the X direction (cf. figure 6.1). The seven longitudinal positions were performed at each height. Apart from the energy calibration, these runs were also used to map the asymmetry curves of the CDEs (cf. subsection 6.3.4 on page 111).

Mixed Beam and Pion Beam

The mixed beam consisted of muons and electrons. Two energies were used, 10 and 20 GeV. These runs were used to demonstrate the particle separation possibility of the calorimeter.

The hadron and mixed beam runs were intended to study the signatures from different types of particles, in this case pions, muons and electrons. It is of interest to show if the calorimeter will be able to distinguish different particles from each other. If this is possible, the GLAST calorimeter could in principle be used for lateral events. Such events need to be triggered from the calorimeter only since they do not pass through the tracker. The Anti Coincidence Detector does not cover the full height of the calorimeter and since the cosmic ray particles are dominant they need to be efficiently discriminated. The analysis of hadron events was, however, not included in this thesis work; that would have extended the scope beyond reasonable time limits.

Electronic Pulser

Several 'runs' were made with an electronic pulser, i.e. without the beam turned on. These were used for the relative calibration between amplifiers and attenuators. Electric pulses of well-defined size were injected into the electronics after the diode (see figure 6.4).

6.2 The Test Setup

The main components of the test setup were: the triggering unit (two plastic scintillators in coincidence) located 6 m upstream from the calorimeter, the silicon strip telescope (precision position measurement), the test calorimeter placed on a movable and turnable table, and the data acquisition system. Figure 6.1 shows a schematic view of the setup. The direction of rotation is indicated in the top view.

As an option, passive material (lead sheets) could be placed in front of the calorimeter, either to mimic the effective thickness of the GLAST tracker, which is approximately 1.3 radiation lengths (X_0), or just to be able to sample the shower later in its development. For example, if using lead sheets with a radiation length corresponding to four crystal layers, then the calorimeter would sample layers 5 to 12. Combining measurements with different number of lead sheets in front of the calorimeter enabled the shower to be sampled in a little more than 20 layers. This technique provided useful information about the high energy shower development.

6.2.1 The Silicon Strip Telescope

The beam telescope detector used in the CERN test experiment was made from silicon strip technology. This is a similar technology as used in the GLAST tracker. It was placed at a distance of about 1 m in front of the calorimeter. It had four layers, two pairs of X-Y layers. The cross-section area of the telescope

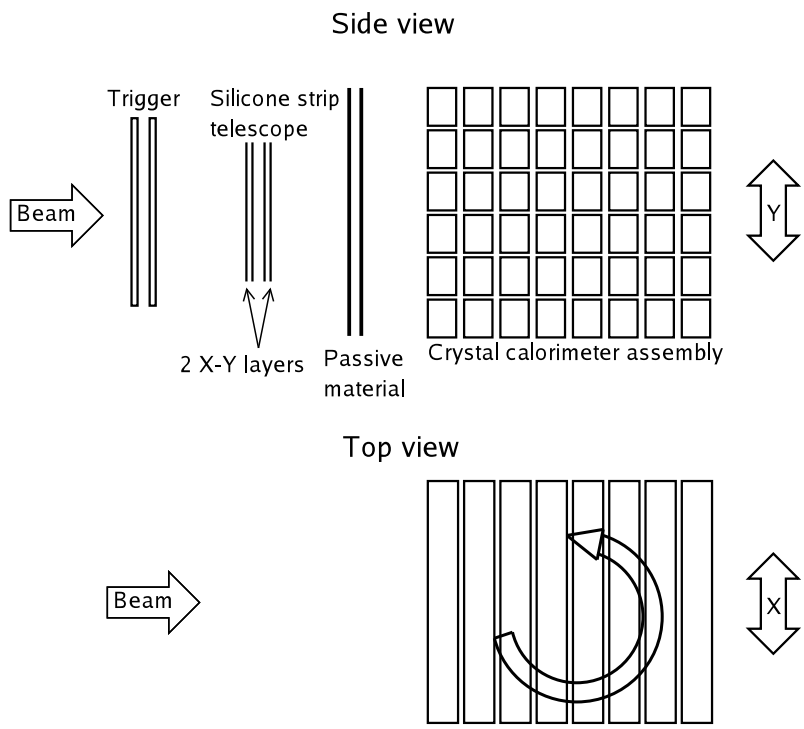

Figure 6.1: *Principle of the experimental setup.*

was 10×10 cm^2, which was sufficiently large to cover the lateral extent of the beam, with good margin. The beam was around 2 cm in diameter. The number of channels in each coordinate was 1000, thus giving a spatial resolution of 0.1 mm. The information from the silicon strip telescope was used to determine the position resolution of the calorimeter.

6.2.2 The Calorimeter

48 CDEs were used for the CERN experiment, which were identical to the ones used for the final full-sized GLAST instrument, i.e. same dimensions, diodes, wrapping material, bonding etc. The CDEs were assembled in eight independent groups of six, held together by an aluminum frame. Thereby, the total depth of the assembly was identical to the depth of the GLAST calorimeter. The frames were mounted on a turnable plate which was placed on a transversely movable table. The rotatable plate enabled alternation of the impact angle of the beam up to an off-axis angle of 40°.

All crystals in one and the same layer are parallel. In the CERN experiment all layers were oriented in the same direction, horizontally as shown in figure 6.1. Since the layer width in the beam test was only 6 crystals instead of 12 as in a GLAST tower, the parallel orientation allowed large beam angles

Figure 6.2: *Assembling of the crystal layers onto the rotatable plate. The six CDEs of the first layer is clearly visible in black cover.*

in one rotation direction. The adjacent perpendicular orientation of the layers would have meant a smaller cross-section of crystal material. The X-Y orientation of the GLAST calorimeter was not necessary during the test experiment, since the determination of the impact position resolution used the beam tracker information.

As an option there were also a number of older prototype crystals from NRL available, which could be mounted behind the 48 main CDEs. However, the NRL crystals had different dimensions being $30 \times 30 \times 190$ mm^3. 15 of these crystals were arranged in three layers of five, which almost covered the width of six CDEs in front. These additional crystals were meant as a complement to allow sampling of the shower at larger depths, and to measure the energy leakage with the test calorimeter tilted (rotation around the crystal longitudinal axis, i.e. the X-direction in figure 6.1). The information from these crystals were, however, not necessary for the present analysis.

6.2.3 Read-out Electronics and Data Acquisition

The CDEs were equipped with dual PIN diodes identical to the diodes used for the flight crystals. The preamplifiers and shaping amplifiers were provided by the Bordeaux group and had been used in previous test runs. The ADCs used were commercially available VME units of type CAEN V785 with 4096 channels.

Each PIN diode has two independent active surfaces, one with a small area and one with a large area, see figure 6.3. The smaller area served the high energy range (approximately above 1 GeV) and was always used together with the low gain amplifier. The big area served the low energy range. The latter had three different readouts, a low gain amplifier with or without passive attenuator, and a high gain amplifier. Figure 6.4 shows the different read-out options. The diodes used on the NRL crystals were single surface. Together with the main assembly, the total number of electronic channels from the calorimeter was 222.

The low gain amplifier was used when the energy deposition in the crystal was high (of the order of a GeV), and the high gain amplifier was used together with the big diode area during the absolute energy calibration with minimum-ionizing particles when the energy deposited in the crystal was in the order of tens of MeV only.

The raw data from the acquisition was saved in PAW++[2] files [48]. This data was broken into subsets of approximately 6000 events with the parameters

[2]Physics Analysis Workstation, analysis software

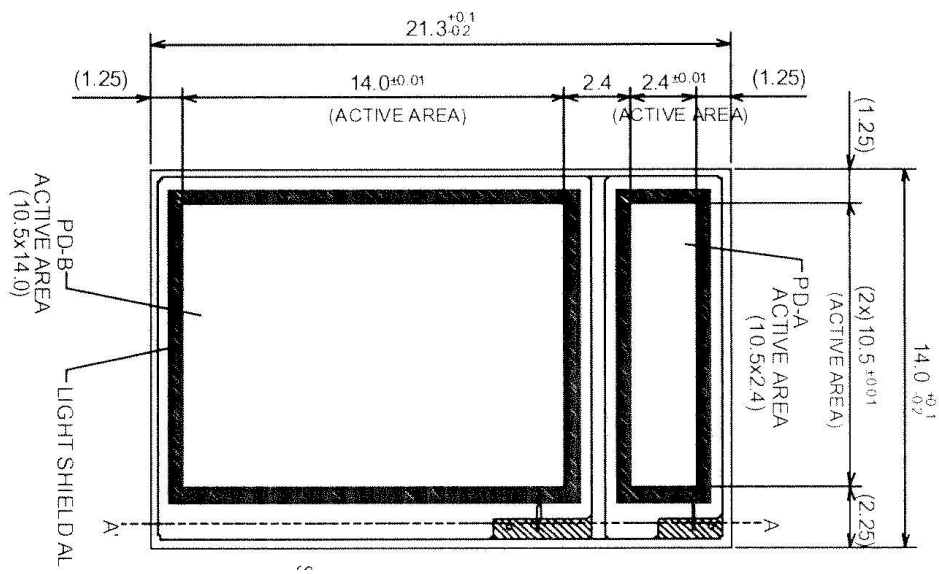

Figure 6.3: *Drawing showing the dual PIN diode active areas (all measurements in mm).*

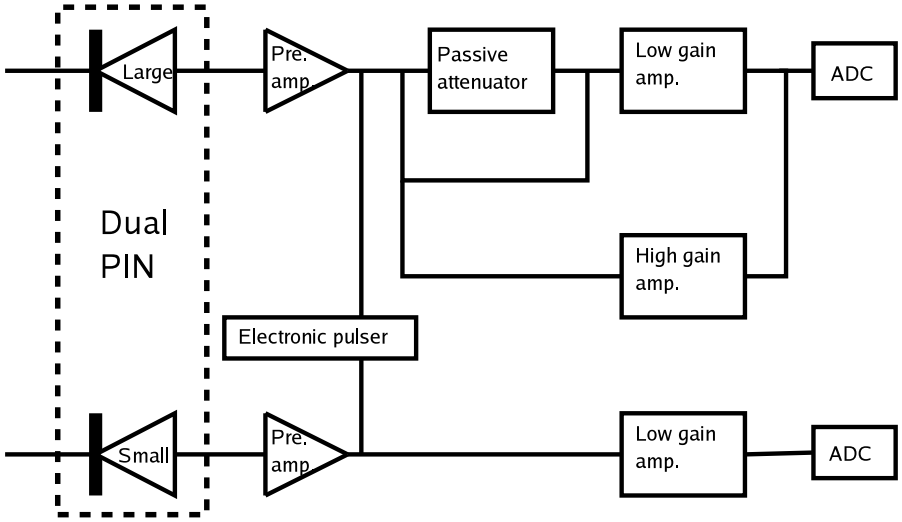

Figure 6.4: *Schematics view of the readout options.*

in an illogical way. Via a separate program these subsets were converted into one file for each run in a simple format and saved as PAW++ Ntuples. The Ntuples are event based arrays, the data is stored like in a table where the variables are the columns and each event is a row. The variables in the beam test were, respectively, the event number, the four numbers from the beam telescope (position coordinates, 2 in x and 2 in y) and the calorimeter ADC-values from all channels (to be converted via calibration to energy), now sorted so that the odd numbers represent the left crystal side and the even numbers the right crystal side, with every other odd, and even number, represent the small and large diode area, respectively (for example, ADC(1) = left side, small diode; ADC(3) = left side, large diode).

6.3 Calibration Procedure

Minimum ionizing muons deposit a well-defined amount of energy when traversing a CsI crystal, and were thus used for absolute calibration. The energy deposited by a muon is 12.5 MeV in each crystal. The energy deposited in a single crystal in an electron-induced shower can be several orders of magnitude larger. The absolute energy calibration had to be performed with the large diode area in combination with the high gain amplifier, since the muon signal was too small to be seen with low gain amplifiers or by the small diode. Therefore, in order to get all channels calibrated, a relative cross-calibration of the different amplifier channels had to be done. This was achieved with the electronic pulser runs, when an electronic pulse was induced at the input of the amplifiers (cf. figure 6.4).

The relative calibration of the small diode channels were based on 120 GeV electron runs when the energy deposited in a crystal was measured by both diodes simultaneously. By plotting the signal in the small diode versus the signal in the large diode on event bases, the small diode calibration could be found from the large diode calibration, the latter which already had been determined by using minimum ionizing muons. Lead sheets (of several radiation lengths thickness) was placed in front of the calorimeter in order to scatter the beam over all crystals. The peripheral crystals of the calorimeter were getting few hits.

From the raw ADC numbers one needs to determine pedestal[3] values of the amplifiers and the energy per ADC-channel for each electronic channel. Figure 6.5 shows a flow chart that summarizes the different steps of the calibration procedure. The result of the calibration procedure is a matrix of calibration constants, converting a value from an ADC number into an energy value, for all diodes and readout options.

6.3.1 Electronic Calibration

The electronic calibration was done by using an electronic pulser. A set of pulses of various amplitudes was induced at the input to the amplifiers (see figure 6.4).

[3] i.e. the zero-point value the ADC gives for no input signal

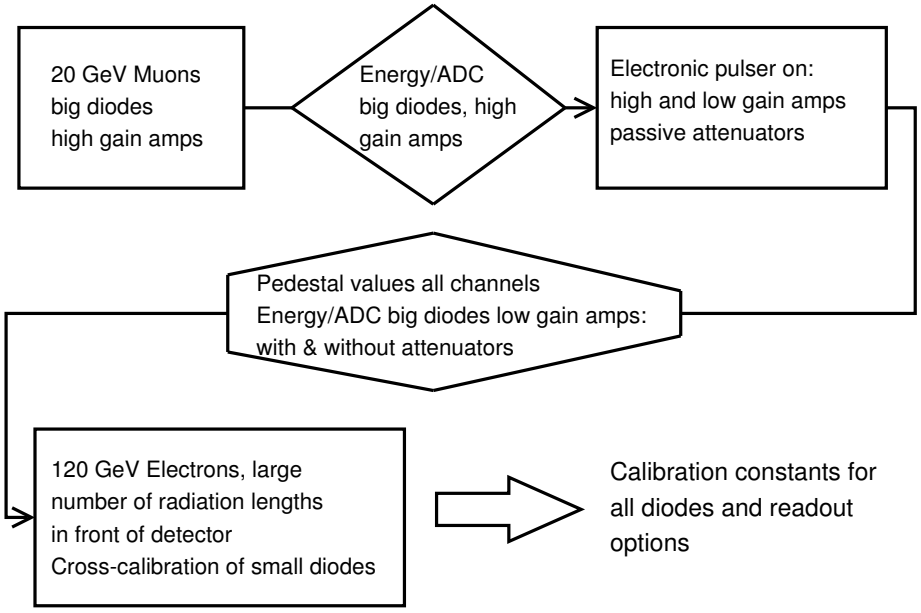

Figure 6.5: *A schematic flow chart of the calibration procedure. Boxes symbolizes calibration runs with specified run conditions. Diamonds specifies obtained calibration data.*

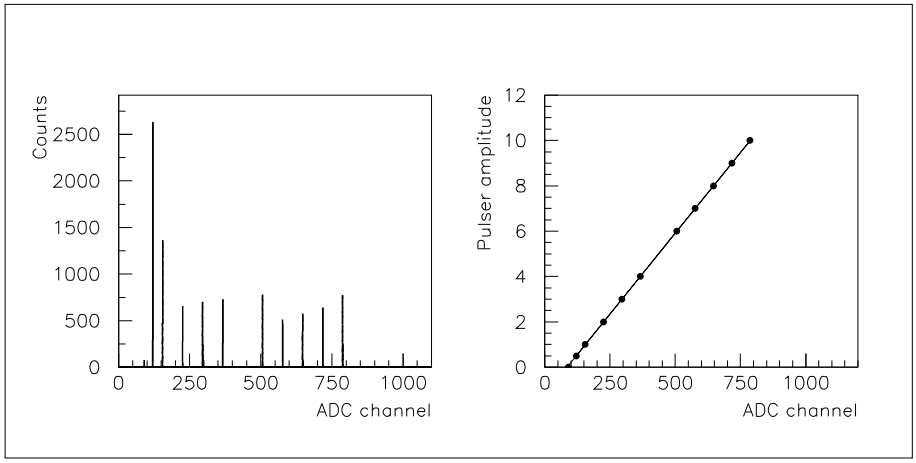

Figure 6.6: *Left: ADC-histograms obtained with the electronic pulser. Right: The plotted pulser amplitude versus the ADC-values.*

The ratios between input amplitudes were well-defined. Each pulse amplitude generated a narrow peak in the ADC histogram. The mean values of these were subsequently plotted versus corresponding pulse amplitude values. Fitting a line to the plotted values allowed for extrapolation down to zero input signal, giving the ADC pedestal values. Figure 6.6 shows an example of the histogrammed ADC-output, and the plotted values with a line fit.

By comparing the slopes from the line fits corresponding to high and low gain readout channels, respectively, the relative gain factors between the two readout channels could be determined. In the same way the attenuation factors for the big diodes (with low gain amplifiers) could be determined. Figure 6.7 shows the resulting gain and attenuation factors for the big diodes of all CDEs.

6.3.2 Energy Calibration

The energy calibration was performed with minimum ionizing muons with an energy of 20 GeV, depositing 12.5 MeV in each CDE. Due to the small signal the crystals had to be read out with the large diodes and the high gain amplifiers.

The muon beam was aimed at 21 positions in total, seven positions horizontally along the crystal and at three different heights. At each vertical position the beam was aimed between two adjacent crystals (cf. figure 6.8). This was efficient since the transverse spread of the beam was approximately 2 cm. The center positions along the crystals were used for the absolute energy calibration and the whole set of 21 runs were used for mapping the optical properties (cf. section 6.3.4).

The energy deposited by a penetrating muon was recorded at each end of a CDE and a histogram was filled for each detection channel giving two histograms for each CDE. By fitting an analytic function to the observed distribution and

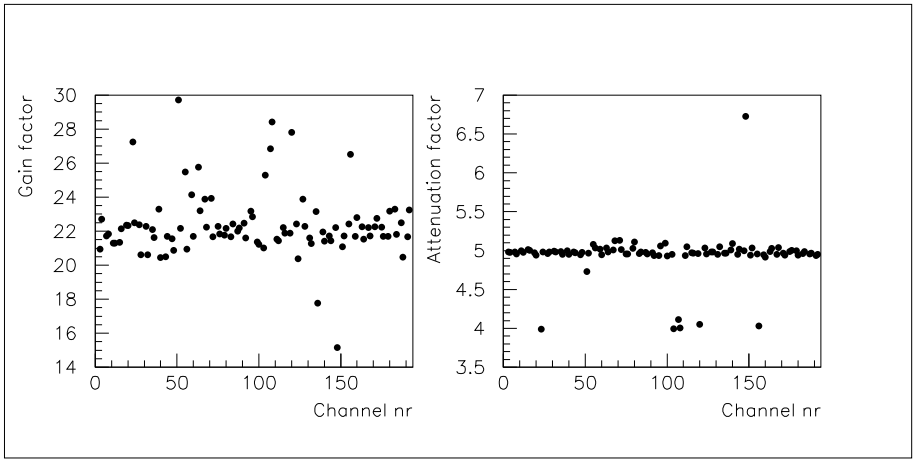

Figure 6.7: *The gain factors (left) and attenuation factors (right) for all large diodes.*

determining its mean value the calibration constants could accurately be determined.

The proper distribution function for the energy loss by fast charged particles penetrating a thin material is the Landau distribution [22]:

$$f(x, \Delta) = \phi(\lambda)/\xi \tag{6.1}$$

where

$$\phi(\lambda) = \frac{1}{\pi} \int_0^\infty exp(-u \ln u - u\lambda) \sin \pi u \, du$$

$$\xi = 2\pi N_a r_e^2 m_e c^2 \rho \frac{Z}{A} \left(\frac{z}{\beta}\right)^2 x$$

$$\lambda = \frac{1}{\xi}[\Delta - \xi(\ln \xi - \ln \epsilon + 1 - C]$$

Δ is the energy loss in the absorber, C is Euler's constant, and

$$\ln \epsilon = \ln \frac{(1-\beta^2)I^2}{2mc^2\beta^2} + \beta^2$$

See page 21 for a definition of the parameters. It should be folded with a Gaussian to account for the detector resolution and to accurately describe the observed histogram. However, finding the expectation value of a probability distribution includes integration:

$$E(x) = \frac{\int xP(\mu, \sigma)\, dx}{\int P(\mu, \sigma)\, dx} \tag{6.2}$$

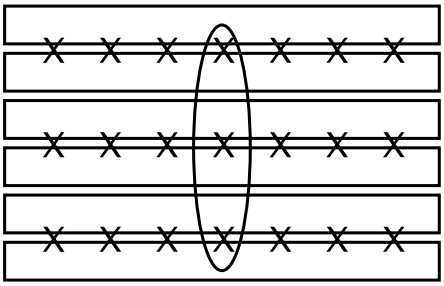

Figure 6.8: *Calorimeter as seen in the direction of the beam. The X marks indicate where the 20 GeV muon beam was aimed. The encircled positions were used for the absolute energy calibration.*

and the integral of the Landau distribution is not analytically soluble. Though it can be done numerically, it is not particular efficient. To facilitate the calibration procedure it was instead decided to use the Moyal distribution:

$$f(x) = C \cdot \exp\left(-0.5 \cdot \left\{\frac{x-\mu}{\sigma} + \exp\left[\frac{x-\mu}{\sigma}\right]\right\}\right) \tag{6.3}$$

which is a good approximation to the observed distribution [49]. Its expectation value is readily found as:

$$E\left(x\right) = \sigma \cdot \left(\gamma + ln\left(2\right)\right) + \mu \tag{6.4}$$

where $\gamma = 0.5772156649$ is Euler's constant, and the variance is:

$$V\left(x\right) = \frac{\sigma^2 \cdot \pi^2}{2} \tag{6.5}$$

where μ and σ are the fit parameters.

When the expectation value E had been determined the pedestal value P was subtracted (both in units of ADC-channels) thus giving the energy per ADC-channel, i.e. the calibration constant C, as the deposited energy (12.5 MeV) divided by the expectation value:

$$C = \frac{12.5\text{MeV}}{E - P} \tag{6.6}$$

Figure 6.9 shows the energy peak and the fitted Moyal distribution for one example crystal (left and right sides, respectively). The energy spectra shown were collected with the muon beam aimed at the crystal center.

As seen from figure 6.9 the Moyal distribution is sometimes too low in the high energy tail of the distribution. The Landau distribution, with its long high energy tail, is strictly valid only in the extreme thin-foil limit in terms of stopping material. As the material becomes 'thicker', the true distribution becomes gradually more symmetric (the Vavilov case [22]) and finally approaches a Gaussian. The Landau case is valid if the ratio between the mean energy

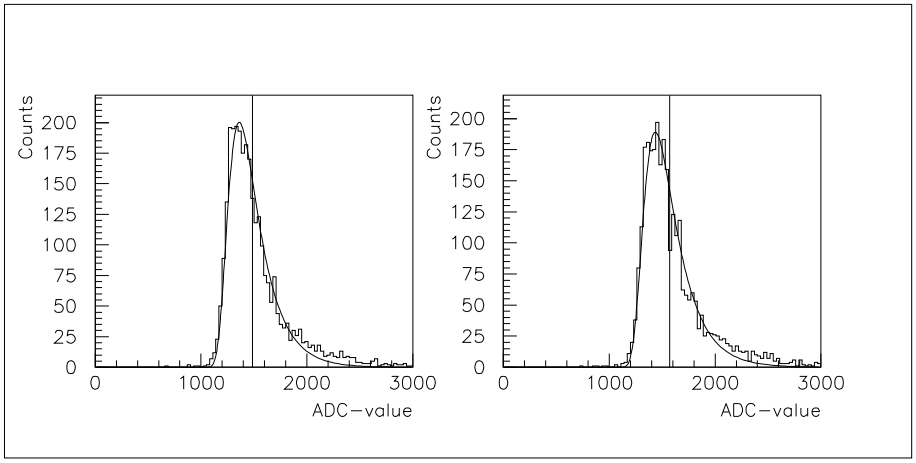

Figure 6.9: *The measured energy peak (histogram) and the fitted Moyal distribution (function) for one crystal, left and right sides respectively. The data was collected with big diodes and high gain amplifiers. The vertical lines represents the expectation value of the fitted Moyal distribution.*

loss and the maximum energy transfer allowed in a single collision is very small ($\leq$0.01). I.e. the maximum allowed energy transfer in a single collision should approach infinity.

6.3.3 Relative Calibration

The energy calibration of the small diodes utilized beam data taken with 120 GeV electrons by simultaneously recording the energy deposit in a crystal with both its small and its large diode. Once the absolute calibration of the big diodes had been accomplished as described in previous section it could be used to cross-calibrate the small diodes. Material of a few radiation lengths thickness in front of the calorimeter was used to scatter enough beam particles so that all crystals in the detector would achieve energy deposition.

The cross calibration was performed in ADC-numbers after subtraction of the pedestal values. Each dual diode was triggered if the event was above the threshold to be seen by the small diode and below the saturation level of the big diode. Events were histogrammed in a two-dimensional histogram with the large diode signal versus the small diode signal. A straight line was fitted to the distribution, providing the cross calibration constant (slope) and offset (intersection). Figure 6.10 shows two examples of the histogrammed events, and figure 6.11 shows the fitted slope and offset for all dual diodes.

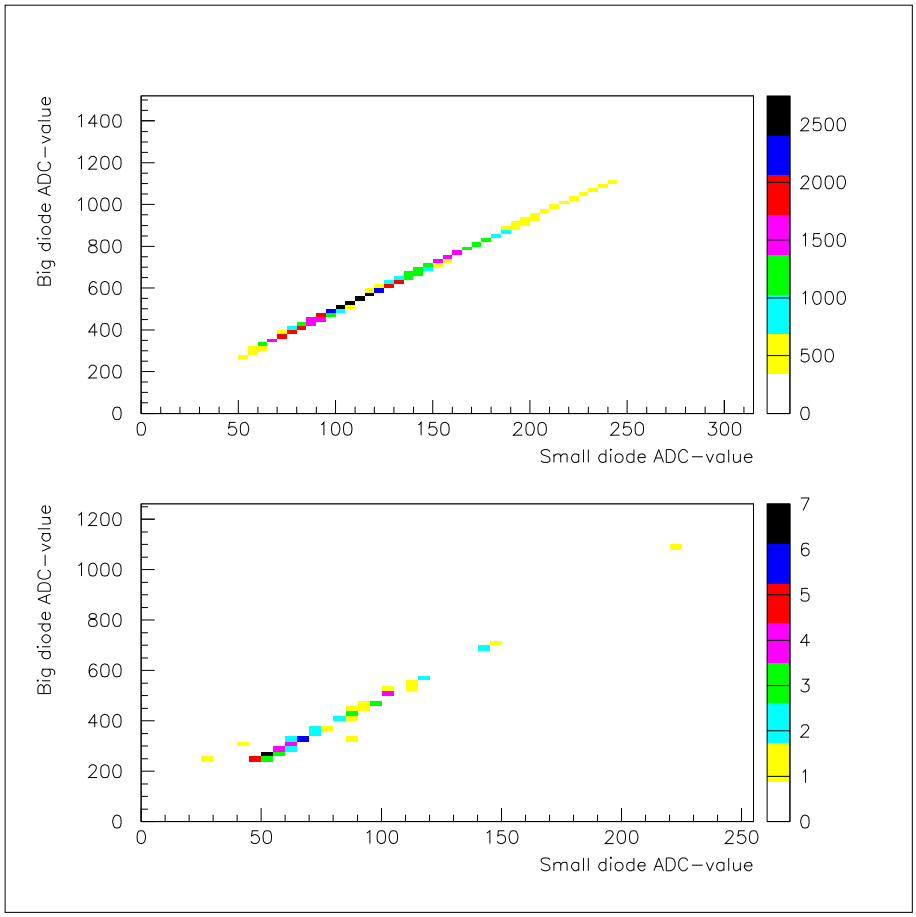

Figure 6.10: *Top: The ADC-values of the large diode plotted against the values from the small diodes for the left side of crystal number 3 in layer 3, which has many events. Bottom: Same as top but for the left side of crystal number 6 in layer 6, a peripheral crystal with few hits.*

6.3.4 Position Calibration

The reconstruction of the shower axis direction through the calorimeter requires two coordinates for each crystal layer, vertical (Y-axis) and horizontal (X-axis); see figure 6.1. Depending on the orientation of the crystals two methods were used. Firstly, the position along the crystal was determined from the asymmetry value between the left and right end signals, giving the x-coordinate for the event. Secondly, the y-coordinate was found by the weighted average of the energy depositions in all six crystals of one layer. This was repeated for all eight layers. The x- and y-coordinates from the adjacent layers were subsequently used to fit the shower direction.

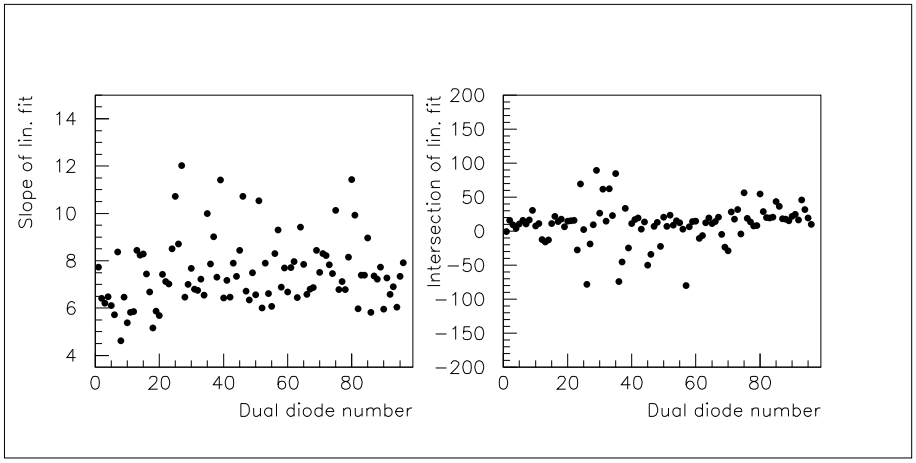

Figure 6.11: *The cross calibration constants for all dual diodes. The left diagram shows the slopes from the linear fits, i.e. the ratio between the big and small diode signal. The diagram to the right shows the intercepts from the linear fits.*

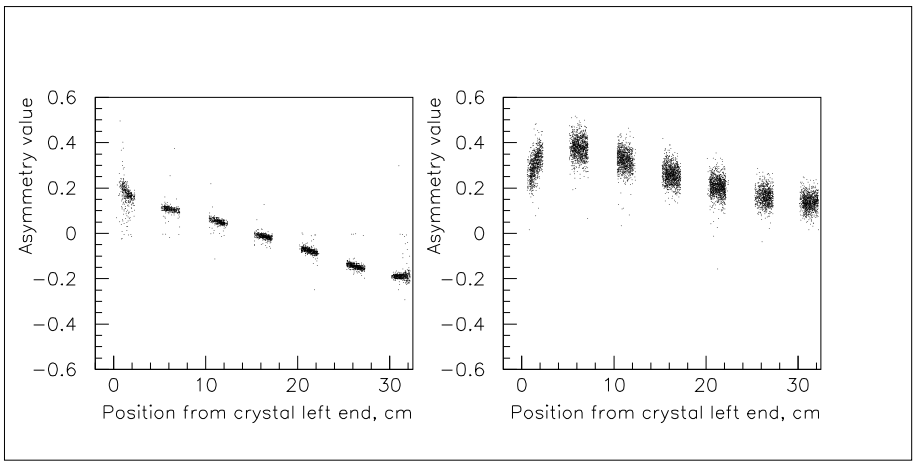

Figure 6.12: *The asymmetry dependence for two crystals. Left: a 'good' crystal with a near linear dependence. Right: A crystal with poor correlation and less linear behaviour. The beam width was approximately 2 cm.*

The asymmetry curves of each crystal were determined by using the 20 GeV muon runs. Two examples are shown in figure 6.12. The asymmetry curves were mapped with the large diode and high gain readout. The calibration constants described in section 6.1 were then used to find the corresponding asymmetry curves for the other two read out options (large diode with low gain amplifier and small diode with low gain amplifier).

6.4 Electromagnetic Shower Reconstruction

The main purpose of the GLAST calorimeter is to measure the energy of the incoming cosmic gamma ray. The hodoscopic-like segmented design of the calorimeter allows it to measure large energy ranges and to supply information for the position and direction of the shower axis to be reconstructed. This section will discuss the results of the shower reconstruction tests from the beam experiment at CERN. The methods of energy reconstruction are described along with the results, followed by a discussion of the position and direction reconstruction abilities.

6.4.1 Methods of Energy Reconstruction

The methods used for energy reconstruction in GLAST depend on the energy of the incoming cosmic gamma ray. Below a threshold level the calorimeter is thick enough to completely absorb the shower and the energy in the calorimeter is easily found by adding the energy deposition in all crystals. However, in this energy range the energy loss in the tracker is not negligible and has to be taken into account. The experiment at CERN did not include any data at this low level.

At higher energies the shower starts to leak out the back of the calorimeter. The choice of reconstruction method in this case depends on whether the shower maximum is contained within the calorimeter or not. If the shower maximum is well contained within the calorimeter, up to around 20 GeV gamma energy, the method called energy leakage compensation (also referred to as last layer correction) is possible to use. If the shower maximum is not contained, or if the shower maximum occurs in the last few layers of the calorimeter, then the reconstruction employs profile fitting of the longitudinal energy deposition.

Longitudinal Profile Fitting

The longitudinal profile fitting method is required for the most energetic events in the GLAST calorimeter. During these events there are vast energy leakages out the back of the calorimeter. The energy contained within the calorimeter is a fraction of the incident gamma energy. The longitudinal profile of the energy deposition of the electromagnetic shower is a well known shape. The energy of each layer is determined by summing calibrated energy values from each crystal in the layer. The profile which fits the energy distribution best is found and the shower energy is determined from the fit parameters.

The commonly used distribution which well fits the longitudinal profile of the shower distribution, is a Γ-function:

$$\frac{dE}{dt} = E_0 \cdot b \cdot \frac{(b \cdot t)^{a-1} e^{-bt}}{\Gamma(a)} \tag{6.7}$$

where a and b are parameters dependent on the absorbing material and the energy of the incident particle, E_0 is the energy of the incident particle and t

is the shower depth measured in radiation lengths. The depth at which shower maximum occurs is given by:

$$t_{max} = \frac{a-1}{b} \tag{6.8}$$

When fitting the Γ-function on event basis, the free parameters were E_0, a and b. The parameters a and b are material dependent and constant for the average longitudinal shower profile. On event basis however the shower development fluctuates and therefore there must be room for variations in the shape of the shower profile.

Figure 6.13 shows how the parameters affects the shape of the distribution. The solid curves in all three diagrams shows the Γ-function with values of E_0,

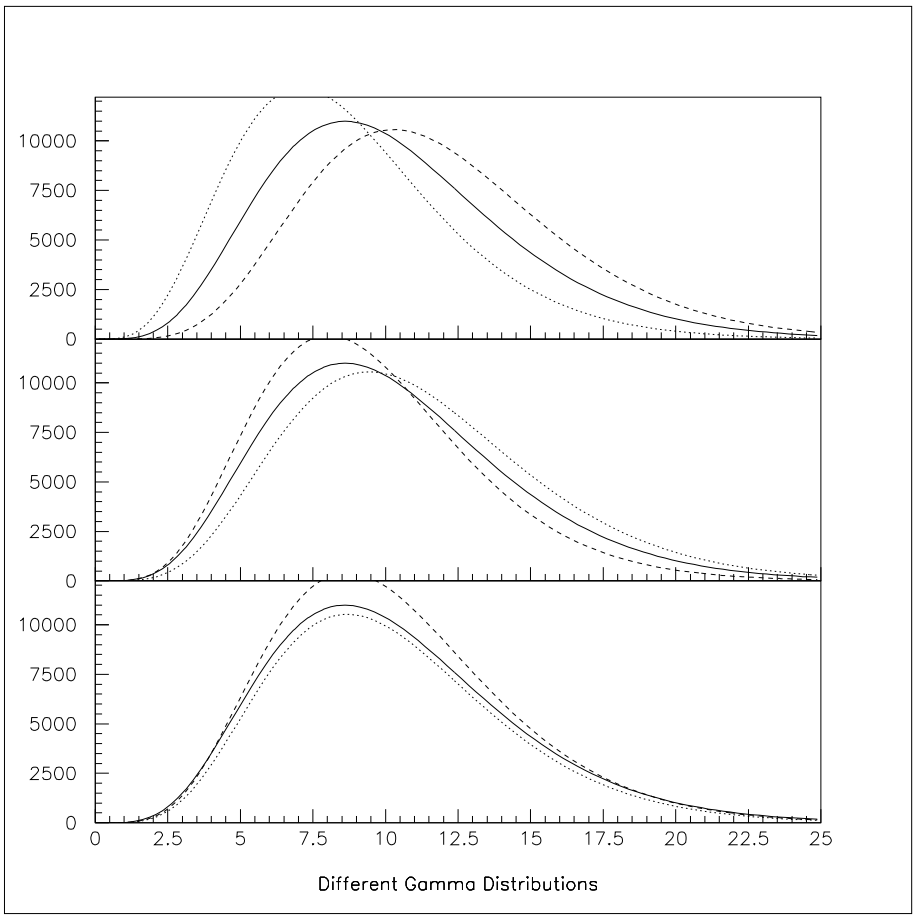

Figure 6.13: *The solid curves are the Γ-function plotted with the average values from 120 GeV electrons, 1.3 X_0. Top: shows how the shape changes when parameter a is varied. Middle: parameter b is varied. Bottom: parameter E_0 is varied.*

a and b taken from the averages of the 120 GeV electron run with 1.3 radiation lengths of passive material in front of the calorimeter (see section 6.4.2). The top graph shows what happens if a is varied (E_0 and b remain unchanged). The dashed curve represents a higher value of a, and vice versa for the dotted curve. In the middle diagram the dashed curve represents a value of b larger than in the average case (E_0 and a constant), and vice verse for the dotted curve. Finally, the bottom graph shows what happens if E_0 is varied.

If a and b were to be kept constant during the fit, the shape could not be fitted, only the height. However, the dashed curve in figure 6.14 represents a possible fluctuated energy distribution which returns the correct value of the

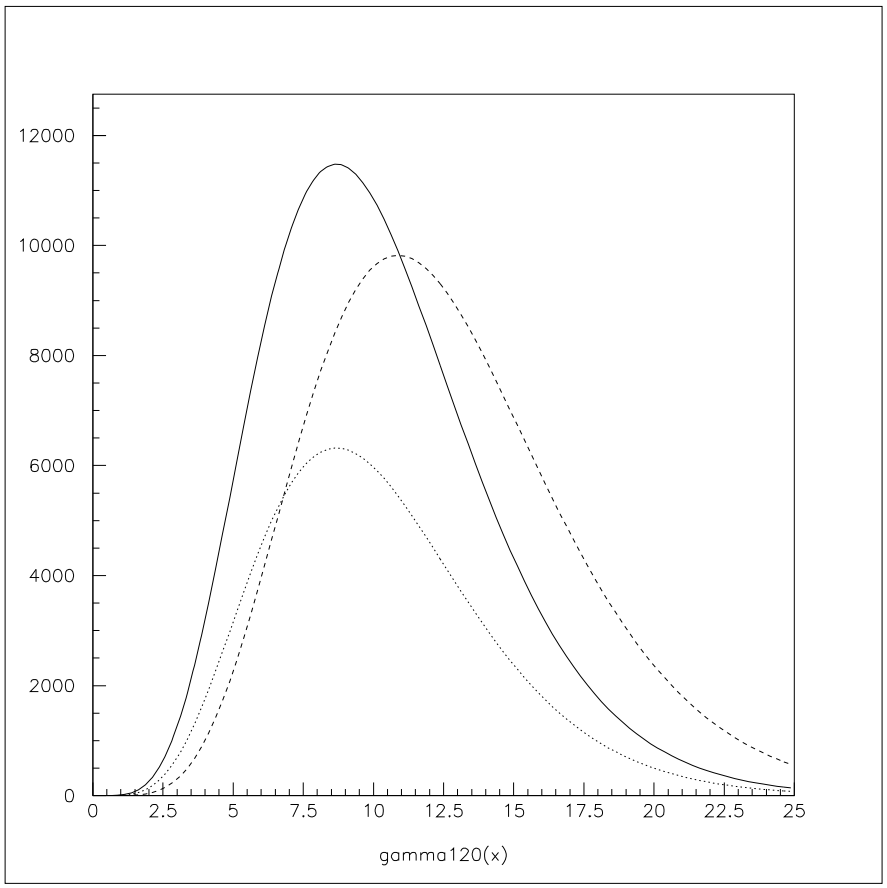

Figure 6.14: *Solid curve shows the* Γ*-function with average values of* a*,* b *and* E_0*. Dashed curve: possible energy distribution with other values of* a *and* b *than the average but which yields the same* E_0*. Dotted curve shows how a fit with fixed* a *and* b *(from solid curve) would look like if it was applied to an energy distribution as the dashed curve.*

incident energy, but it has not the average values of a and b. Thus, the fit would try to force it to the locked shape and the result would look something like the dotted curve, which represents an energy being less than the true incident energy (in the displayed example approximately 55 % of the incident energy). Since the energy distribution do fluctuate, a and b were kept free during the reconstruction and then compared to a run with the parameters a and b fixed to their average values, see page 128.

Last Layer Leakage Compensation

When the critical energy of the shower is reached, the production of new particles ceases (page 28). This also corresponds to the shower maximum in the longitudinal profile (equation 6.8). The leakage compensation method is based on the assumption that the energy which leaks out of the calorimeter, is proportional to the energy measured in the last layer. The incoming energy could then be found by summing the total deposited energy in the calorimeter and the estimated leakage:

$$E_0 = E_{meas} + E_{leak} \tag{6.9}$$

or

$$E_0 - E_{meas} = E_{leak} = k \cdot E_8 \tag{6.10}$$

where E_0 is the incident energy, E_{meas} is the energy measured in the calorimeter, k is a constant depending on energy, and E_8 is the energy measured in the last (8th) layer. Thus, if plotting the energy leakage $E_0 - E_{meas}$ (beam energy subtracted with the measured energy), versus E_8, the energy measured in the last layer, it should ideally be distributed around a straight line through the origin and having a positive slope.

During the reconstruction of events, a value of k is chosen depending on the values of E_8 and E_{meas} and the corrected energy is determined. However, the energy leakage at the energy levels tested is overestimated. Therefore, the leakage must be written as:

$$E_{leak} = k \cdot E_8 - E_{o.e.} \tag{6.11}$$

where $E_{o.e.}$ is the amount of overestimation which, just as the slope k, is energy dependent. The line (equation 6.11) is found by fitting a two-dimensional Gaussian to the two-dimensional histogram of E_8 versus E_{leak}:

$$f(E_8, E_{leak}) = A \cdot exp\left[-\frac{1}{2\sigma}\left(\frac{X^2}{\alpha^2} + \frac{Y^2}{\beta^2}\right)\right] \tag{6.12}$$

$$X = (E_8 - E_8^{max})\cos\theta + (E_{leak} - E_{leak}^{max})\sin\theta$$
$$Y = -(E_8 - E_8^{max})\sin\theta + (E_{leak} - E_{leak}^{max})\cos\theta$$

which is an ellipse with its centre at E_8^{max} and E_{leak}^{max}, A is a normalization constant, α and β are the major and minor axis respectively and θ is the angle

between the major axis and the x-axis from which the slope k is determined [50].

This method requires the shower maximum to be within the calorimeter. If the shower maximum is located rather late in the calorimeter, which is the case at high energies, the fluctuation of the energy distribution is quite large resulting in larger energy resolution. At higher energies there is also larger energy leakage out from the sides and due to backscattering. As was seen from the beam test experiment this method is feasible at 20 GeV, but at 50 GeV the energy resolution becomes bad, and it does not work at all at 80 and 120 GeV.

6.4.2 Results of the Energy Reconstruction Test

Results from the Γ-function fit will be presented in detail for the 120 GeV runs, with 0 and 1.3 radiation lengths (hereafter denoted X_0) of passive material in front of the detector. A summary of the results for the other energies 20, 50 and 80 GeV, is presented on page 128. The energy leakage compensation will be presented for the 20 GeV run, where it works well, and 50 GeV run where it is possible to use (if there is 1.3 X_0 of dead material in front). At 80 and 120 GeV this method is not possible to use, as will be shown.

Γ-Function Fit of the 120 GeV Runs

The longitudinal shower profile from 120 GeV electrons, with normal incidence and aimed at the center of the calorimeter looks like in figure 6.15. The distribution is composed from five runs with respectively 0, 4, 8, 12 and 14 X_0 of passive material in front of the detector, thus covering a calorimeter depth corresponding to 22 X_0. The solid curve represents the fitted values of E_0, a and b (all free parameters in the fit) for the average profile of the run with 0 X_0 in front of the calorimeter. The dashed curve is drawn with the fitted values from the average profile of the run with 1.3 X_0.

At large depths there is a difference between the average reconstructed curves and the measured energy distribution. This means that the mean reconstructed energy value will be slightly underestimated, something which is seen in the results below. The fact that the two curves (0 X_0 and 1.3 X_0) are so close together implies that the value of the reconstructed energy is rather independent on whether the incoming gamma ray converts early or late in the tracker.

120 GeV Beam Energy, 1.3 X_0 Passive Front Material

Figure 6.16 shows the reconstructed energy using the longitudinal profile fit of a Γ-function together with the energy measured in the whole calorimeter. The reconstructed energy distribution has a shape which is close to Gaussian but with a small low energy tail and a somewhat larger high energy tail (large energy fluctuations results in a large overestimation of the energy). The full width half maximum (FWHM) of the peak is 21.9 GeV, which corresponds to a σ-resolution of 8.7 %. The most probable value of the peak is 107.4 GeV. The statistical mean is 114.7 GeV and the rms-value is 27 GeV, corresponding to a

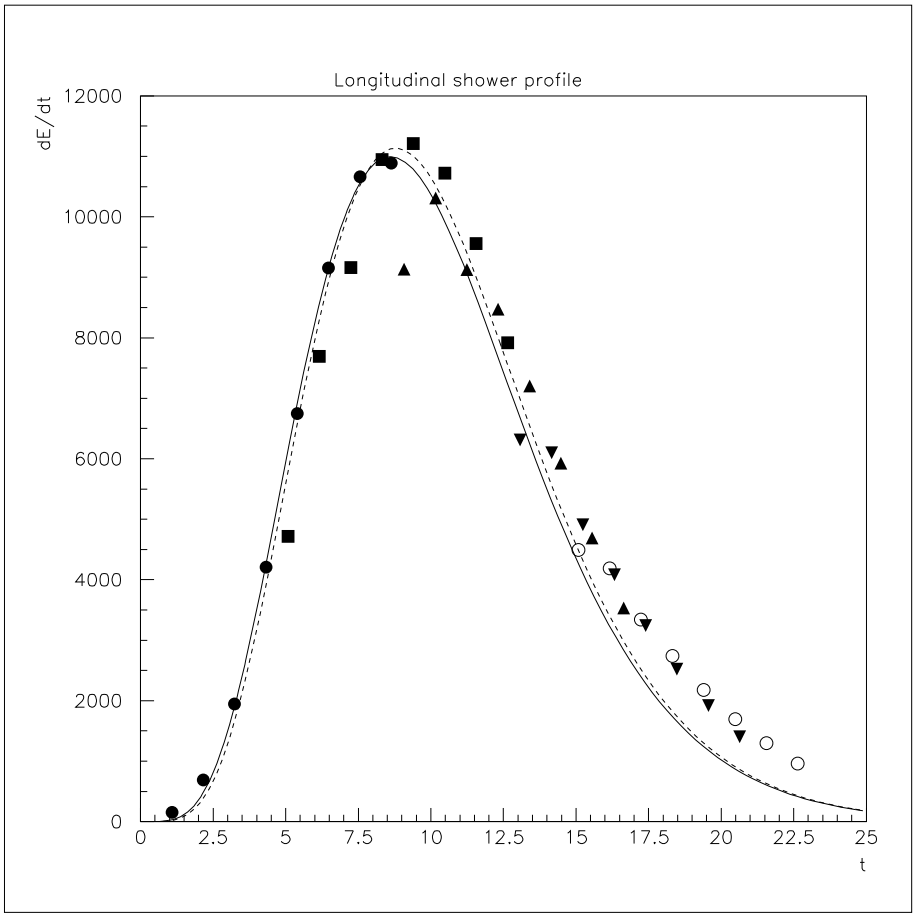

Figure 6.15: *Longitudinal shower profile as obtained from several 120 GeV runs with different amount of passive material in front. Filled circles - 0 X_0, filled squares - 4 X_0, triangles pointing up - 8 X_0, triangles pointing down - 12 X_0, open circles - 14 X_0.*

σ-resolution of 24 %, due to the large high energy tail. The problems with the high energy tail is further discussed on page 128. The slight underestimation of the energy implies an overall calibration factor of 1.1. That the Γ-function results in an underestimation of the energy have been observed in simulations [50] and was evident from figure 6.15.

Figure 6.17 shows the distributions of the parameters a and b. The average value of the parameter a is 6.37 and the average value of b is 0.62. Figure 6.18 shows the correlation between the a and b parameters, and the distribution of the calculated depths of the shower maximum [eq. (6.8)]. The most probable depth according to the distribution is 8.5 X_0. If calculated from theory with the average values of a and b it is 8.7 X_0. Similar correlation between a and b

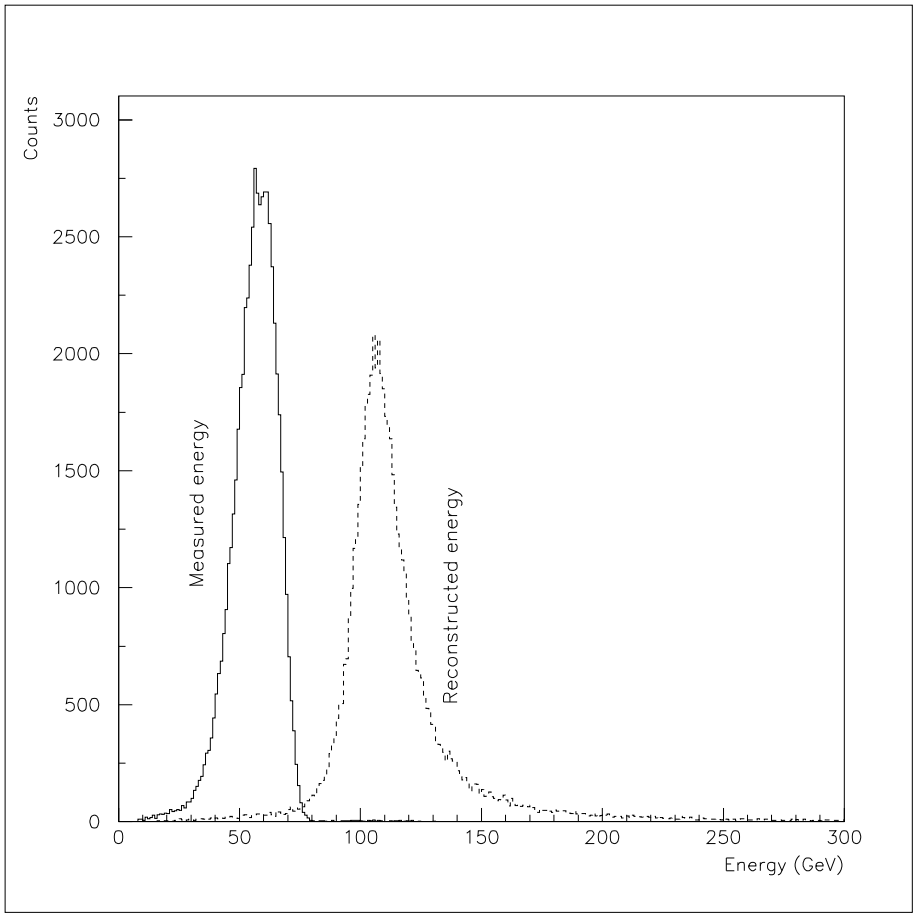

Figure 6.16: *Reconstructed (right peak) and measured energy (left peak), respectively. 1.3 X_0 of passive material in front of the calorimeter.*

is present in all the electron runs.

Figure 6.19 shows the energy deposition in each layer of the calorimeter. Figure 6.20 shows the average profile with the energy deposition in each layer taken from the arithmetic mean of the distributions in figure 6.19. Also shown are the energy fluctuations. If a Γ-function is fitted to the average profile then the E_0 increases somewhat, from 107.4 to 110.7 GeV, a goes from 6.37 to 6.26 and the value of b from 0.624 to 0.595.

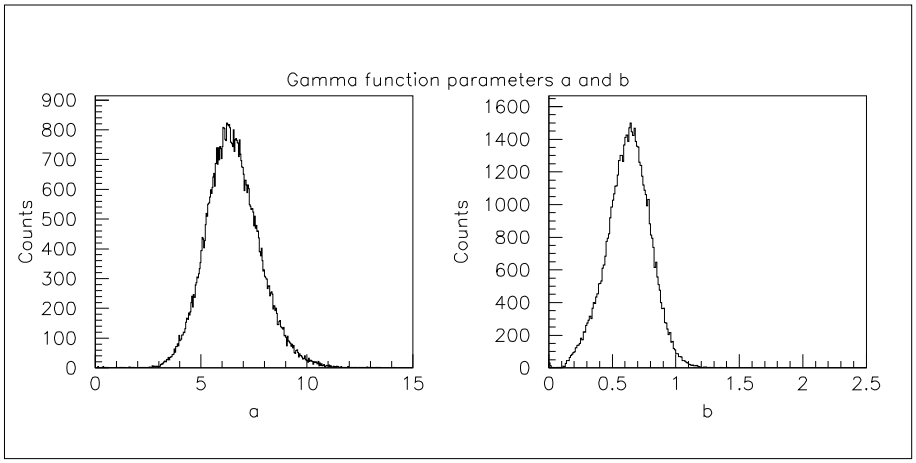

Figure 6.17: *The distributions of the fitted parameter values a (left) and b (right) from the* Γ*-function as obtained from the 120 GeV run. 1.3* X_0 *of passive material in front of the calorimeter.*

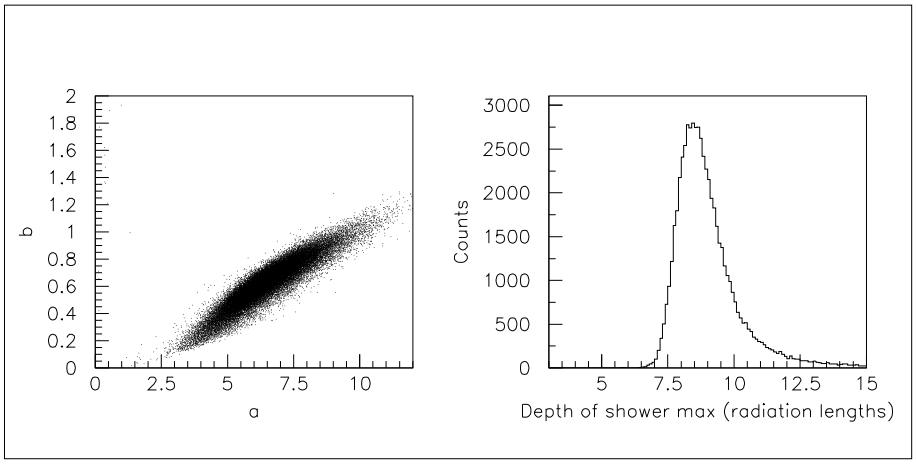

Figure 6.18: *Left: the correlation between the values of the fitted a and b parameters. Right: depths of the maximum of the fitted* Γ*-function. 1.3* X_0 *of passive material in front of the calorimeter.*

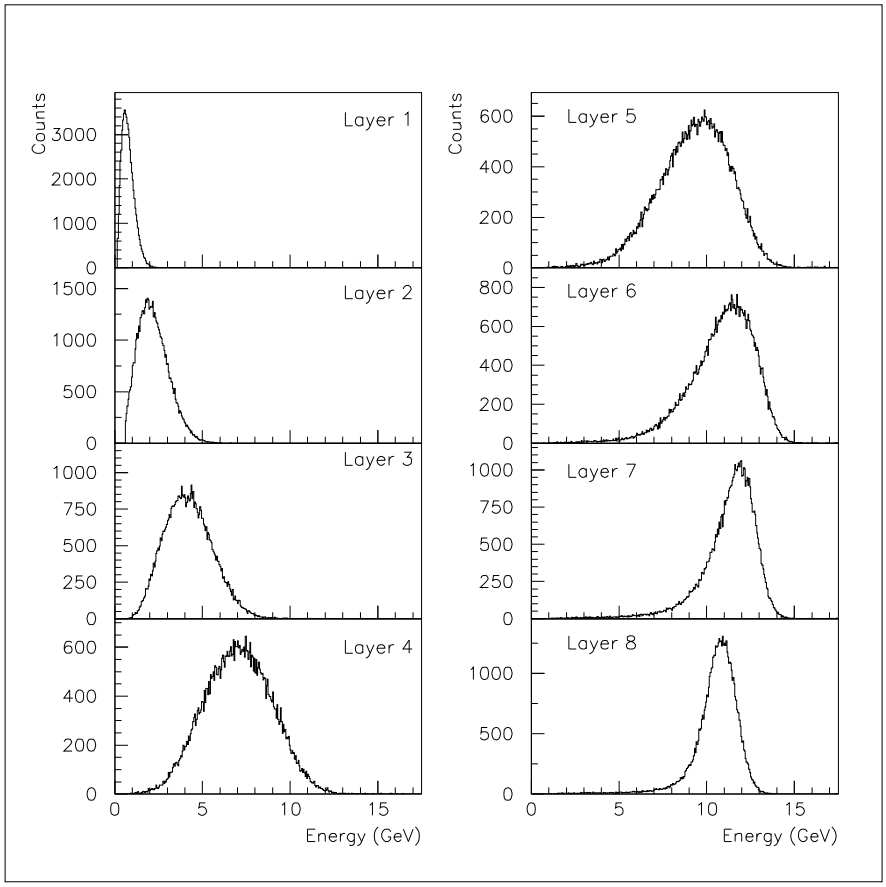

Figure 6.19: *Shower development with 120 GeV electrons and 1.3 X_0 passive front material. Shown is the energy deposited in each crystal layer.*

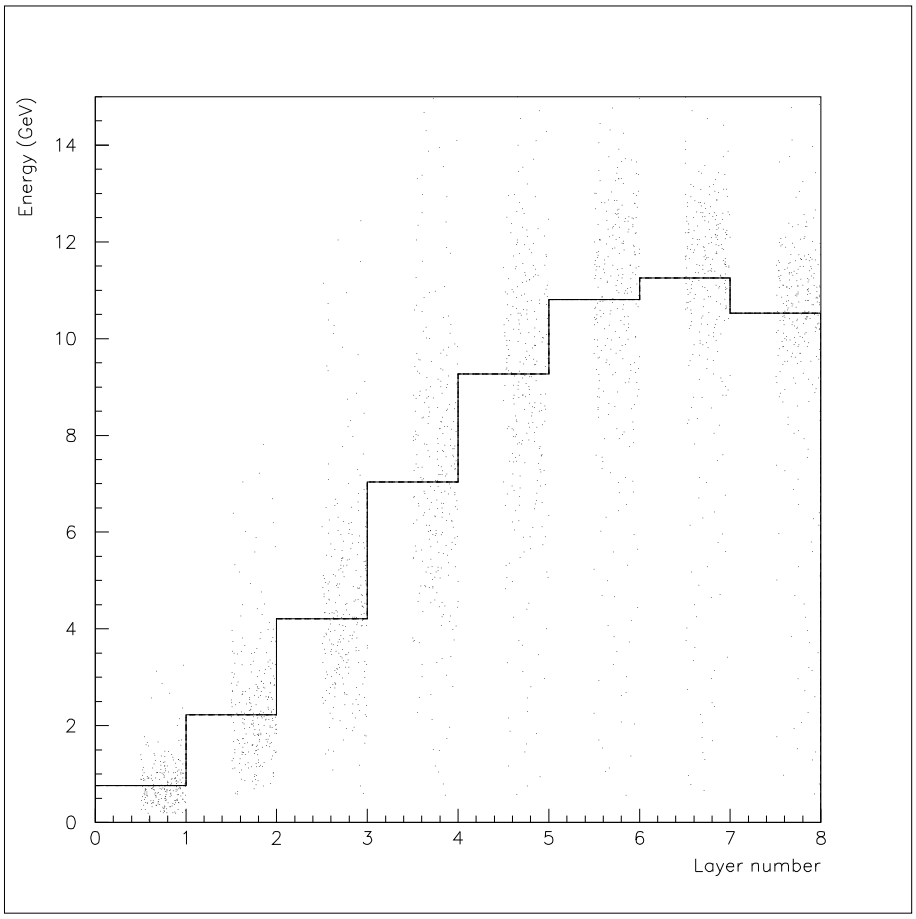

Figure 6.20: *The shower fluctuations together with the fitted average profile (histogram). 1.3 X_0 of passive material in front of the calorimeter.*

120 *GeV* Beam Energy, 0 X_0 Passive Front Material

Figure 6.21 shows the distribution of the reconstructed shower energies and the total measured energy in the calorimeter, with no passive material in front of the calorimeter. Compared to figure 6.16, which was with 1.3 X_0 of passive material in front, it is clearly seen that the distribution of the total measured energy is shifted towards lower values, whereas the reconstructed energy distribution is not affected to the same amount. The most probable value of the peak of the reconstructed energy is 106.6 GeV with a σ-resolution of 13 % (from the FWHM of the peak). The most probable value of the calculated depth of the shower maximum is 8.5 X_0, as in the case of 1.3 X_0 in front. The average values of a and b are 6.12 and 0.597 respectively. Figure 6.22 shows the average longitudinal

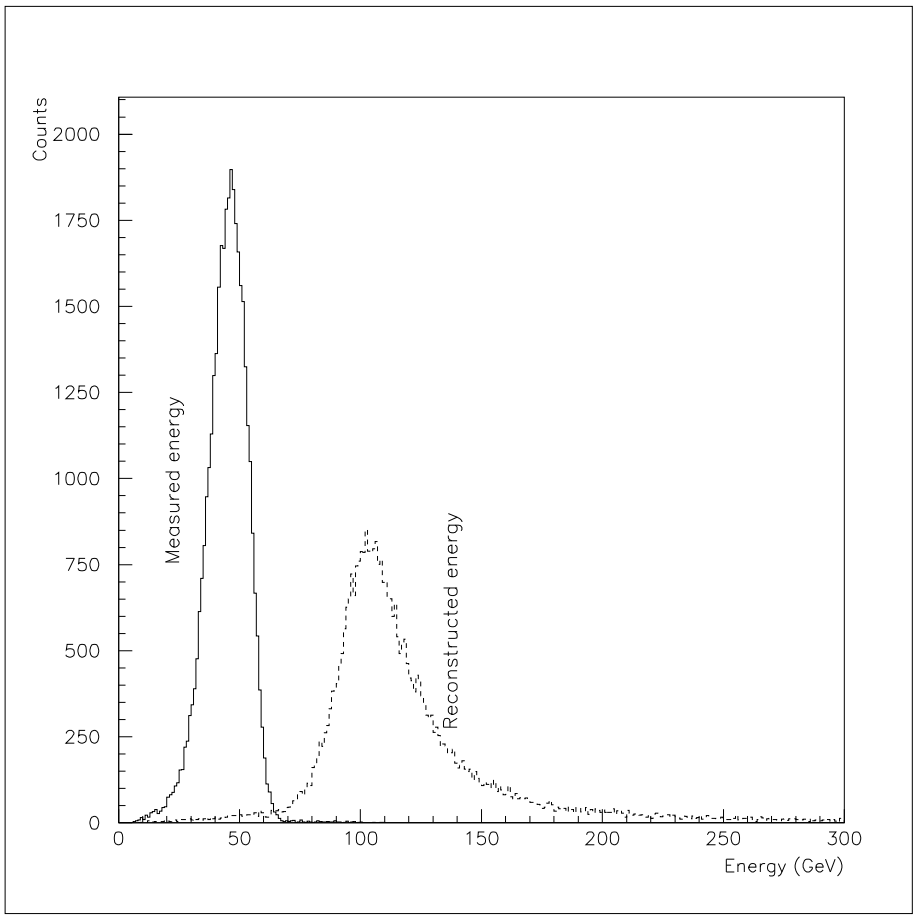

Figure 6.21: *To the left in the figure is the distribution of the total measured energy in the calorimeter, and to the right is the reconstructed energies. The beam energy was 120 GeV. No passive material in front of calorimeter.*

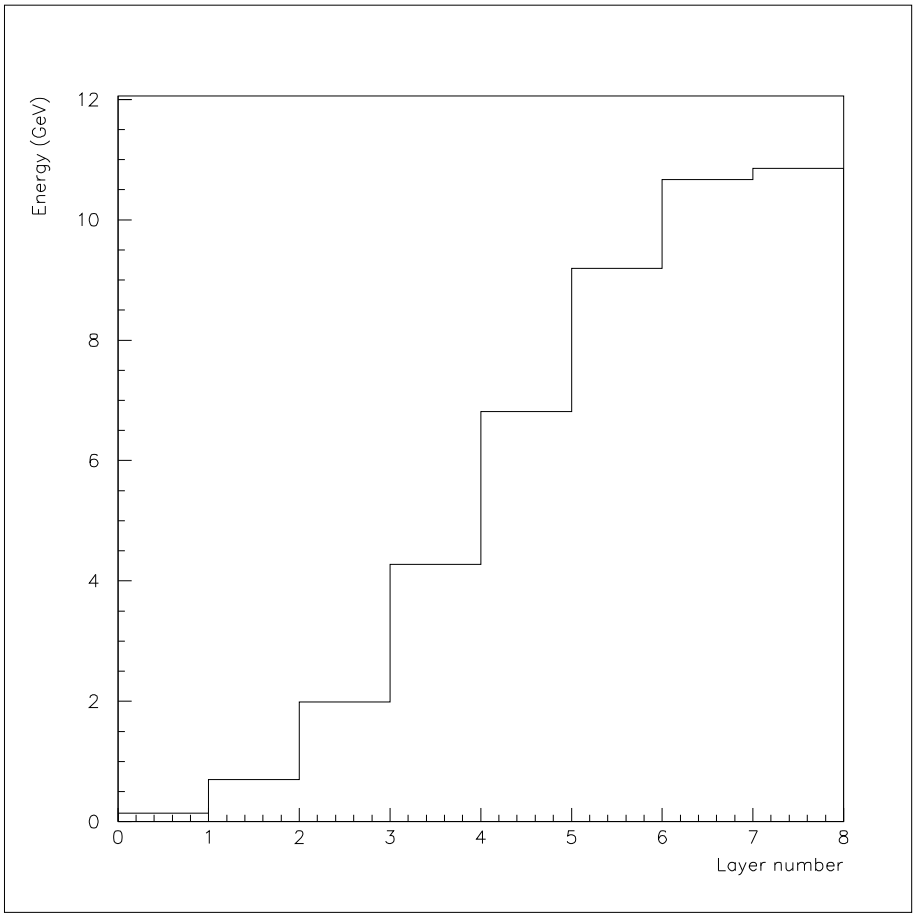

Figure 6.22: *Average longitudinal shower profile with no passive material in front of the calorimeter. The beam energy was 120 GeV.*

profile. The shower maximum is (for the average profile) not contained within the calorimeter as was the case with 1.3 X_0 in front. This has little effect on the reconstructed energy, but the energy resolution becomes worse.

In general, the results for the other energies 80, 50 and 20 GeV (see the summary on page 128) are similar to the ones shown above for 120 GeV. That is, the reconstructed energy underestimates the true beam energy (a correction factor of 1.1 needed), the energy resolution σ is of the order of 10 % and there is an obvious correlation between the a and b parameters.

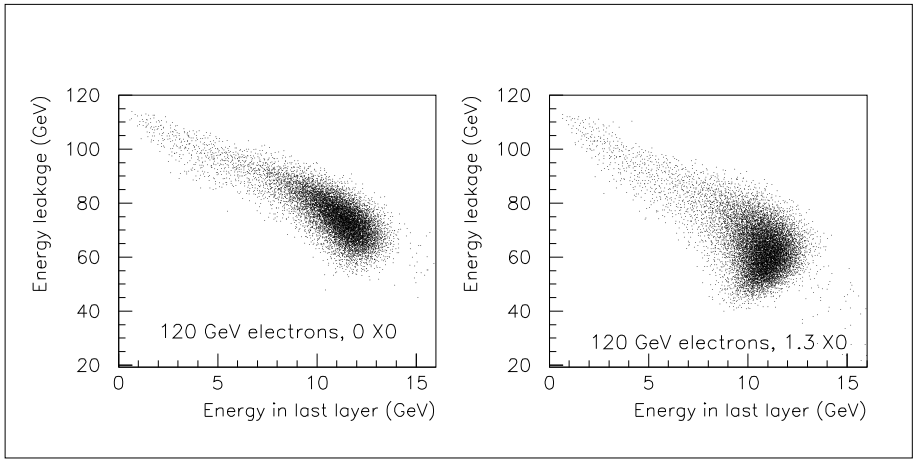

Figure 6.23: *Last layer correlation plot for 120 GeV electrons with 0 and 1.3 X_0, respectively.*

Last Layer Leakage Compensation

Figure 6.23 shows the energy leakage $E_{leak} = E_0 - E_{meas}$ plotted versus the energy E_8 measured in the last layer for 120 GeV electrons with 0 and 1.3 X_0 of passive material in front, respectively. The slope of the correlation would in the case of 0 X_0 clearly be negative. With 1.3 X_0 it starts to shift towards a positive slope but an attempt to fit a two-dimensional Gaussian results in a very steep slope. The same behaviour is seen in the 80 GeV electron runs with 0 and 1.3

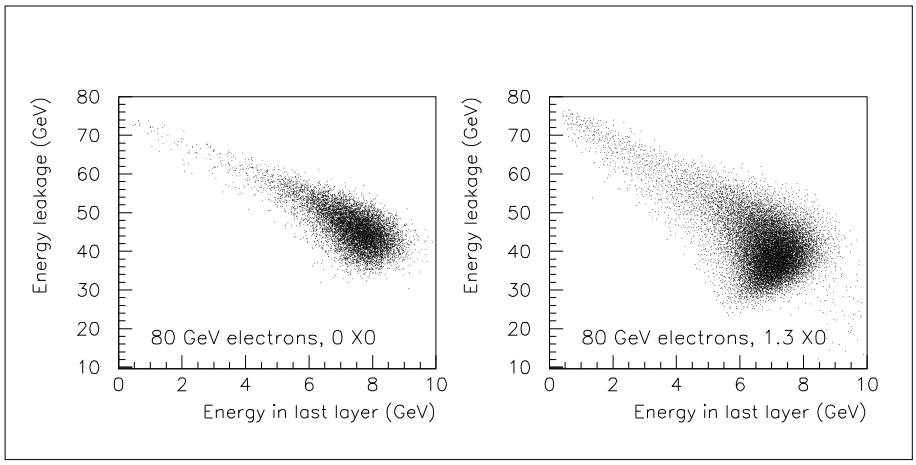

Figure 6.24: *Last layer correlation plot for 80 GeV electrons with 0 and 1.3 X_0, respectively.*

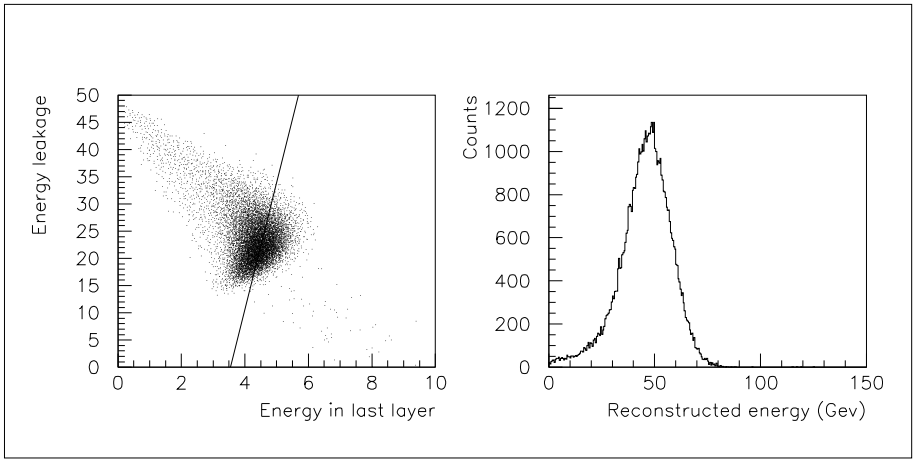

Figure 6.25: *Energy leakage correlation plot for 50 GeV electrons with 1.3 X_0 to the left, together with the line from the fitted bigaussian. To the right is the distribution of the reconstructed energies.*

X_0, see figure 6.24. This shows that this method does not give a meaningful result at these energy levels.

Figure 6.25 shows the energy leakage correlation plot for a 50 GeV run with 1.3 X_0 on the left, together with the line from the fitted bigaussian, and the reconstructed energies which results from using the values of the fitted line to the right. The mean value of the reconstructed energy is 46.6 GeV and the resolution σ is 23 %, which is clearly worse than the 9 % achieved from the Gamma-function fit (see table 6.1 on page 128). There were no run performed at 50 GeV with 0 X_0, but it would be expected from the 80 and 120 GeV runs that the energy resolution would have become even worse. It might even not be possible to use this method at 50 GeV as suggested by simulations [50].

At 20 GeV with 1.3 X_0 the correlation between the energy deposited in the last layer and the energy leakage is stronger, the left plot in figure 6.26, and the distribution of the reconstructed energy is narrower, the right histogram in figure 6.26. The mean value of the reconstructed energy is 19.3 GeV with a resolution of 10 %. The resolution is at this energy level of the order of what is achieved with the Gamma-function fit. As in the case of 50 GeV there is no run with 0 X_0 available, but a higher value of the energy resolution would be expected.

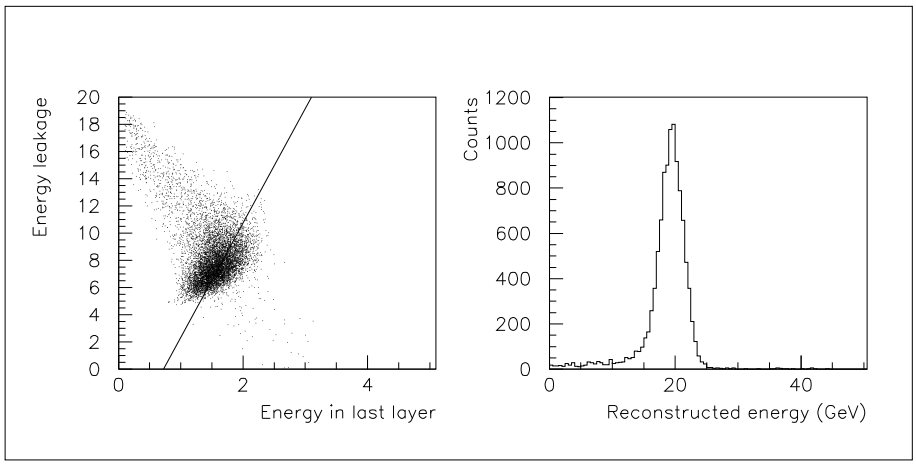

Figure 6.26: *Energy leakage correlation plot for 20 GeV electrons with 1.3 X_0 to the left, together with the line from the fitted bigaussian. To the right is the distribution of the reconstructed energies.*

Summary of Energy Reconstruction Results

Table 6.1 summarizes the results from the longitudinal profile fitting. As can be seen, for this test experiment there is a need for an overall calibration factor of 1.1 in order to get the correct value of the incident beam energy.

Energy	X_0	E_0	E_{res} (σ)	a	b	t_{max}	**Cal. factor**
120	0	106.6	13%	6.12	0.597	8.5	1.1
120	1.3	107.4	8.7%	6.37	0.624	8.5	1.1
80	1.3	71.0	9.3%	6.21	0.622	8.0	1.1
50	1.3	45.7	8.4%	5.88	0.61	7.8	1.1
20	1.3	18.1	8.3%	5.34	0.62	6.85	1.1

Table 6.1: *Summary of the results of the energy reconstruction using the longitudinal profile fit. The E_0-values are the most probable values of the peak and the E_{res}-values are calculated from the FWHM of the peak.*

If the parameters a and b are kept fixed at the corresponding average values during the reconstruction (E_0 being the only free parameter) then the high energy tail is cut off and E_0 is slightly shifted towards lower values (lower statistical mean value), as expected (cf. page 116). The effect is shown in figure 6.27 where the solid histogram represents the reconstruction with free a and b, and the dashed histogram represents the run with fixed values of a and b. The statistical RMS-value becomes smaller (17 % as compared to 24 %) when the high energy tail is removed which improves the overall energy resolution.

According to simulations the energy resolution can be further improved, to approximately 7 % at 100 GeV normal incidence, by a different parametization and constraining the parameters of the fit depening on the energy distrubution through the layers. In short, the more the energy distribution deviates from the average profile the narrower should the constraints be. For more details see [51].

Other simulations done on a GLAST-like segmented calorimeter [50] showed that the last layer correction method is most suitable for events in the energy range $1 - 10$ GeV. The simulations also showed that last layer correction did not work at 50 GeV since the correlation plot already at this energy would have a negative slope (figure 6.28). As seen from the beam test results this method works as well as longitudinal profile fitting up to 20 GeV. The beam test results also showed that the last layer correction method is possible, but with a much worse energy resolution, at 50 GeV.

Figure 6.29 shows how the total energy measured in the calorimeter is distributed for four beam energies, all with 1.3 X_0. It can be seen that at the higher energy levels the contamination is of the order of 20 %. However, after the energy reconstruction (longitudinal profile fit), shown in figure 6.30, the contaminations have decreased to approximately half.

Figure 6.31 shows how the energy fraction contained in the calorimeter (the average of the total measured energy) depends on the incident energy.

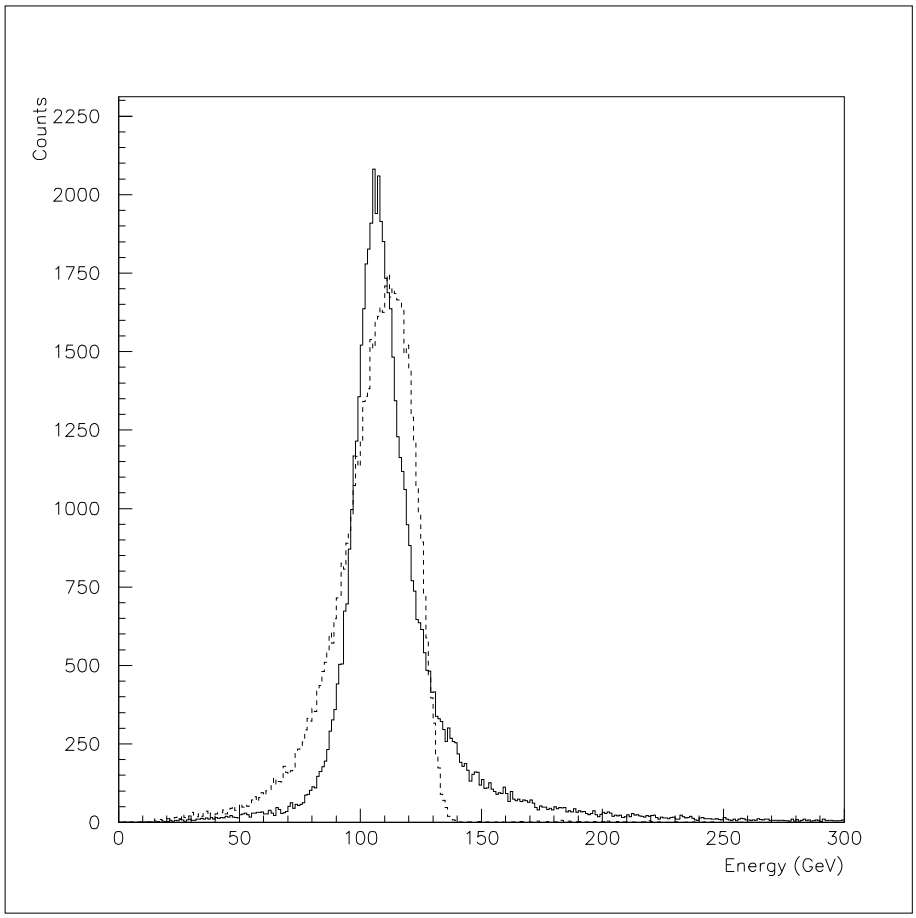

Figure 6.27: *Reconstructed energy with 120 GeV electrons and 1.3 X_0 of passive material in front of the calorimeter. The dashed histogram was obtained by fixation of the a and b parameters, in the solid histogram all parameters were running freely.*

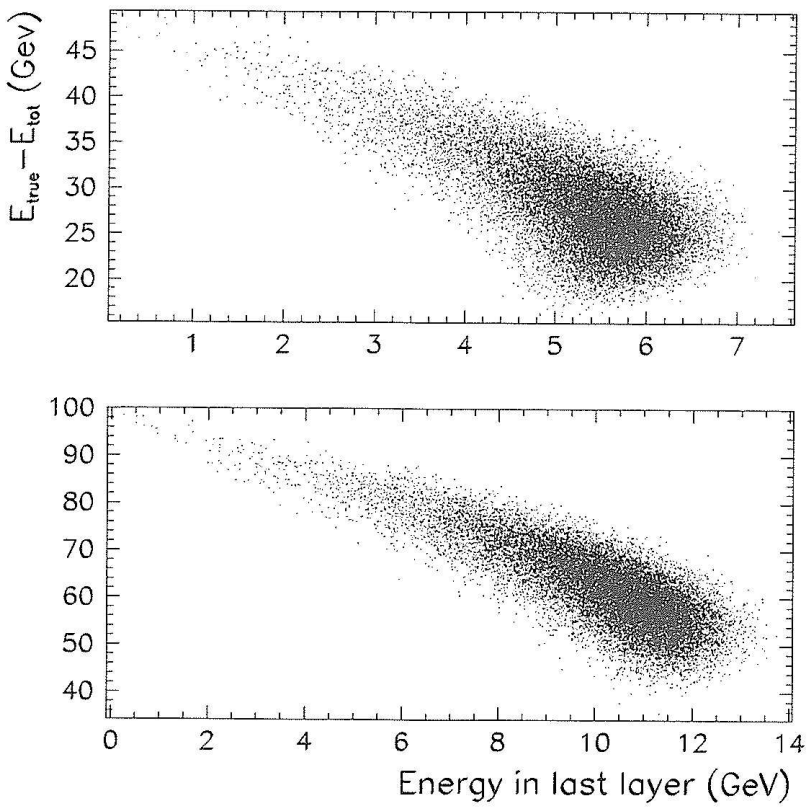

Figure 6.28: *The last layer correlation plots for simulated events in a GLAST-like segmented calorimeter. Top: 50 GeV electrons. Bottom: 100 GeV electrons. Figure adapted from [50].*

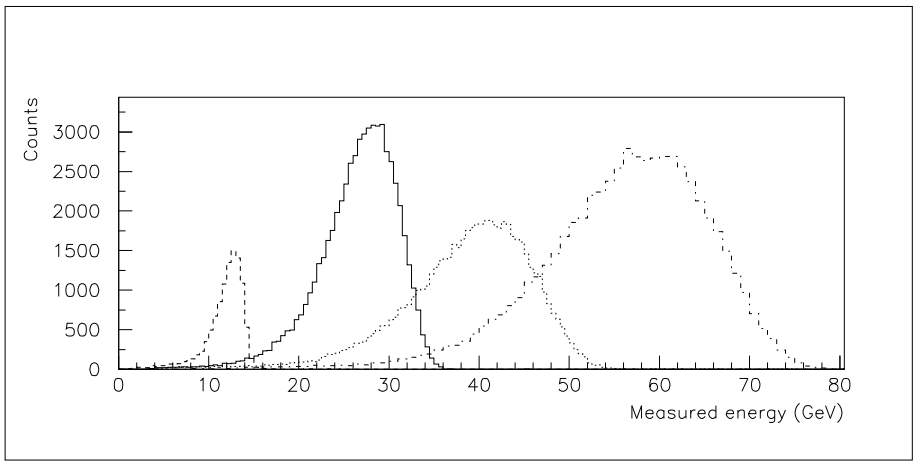

Figure 6.29: *The total measured energy in the calorimeter for four different beam energies, from the left: 20, 50, 80 and 120 GeV, respectively.*

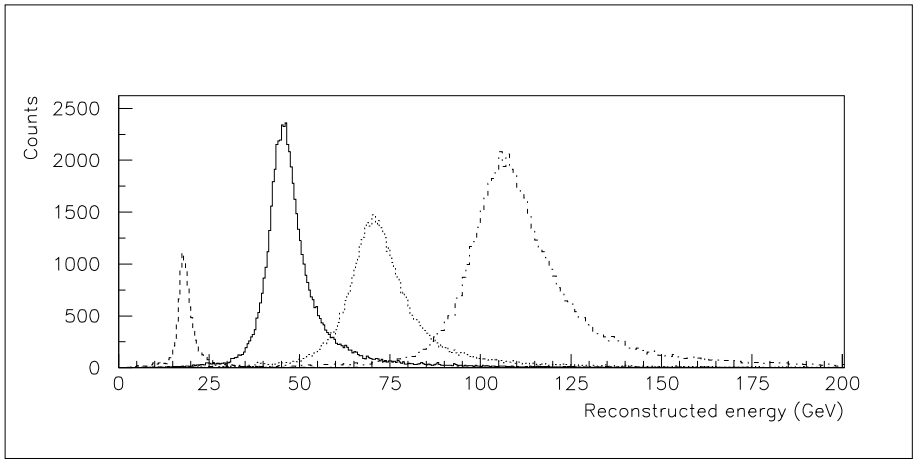

Figure 6.30: *The reconstructed energy in the calorimeter for four different energies, from the left: 20, 50, 80 and 120 GeV, respectively.*

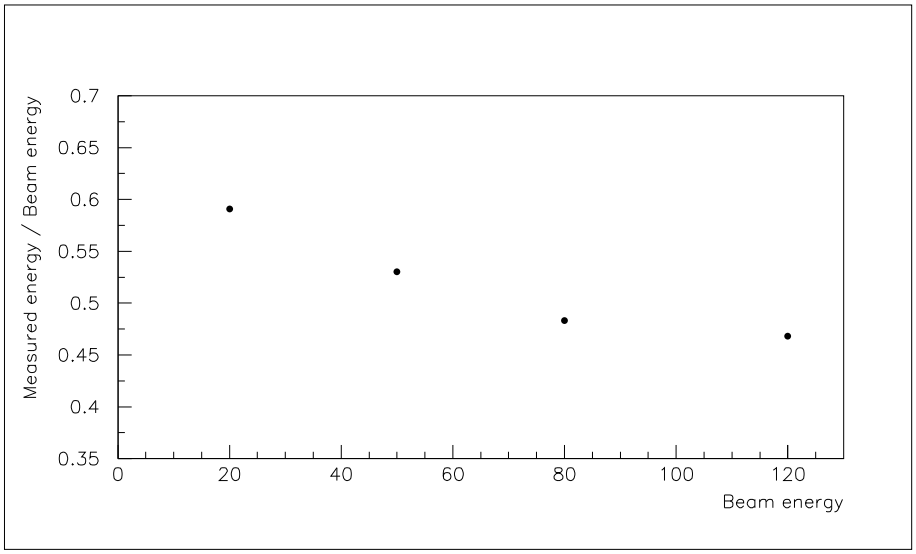

Figure 6.31: *Variation of the ratio between the measured energy and the incident energy with respect to the incident energy. From left: 20, 50, 80 and 120 GeV, respectively.*

6.4.3 Position Reconstruction

The main purpose of the position reconstruction analysis from the CERN beam test data was to determine the position resolution along the crystal axis using the asymmetry values. It was not the goal to make a full position reconstruction, since the crystals in adjacent layers were positioned parallel to each other instead of, as it will be in the LAT calorimeter, with their axes perpendicular to each other.

The location of the energy deposition in the test calorimeter was determined in two ways. On one hand, the asymmetry between left and right end signals from one and the same crystal was used to get a longitudinal position along the crystal. On the other hand, the shower spread transversely over adjacent crystals in a layer was used to get a transverse position perpendicular to the crystal axis.

The recorded positions from the silicon strip beam telescope were used as reference positions. The strip resolution in the beam telescope was 0.1 mm, being an order of magnitude better than the calorimeter's.

Longitudinal Crossing of Shower

The longitudinal position along a crystal axis where the shower axis crosses a crystal layer was found by using the asymmetry value (cf. page 56) from the crystal with maximum energy deposition in the layer. In order to demonstrate the resolution of the reconstructed crossing position the value derived from the asymmetry value X_c was subtracted by the beam telescope value X_t event by event, and then translated with the mean from the beam telescope position (see figure 6.32) before being histogrammed. Figure 6.33 shows an example from one crystal in layer 7 and with 80 GeV electrons and 1.3 X_0 of dead material in front of the detector. To the left is a correlation plot showing the recorded value from the beam telescope versus the reconstructed position as obtained from the asymmetry. The histogram to the right shows the value of $\Delta X = X_c - X_t$. A Gaussian was fitted to the right histogram and the resolution taken as the σ-value of the fit.

The requirement for the GLAST calorimeter for the position resolution (1 σ) was to be less than 1.5 cm (for muons). The position resolutions obtained longitudinally in the CERN test experiments at 0° incidence were typically (for showers) of the order of 1 to 4 mm for the σ-values.

Table 6.2 summarizes the longitudinal position resolutions for three layers with different electron energies, different amounts of passive material in front, and with different angles.

Figure 6.34 shows a set of three runs from layer 4 with 120 GeV electrons (using 1.3 X_0 of passive material) at the same height but at different horizontal positions along the crystal axis, i.e. transverse to the beam direction. When changing the coordinates for the beam impact position, the calorimeter was actually moved relative to the beam and beam telescope. The histograms show the values of $X_c - X_t$. The runs were spaced 50 mm from each other. Table 6.3 shows the distances between the three run positions as acquired from the

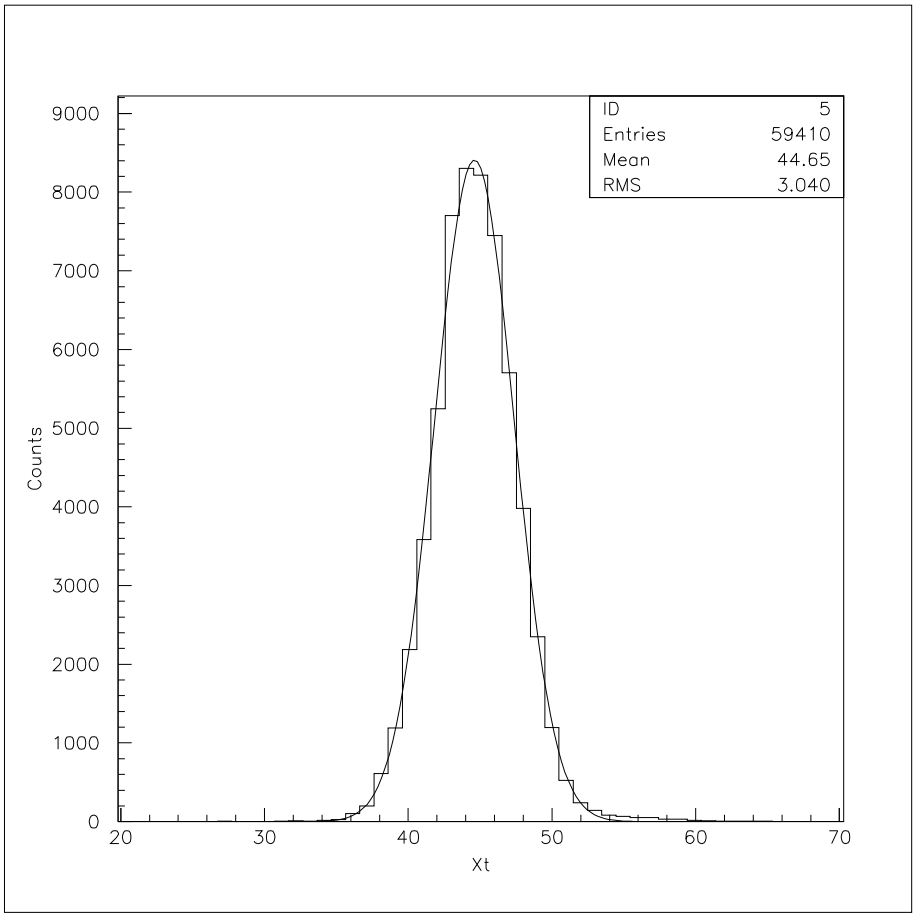

Figure 6.32: *The position distribution in the beam telescope. The mean value corresponds to the X-coordinate for which the beam was aimed.*

reconstructed positions for all layers.

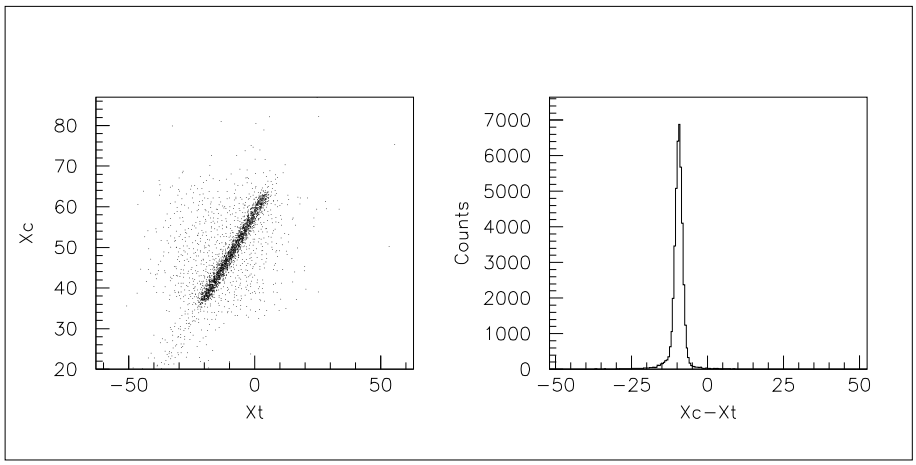

Figure 6.33: *Left plot shows telescope position X_t versus reconstructed position X_c. Right plot shows $X_c - X_t$. Data is from layer 7 and 80 GeV electrons with 1.3 X_0 of dead material in front of the detector.*

Energy (GeV)	$\mathbf{X_0}$	**Angle** (degrees)	σ		
			Layer 1 (mm)	Layer 4 (mm)	Layer 8 (mm)
120	0	0	3.7	2.2	1.4
120	1.3	0	3.1	1.8	1.3
120	4	0	2.3	1.1	2.5
120	8	0	2.1	2.1	3.6
120	12	0	3.1	3.2	5.6
120	1.3	15	3.2	1.5	1.2
120	1.3	30	2.1	1.3	1.8
120	1.3	40	4.2	1.4	2.5
80	1.3	0	3.2	2.4	2.1
50	1.3	0	2.3	1.8	2.1
50	1.3	30	2.8	2.7	3.6
20	1.3	0	2.9	1.4	2.5

Table 6.2: *Summary of results for the reconstructed longitudinal position resolution.*

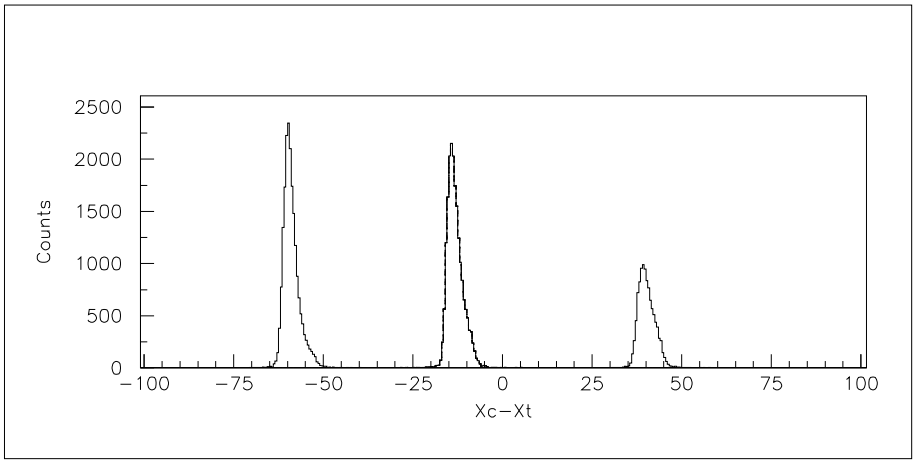

Figure 6.34: *The histograms of $X_c - X_t$ with the beam aimed at three different longitudinal positions (equally spaced 50 mm from each other). Data is taken from layer 4 and the peak in the middle corresponds to having the beam aimed at the center of the crystals.*

Layer	**Distance, from left between peaks** (mm)	
	1 and 2	2 and 3
1	54.7	44.5
2	53.0	41.1
3	56.4	58.0
4	45.9	53.5
5	52.0	41.9
6	51.0	51.3
7	54.9	48.8
8	55.6	49.8

Table 6.3: *The distances between the peaks from figure 6.34 for all layers. The true difference in the beam coordinate between adjacent positions are 50 mm.*

Transverse Position of Shower Axis

The transverse position of the shower axis crossing in a calorimeter layer can be found by plotting the energy deposition in each crystal of one and the same layer and then fit a Gaussian to this distribution. The transverse direction is referred to as transverse the longitudinal crystal direction (Y in figure 6.1). Figure 6.35 shows how the energy is distributed across the crystals in a layer for all eight layers. The mean value of the Gaussian was taken as an estimate of the transverse position Y_c where the shower axis crosses the layer.

The resolution of the transverse position reconstruction was determined by using the same technique as for the resolution of the asymmetry reconstructed

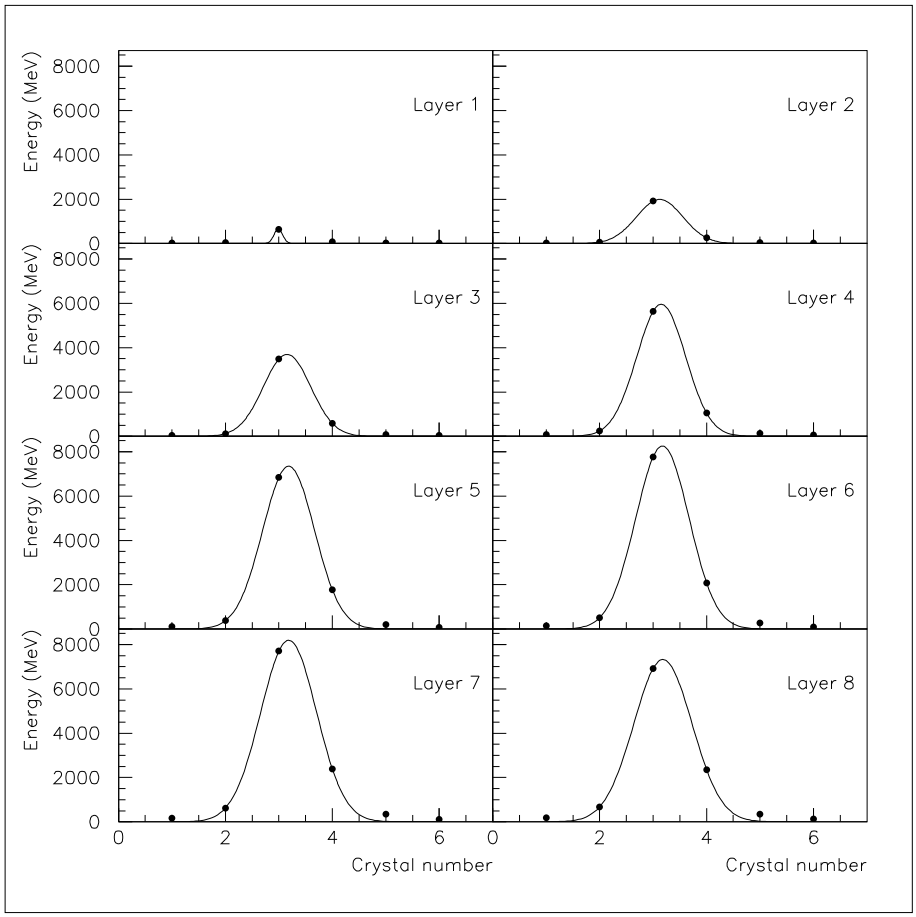

Figure 6.35: *The transverse energy distribution for each crystal layer. The data shown is taken from a run with 120 GeV electrons, normal incidence and 1.3 X_0 of passive material in front of the detector. In each layer crystal number 1 is at the bottom. Layer 1 is the first as seen from the beam.*

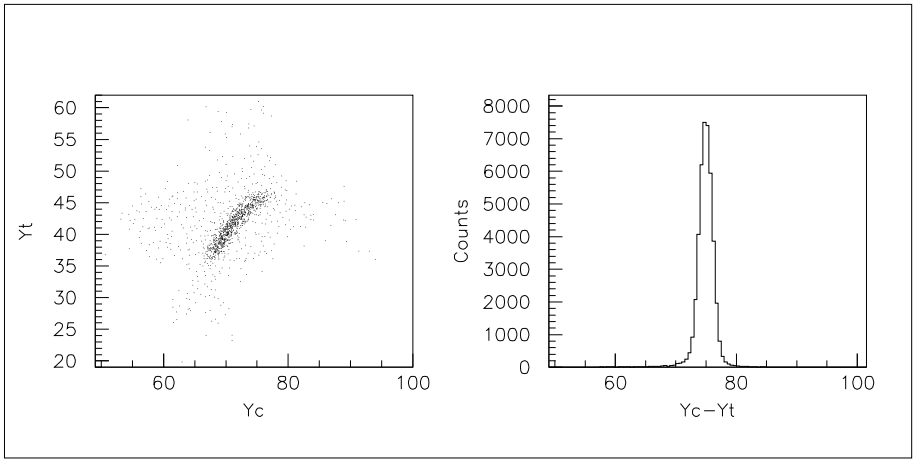

Figure 6.36: *Left: The recorded beam telescope position Y_t on the Y-axis and the reconstructed position Y_c on the X-axis. Right: Histogram of the values $Y_c - Y_t$. Data is from layer 7 and 80 GeV electrons with 1.3 X_0 of passive material in front of the detector.*

position. Figure 6.36 shows to the left a scatter plot of the beam telescope position Y_t versus the reconstructed value Y_c. $\Delta Y = Y_c - Y_t$ is shown to the right. As can be seen the transverse position resolution across the layer is of the same order of magnitude as the longitudinal position resolution determined from the asymmetry values. Table 6.4 gives a summary of the transverse position resolution found in different runs with different beam energies. At high energies the shower spreads significantly across the crystals in a layer (except for the first layers), which tends to improve the transverse position resolution.

Figure 6.37 shows the histogrammed distributions of $Y_c - Y_t$ for three different runs taken at different vertical heights, i.e. Y-coordinates (cf. figure 6.1). The beam impact position in the X-direction was at the center of the

Energy (GeV)	$\mathbf{X}_0$	**Angle** (degrees)	σ		
			Layer 1 (mm)	Layer 4 (mm)	Layer 8 (mm)
120	0	0	2.5	1.0	0.74
120	1.3	0	2.4	0.86	0.72
120	4	0	1.3	0.80	1.03
120	8	0	1.3	1.2	2.20
120	12	0	2.1	2.2	3.5
80	1.3	0	3.1	1.4	1.2
50	1.3	0	3.0	1.5	1.5
20	1.3	0	3.0	1.8	2.1

Table 6.4: *Summary of results for the reconstructed transverse position resolution.*

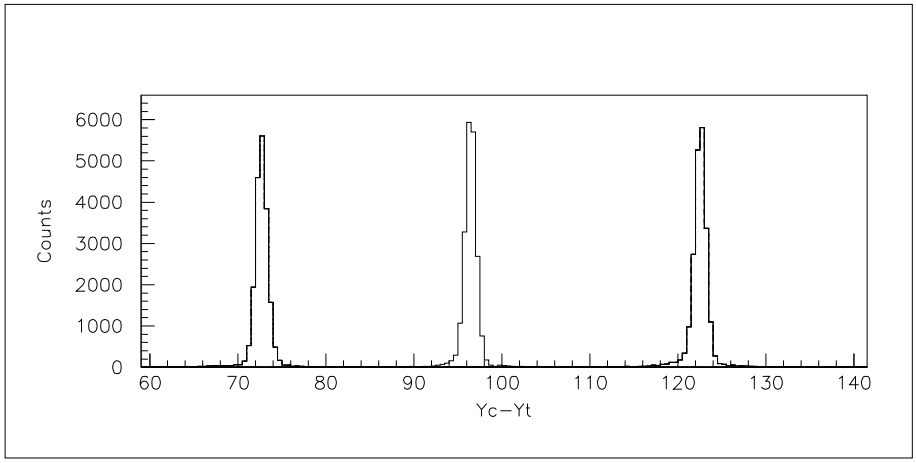

Figure 6.37: *The histogrammed values of $Y_c - Y_t$ with the beam aimed at three different heights. Data is from layer 7 with 120 GeV electrons and 1.3 X_0. The leftmost peak is the third crystal from the top. Peaks 2 and 3 are from crystals number four and five, respectively.*

crystals (longitudinally). Table 6.5 gives the resulting distances between the reconstructed transverse positions, which corresponds to the geometrical change of the vertical beam coordinate.

Layer	**Distance, from left between peaks** (mm)	
	1 and 2	2 and 3
1	24.9	26.8
2	24.7	25.8
3	24.9	25.8
4	25.0	25.6
5	24.7	25.1
6	25.1	25.3
7	24.3	26.1
8	24.3	26.2

Table 6.5: *The distances between the peaks from figure 6.37 for all layers. The true difference in the beam coordinate between adjacent positions are 27.0 and 25.9 mm, respectively.*

6.4.4 Fitting the Shower Direction

The shower direction trough the calorimeter was found by fitting a line to the center-of-mass of the energy deposition in each layer. The z-axis was taken along the direction of the beam axis, the x-axis was taken horizontally along the longitudinal crystal axis and the y-axis was taken vertically transverse the crystals, cf. figure 6.1. For each layer the position (x, y), where the shower axis crossed the layer, was estimated using the asymmetry and weighted average as described in previous subsections. By combining the x- and y-values respectively with the z-values for the various layers two lines could be fitted, one in the XZ-plane and the other one in the YZ-plane, being the two projections of the shower direction. The fit was a χ^2-fit and the x- and y-values were weighted by the σ-values of the measured distributions (see figures 6.33 and 6.36, and tables 6.2 and 6.4). The polar angle between the z-axis and the shower axis was computed and histogrammed to determine the angular resolution.

Available data sets consisted of a few electron runs at 120 GeV with angles of incidence at 15°, 30° and 40°. In all these runs the calorimeter rotation was in the XZ-plane, so that the given incident angles are between the direction of the beam and perpendicular to the crystal's longitudinal axis. Figure 6.38 shows the reconstructed positions (x, z) in the various layers i.e. calorimeter seen from above. Four different incidence angles are shown: 0°, 15°, 30° and 40°. Also shown are the reconstructed directions (solid lines) and the beam direction (dashed lines).

As can be seen in figure 6.38, the reconstructed shower direction and the beam direction do not match when the beam is inclined. Figure 6.39 shows the difference between the reconstructed direction and the true beam direction versus the reconstructed angle. The discrepancy gets larger with increasing angle of incidence. This systematic deviation can easily be corrected for:

$$\Delta\theta = const. \cdot \theta_{measured} \tag{6.13}$$

which gives the beam angle as:

$$\theta = \theta_{measured} - \Delta\theta \tag{6.14}$$

The effect is due to the non-transverse sampling of the shower. At normal incidence the energy deposition in each crystal is sampled symmetrically around the shower axis. I.e., the samples compared when computing the asymmetry values are taken symmetrically around the shower axis. When the incidence is at an angle, each crystal samples the shower asymmetrically. I.e., sampling on one side of the axis is at another depth than sampling on the other side. Apparently the computed asymmetry value then will become systematically shifted, a shift which readily can be corrected for.

Another minor reason for the shift might be the slight non-linearity of the asymmetry curves. The asymmetry curves are in the reconstruction assumed to be linear, and calibrated such that the zero asymmetry value corresponds to the center of the crystal. If the asymmetry curve is non-linear there will be

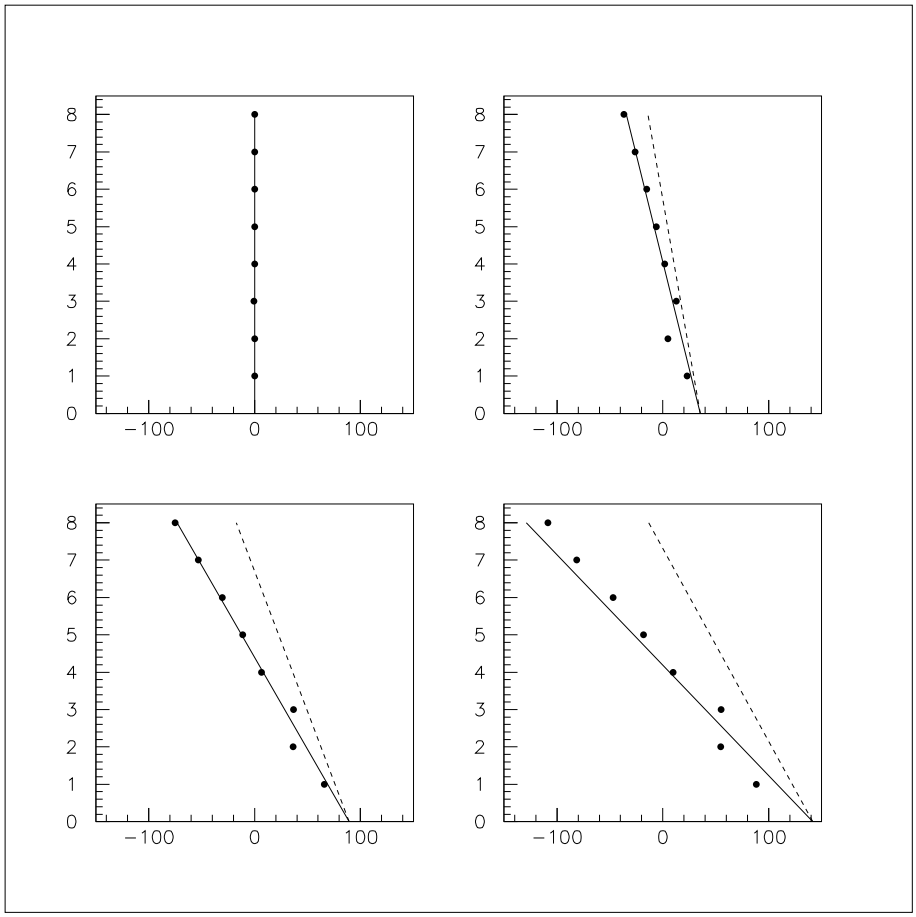

Figure 6.38: *The reconstructed longitudinal position versus the layer number for the angles of incidence 0°, 15°, 30° and 40°. The solid lines represent the fitted directions and the dashed lines the actual beam direction.*

a discrepancy between the actual longitudinal position and the reconstructed. This effect is minor though. Another source of error is shower leakage, of course.

Figure 6.40 shows a scatter plot for 0° incidence of the impact positions (x, y) as calculated from the direction line fit after passing all eight layers. Also shown are the projections onto the x- and y-axis. The resulting angular resolution is in this case 1.6° (FWHM). Table 6.6 gives the angular resolutions for the different incidence angles.

Beam angle	Angular resolution (FWHM)
0°	1.6°
15°	1.5°
30°	1.4°
40°	1.5°

Table 6.6: *The angular resolutions for beam angles 0°, 15°, 30° and 40°. Data is from 120 GeV electrons with 1.3 X_0 of passive material in front of the calorimeter.*

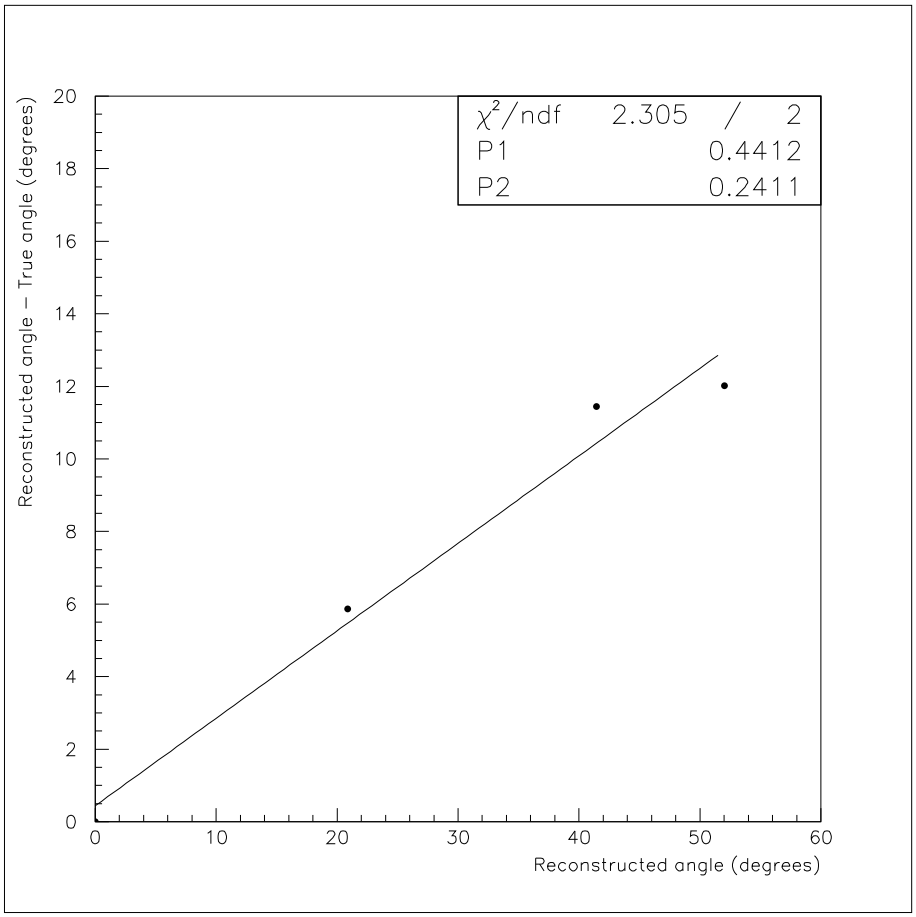

Figure 6.39: *Shown is the difference between reconstructed and actual angle versus the reconstructed angle.*

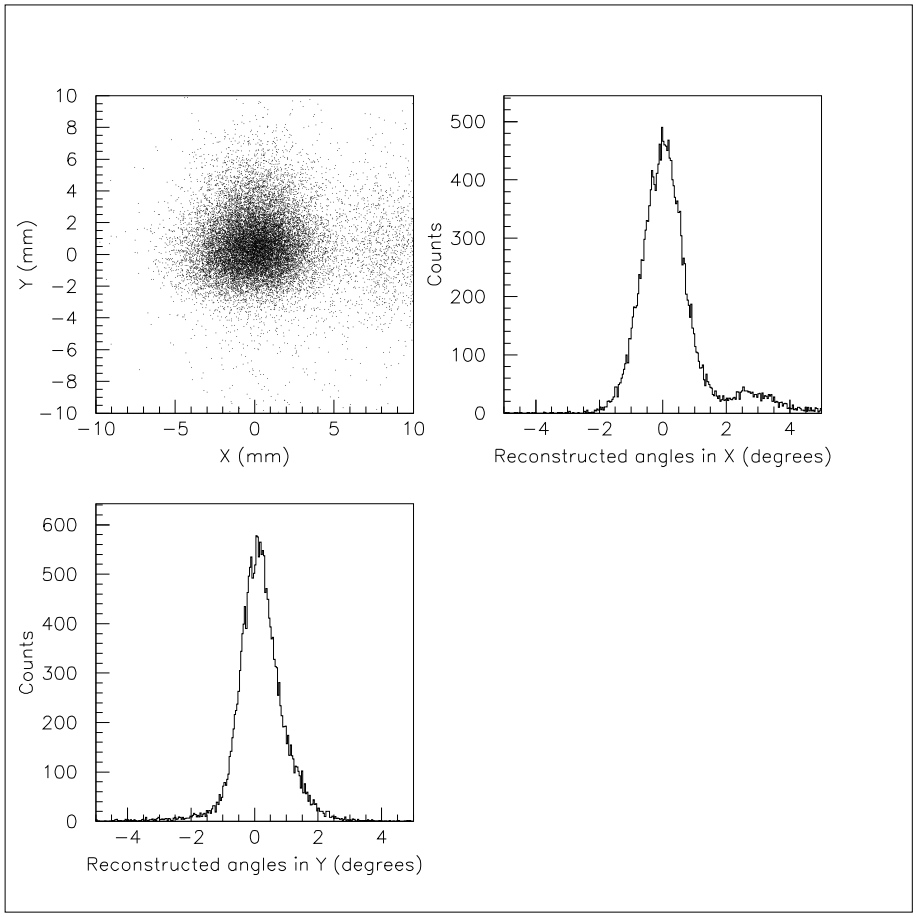

Figure 6.40: *Top left: Scatter plot (the XY-plane) of the reconstructed impact positions (x,y). Right top: Distributions of the angles between the fitted line and the z-axis in the XZ-plane. Bottom left: Distributions of the angles between the fitted line and the z-axis in the YZ-plane.*

Chapter 7

Summary and Conclusions

In this last concluding chapter I have in the first section summarized the main results of this thesis work. The following sections give further details and some discussion

The successful production of test and flight crystals for the GLAST mission did to a large extent depend on fast, accurate and reliable test procedures and equipment. It was our task to construct the test equipment and to develop adequate test procedures, as well as to carry through the entire acceptance test program for all GLAST crystals. We developed and implemented this procedure in a fruitful collaboration with the manufacturer.

It was also part of my work to verify performance of an assembly of single crystal detector elements as an electromagnetic shower calorimeter. An assembly of 48+15 crystals mounted together to resemble a GLAST tower-like detector was tested in an accelerator beam at CERN. It was my task to analyze data from these beam tests.

7.1 Summary of Results

Crystal Production

Amcrys-H of Ukraine has been the provider of more than 2000 crystals for the GLAST project. They managed successfully to produce this large number of high quality crystals at a considerable delivery rate and to a modest cost. Major achievements were:

- Optically well-controlled and uniform behaviour.
- Light output constant within ±10 % for more than 1800 crystals.
- Light taper curves and asymmetry values kept within the desired range.
- Good understanding of the optical effects of surface treatments, wrapping material and read-out optical connections.

- High purity and uniform thallium concentration resulting in good radiation hardness well within GLAST requirements.
- Mechanically uniform results within ±0.3 mm for the entire production of more than 2000 crystals.
- Able to keep up with a tight time schedule.
- Constructive collaboration featuring flexibility to changes in procedures and specifications.
- Substantial cost effective alternative as compared to western manufacturers.

Beam Test

The results from the accelerator beam test experiment at CERN on a GLAST-like calorimeter indicate a performance which well meets the GLAST design goals. The main results were:

- Energy resolution σ less than 13 % in the interval 20 – 120 GeV.
- Position resolution σ of a few mm for electromagnetic showers.
- Angular resolution σ for reconstructed shower axes of 0.7°

7.2 Collaboration with Amcrys–H

Amcrys–H in Ukraine produced more than 2000 CsI crystals for the GLAST project. These 33 cm long crystal logs constitute the active material of the LAT calorimeter. At least 1807 crystals had to be within the GLAST specifications for flight crystals. We constructed adequate test equipment and developed a thorough test procedure in order to verify optical performance and mechanical specification for each individual crystal.

Initially Amcrys-H had some minor problems with the crystal production, both in getting the crystals optical properties correct and keeping them within mechanical tolerances. By developing a close collaboration with the manufacturer and, in particular, by placing a test station at the factory and training one of their engineers in the test procedure, they managed to get good control over the production parameters. The manufacturing process was altered to obtain a more uniform result for mechanical dimensions. Eventually, virtually all flight crystals were found to be within specifications.

The surface treatment of the crystals in order to obtain a desired tapering of the light output from the crystal appears to be an art that the engineers of Amcrys-H master well. They readily obtained the specified requirements and managed to produce more than 80 % of the crystals within specification, most of the rest being just barely outside specifications. Most of these latter crystals were successfully reworked by us by modifying their surface treatment and had not to be sent back to the manufacturer.

7.3 Simulation of Optical Behaviour

A ray-tracing Monte Carlo simulation was developed in order to understand the optical performance of a crystal log. The simulation demonstrated that the optical behaviour can be understood from surface roughness and the choice of wrapping material. The surface roughness simulated in the code was inferred from observations of the actual crystal surface under an 800 times magnification microscope.

Variation of the optical parameters in terms of tapering and light output could easily be obtained by varying the parameters of the simulation and the results agreed well with experimental findings.

7.4 Optical Acceptance Tests

The optical acceptance test was designed to give a fast and reliable check of all crystal properties that had to fulfill the GLAST requirements. Some compromises had to be done, though. E.g., we decided to use just an air gap between crystal and PMT, since it gave much less fluctuations in light losses than using an optical connecting material like Sylgard. The overall light yield went of course down with an air gap but was, on the other hand, increased by the use of another wrapping material. Initially the crystals were wrapped in Tyvek, which is a diffuse reflector. By instead using VM2000 being a specular reflector the light yield was considerably increased. At the same time the light tapering of the crystal gets less steep unless a more progressive surface treatment is applied. VM2000 was eventually chosen as wrapping material for the GLAST flight crystals due to its larger light output.

7.5 Radiation Hardness

Small sample crystals were delivered from the top and the bottom of each crystal boule before the manufacturer cut it into crystal logs. We exposed these sample crystals to severe dosages of gamma radiation, using a hot ^{60}Co source for clinical purposes. The deterioration of signal size from these crystals nicely correlated to the concentration of thallium. It is clear that Amcrys-H has developed a crystal growing technique, which allows for good control of the thallium concentration, which also is near homogeneous throughout the entire boule.

It was also verified that the signal deterioration of the small sample crystals well corresponded to that expected for a full size crystal log. The radiation damage from protons was also studied with a full size crystal log. Signal deterioration and induced activity were found to be well within specifications and will unlikely be the limiting factor for the lifetime of the GLAST instrument.

7.6 Beam Tests of a Detector Assembly

The purpose of the test experiment in a particle beam at CERN was to get a first preliminary result of how an assembled electromagnetic calorimeter setup of GLAST-sized flight crystals would perform when measuring electromagnetic showers, which will be the case in GLAST. The setup used at CERN consisted of 48+15 crystals mounted in a setup that was similar to a GLAST tower in size and had the crystals oriented transverse to the beam in a hodoscopic fashion like in the LAT. Alternating layers did not have the crystals oriented perpendicular, though, but did not limit these preliminary studies.

Energy Resolution

The beam tests were made at several different beam energies up to 120 GeV. In this work two different methods were used to estimate the energy of the beam particle initiating the electromagnetic shower in the detector. One method was to fit the longitudinal profile of the shower, the other the so called last layer leakage compensation method. It was found that for beam energies above 20 GeV the total shower energy is best estimated by fitting the longitudinal shower profile to a Γ-function. The resulting energy resolution σ was found to be better than 13 % almost independent of energy within the interval 20 – 120 GeV. Below 20 GeV the method of energy leakage compensation by applying last layer correction becomes possible. Simulation results in [50] indicate that at these lower energies the energy resolution obtained for the leakage compensation method could be slightly better. In general the CERN beam tests are in reasonable agreement with the simulation results in [50].

Position Resolution

The shower direction is important to be able to reconstruct accurately in GLAST in order to trace the incoming cosmic gamma back to its origin on the sky. The shower direction is determined by reconstructing the crossing position of the shower axis through the crystal layers of the detector. The crossing position of the shower axis through the crystal layers of the assembly used at CERN was reconstructed in two ways. The x-coordinate along the crystal axis was estimated by using the asymmetry between left and right output signals from the crystal holding the maximum energy in the layer. The y-coordinate transverse to the crystal axis was estimated by fitting a Gaussian to the energy spread over the eight crystals within the layer.

The two methods gave similar results concerning the uncertainty in the reconstruction. σ was between 1 and 4 mm in both directions.

Angular Resolution

The GLAST design goal for the angular resolution is 0.25° FWHM for energies above 10 GeV. This is specified for the tracker. However, only 65 % of the cosmic gamma rays above 10 GeV hitting the LAT will convert to an e^+e^- pair

in the tracker. The angular resolution for the remaining 35 % of all cosmic gamma events will be the one of the CsI calorimeter. The angular resolution σ of the calorimeter was specified with respect to cosmic muons traversing all eight layers and was required to be better than $15° \cdot \cos^2\theta$, with θ being the off-axis angle.

By using the (x,y)-coordinates of the shower axis crossings through the eight crystal layers of the detector, the direction of the shower axis can subsequently be obtained by fitting a straight line. The angular resolution σ of the reconstructed direction of the shower axis was in this way found to be 0.7° for the setup used at CERN.

7.7 Concluding Remarks

We have successfully carried through the quality assurance tests for 2000 crystal elements for the GLAST instrument, including crystal specification update and improved performance. This was done within a narrow time schedule and meeting all requirements.

The CERN beam test experiment showed a shower reconstruction capability and resolutions well within the specified requirements for the GLAST calorimeter.

Each tower of 96 crystals of the LAT has successfully passed a further thorough test program, all 16 towers has been mounted in the LAT-detector and the GLAST instrument is assembled all together. Launch is presently scheduled to the 16th of May 2008.

Acknowledgements

I would like to thank my supervisors at the Faculty of Engineering at Lund University professor Kjell Lindström and professor Hans Persson for giving me the opportunity to do a PhD-thesis. I also would like to express a word of gratitude to docent Johan Nilsson, head of Electrical Measurements, for his time and effort. I also wish to thank docent Staffan Carius, my supervisor at Kalmar University, for all the help and support during these years and for being a major source of inspiration.

My thanks also go to the Swedish GLAST collaboration, who invited me into this exciting project, especially professor Per Carlson at Royal Institute of Technology and professor Lars Bergström at Stockholm University.

The development of the crystal evaluation procedures was done in close collaboration with the GLAST group at the Naval Research Laboratory in Washington D.C. I wish to thank Neil Johnson, Eric Grove, Nick Vermani and Patty Sandora for constructive discussions and for their hospitality during my visits. The beam test experiment at CERN is an important part of this work. I would like to thank Benoît Lott and his colleagues of the GLAST group at Bordeaux for making the necessary arrangements for this experiment.

Much of the crystal acceptance tests program would not have been possible without the dedicated work by our engineer Leif Nilsson. The acceptance tests would not have been possible to perform within the tight time schedule without our two technicians Tatjana Kirchberg and Maria Sagerfors. For this I wish to thank them. I like to direct a special word of gratitude to Tatjana Kirchberg, who also served as an excellent interpreter in the contacts with Amcrys–H, an important contribution to our success. The radiation hardness tests were carried out together with my fellow graduate student in this project Sara Bergenius-Gavler. I wish to thank Sara for a nice collaboration (and interesting discussions).

I also would like to express a word of gratitude to the people at Amcrys–H, which provided a most efficient, constructive and flexible collaboration when it came to optimizing crystal design and keeping up to the delivery plan.

I wish to thank the K A Wallenberg foundation for their financial support, which made the Swedish contribution to GLAST possible.

One cannot choose ones family, but I have been very lucky. I wish to thank my parents and my brother for being so supportive, for believing in me and for giving me a helping hand in all my projects. I also would like to thank my

girlfriend for all her love, support and patience.

I would like to thank my friends for being around and for putting up with me.

Finally I would like to direct my last word of appreciation to all the composers (living and deceased), musicians and bands around the globe who make interesting, complex, beautiful, exciting and progressive music. For me music is as essential as food and has during these years provided both necessary energy boosts during long hours and relaxation in between.

Bibliography

[1] Feenberg E. ; Primakoff H. Phys. Rev. **73** 449 (1948)

[2] Hayakawa S. Proc. Phys. Soc. **A65** 215 (1952)

[3] Morrison P. Rev. Mod. Phys. **29** 235 (1957)

[4] Homepage of NASA Goddard Space Flight Center, student outreach "Imagine the universe":

http://imagine.gsfc.nasa.gov/docs/science/know_l1/history_gamma.html

[5] Homepage of NASA Goddard Space Flight Center, the Compton Gamma Ray Observatory:

http://cossc.gsfc.nasa.gov/docs/cgro/cgro/

[6] Homepage of NASA Goddard Space Flight Center, EGRET technical information:

http://cossc.gsfc.nasa.gov/docs/cgro/egret/egret_tech.html

[7] Homepage of NASA Goddard Space Flight Center, Introduction to EGRET:

http://cossc.gsfc.nasa.gov/docs/cgro/egret/egret_doc.html

[8] Official NASA GLAST Website:

http://glast.gsfc.nasa.gov/science/instruments/table1–1.html

[9] Michelson P.F. et al., NASA Proposal *GLAST Large Area Telescope Flight Investigation: A Particle-Astrophysics Partnership Exploring the High-Energy Universe* Stanford University (November 1999, Reissued January 2000)

[10] Stecker F. W. *et al.* Astrophys. J. **464** 600 (1996)

[11] Salamon M. H. *et al.* Astrophys. J. **493** 547 (1998)

[12] S. Perlmutter *et al.* Astrophys. J. **483** 565 (1997) ; S. Perlmutter *et al.* Astrophys. J. **517** 565 (1999) ; P.M. Garnavich *et al.* Astrophys. J. Lett. **493** 53 (1998) ; A. Riess *et al.* Astron. J. **116** 1009 (1998) ; J.L. Trony *et al.* Astrophys. J. **594** 1 (2003) ; R.A. Knop *et al.* arXiv:astro-ph/0309368

[13] C.L. Bennett *et al.* Astrophys. J. Suppl. **148** 1 (2003)

[14] L.Bergström Nuclear Physics B (Proc. Suppl.) **70** 31 (1999)

[15] L. Bergström Nuclear Physics B (Proc. Suppl.) **138** 123 (2005)

[16] J.F. Navarro, C.S. Frenk and S.D.M. White Astrophys. J. **462** 563 (1996)

[17] H. Mayer-Hasselwander *et al.* Astron. Astrophys. **335** 161 (1998)

[18] A. Cesarini *et al.* Astrop. Phys. **21** 267 (2004)

[19] Official NASA GLAST Website, Anti-coincidence detector:
http://glast.gsfc.nasa.gov/acd/images/dtj/tilecurv_4.html

[20] Sonoma State University's GLAST website:
http://www-glast.sonoma.edu/resources/multimedia/gallery/brochure/index.html

[21] Knoll G. F. *Radiation Detection And Measurement* (John Wiley & Sons, 1989)

[22] Leo W. R. *Techniques for Nuclear and Particle Physics Experiments* (Springer-Verlag, 1994)

[23] Scintillator crystal properties:
http://www.marketech-scintillators.com/index.html
MarkeTech International Inc.

[24] Weber M.F. *et al.* Science **287** 2451 (2000)

[25] Johnson N. et al., *GLAST Large Area Telescope Calorimeter Subsystem Peer Design Review 17 & 18 March 2003* Naval Research Laboratory (2003)

[26] Wigmans R., Zeyrek M.T. Nucl. Instr. and Meth. in Physics Research **A485** 385 (2002)

[27] Ahn H.S. *et al.* Nucl. Instr. and Meth. in Physics Research **A410** 179 (1998)

[28] Ikeda H. *et al.* Nucl. Instr. and Meth. in Physics Research **A441** 401 (2000)

[29] Barlow R.J. *et al.* Nucl. Instr. and Meth. in Physics Research **A420** 162 (1999)

[30] Bridgman P.W. Patent No. 1,793,672, Filed Feb.16, 1926, Granted on Feb.24, 1931

[31] Zaslavsky B.G. Journal of Crystal Growth **200** 476–482 (1999)

[32] Hamada M. *et al.* Nucl. Instr. and Meth. in Physics Research **A486** 330 (2002)

[33] Chowdhury M.A.H. *et al.* Nucl. Instr. and Meth. in Physics Research **A413** 471 (1998)

[34] Chowdhury M.A.H. *et al.* Nucl. Instr. and Meth. in Physics Research **A432** 147 (1999)

[35] Zhu R. Nucl. Instr. and Meth. in Physics Research **A413** 297 (1998)

[36] Kazui K. *et al.* Nucl. Instr. and Meth. in Physics Research **A394** 46 (1997)

[37] Grove E., GLAST LAT Document nr. LAT-SS-00210-04, *LAT CAL Subsystem Specification – Level IV Specification*, NRL, Washington D.C. (August 2004)

[38] Johnson N.W., GLAST LAT Document nr. LAT-SS-00018-09, *LAT CAL Subsystem Specification – Level III Specification*, NRL, Washington D.C. (November 2001)

[39] Gayshan V. *et al.* Nucl. Instr. and Meth. in Physics Research **A505** 97 (2003)

[40] Labview manual: http://www.labview.com, National Instruments Corporation, 11500 N Mopac Expwy, Austin, TX 78759-3504, United States

[41] Grove E., GLAST LAT Document nr. LAT-SS-00108-02, *Calorimeter Crystal Optical Test Station Software Requirements*, NRL, Washington D.C. (July 2001)

[42] Sylgard 184 Elastomer: http://www.dowcorning.com, Dow Corning Corporation, Corporate Center, PO box 994, MIDLAND MI 48686-0994, United States

[43] Grove E., *CsI Light Asymmetry and Position Resolution: SLAC '97, MSU'98, and CERN '98*, GLAST Calorimeter Meeting, Saclay, France (1998)

[44] Bergenius S., *GLAST CsI(Tl) Crystals* Licentiate Thesis, Royal Institute of Technology, Stockholm, Sweden (2004)

[45] National Insitute of Standards and Technology Physics Laboratory home page:

http://www.physics.nist.gov/PhysRefData/XrayMassCoef/tab4.html

[46] Bergenius Gavler S. *et al.* Nucl. Instr. and Meth. in Physics **A545** 842 (2005)

[47] Beylin D.M. *et al.* Nucl. Instr. and Meth. in Physics **A541** 501 (2005)

[48] PAW++ reference manual, available at:

http://paw.web.cern.ch/paw/

[49] Walck C. *Hand-book on Statistical distributions for experimentalists* Internal Report, Stockholm University, Sweden (2000)

[50] Bergenius Gavler S., *Counting Calories – Studies of Energy Loss in a Segmented Calorimeter* Doctoral Thesis, Royal Institute of Technology, Stockholm, Sweden (2006)

[51] Bruel P., *Energy reconstruction at high energy with the LAT* Internal report, Ecole Polytechnique, Palaiseau, France (2005)

Appendix A

Reprinted from **Nuclear Instruments and Methods in Physics Research**, **A545**, S. Bergenius Gavler, S. Carius, P. Carlson, G. Johansson, W. Klamra, M. Pearce, *Radiation tests of CsI(Tl) crystals for the GLAST satellite mission*, p.842–851, copyright 2005, with permission from Elsevier.

Available online at www.sciencedirect.com
SCIENCE DIRECT®
ELSEVIER
Nuclear Instruments and Methods in Physics Research A 545 (2005) 842–851
NUCLEAR INSTRUMENTS & METHODS IN PHYSICS RESEARCH Sect. A
www.elsevier.com/locate/nima

Radiation tests of CsI(Tl) crystals for the GLAST satellite mission

S. Bergenius Gavler[a,*], S. Carius[b], P. Carlson[a], G. Johansson[b], W. Klamra[a], M. Pearce[a]

[a]*The Royal Institute of Technology (KTH), Physics Department, AlbaNova University Center, 10691 Stockholm, Sweden*
[b]*University of Kalmar, Department of Technology, Kalmar, Sweden*

Received 2 February 2005; accepted 14 February 2005
Available online 26 April 2005

Abstract

The electromagnetic calorimeter of the Gamma-ray Large Area Space Telescope (GLAST) consists of 16 towers of CsI(Tl) crystals. Each tower contains 8 layers of crystals (each $326.0 \times 26.7 \times 19.9\,\mathrm{mm}^3$) arranged in a hodoscopic fashion. The crystals are read out at both ends with PIN diodes. Crystals produced by Amcrys-H are used. As a part of the quality control procedure during crystal production, samples from the uncut boules were systematically irradiated with gamma-rays from a ^{60}Co source. The decrease in light yield due to radiation damage was measured, determining the radiation hardness of the boule. All boule samples passed the radiation hardness requirements, showing an average decrease in light yield of (14±4)% after having received a dose of 200 Gy. Studies have also been carried out to verify the correspondence between the post-irradiation properties of the boule samples and the full-size crystals which are subsequently cut from the boule. A crystal log was irradiated with gamma-rays from a ^{60}Co source and showed a decrease in light yield of (24±4)% after a dose of 180 Gy. A full-size crystal was also irradiated with a 180 MeV proton beam and the radiation induced attenuation and induced radioactivity was studied. The light yield was found to have decreased with (22±5)% after 175 Gy, and the dominant radioactive isotopes were identified.
© 2005 Elsevier B.V. All rights reserved.

PACS: 95.55.Ka; 29.40.Vj; 07.87.+v

Keywords: GLAST; Gamma-rays; Calorimeter; Crystal scintillators; CsI(Tl); Radiation damage

1. Introduction

The Gamma-ray Large Area Space Telescope (GLAST) [1] will study the gamma-ray sky across the energy range 10 keV–300 GeV. It will continue

*Corresponding author.
E-mail address: sarabe@particle.kth.se (S. Bergenius Gavler).

0168-9002/$ - see front matter © 2005 Elsevier B.V. All rights reserved.
doi:10.1016/j.nima.2005.02.032

the work started by EGRET [2] and identify sources that could not be resolved as well as further exploring the high-energy gamma-ray spectrum. The GLAST collaboration is multinational and consists of institutions from France, Germany, Italy, Japan, Sweden and USA. Launch is scheduled for 2007, and the design lifetime is 5 years. GLAST comprises of two instruments, the Large Area Telescope (LAT) and the GLAST Burst Monitor (GBM).

The LAT is built up by 4×4 identical towers, each tower consisting of a silicon tracker and an electromagnetic calorimeter. Incident gamma-rays interact in the converter foils of the tracker [3] and convert to an electron–positron pair, whose energy can be measured through the electromagnetic showers induced in the calorimeter. The whole instrument measures about $1.6 \times 1.6 \times 0.75\,\mathrm{m}^3$, and has a total depth of $10X_0$.

The calorimeter [4] will measure the energy and direction of the gamma-rays in the energy range 10 MeV–300 GeV. It consists of 1536 CsI(Tl) crystal logs, each measuring $326.0 \times 26.7 \times 19.9\,\mathrm{mm}^3$, and has a depth of $8.5X_0$. Each tower consists of 8 layers of 12 crystals, stacked so that alternate layers are arranged orthogonally (Fig. 1). The crystal logs have a cross-section which is smaller than the Molière radius (38 mm) for electromagnetic showers. This level of segmentation is sufficient to allow spatial imaging of the shower and reconstruction of the incident photon direction. Each crystal is optically isolated by a reflective material and the scintillation light is read out with dual PIN diodes (Hamamatsu S8576) at each end. The position of the energy deposition along a crystal log is determined by comparing the light yield from the crystal ends.

Fig. 1. Each calorimeter tower consists of 8 layers of 12 CsI(Tl) crystals stacked in an x–y configuration. A calorimeter tower contains 96 crystal logs and measures about $40 \times 40 \times 20\,\mathrm{cm}^3$. In total there are 1536 crystals.

In orbit, the crystals will be exposed to cosmic radiation causing a gradual degradation of the light yield. To test the radiation hardness, CsI(Tl) crystals have been irradiated with both gamma-rays and protons. Three different types of radiation tests have been performed. In the first two tests, ^{60}Co gamma-rays were used to irradiate boule samples and 'full-size' crystals, i.e. crystals with the same dimensions as flight crystals. In the third test a full-size crystal was irradiated with 180 MeV protons. The purpose of the second test was to obtain a correspondence between the radiation hardness of the boule sample and a full-size crystal. By using the result from this it is possible to get an estimate of the expected performance of the full-size crystals from that boule. The purpose of the third test was to measure the effect of protons, the main background for GLAST, and compare the results with those of gamma-ray irradiation.

The radiation environment and its possible effects on the light yield are described in the next section, followed by a description of the CsI(Tl) crystals used in the radiation hardness tests (Section 4). Sections 5–9 describes the different radiation tests of the CsI(Tl) crystals, and the results. Conclusions are presented in the final section.

2. Radiation environment

GLAST will orbit the earth at an altitude of 600 km and at an inclination of 28.5°. At this altitude there are four main sources of background particles; galactic cosmic rays (GCR), trapped particles, solar energetic particles (SEP) and albedo particles. The trapped particles are low-energy (<100 MeV) charged particles from the solar wind or products from particle interactions in the atmosphere, caught by the magnetic field surrounding the Earth. The trapped particle belts are well above the GLAST orbit, except for a

region over the southern Atlantic Ocean due to an irregularity in the Earth's magnetic field. This region of highly increased particle flux is called the South Atlantic Anomaly (SAA). Outside the SAA (~90% of the GLAST orbit) the GCRs are the dominant source of charged particles. The SEPs are primarily protons from coronal mass ejections and are well shielded by the magnetosphere. The estimated SEP rate is about 10% of the GCRs [5]. Albedo particles are secondary products created in collisions of cosmic-rays with the upper atmosphere. The albedo particles dominate at low energies, where the GCRs are depleted by the Earth's magnetic field.

The particle rate in the calorimeter outside the SAA averaged over many orbits is estimated to be ~2900 (2300) s^{-1}, and the peak rate is ~16000 (13000) s^{-1} for solar minimum (maximum) [5]. However, the major contribution to the total dose in the calorimeter is from low-energy trapped protons from the SAA, where the rate is $\sim 3 \times 10^7 s^{-1}$ on average with a peak rate of $\sim 2 \times 10^8 s^{-1}$.

GLAST is designed to withstand a total dose of 100 Gy during its 5 year mission, whereas the actual total dose is expected to be around 20 Gy. It is primarily the outer layers of crystals in the calorimeter that will receive such a dose, since the trapped charged particles are not energetic enough to penetrate to the inner parts of the calorimeter.

3. Radiation effects

Radiation damage in scintillation crystals can cause a degradation in luminescence and in transparency. The radiation-induced defects and traps decrease the number of carriers (electrons and holes) available to transfer energy to the luminescence centres, resulting in less scintillation light. If the traps are shallow, trapped carriers may be released thermally and contribute to the scintillation process. This delayed scintillation light is known as 'afterglow'. Degradation in transparency is due to trapped electrons forming so-called colour centres, which can absorb optical photons, thus introducing absorption bands in the emission spectrum of the scintillator. This self-absorption is especially problematic in the gamma detectors used in high-energy physics, where large scintillators often are required. The GLAST CsI(Tl) crystals are long and narrow and a small decrease in optical transmission can therefore become significant when accumulated over the length of the scintillator.

Irradiation with gamma-rays causes ionisation or a small recoil of the atoms in the crystal lattice. The displacement can be restored over time by, for instance, thermal annealing. However, the damage due to protons can cause permanent displacements. Protons can also cause activation of the crystal by nuclear interaction with the crystal atoms. The amount of induced activity depends on the rate of isotope creation in the crystals and the half-life of the induced isotopes. If the production rate is larger than the decay rate radioactivity is built up, inducing noise at energies corresponding to the gamma-rays from the decays.

The luminescence in CsI(Tl) is mainly due to the presence of Tl doped into the CsI crystal material. However, the radiation damage depends on the amount of impurities in the crystal, of which Tl is the most abundant. Hence, the radiation hardness increases with decreasing Tl-concentration. The GLAST CsI(Tl) crystals are manufactured by Amcrys-H [6] in Ukraine, and have a uniform Tl-distribution and low Tl-concentration resulting in relatively radiation hard crystals.

4. CsI test samples

The GLAST CsI(Tl) crystals grown by Amcrys-H are cut from boules. A typical boule measures about 300 mm in diameter, 400 mm in height, weighs about 400 kg, and between 25 and 50 crystal logs can be cut from one boule. Two cylindrical 'boule samples', 25.0 mm in diameter and 25.0 mm in height, are cut from the top and the bottom of the boule.

The Tl-concentration is usually higher at the bottom of a CsI boule, and therefore the bottom sample is more radiation soft. To test the radiation hardness of the GLAST calorimeter crystals, the bottom sample of every boule is irradiated with gamma-rays. This is taken as a measurement of the

radiation hardness of the boule. The boules are accepted if the boule sample exhibits less than 50% degradation in light output after having received a dose of 100 Gy of gamma-rays (1.173 and 1.333 MeV) from ^{60}Co. When a boule is approved, the calorimeter crystal logs are cut from the boule (Fig. 2), and labelled according to which boule they are cut from and their position in the boule.

In order to determine whether boule samples represent well the radiation hardness of the boules, a crystal log was irradiated with gamma-rays. The decrease in light yield from the log was compared with the results from the boule sample tests.

5. Radiation hardness tests of boule samples

The boule sample acceptance tests were conducted at an intense ^{60}Co source located at the Karolinska Hospital (KS) in Stockholm, Sweden. The source is calibrated once a year using ion-chamber dosimetry, where the dose rate is measured in a water sample placed at a known distance from the ^{60}Co source, and at 5 mm depth in the water where the dose is maximum. Ion-chamber dosimetry is accurate to 0.1%. The dose rate in CsI can be calculated by considering the absorption coefficients for water and CsI at 1.25 MeV (the average energy of a decay event of ^{60}Co), and it was found to be 0.81 of that in water. The dose deposited in a CsI crystal can be determined with an accuracy of ~1%, where the main contribution to the uncertainty comes from determining the distance from the ^{60}Co source to the crystal.

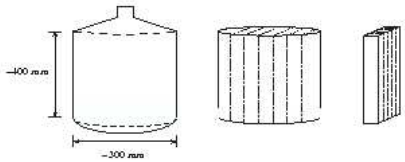

Fig. 2. CsI(Tl) boule cutting procedure. the dashed lines indicate how the crystal logs are cut. Left: the uncut boule. Middle: top and bottom has been removed and slices are cut from the boule. Right: a slice is cut into crystal logs.

Each boule sample irradiated had a PIN diode (Hamamatsu 3590-05) attached on the end surface with a wax-like meltmount substance [7]. The boule sample with its PIN diode was wrapped in a reflective layer of Tyvek [8] and light-tight Tedlar [9]. The light yield of the crystal sample was measured by using a small ^{22}Na source, with gamma energies of 0.511 and 1.275 MeV, placed against the crystal surface opposite to the PIN diode. The signal from the PIN diode was read out using a preamplifier mounted close to the diode, and further amplified using a NIM linear amplifier. The preamplifier was shielded to reduce noise pickup from external fields. The test set-up is shown in Fig. 3. A multichannel analyser (MCA) with 4096 channels allowed the ^{22}Na energy spectrum to be reconstructed. The channel number of the 0.511 MeV peak was used as a measure of the light yield from the crystal. The statistical uncertainty from the 0.511 MeV fit is small, and the dominant error in peak position is systematic and comes from limited reproducibility of light yield measurements. The reproducibility of the ^{22}Na spectrum was tested by disconnecting and reconnecting an unirradiated boule sample from the test set-up. The uncertainty was found to be 0.7% during 48 h, which is the time-scale of an acceptance test.

Before the irradiation of a crystal started, a reference spectrum was taken with the ^{22}Na source. The crystal, with its diode mounted, was

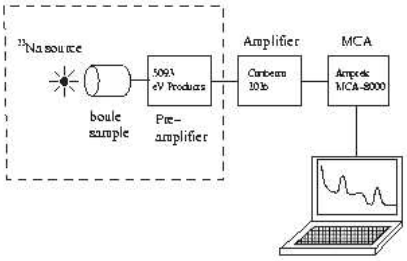

Fig. 3. Test set-up electronics and data taking system for the light yield measurement of the boule samples. The ^{22}Na source, crystal and preamplifier were housed in a metal box (dashed line). The MCA has 4096 channels.

then disconnected from the electronics set-up and exposed to the ^{60}Co source, with its cylinder axis perpendicular to the radiation field. The effects of radiation damage of the PIN diodes are regarded as negligible. The crystal was subsequently connected to the data taking system again, and the light yield was measured. After each irradiation period, the boule sample was rotated 90° along its cylinder axis to ensure a uniform irradiation.

6. Results of boule sample tests

The effect of afterglow was monitored for a boule sample by measuring the light yield with the ^{22}Na source every 20 min after irradiation during 1 h. The average dose rate was 2.8 kGy/h in the crystal. The crystal clearly became more noisy after irradiation, and Fig. 4 shows that both the light yield and the full-width at half-maximum (FWHM) of the 0.511 MeV peak increased after irradiation. This effect decreased with time. One hour after irradiation the light yield had stabilised. Therefore, the crystal was left to 'cool down' for 1 h after irradiation before light yield was measured, to minimise any systematic effects from afterglow.

Radiation damage of CsI(Tl) crystals depends not only on accumulated dose but also on the dose rate [10]. This was verified by irradiating boule samples at two different dose rates, 2.6 kGy/h and 31 Gy/h. The bottom and top boule samples from two different boules were used. The boule samples exposed to a higher dose rate show a more rapid decrease in light yield as shown in Fig. 5. After a dose of about 100 Gy, the total degradation in light yield is at least 5% worse for the higher dose rate compared to the lower. The dose rate chosen for the final boule sample acceptance tests was 20 Gy/h. In orbit the expected dose rate will be $\sim 10^4$ times lower, the acceptance tests will therefore set a conservative upper limit for the degradation in light yield.

All boule sample crystals show a fast initial decrease in light yield after a dose less than approximately 20 Gy, followed by a slower decrease. Fig. 6 shows the result of the acceptance

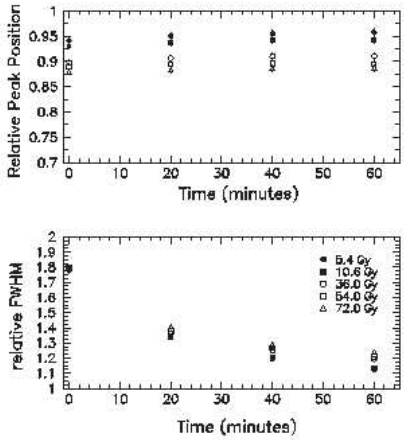

Fig. 4. Light yield (top) and the relative FWHM (bottom) of the boule samples measured up to 1 h after irradiation. Relative peak position is defined as the relative change in channel number of the 0.511 MeV peak as compared to the unirradiated crystal.

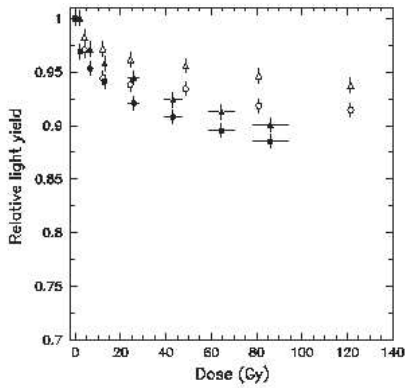

Fig. 5. Decrease in light yield for 4 different boule samples irradiated at different dose rates. Open and filled symbols show the result of irradiation with a dose rate in CsI of 31 Gy/h and 2.6 kGy/h, respectively. Boule samples from the same boule are represented by the same symbol.

tests. The observed decrease in light performance is expected [10,11] and is well within the limits specified for the GLAST CsI(Tl) crystals. The decrease in light yield is less than 27% for all crystal samples after a dose of 100 Gy. The average degradation at 100 Gy is $(12 \pm 3)\%$, and $(14 \pm 4)\%$ at 200 Gy. The errors are statistical.

7. Gamma irradiation of CsI(Tl) logs

A CsI crystal log was irradiated at the ^{60}Co source at KS. The crystal had all surfaces polished and was wrapped in VM2000 [12], a highly reflective multi-layer polymeric film, while both ends were left naked. Scintillation light was read out at each end by PMTs (Hamamatsu R669) via a 2 mm air gap. Air gaps were found to give better reproducibility than a direct optical connection and this was considered an advantage since the loss of light was relatively small.

The light yield was measured using the 0.846 MeV gamma-ray peak from a collimated ^{56}Co source. The reason for changing the reference source was because of the much higher level of afterglow noise from the crystal logs. The large amount of afterglow, which was not seen in the boule sample measurements, can be explained by accumulation over the crystal length. It was difficult to resolve the 0.511 MeV peak of the ^{22}Na source due to the afterglow, and a reference source with a gamma-line at higher energies was needed.

When measuring the light yield, the crystal, PMTs and the ^{56}Co reference source were contained in a light-tight box, as shown in Fig. 7. The collimator and source can be mechanically moved with an accuracy of about 2 mm, enabling the light yield to be measured stepwise along the crystal. The signals from the PMTs were amplified using a NIM linear amplifier and fed to two ADCs.

Before and after irradiation, the light yield was measured at both ends whilst placing the ^{56}Co source at several longitudinal positions of the crystal. During irradiation, the crystal was removed from the test box and placed with its long axis perpendicular to the radiation field of the ^{60}Co source. The crystal was rotated 180° along its long axis after each irradiation step, so that

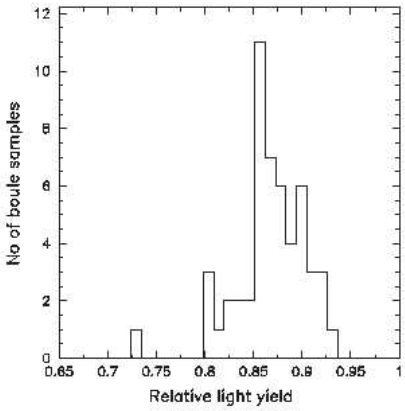

Fig. 6. Degradation in light yield of the boule sample crystals at 100 Gy.

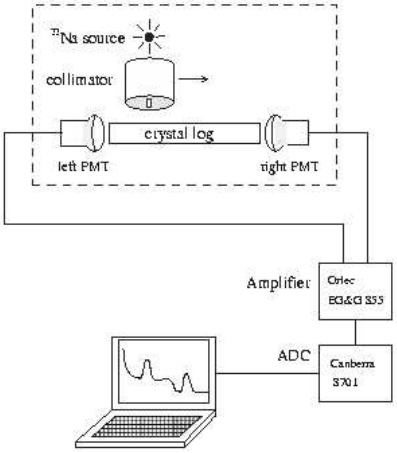

Fig. 7. Test set-up for the radiation hardness test of a crystal log. The PMTs and the crystal were contained in a light-tight box (dashed line).

deposited gamma energy would be as uniformly distributed as possible throughout the crystal volume. The dose rate was chosen to be 20 Gy/h in the crystal and irradiation proceeded in steps so that the accumulated dose became 20, 50, 150, and 180 Gy.

8. Results of gamma irradiation of CsI(Tl) logs

The crystal log showed substantial afterglow even several hours after irradiation, and this complicated the light yield measurements. After 6 h of cool-down, the afterglow from the crystal log gave a 20–30% larger light yield compared to the unirradiated crystal due to light pile-up. In order to correct for the pile-up, the light yield was measured continuously after the last irradiation period and the afterglow decay as a function of time was determined. After 70 h, the light yield had become stable showing a decrease of approximately 30% compared to the unirradiated crystal, and remained so up to 140 h after irradiation had stopped. The light yield after 20, 50 and 150 Gy was measured 6 h after irradiation, and had to be corrected by subtracting the afterglow using the decay relation.

The large level of afterglow seen in the crystal logs after irradiation will not cause any problem for the GLAST mission, since the readout threshold will be above the low-energy afterglow noise. In addition, the afterglow bias will be removed when the calorimeter is calibrated.

The decrease in light yield from the crystal is presented in Table 1. Close PMT is defined as the light yield from the end of the crystal which the reference source is held close to. After 180 Gy, the average light yield from the crystal had decreased by $(24 \pm 4)\%$, the error coming from uncertainty of losses in the light connection between the crystal and the PMTs. Afterglow correction introduced a relatively small systematic error.

No significant difference could be seen between left and right PMT with the ^{56}Co source located at the same relative position along the crystal. However, with the source located at the end of the crystal there is a significant difference in the decrease of light yield between the end close to and the end far from the source. For a 180 Gy dose, the close PMT shows a decrease of $(18 \pm 4)\%$, whereas the far PMT shows a $(30 \pm 4)\%$ decrease. This is interpreted as being due to two different components contributing to the light loss. When the source is placed far from the PMT, and the light has to travel throughout the crystal, the decrease in light yield is significantly larger than when the source is placed close to the PMT. This effect was similar for both left and right PMT. Thus, the conclusion is that both light production as well as light attenuation in the crystal material becomes worse after irradiation, where light production is reduced by $(18 \pm 4)\%$. Light attenuation was found to be about 0.4% per cm in the crystal.

Table 1
Decrease of light yield from the crystal log after gamma irradiation

Dose(CsI) (Gy)	Close PMT (%)	Far PMT (%)	Average (%)
0	0	0	0
20	1 ± 5	18 ± 5	10 ± 5
50	14 ± 5	29 ± 5	22 ± 5
150	18 ± 5	34 ± 5	26 ± 5
180	18 ± 4	30 ± 4	24 ± 4

The second (third) column shows the average of left and right PMT when the source is positioned close to (far from) the PMTs. The forth column shows the average of columns two and three. The light yield measured after 20, 50 and 150 Gy has been corrected for afterglow.

The result of the gamma irradiation of the crystal log can be compared with the results of boule sample tests, by considering the light yield when the reference source is close to the PMT. In this position the direct scintillation light travels approximately the same distance to the photosensor as for the boule sample. The average decrease in light yield for the boule samples at 200 Gy is $(14 \pm 4)\%$, which agrees well with the number $(18 \pm 4)\%$ after 180 Gy found for the long crystal logs when the source was placed close to the PMT.

9. Proton irradiation of CsI(Tl) logs

A crystal log was irradiated at the TSL (The Svedberg Laboratory) cyclotron at Uppsala

University, which delivered a 180 MeV proton beam. The CsI(Tl) signal was read out with PIN diodes attached to each end of the crystal, using silicon grease [13] as an optical connector. The crystal was wrapped in reflective VM2000, and light-tight Tedlar. The signals from the PIN diodes were treated as described in the boule sample test set-up (Section 5).

Substantial noise from afterglow and induced isotopes was expected after the proton irradiation. Therefore, the light yield of the crystal was measured with cosmic-ray muons, since they can be externally triggered. The muons have an energy loss dE/dx close to minimum and therefore deposit on average 5.6 MeV/cm per particle in the crystal [14]. A penetrating muon was identified by a telescope made of two 2 cm wide plastic scintillators placed above and below the crystal at its centre. A simultaneous signal from both plastic scintillators triggered the readout of the scintillation light from the crystal. The peak position of the fitted muon distribution was taken as a measure of the light yield. The set-up was calibrated by taking a muon spectrum before the crystal was exposed to the proton beam.

During irradiation, the CsI(Tl) crystal log was placed 13 m downstream from the beam pipe window as shown in Fig. 8. The protons were scattered in an aluminum foil at the window resulting in a wide, symmetric beam profile at the location of the crystal. Before irradiation the beam profile was mapped out, showing that the proton intensity decreases 10 cm from the beam centre and outwards. Therefore, the crystal log was placed at an angle of 45° to the beam axis in order to obtain as uniform illumination as possible. The variation in beam intensity along

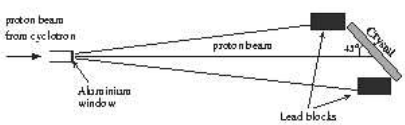

Fig. 8. Schematic figure of the proton beam test set-up. The PIN diodes are shielded by lead blocks during proton irradiation.

the length of the crystal was less than 20% from the centre of the crystal to its ends, and the average value was 93.8% of the peak intensity of the beam. The crystal was placed with the 26.7 mm side facing the beam direction so that the protons had to penetrate the shortest distance. The PIN diodes were attached during proton irradiation and were therefore shielded by 10 cm lead blocks, placed in front of each crystal end as shown in Fig. 8. The beam intensity was continuously monitored by a beam telescope put at 30° scattering angle from the aluminum window. The calibration of the telescope counting rate versus beam intensity at the crystal location was performed before irradiation, giving a dose rate of 7.4 Gy/h in the CsI crystal. Protons deposited 41 MeV in the crystal with a variation of 18% less at the front surface than at the rear surface because of the increase of energy loss dE/dx with decreasing proton energy. The total dose was 175 Gy in the crystal.

10. Result of proton irradiation

Before the crystal was irradiated with protons, the intrinsic gamma activity was measured down to 40 keV with a Ge(Li) detector during approximately 4 h. Only a few gamma-ray lines were observed, and the total intensity of the background was found to be ~2 counts/s, mainly coming from β^+ annihilation and ^{40}K giving a line at 511 and 1460.8 keV, respectively.

Light yield was measured and averaged over the left and right end of the crystal log during 7 days after the proton irradiation had terminated. It had decreased by (22 ± 5)% on average, which is of the same magnitude as for gamma-rays. The error reflects the maximum deviation from the average.

The first gamma spectrum of the irradiated crystal measured with the Ge(Li) detector after completion of irradiation showed some 40 gamma lines. Many different nuclear reactions are possible, such as (p,xn), (p,pxn), $(p,\alpha xn)$ and $(p,\alpha pxn)$. In addition, secondary neutrons may induce reactions, and as a result many different isotopes are produced. Some could easily be identified like ^{127}Xe (from ^{127}I). Table 2 shows the identified isotopes. Many of these are short-lived and will

not cause any build-up of light background noise in orbit, since the dose rate in orbit will be 10^4 times lower than during the TSL test. A few isotopes like ^{133}Ba having half-life of 10 years are a potential risk.

In Fig. 9 the gamma intensity measured with the Ge(Li) detector is plotted as a function of the time after irradiation stopped. Clearly, the bulk of the induced activity has decreased after 10 days, indicating that activation of the calorimeter crystals should not be a problem since the activation rate in space is much lower than during the TSL test.

11. Conclusions

All boule samples tested passed the acceptance tests. The average decrease in light yield after 200 Gy gamma irradiation from a ^{60}Co source was $(14 \pm 4)\%$, and no boule sample showed a decrease larger than 27%. The gamma-ray irradiation of a crystal log showed a decrease of $(24 \pm 4)\%$ after a dose of 180 Gy. It also revealed two different components of radiation damage, a decrease in light production and increased light absorption. This was found when comparing the light yield from one end when placing the reference source close and far from it. Light attenuation was found to be about 0.4% per cm in the crystal, and may explain the difference between the result for the boule samples and crystal logs. The average decrease in light yield for the boule samples at 200 Gy is $(14 \pm 4)\%$, which is compatible with that found after 180 Gy, $(18 \pm 4)\%$, for the long crystal logs when the source was placed close to the PMT. The conclusion is that radiation hardness tests of boule samples may well represent the radiation hardness of the GLAST CsI(Tl) crystals.

Table 2
Identified isotopes from the activated CsI(Tl) crystal

Isotope	Half-life	Energy (keV)
^{131}Ba	12 d	496.3, 373.2, 216.1
^{132}Cs	6.5 d	667.7
^{129}Cs	32.3 h	371.9, 411.5
^{127}Xe	36.4 d	202.9, 172.1, 375.0
^{127}Cs	6.2 h	412.0, 287.2, 462.3, 587.0
^{125}Xe	17.0 h	188.4 243.4
^{124}I	4.2 d	602.7, 1691.0
^{121}I	13.0 h	159.0
^{122}Sb	2.7 d	564.2
^{121}Te	16.8 d	573.1
^{117}Sb	2.8 h	158.6

The identification was partly possible from studies of the decay of gamma lines. All nuclear data are from Ref. [15].

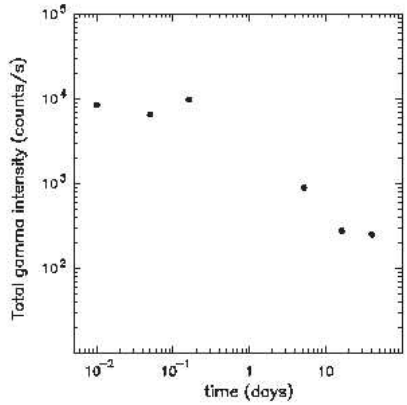

Fig. 9. The total gamma intensity of the activated crystal measured with a Ge(Li) detector.

Irradiation of crystal logs with 180 MeV protons show a decrease in light yield of $(22 \pm 5)\%$ after 175 Gy, a result which is comparable to the gamma irradiation test. The induced gamma activity in the crystal log was measured with a Ge(Li) detector up to 40 days after irradiation, and some of the induced isotopes were identified. After 175 Gy the gamma activity had increased with a factor of 10^4 relative to the initial activity. After 10 days it had decreased with a factor of 10^2, leaving a more slowly decaying gamma background assumed to be due to more long-lived isotopes. The dose and dose rate during the proton irradiation test were 10, respectively, 10^4 times higher than expected in orbit for the GLAST crystals. The proton irradiation test therefore gives an upper limit of the induced gamma activity in the CsI(Tl) logs during the mission.

Acknowledgements

The authors would like to thank the staff at KS and TSL for their help during the experiments, Eric Grove for valuable correspondence and Leif Nilsson technical support. We also thank the K.A. Wallenberg foundation, The Swedish Research Council and The Swedish National Space Board for financial support.

References

[1] P.E. Michelson. GLAST: a detector for high-energy gamma-rays. SPIE Conference on Gamma-Rays and Cosmic-Ray Detectors. Techn. Missions 2806 (1996) 31.
[2] G. Kanbach. et al.. Space Sci. Rev. 49 (1988) 69.
[3] R.P. Johnson. The GLAST LAT Silicon Tracker. Proceedings of the 47th SPIE Meeting. Seattle. WA. 2002.
[4] W.N. Johnson. J.E. Grove. B.F. Phlips. J.P. Norris. A.A. Moiseev. A CsI(Tl) hodoscopic calorimeter for the GLAST mission. IEEE Nuclear Science Symposium. vol. 1. 1997. pp. 27–31.
[5] GLAST Internal Report. Eric Grove. Particle Background Estimates for GLAST. http://heseweb.nrl.navy.mil/glast/tech_memos/tech_memos.htm
[6] http://www.amerys-h.com/
[7] Meltmount* 1.704. http://www.cargille.com/meltmount
[8] DuPont Tyvek.
[9] DuPont Tedlar PVF film.
[10] R.Y. Zhu. Nucl. Instr. and Meth. A 413 (1998) 297.
[11] M.A.H. Chowdhury. et al.. Nucl. Instr. and Meth. A 432 (1999) 147.
[12] Radiant light film. 3M company.
[13] General Electric. Viscasil 60M 1.4035. http://www.gesilicones.com/
[14] D.E. Groom. et al.. Eur. Phys. J. C 15 (2000).
[15] NuDat 2.0. http://www.nndc.bnl.gov/nudat2. National Nuclear Data Center. Brookhaven National Laboratory.